University of Cape Town

Department of Chemical Engineering

PHASE EQUILIBRIA STUDIES AND BENEFICIATION OF TITANIFEROUS SLAGS

By

Xolisa Camagu Goso (GSXXOL002)

A thesis submitted to the Faculty of Engineering and the Built Environment, University of Cape Town, in fulfilment of the requirements for the degree

Doctor of Philosophy (PhD)

DEPARTMENT OF CHEMICAL ENGINEERING

UNIVERSITY OF CAPE TOWN

October 2019

Supervisor	**:**	**Prof Jochen Petersen (UCT)**
Co-supervisor	**:**	**Dr Johannes Nell (Hatch)**

DECLARATION

I, Xolisa Camagu Goso, hereby declare that the work on which this thesis is based is my original work (except where acknowledgements indicate otherwise) and that neither the whole work nor any part of it has been, is being, or is to be submitted for another degree in this or any other university.

I empower the university to reproduce for the purpose of research either the whole or any portion of the contents in any manner whatsoever.

Signed by candidate on this 8th day of October 2019

(Candidate)

ABSTRACT

Titaniferous magnetite (titanomagnetite) offers a unique opportunity for the production of three valuable products from one resource. It generally contains economically appreciable reserves of vanadium and iron as well as significant contents of titanium. Titanomagnetite is typically smelted in blast or electric furnaces in the presence of reductant and fluxes (dolomite and quartz) to produce a valuable vanadium bearing pig iron and a virtually valueless titaniferous slag. The titaniferous slag by-products are generally defined by the Ca-Mg-Al-Si-Ti-O system. These fluxed slags can contain as high as 20-40wt% TiO_2 (titania). The lack of interest in processing titaniferous slags to produce saleable titania materials is attributed to the presence of chemically inert phases, like the spinel solid solution [$Mg(Al,Ti,V)_2O_4$] that cannot be handled by the available titania slag upgrading technologies.

The understanding of phase relations in titaniferous slags is thus important in order to be able to implement a suitable fluxing strategy for the production of a treatable titaniferous slag with no inert spinel phase. The available phase equilibria data established in air for titaniferous slags is inconclusive about the possible crystallisation of the detrimental spinel. However, literature on phase compositions of plant titaniferous slags are conclusive about the crystallisation of $Mg(Al,Ti,V)_2O_4$ in high MgO and Al_2O_3 bearing slags. It is thus clear that the understanding of phase relations in titaniferous slags requires further development.

The objective of the current project was to investigate the phase equilibria and beneficiation of titaniferous slags to produce a saleable titania product. As a development to previous work, the composition of the slag for review was based on the available work, namely; TiO_2 = 37.19wt%, SiO_2 = 19.69wt%, and Al_2O_3 = 13.12wt%, at varying proportions of CaO (30-0wt%) and MgO (0-30wt%). The phase equilibria studies followed a systematic approach involving the review and validation of the available equilibrium phase diagram produced in air, followed by the determination of updated phase equilibria at low oxygen partial pressures (pO_2) of 10^{-16} atm applicable to titanomagnetite smelting. The generic approach of studying phase equilibria in multicomponent systems was followed, namely; (1) literature survey of the available thermodynamic and phase equilibria data applicable to the reviewed system, (2) calculation and re-drawing of the equilibrium phase diagrams using FactSage thermochemical software, and (3) equilibration-quench-(electron probe micro analysis) (EPMA) experiments to the validate calculated equilibrium phase relations. A titaniferous

slag with little crystallisation of the inert spinel phase, based from the best fluxing strategy with an MgO-free limestone, was produced by smelting in conventional (using alumina crucible) and cold copper crucible induction furnaces for subsequent beneficiation using the established Upgraded Slag (UGS) process. A conceptual flowsheet for the production of vanadium, steel and titanium products was therefore designed and subsequently subjected to economic evaluation using the discounted cash flow (DCF) modelling approach.

Thermodynamic and phase equilibria literature for the Ca-Mg-Al-Si-Ti-O system demonstrated that this system and some subsystems are well researched in air, and not as much in low pO_2 atmospheres applicable to smelting operations.

The FactSage software used in the current study for the calculation of phase equilibria in the Ca-Mg-Al-Si-Ti-O system applicable to titaniferous slags does not have tialite (Al_2TiO_5) modelled as a component in the customary pseudobrookite solution database - Al_2TiO_5 is a component of the pseudobrookite solution reported in literature for the current system. Hence, a private pseudobrookite solution database applicable to the reviewed system, i.e. $MgTi_2O_5$-Al_2TiO_5-Ti_3O_5, was developed and incorporated into FactSage before any calculation could be conducted. Thermodynamic modelling of the $MgTi_2O_5$-Al_2TiO_5-Ti_3O_5 system was conducted through the CALculation of PHase Diagram (CALPHAD) method. The sublattice model coupled with compound energy formalism (CEF) and Redlich-Kister polynomial were adopted. The model information was incorporated into FactSage to create a private database for subsequent calculations of phase equilibria of titaniferous slags.

The equilibrium phase diagram for the Ca-Mg-Al-Si-Ti-O system in the same compositional range as in the available literature was then calculated in air. The liquidus surfaces and phase relations in the equilibrium phase diagrams of available literature and FactSage calculation are fairly comparable. However, at high MgO concentrations: FactSage calculation predicts that $Mg(Al,Ti)_2O_4$ is the primary phase, followed by successive crystallisation of pseudobrookite solid solution ($MgTi_2O_5$-Al_2TiO_5) and forsterite (Mg_2SiO_4); and the available literature reports $MgTi_2O_5$-Al_2TiO_5 as the primary phase, followed by Mg_2SiO_4. The crystallisation of spinel phase in the available phase diagram produced in air is not predicted. The crystallisation of the spinel solid solution phase in titaniferous slags is extensively reported in the open literature. Equilibration-quench-EPMA experimental results produced in air generally compared well to the FactSage calculations. The inability of the available phase diagram to predict spinel phase crystallisation was attributed to the

lack of sensitive analytical techniques in the late 1960s, when the available phase diagram was developed.

The phase equilibria of titaniferous slags were further calculated at low pO_2 atmospheres of 10^{-16} atm. In the reviewed compositional range of titaniferous slags, the liquidus surface and Ti^{3+}/Ti^{4+} mass fraction ratio increased with decreasing the pO_2. There was no significant difference in terms of the crystallisation of phases between the calculated results in air and at pO_2 of 10^{-16} atm, except that the size of the primary phase field at higher MgO concentrations than the composition for the minimum liquidus temperature increased and the pseudobrookite solution included Ti^{3+} bearing phase, i.e. $MgTi_2O_5$-Al_2TiO_5-Ti_3O_5. Equilibration-quench-EPMA experimental results produced at pO_2 of 10^{-16} atm generally compared well to the FactSage calculations. The new phase equilibria at low pO_2 of 10^{-16} atm shows that the crystallisation of the chemically inert $Mg(Al,Ti)_2O_4$ in titaniferous slags would occur if the slag contains high Al_2O_3 concentration and MgO concentration of 2wt% and above. However, the crystallisation of $Mg(Al,Ti)_2O_4$ in titaniferous slag is not significantly sensitive to variation in the TiO_2 concentration in, and basicity of the slag.

To produce a titaniferous slag with minimum possible inert spinel content for subsequent beneficiation, the South African Main Magnetite Layer (MML) titanomagnetite concentrate was smelted in the presence of an MgO-free lime and low ash Sasol carbon (SASCARB) reductant. This smelting approach would produce a titaniferous slag with about 4wt% MgO, which would come from the titanomagnetite – based on the phase equilibria, this slag should crystallise a small amount of the inert spinel. When the smelting was conducted in an alumina crucible placed inside a conventional induction furnace, the slag was inevitably contaminated by Al_2O_3 from the refractory container. This slag crystallised a significant $Mg(Al,Ti)_2O_4$ with the content approximated by the MgO concentration – the significant $Mg(Al,Ti)_2O_4$ crystallisation was attributed to the Al_2O_3 saturation in the titaniferous slag.

A titaniferous slag containing a treatable ulvospinel phase was produced in a cold copper crucible induction furnace – the crystallisation of the ulvospinel, instead of the chemically inert spinel solid solution was attributed to the saturation of the slag by iron from the incomplete reduction process due to the inevitable stoppage of the heat supply to the induction furnace as soon as the susceptor iron metal and produced pig iron settled at the bottom of the copper crucible. For the purpose of demonstrating the feasibility of producing

titania products from titaniferous slags, this slag was also subjected to beneficiation using UGS process.

The current study successfully demonstrated that the titaniferous slags can be beneficiated to saleable titania products using the UGS process: the TiO_2 in the $Mg(Al,Ti)_2O_4$ bearing waste titaniferous slag produced by the defunct Evraz Highveld Steel and Vanadium Corporation (EHSV) was upgraded from about 33wt% to 75wt%, while the TiO_2 in the titaniferous slags produced in conventional and cold crucible induction furnaces were upgrade from about 30wt% to 67wt% and 22.00wt% to 90.45wt%, respectively. The remaining impurities in the 75wt% and 67wt% TiO_2 UGS products were mainly MgO and Al_2O_3 contained in the refractory spinel solid solution. In the case of the 67wt% TiO_2 product, there was excess Al_2O_3 in the spinel structure – the excess Al_2O_3 remained in the glass phase.

Though the 90.45wt% TiO_2 product is attractive for use as feedstock for the production of the preferred chloride pigment, this product however contained finer PSD and higher concentrations of impurities such as SiO_2, Al_2O_3, and CaO, than the specification for the chloride process feedstock. This product was thus not a suitable feedstock for the chloride pigment production. Further optimisation of the UGS conditions has a potential to reduce the concentrations of impurities to levels suitable for feedstock for the preferred chloride pigment production process. Further investigations are also required to study the feasibility of the chlorination of micro-pellets of the UGS product. Since the UGS product is mainly composed of rutile structure, it would not be a suitable feed for the sulfate pigment production as the sulfuric acid lixiviant is unable to dissolve the rutile structure. Only if soluble in sulfuric acid, this high TiO_2 bearing UGS product produced from titaniferous slags could be used as advantageous feedstock for the sulfate pigment production in terms of the minimization of the reagent consumption and the amount of the toxic sulfate waste.

Based on the work of the current study, literature data and Pyrosim simulations, a conceptual process flowsheet for the production of vanadium slag, steelmaking pig iron and titania product was proposed. The economic modelling of the conceptual flowsheet for a 20 year operational projection showed that the process is economically viable. The process economic viability is sensitive to variation in the Opex and Revenue. In addition, additives, such as the amount and type of reductant, fluxes, and reagents account for about 75% of the Opex. It is possible that the additives are overestimated in the process as the recycle streams

were not included in the proposed process and economic model. At the same time, the economic model does not consider the environmental and waste management costs. Hence, the economic analysis is considered to be preliminary in nature, or indicative at best.

The current study has demonstrated that (1) a titaniferous slag containing little or no inert spinel phase that is suitable for upgrading can be produced when the MgO content in the slag is below 2wt% - the best approach to producing a slag with minimum possible MgO content would be to smelt the titanomagnetite in the presence of an MgO-free limestone flux and low ash reductant, and (2) it is technically and economically feasible to produce three products, i.e. V slag, steelmaking pig iron, and titania product, from titanomagnetite.

DEDICATION

To my late parents:

Gen. King David Zamukulungisa Goso

Mrs. Essina Nolusapho Goso

ISAIAH 40:31 (NIV)

"but those who hope in the Lord will renew their strength. They will soar on wings like eagles; they will run and not grow weary, they will walk and not be faint."

ACKNOWLEDGEMENTS

I am very grateful to all contributions that made this project work. The following organisations and people receive the well-deserved acknowledgement:

- Prof Jochen Petersen from the University of Cape Town and Dr Johannes Nell from Hatch provided great support and advice throughout the duration of the project as my supervisors – an average idea was developed into a PhD level project with their great assistance. The time given by my supervisors for technical meetings, including the training on the use of FactSage software is greatly appreciated.

- Mintek provided funds for the registration of the project for PhD studies at the University of Cape Town. The project was also funded and completed at Mintek through the ferrous minerals science vote cluster. Appreciation is also extended to the Norwegian University of Science and Technology (NTNU) in Norway for availing their cold crucible induction furnace for completion of some of the experiments under the INTPART metal production project.

- Great thanks to Mr Archie Corfield of Mintek's mineralogy division (MNL) for assistance in the preparation and analyses of various samples using mineralogical analysis techniques. Gratitude is extended to Dr Vincent Canaguier of NTNU for training on the operation of the cold crucible induction furnace. Appreciation is also extended to the Analytical Services Division of Mintek for assistance with the bulk chemical analyses of various samples. I am also grateful for the process economic evaluation guidance provided by Ms Thandazi Mnisi and Mr Thandukwazi Bungane from the Mintek's mineral economic support unit of Mintek (MESU).

- Special thanks to Prof Petersen and his team of postgraduate students at the Chemical Engineering Dept. of UCT for the valuable input during the usual seminars – the food was also delicious. Special thanks is also extended to Dr Joalet Steenkamp and the entire team participating in the reputable 'Soapbox' presentation skills development platform at Mintek's pyrometallurgy division (PDD) – the comments and advice provided during these sessions were very helpful.

- I am grateful for the many efforts that contributed to the success of the project, particularly the high temperature laboratories (HTL) team of PDD, i.e. Herman, Sanele, Patricia, Metro, Vincent, Moshe, and Martin (as well as to student trainees:

Kgomotso, Mohau, Boitumelo and Mukovhe). The daily friendship that kept us together for the duration of my studies is appreciated.

- I owe my loving thanks to my family for the great inspiration and emotional support: late parents (Zama and Nolusapho), wife (Nosivuyise), children (Chulumanco, Babaliwe, Zozibini and Milani), siblings, cousins, aunts and friends.
- The Almighty God has done it again!

Kind regards,

Xolisa Camagu Goso

TABLE OF CONTENTS

LIST OF FIGURES

LIST OF TABLES

CHAPTER 1

INTRODUCTION

1.1 Introduction

Titaniferous magnetite (titanomagnetite) is defined as magmatic accumulations of magnetite and ilmenite with titanium dioxide (TiO_2/ titania) concentrations of more than 1wt%. It generally occurs with vanadium in many mineral deposits (Fischer, 1975). Vanadium bearing or vanadiferous titanomagnetite deposits are found in various countries throughout the world with the principal deposits found in Russia, China and South Africa (Taylor, et al., 2006; Cawthorn & Molyneux, 1986; Reynolds, 1985; Fischer, 1975)

Vanadiferous titanomagnetite contains economically appreciable reserves of iron and has become a primary source of vanadium throughout the world (Fischer, 1975). In addition, it has the potential to become a significant source of titanium. The iron that is recovered from titanomagnetite is mainly used to produce steel which is a primary material used in civil engineering and manufacturing industries (Roskill, 2007). Vanadium finds application in a number of industries including in ferroalloys as ferrovanadium (FeV) for the production of special alloys such as Fe-Ti-Al-V-Si and in catalysis as vanadium pentoxide (V_2O_5), an oxidation catalyst used for the production of various products including sulfuric acid from sulfur dioxide (Roskill, 2010). Titanium is primarily used as titania pigments for numerous applications including in paint, plastic and paper industries (Roskill, 2003).

Numerous commercial operations exist for the metallurgical processing of titanomagnetite for the extraction of primarily iron and vanadium with titanium generally deporting to the by-product stream (Steinberg, et al., 2011; Zhang, et al., 2007; Taylor, et al., 2006; Moskalyk & Alfantazi, 2003; NTMK, 2003; Kelly, 1993; Gupta & Krishnamurthy, 1992). Some of the commercial processes were designed based on the relative amounts of iron, vanadium and titanium in the respective titanomagnetite resources. Several industrial processes also differ depending on the era of the commencement of the operation (Taylor, et al., 2006). In some cases, vanadium is the primary product which is generally produced by the direct roast-leach processing of titanomagnetite; this process is also referred to as the vanadium primary production process (Roskill, 2010). In another case, steelmaking which is generally coupled with ‘co-production of vanadium’ is the primary focus (Steinberg, et al., 2011; Roskill, 2010; Taylor, et al., 2006; Moskalyk & Alfantazi, 2003; Gupta & Krishnamurthy, 1992).

Titanomagnetite is not an established titanium ore. With the exception of the projected Nyanza Light Metals operation to be built in South Africa (Africa, Mining review, 2017; Fin24.com, 2017), there is currently no commercial process for the primary recovery of titanium or titania from titanomagnetite and its by-products.

Titanomagnetite is typically processed by the steel and vanadium co-production process. In this process, the titanomagnetite is generally blended with a flux and reductant followed by smelting in a furnace to produce a valuable vanadium bearing pig iron and a low titania grade slag by-product. The process was established as a result of a pioneering research conducted by Bleloch (1949), in which he successfully demonstrated the use of submerged arc furnace (SAF) technology for the smelting of titanomagnetite (containing more than 12wt% TiO_2) which was mined from the Bushveld Complex in South Africa (Bleloch, 1949). The technology was established in the late 1960s and subsequently adopted by Evraz Highveld Steel and Vanadium Corporation (EHSV) in South Africa and New Zealand Steel (NZS – for processing iron sands) in New Zealand. EHSV adopted the SAF smelting technology. NZS however opted to use a partially open slag bath furnace (OSBF) technology. Later, both EHSV and NZS upgraded to full OSBFs in order to improve their process control and maximise the overall process productivity and vanadium recoveries to the pig iron (Steinberg, 2008; Rohrmann, 1985).

During the development of the technology for titanomagnetite smelting, the use of the conventional iron ore smelting blast furnace (BF) technology for smelting titanomagnetite containing in excess of 10wt% TiO_2 was deemed unfeasible. This view was attributed to the possible formation of reduced titanium species, i.e. titanium (oxy) carbides and nitrides, which would result in a slag with high viscosity and entrained metal, slag foaming, and blast tuyere blockages. These phenomena, individually or combined, would result in abnormal and poor performance of the blast furnace operation with reduced production rates as well as reduced iron and vanadium recoveries (Steinberg, 2008). However, some years later after the development of a procedure to dilute titania in the titanomagnetite feedstock, the BF technology for smelting titanomagnetite was successfully commissioned in China by Panzhihua Iron and Steel Limited (Pangang) and later by Chengde Iron and Steel (Chengde), and in Russia by EVRAZ Nizhny Tagil Iron and Steel (NTMK) (Roskill, 2010; Zhang, et al., 2007; Taylor, et al., 2006; NTMK, 2003).

As stated above, in a typical co-production process flowsheet, titanomagnetite is blended with carbon for selective reduction of vanadium and iron, and flux for the control of the slag liquidus temperature, thus the operational temperature. The blend is smelted in an electric or blast furnace to produce a valuable vanadium bearing pig iron and an essentially valueless low grade or diluted titania slag. The vanadium bearing pig iron is generally processed further to produce vanadium and steel products (Steinberg, et al., 2011; Roskill, 2010; Zhang, et al., 2007; Taylor, et al., 2006; NTMK, 2003; Kelly, 1993).

The corresponding slag, typically referred to as titaniferous slag (Jochens, et al., 1969), may contain between 20wt% and 40wt% TiO_2 as shown in Table 1, as a consequence of the inherently low titania content in the feed titanomagnetite and the dilution by the essential flux addition which is typically adopted to control the smelting temperatures (Bill, 2013; Steinberg, et al., 2011; Roskill, 2010; Taylor, et al., 2006).

The titania grades in the typical titaniferous slags are generally too low for the slags to be directly marketed as titania product. Case in point, a minimum feedstock grade for the preferred chloride process for the production of titania pigment is 85wt% TiO_2 (Pistorius, 2008). In addition, titaniferous slags are generally composed of complex phase chemistries that cannot be handled by the available titania slag upgrading technologies. Hence, the complex phase chemistry is partly responsible for the lack of interest in the secondary processing of these slags to produce saleable titanium products (Pistorius, 2011; Van Vuuren & Tshilombo, 2011). In view of the general desire to improve the overall process economics and maximise the exploitation of valuable resources, it is essential that the titaniferous slags are upgraded to saleable TiO_2 products.

Table 1: Chemical compositions of some titaniferous slags produced around the world (wt%)

Operation	Fluxed/ fluxless	FeO	MgO	Al_2O_3	SiO_2	CaO	**TiO_2**	**V_2O_5**
NZS*	Fluxed	2.11	13.3	17.8	15.2	15.9	**32.1**	**0.20**
Pangang[#]	Fluxed	nr	7.0	14.0	22.0	27.0	**22.0**	**nr**
NMTK and CHMP*	Fluxed	0.6-1.0	11-13	14-15	28-30	30-32	**8-10**	**0.18-0.30**
EHSV[+]	Fluxed	1.0	14.1	18.0	16.2	14.1	**35.6**	**0.90**
Mintek demo[$]	Fluxless	2.30	2.25	8.35	14.5	7.75	**62.0**	**0.78**

* (Hassell, et al., 2016), [#] (Sui, et al., 2004), [+] (Steinberg, 2008), [$] (Boyd, et al., 1993), nr – not reported

1.2 Problem statement

The titaniferous slags are generally described by the Ca-Mg-Al-Si-Ti-O system (Jochens, et al., 1969). Though these slags contain attractive titania grades of more than 20wt%, they are still not processed further to extract the titania because they generally comprise complex and inert chemical phases, like the spinel ($MgAl_2O_4$) or spinel solid solution [$(Mg)(Al,Ti)_2O_4$], which render the upgrading of these slags to saleable titania products technically challenging (Pistorius, 2011; Van Vuuren & Tshilombo, 2011). Fundamental understanding of the phase relations in the Ca-Mg-Al-Si-Ti-O system is therefore essential in order to be able to implement a suitable fluxing strategy for the production of a treatable titaniferous slag with little or no spinel.

Fortuitously, in his PhD research, Jochens (1967) studied the TiO_2-SiO_2-Al_2O_3-MgO-CaO system for fluxed titanomagnetite smelting at varying proportions of CaO and MgO, and subsequently established an equilibrium phase diagram which is shown in Figure 1 (Jochens, 1967). However, Jochens' phase diagram was established in air and is unreliable for predicting phases that would crystallise at applicable oxygen partial pressures (pO_2) to the titanomagnetite smelting operations. In particular, Jochens' phase diagram does not predict the crystallisation of reduced titanium phases, like Ti_3O_5, which were reported by Zhao et al. (2009) in their study of the Ca-Mg-Al-Si-Ti-O system applicable to blast furnace slags. In addition, the phase diagram does not predict the crystallisation of the chemically inert spinel phase which has been reported to be present in numerous commercial plant titaniferous slags (Pistorius, 2011; Steinberg, 2008).

Jochens' phase diagram is unreliable for the prediction of the correct equilibrium phases produced at the applicable pO_2 to titanomagnetite smelting operations. The understanding of phase relations in titaniferous slags therefore required further development with a view of identifying a slag chemistry with little or no spinel to facilitate further upgrading to produce titanium products.

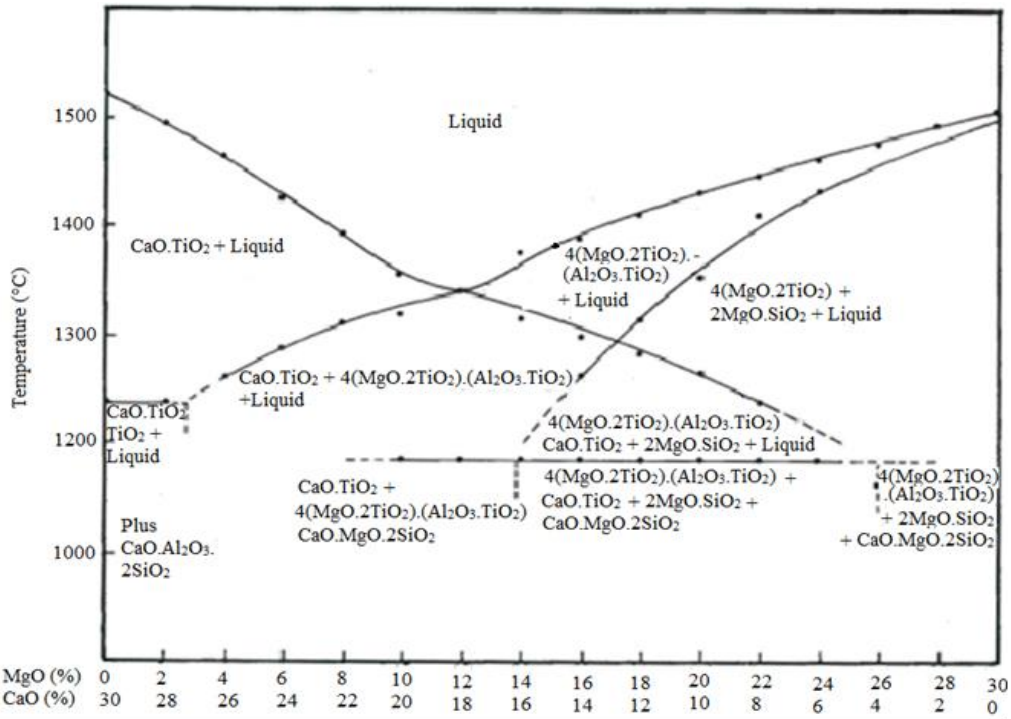

Figure 1: Equilibrium phase diagram established in air for the slag system: TiO_2 = 37.19wt%, SiO_2 = 19.69wt%, and Al_2O_3 = 13.12, at varying proportions of CaO (30-0wt%) and MgO (0-30wt%) (Adapted from Jochens, 1967)

1.3 Focus of the study

For reliable predictions of the crystallisation of phases in titaniferous slags and possibly the identification of treatable slag chemistries with little or no spinel for titania recovery, it is essential to review and validate Jochens' phase diagram in air and at applicable pO_2 to titanomagnetite smelting. The applicable pO_2 to titanomagnetite smelting was deduced from Ellingham phase diagrams for the reduction of vanadium oxide to vanadium metal to be about 10^{-16} atm at operational temperatures of 1500°C (Habashi, 2002) – the operational pO_2 in the furnace is, of course, not exclusively driven by the pO_2 for a pure V metallization; this approach was adopted in order to have a reference point (see section 3.3.1.2 for the rationale). Phase equilibria for titaniferous slags at varying flux compositions at low pO_2 were studied through a combination of the review of available thermochemical and phase equilibria data, simulation using a thermochemical software, and experimentation. A study for re-drawing a suitable phase diagram for typical titaniferous slags was conducted with a view of finding conditions for crystallising treatable slag chemical phases for subsequent titania recovery from the titaniferous slags.

A titaniferous slag composition with minimum chance of spinel crystallisation was targeted and produced for subsequent beneficiation using the established upgraded slag (UGS) process for the production of high grade titania materials (Borowiec, et al., 1998; Doan, 1996). A flowsheet for the production of vanadium, steel and titanium products was designed and subjected to economic evaluation to investigate its viability.

The following set of objectives was thus formulated to study the phase relations in, and subsequent production of titania products from, titaniferous slags.

- Thermochemical calculation of the phase relations in the Ca-Mg-Al-Si-Ti-O system in air and at applicable pO_2 to titanomagnetite smelting using FactSage thermochemical software. As part of this objective, thermodynamic modelling to develop a suitable pseudobrookite solid solution was undertaken and the established solution database was uploaded into FactSage for thermochemical simulation and calculation. Selected experiments to review and validate Jochens' and calculated phase equilibria in air and at applicable pO_2 in titanomagnetite smelting were conducted.
- Production of titaniferous slags containing no spinel and beneficiation to demonstrate the production of saleable titanium products.
- Preliminary development and evaluation of an integrated titanomagnetite process flowsheet for the production of Fe, V and Ti products.

1.4 Scope of the work

The scope of the study entailed (1) the phase equilibria studies to re-draw Jochens' phase diagram in air for validation purposes and at pO_2 applicable in titaniferous smelting for the establishment of a reliable phase diagram applicable to titaniferous slags, (2) production and beneficiation of selected titaniferous slags for the production of titania products, and (3) evaluation of an integrated flowsheet for the processing of titanomagnetite to produce Fe, V and Ti products.

1.4.1 Phase equilibria studies in the Ca-Mg-Al-Si-Ti-O system

The phase relations in the multicomponent Ca-Mg-Al-Si-Ti-O system are in fact very complex (Pistorius, 2011). Following the typical approach to studying phase equilibria in multicomponent and multiphase systems, the phase equilibria study in the current testwork included (a) survey of the available thermodynamic and phase equilibria data in the Ca-Mg-Al-Si-Ti-O system, (b) calculation and redrawing of suitable equilibrium phase diagram using a thermochemical software, and (c) strategic experimentation to validate calculated phase diagrams.

1.4.1.1 Literature survey in the Ca-Mg-Al-Si-Ti-O system

To understand the phase equilibria in multicomponent or higher order systems, subsystems are generally reviewed (Jung, et al., 2009; Wulandari, et al., 2009; Jak & Hayes, 2004). For the literature review of thermochemical and phase equilibria data in the Ca-Mg-Al-Si-Ti-O system, numerous subsystems were reviewed. Due to numerous possible lower order combinations in the high order Ca-Mg-Al-Si-Ti-O system and the fact that the titaniferous slags are characterised by the presence of TiO_2, the reviewed binary, ternary and quarternary subsystems were subjectively limited to those containing TiO_2.

1.4.1.2 Calculation of phase equilibria

It is essential to take advantage of available computational thermochemical and thermodynamic software for simulating and depicting complex phase equilibria. In the present work, the thermodynamic predictions of phase equilibria in the Ca-Mg-Al-Si-Ti-O system were conducted using FactSage software, an established commercial computer package used worldwide for the calculation of multi-component phase equilibria and thermodynamic properties (Bale, et al., 2002).

In his study of the Ca-Mg-Al-Si-Ti-O system applicable to titaniferous slags in air, Jochens (1967) reported, amongst other things, that $4(MgO.2TiO_2).Al_2O_3.TiO_2$ or stoichiometrically $4MgTi_2O_5$-Al_2TiO_5 crystallises as the primary phase at relatively high MgO concentrations in the reviewed compositional range. The latest FactSage 7.2 version does not have Al_2TiO_5 modelled as an endmember in the pseudobrookite (M_3O_5) solid solution database (Centre for Research in Computational Thermochemistry, 2018). In addition, Berezhnoi and Bulko (1955) and Krajewski (1992) reported in their studies of the Al-Mg-Ti-O system that under

reducing conditions, Ti_3O_5 would crystallise in the M_3O_5 solution. Hence, the latest FactSage 7.2 model would not be able to correctly predict the phase relations in the Ca-Mg-Al-Si-Ti-O system in air and at low pO_2 atmospheres in which case the M_3O_5 solid solution is anticipated to be composed of $MgTi_2O_5$, Al_2TiO_5, and Ti_3O_5 endmembers.

Pseudobrookite solid solution thermodynamic models for the $MgTi_2O_5$-Ti_3O_5, $MgTi_2O_5$-Al_2TiO_5, and Al_2TiO_5-Ti_3O_5 subsystems were developed and integrated to ternary $MgTi_2O_5$-Al_2TiO_5-Ti_3O_5 system, and subsequently incorporated into FactSage as a private pseudobrookite solid solution database. The principles of the CALculation of PHAse Diagram (CALPHAD) method were adopted during the development of the private pseudobrookite solid solution database for the correct calculation of phase equilibria using the evaluated and optimized thermochemical data in the literature. The application of the CALPHAD method in the current study is shown in Figure 2. It should be noted that the experimentation for the optimisation of the private pseudobrookite database fell outside the scope of the current work and was not conducted; instead optimized thermodynamic data from literature was used (Bale, et al., 2002; Pelton, et al., 1998). Following the established thermodynamic approach, the pseudobrookite solid solution was modelled using the sublattice model coupled with Compound Energy Formalism (CEF) and Redlich-Kister polynomial. In real multicomponent and multi-phase systems, the Gibbs energy of a solid solution can be expressed as shown in Equation [1.1] (Pelton, 2006; Hillert, 2001; Shi, et al., 1992).

$$G_m = \sum_i \sum_j y_i' \, y_j'' G_{ij}^0 - TS^{config} + G^{excess} \qquad [1.1]$$

Where y_i' and y_j'' are site fractions on first and second sublattices, G_{ij}^0 is the Gibbs energy of formation of the compound ij, also called 'endmember', S^{config} is the ideal entropy of mixing. The main parameters of the CEF stage of the model are the endmember Gibbs energies. The G^{excess} is the excess Gibbs energy of mixing of the real solution described by the Redlich-Kister polynomial.

FactSage 7.2 equipped with the private pseudobrookite solid solution database was used to calculate and reproduce Jochens' phase diagram (Figure 1) in the same compositional range in air. The scope of FactSage calculations was increased to include the predictions of phase equilibria in the same and other compositional ranges at low pO_2 applicable to titanomagnetite smelting.

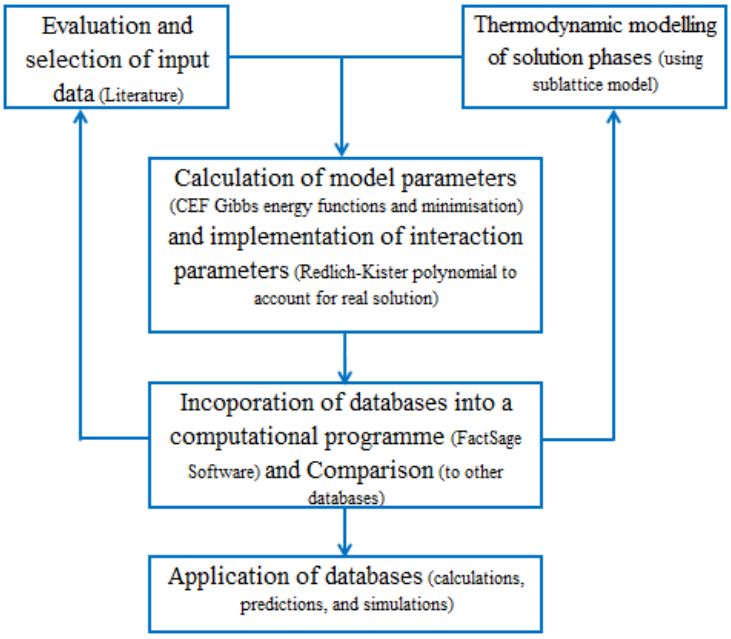

Figure 2: CALPHAD method adopted for database development and calculations of phase diagrams

1.4.1.3 Experimentation

Systematic experimental equilibrium phase stability studies in air and at pO_2 of 10^{-16} atm using the established integrated high temperature equilibration, quench and Electron Probe Micro Analysis (EPMA) approach (Jak & Hayes, 2010) were undertaken to cross-validate the FactSage predictions of phase relations in the Ca-Mg-Al-Si-Ti-O system.

1.4.2 Beneficiation of titaniferous slag

A slag chemistry with a minimum chance of the crystallisation of the detrimental spinel solid solution [$(Mg)(Al,Ti)_2O_4$] was identified on the updated phase equilibria at low pO_2 applicable to titanomagnetite smelting. The targeted titaniferous slag was produced by smelting using the conventional and cold crucible induction furnaces. The slag was subjected to beneficiation testwork to demonstrate the production of a saleable titania product from a titaniferous slag.

Some processes dedicated to the upgrading of dilute titania resource, like titaniferous slags, to saleable TiO_2 products are reported in the open literature (Hassell, et al., 2016; Van Vuuren & Tshilombo, 2011; Zhang, et al., 2007; Fouad, 2005; Becker & Dutton, 2002). These processes have several disadvantages including the production of materials of still

insufficient titania grades to qualify as high titania materials, and poor titania recoveries. There is a market for the titania product with a minimum of 70wt% TiO_2 (Shijiazhuang Leveling import and export Co., Ltd., 2014); the first prize is however to produce a suitable feedstock for the preferred chloride pigment production process.

Titaniferous slags typically contain high levels of alkaline earth impurities like MgO and CaO from the gangue, and from the flux in the case of dolomite/ limestone fluxed smelting. An oxidative-reductive roast and leach process, typically known as the Upgraded Slag (UGS) process, is established for upgrading titania slags with high levels of alkaline earth impurities. In the UGS process, the phase composition of the slag is modified through roasting to increase the leachability of the impurities. The UGS process is used commercially at Rio Tinto Fer et Titane (RTFT) in Canada for upgrading the SORELSLAG® slag generated from the Allard Lake ilmenite that contains relatively high levels of the alkaline earth impurities (Borowiec, et al., 1998; Doan, 1996). The scope of the current work involved a preliminary investigation of the best combination of UGS process conditions, in particular the leaching conditions, for the beneficiation of the selected titaniferous slag with little or no spinel to produce a saleable titania product.

An integrated flowsheet for the production of steel, vanadium and titanium products from a titanomagnetite feed was developed and subsequently subjected to economic evaluation using the discounted cash flow (DCF) model.

1.5 Layout of the thesis

The thesis is structured as presented below.

Chapter 1: Introduction: This section of the thesis offers a summary of the background and introduction, the problem statement, the focus and the scope of the project.

Chapter 2: Literature Review: This chapter provides literature pertinent to titanomagnetite resources and metallurgical processing, phase relations in the Ca-Mg-Al-Si-Ti-O system applicable to titaniferous slags with the introduction of thermodynamic modelling and simulation of some associated solid solution phases, experimentation in thermochemical studies, and beneficiation technologies of titania bearing resources to produce marketable titania materials.

Chapter 3: Materials and equipment: This section of the thesis gives details of the materials and equipment that were used in the current project. Fundamental operational principles, calibration and validation of some equipment are also discussed in this chapter.

Chapter 4: Phase equilibria of titaniferous slags: This section of the thesis includes the experimental and thermochemical simulation of the phase equilibria in the Ca-Mg-Al-Si-Ti-O system applicable to titaniferous slags in air and at applicable pO_2 to titanomagnetite smelting. This chapter also includes the thermodynamic modelling of the pseudobrookite solid solutions necessary for correct calculation of phase equilibria in the Ca-Mg-Al-Si-Ti-O system using FactSage thermochemical software.

Chapter 5: Beneficiation of titaniferous slags: This section details the work conducted for the smelting production of titaniferous slag, followed by beneficiation using the UGS process to demonstrate the production of a saleable titania product. A preliminary process flowsheet is developed based on the best combination of test conditions, and subsequently subjected to economic evaluation.

Chapter 6: Conclusions and Recommendations: The implications of the findings of the current work are summarised in this section. In addition, this section includes recommendations for future work in order to establish an economically robust and integrated operation for the production of vanadium, steel and titanium products from the titanomagnetite.

CHAPTER 2

LITERATURE REVIEW

2.1 Introduction

Titaniferous magnetite (titanomagnetite) is a mineral deposit that is composed of accumulations of ilmenite ($FeO.TiO_2$) and magnetite (Fe_3O_4) with a titania (TiO_2) concentration of more than 1wt%. Titanomagnetite deposits are commonly concentrated with vanadium (Fischer, 1975). It thus possesses a unique capacity to be used as a source of three commodities, namely; iron, vanadium and titanium (Taylor, et al., 2006).

Iron is a chemical element with symbol Fe and appears on number 26 in the Mendeleyev's periodic table. The symbol Fe originates from a Latin word 'ferrum' which means 'iron'. Iron forms much of the outer and inner core of the earth. In terms of mass, it is the most common element on earth. It is however the fourth most abundant element in the earth's crust. Fe metal is very strong and relatively inexpensive. The primary use of iron is as steel found in numerous applications including in manufacturing machine tools, automobiles, ships, machine parts and building parts (Roskill, 2007).

The element vanadium has symbol V. It appears on number 23 in the periodic table. Vanadium was named after the Scandinavian goddess of beauty and fertility, Vanadis, because of its beautiful colour, which is steel grey with a bluish tinge. V is one of the hardest of all the metals hence it is primarily used in the production of wear resistant and high speed tool steels (Mitchell, 2000).

Titanium (Ti) is a chemical element that is found on number 22 in the periodic table. It was named after the Titans of Greek mythology. Ti is the ninth most abundant chemical element in the earth's crust. Metallic Ti is mainly used in alloys with metals of other chemical elements including iron, aluminium, vanadium and molybdenum – the lightweight Ti alloys are used in aerospace, military, dental implant, jewellery and other applications. Ti metal is as strong as some common steels; hence, it has replaced steel in some applications because it has a relatively high strength-to-weight ratio. Nevertheless, the primary use of Ti is as titania or titanium dioxide (TiO_2), which is used as pigment for various applications including paint, plastic and paper industries (Roskill, 2003).

Titanomagnetite is an established source of Fe used in steelmaking and is the primary source of vanadium throughout the world (Fischer, 1975; Rohrmann, 1985). It has a potential to become an appreciable source of the valuable titanium metal and titania.

2.2 Geology of titanomagnetite

Titanomagnetite deposits are found in various countries around the world in mafic or basic, ultrabasic igneous rocks, commonly with gabbro and anorthosite, and sometimes in metamorphic rocks. The titanomagnetite deposits occur in the form of tubular or irregular ore bodies, seams or vein-like structures forming multi layers within mafic intrusions (Cawthorn & Molyneux, 1986; Reynolds, 1985). Titanomagnetite deposits are thus defined as layered mafic or ultramafic intrusions of primarily ilmenite ($FeTiO_3$) and magnetite (Fe_3O_4) (Fischer, 1975). A layered titanomagnetite deposit is shown in Figure 3 with the distribution of the different types of titanomagnetite deposits in the South African Bushveld Complex mineral base used as an example (Waldeck, 2013).

Titanomagnetite deposits are typically composed of ilmenite and magnetite with hematite (Fe_2O_3), rutile (TiO_2) and perovskite ($CaTiO_3$) reported in some deposits. The deportment of these minerals in the respective deposits is in the form of medium- to fine-grained intergrowths as well as in exsolution and solid solution. The exsolution and solid solution minerals are generally in the form of large ulvospinel (Fe_2TiO_4) and titanomagnetite [$Fe^{2+}(Fe^{3+},Ti^{3+})_2O_4$] deposits. Though some vanadium in the titanomagnetite occurs in different minerals like ilmenite and titanium minerals in the exsolution and solid solution, it is generally exsolved in the magnetite or magnetic concentrates as coulsonite [$(Fe,V)_3O_4$]. Discrete vanadium minerals are not reported in the prominent titanomagnetite deposits in the world (Cawthorn & Molyneux, 1986; Reynolds, 1985; Fischer, 1975).

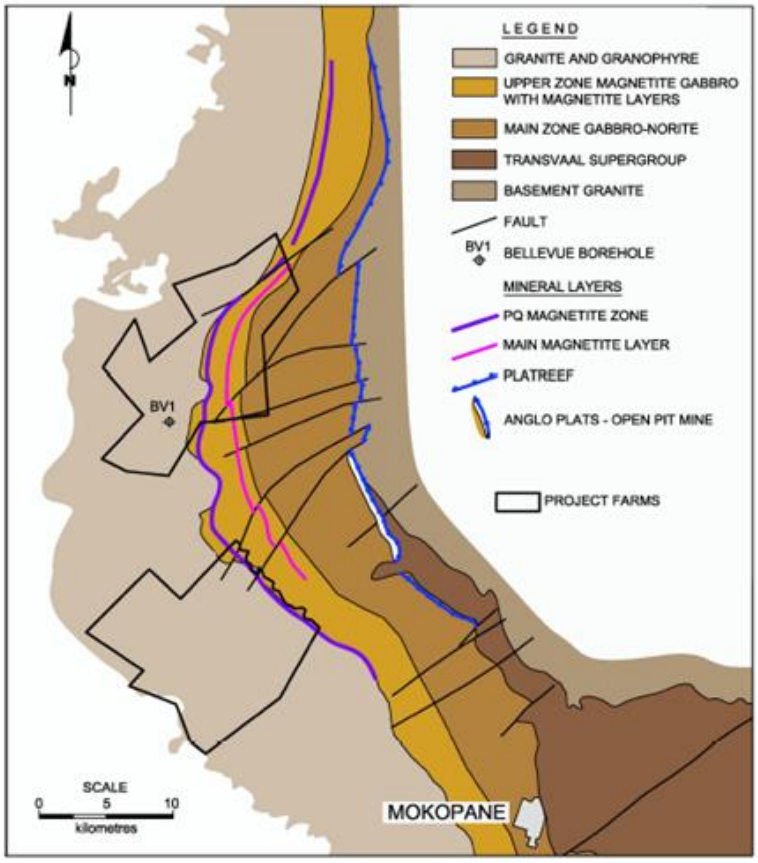

Figure 3: Distribution of the main zone and the upper zone of the Rustenburg layered suite showing the locations of the different titanomagnetite and other mineral deposits of the Bushveld Complex (Waldeck, 2013)

2.2.1 Deposits of titanomagnetite

Vanadium bearing or vanadiferous titanomagnetite deposits vary in size – from the economically insignificant deposits to large deposits of billions of tons of the ore. Economically significant titanomagnetite deposits are found in various countries throughout the world, including India, Australia, New Zealand, United States, Russia, China and South Africa (Roskill, 2010; Taylor, et al., 2006). Figure 4 shows the titanomagnetite global distribution and the economic class of countries where major deposits are located (Goldberg, et al., 1990). Vanadium bearing titanomagnetite deposits continue to be discovered and developed. For example, additional and valuable titanomagnetite deposits have recently been established in Uzbekistan (Dmitriev, et al., 2005).

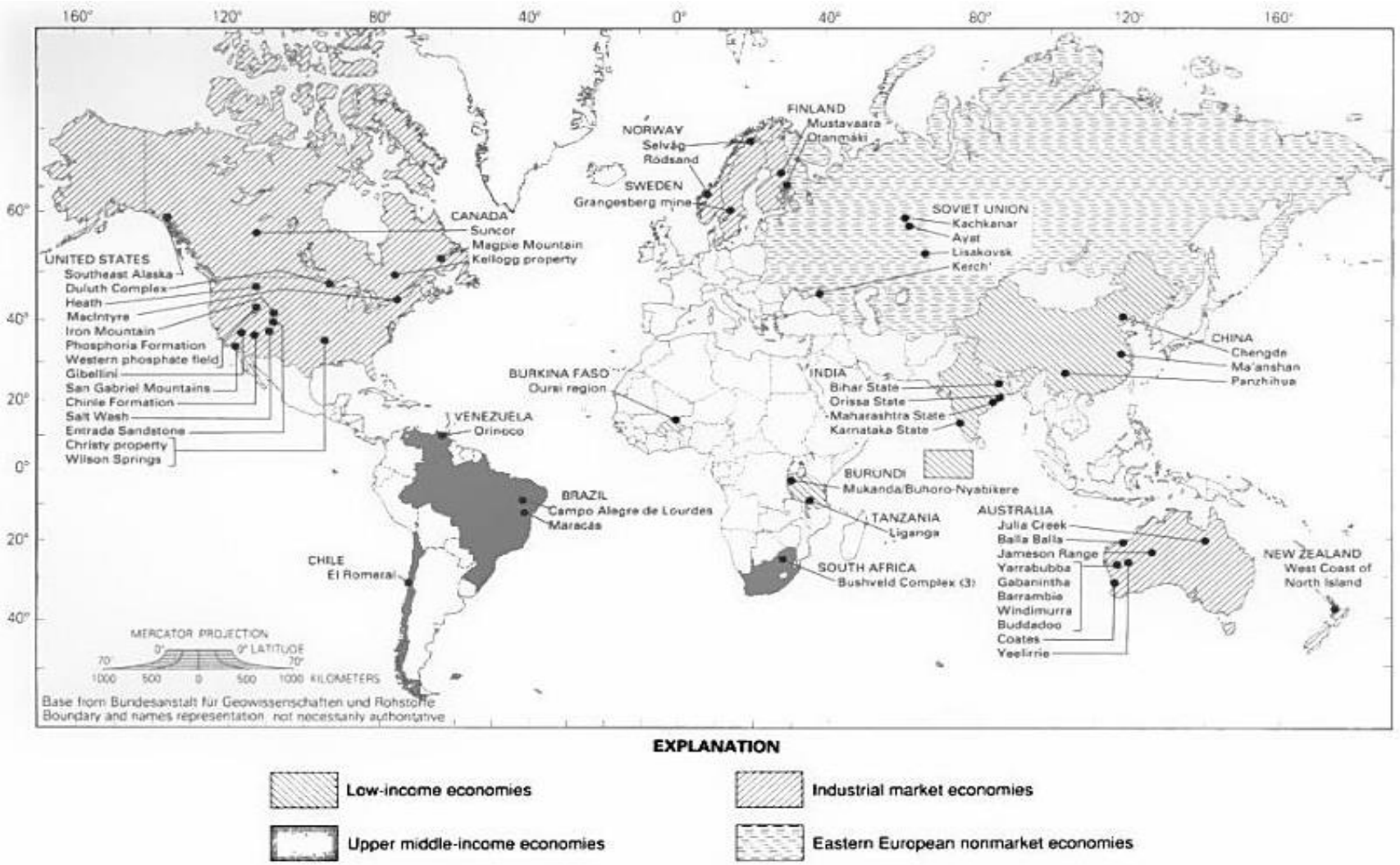

Figure 4: Distribution of vanadiferous titanomagnetite deposits in the world (Goldberg, et al., 1990)

Titanomagnetite deposits of major economic significance that have, in the past, been used primarily for the production of vanadium are found in Russia, China and South Africa (Taylor, et al., 2006). In Russia, titanomagnetite deposits are primarily found in Mount Kachkanar which is located in the central Ural Mountains or Urals that run approximately from north to south through western Russia. The major Chinese deposits of titanomagnetite make up more than 10% of the world's total. The major titanomagnetite deposit in China is referred to as Panzhihua mineral base and is located in the Sichuan province. The Panzhihua deposit accounts for over 70% of vanadium production in China (Taylor, et al., 2006; Moskalyk & Alfantazi, 2003; Goldberg, et al., 1990; Fischer, 1975).

South Africa boasts one of the largest known deposits of the titanomagnetite in the world. The titanomagnetite deposits in SA are primarily found in the legendary Bushveld Complex (BC) (Reynolds, 1985; Cawthorn & Molyneux, 1986; Goldberg, et al., 1990; Moskalyk & Alfantazi, 2003). The titanomagnetite deposits in the BC are the world's largest known layered intrusions, with an estimated area of 66 000 km^2 (Cawthorn & Molyneux, 1986). Essentially, the BC deposit is composed of an ultrabasic to basic unit, with a thickness of up to 9 km (Cawthorn & Molyneux, 1986; Reynolds, 1985).

The most important minerals in the BC, including the vanadiferous titanomagnetite, are concentrated in the Rustenburg layered suite, shown in Figure 3, which is further divided into zones, namely; the lower zone, critical zone, main zone and upper zone. The respective zones are distributed in three major mineral areas in the BC, which are known as the northern, eastern and western limbs. The lower zones, which are spread in all three limbs, host a number of important minerals including those of magnesium, chromium, nickel and precious metals (Edison, 2013; Kinnaird, 2005). The critical zone is located in the eastern and western limbs of the BC. This zone is composed of the established Merensky and UG2 reefs which are mined for platinum group metals (PGMs) and chromite. The main zone, on the other hand, is the thickest layer in the Rustenburg suit. The economic importance of the main zone is due to the PGMs and chromite that are concentrated in the Platreef located at the base of this zone (Kinnaird, 2005).

The upper zone of the Rustenburg layered suite is home to iron, titanium, vanadium and phosphorus-bearing ore layers formed from anorthosite and gabbronorite mineralisation (Kinnaird, 2005). One of the significant deposits in this zone is in the form of the vanadium

bearing titanomagnetite. The vanadiferous titanomagnetite layers are distributed across the eastern, western and northern limbs of the BC. The eastern limb primarily hosts the relatively high vanadium bearing titanomagnetite layer known as the Main Magnetite Layer (MML). The MML deposit has been mined since the 1950s and most recently was mined at the Mapochs mine for processing by the recently closed Evraz Highveld Steel and Vanadium (EHSV) operation (Steinberg, 2008). Some MML deposits have also been identified in the northern limb of the Rustenburg layered suit (Edison, 2013).

There is also a relatively low vanadium bearing titanomagnetite deposit that occurs above the MML deposit. This titanomagnetite deposit is referred to as the P-G magnetite zone, P-Q zone or Layer 21. The P-Q zone is thicker than the MML with an average thickness of 45 m. The distribution of the main zone and upper zone in the northern limb with respect to the position of the MML, P-Q zone and the Platreef deposits in the Rustenburg suit is shown in Figure 3 (Waldeck, 2013).

The typical chemical compositions of the MML and P-Q deposits are given in Table 2 (Waldeck, 2013). The obvious and significant differences in the two deposits are in the Fe and V_2O_5 concentrations. The MML deposit is more concentrated with both species; thus, it offers a relatively high Fe and V value for a ton of material processed.

Table 2: Typical chemical compositions of the MML and P-Q zone deposits of the BC (wt%)

Deposit	SG (g/ ml)	Fe	TiO_2	V_2O_5	SiO_2	Al_2O_3	P_2O_5	S
MML	4.04	44.7	9.70	1.48	11.2	8.30	0.01	0.01
P-Q zone	3.65	33.3	10.8	0.21	22.6	9.73	0.04	0.39

2.3 Metallurgical processing of titanomagnetite

In South Africa, titanomagnetite is regarded as one of the mineral resources of major economic importance. Thus, Mintek, the science council of the South African government, has been mandated to focus on titanomagnetite as a strategic mineral in order to provide research, development and technology transfer to foster the development of industries for titanomagnetite processing in South Africa (Lydall & Craven, 2013).

Titanomagnetite can be used as an unmatched source of three commodities, namely; iron, vanadium and titanium (Taylor, et al., 2006). To date, the titanomagnetite is an established source of iron used in steelmaking and is also established throughout the world as the primary source of vanadium used in ferro-alloys and chemical industries typically as FeV and V_2O_5, respectively (Roskill, 2010; Moskalyk & Alfantazi, 2003; Fischer, 1975).

Titanomagnetite is typically mined through open-cast mining followed by jaw crushing of coarse ore, milling to magnetite liberation size using autogenous or high pressure grinding roll (HPGR) mills (Liddell, 2011). Some development-scale titanomagnetite mineral processing work conducted at Mintek have included wet ball milling, magnetic separation and filtering on a belt filter to form a titanomagnetite concentrate stockpile (Thiele & Da Corte, 2013; Dawson & Bachmann, 1991; Koekemoer, 1991). The titanomagnetite concentrate is generally prepared for downstream metallurgical processing for vanadium primary- or co- production (Liddell, 2011).

Numerous metallurgical processes for the extraction of vanadium and iron from titanomagnetite are described in the open literature as summarised in the following subsections. The reviewed processes include development and commercial operations and can be classified in the following manner:

- Roast-leach process for vanadium primary production (Gupta & Krishnamurthy, 1992; Steele & Wilson, 1966)
- Direct reduction coupled with leaching for V, Fe and Ti production (Zhao, et al., 2014; Chen & Chu, 2014; Chen, et al., 2013; Chen, et al., 2011)

- Smelting process with high iron in the slag (for production of high grade pig iron and recovery of V and Ti from the slag) (Jena, et al., 1994) and with low iron in the slag for vanadium and steel co-production in the metal and production of a titania bearing or titaniferous slag (Boyd, et al., 1993; Bleloch, 1949)

2.3.1 Roast-leach process

The roast-leach process is used as a vanadium primary production process from titanomagnetite – in this process, iron and titanium generally form part of the waste stream. The conventional roast-leach process entails the oxidative roasting of the vanadium bearing titanomagnetite (or any vanadium bearing material like the vanadium slag) in the presence of an alkali or alkali earth reagent to produce the acid, base, or water soluble alkali or alkali earth vanadate compound. The vanadium in solution is typically precipitated and subsequently calcined to produce vanadium pentoxide (V_2O_5) for use in the chemical and catalysis industries and for the production of other vanadium products like ferro-vanadium (FeV) and other alloys (Taylor, et al., 2006; Moskalyk & Alfantazi, 2003; Gupta & Krishnamurthy, 1992).

The typical roast-leach approaches are summarised in the form of chemical reactions in Table 3. Due to the stringent environmental requirements and moderate operational temperature, the roast-leach processing of titanomagnetite is typically conducted using the soda ash option, i.e. Na_2CO_3 roasting, followed by water leaching. The vanadium in solution is generally precipitated as ammonium polyvanadate (APV) or ammonium metavanadate (AMV). The precipitate is typically subjected to de-ammoniation, and subsequently oxidised and fused at 850°C to produce high purity V_2O_5 flakes (Roskill, 2010; Taylor, et al., 2006; Gupta & Krishnamurthy, 1992).

The roast-leach processing of titaniferous magnetite for vanadium primary production is established, and is used in many commercial operations around the world including Vantra (Vanchem – which has recently been closed in South Africa) and Windimurra processes (Taylor, et al., 2006; Gupta & Krishnamurthy, 1992).

Table 3: Summary of the typical roast-leach processes for recovery of vanadium from titanomagnetite

Roasting type	Salt roast	Sulfate roast	Soda roast	Calcium salt roasting	Oxidative roasting (blank)
Reagent	O_2, NaCl	O_2, Na_2SO_4	O_2, Na_2CO_3	O_2, $CaCO_3$ (CaO)	O_2
Temperature, ˚C	800-900	1200-1230	900-1200	800-950	800-900
Chemical reaction	$2NaCl + ½ O_2 = Na_2O + Cl_2$ $Na_2O + V_2O_5 = 2NaVO_3$ $2NaCl + H_2O + V_2O_5 = 2NaVO_3 + 2HCl$	$Na_2SO_4 + V_2O_5 = 2NaVO_3 + SO_2 + 0.5\ O_2$	$Na_2CO_3 + V_2O_5 = 2NaVO_3 + CO_2$	$CaCO_3 + V_2O_5 = Ca(VO_3)_2 + CO_2$	$V_2O_3 + O_2 = V_2O_5$
Advantage	low reagent cost, selectivity	selectivity	Lower cost	environmentally friendly	Cheaper
Disadvantage	Low recovery dangerous HCl and Cl_2 are liberated – environmental and corrosion problems	Higher temperature Water contamination with Na	Non-selective CaO in feed should be <1.5wt%	Low recovery	low recovery

2.3.2 Direct reduction and leaching

The solid state direct reduction of titanomagnetite followed by magnetic separation and leaching is a development-scale process. Different versions of the process are described in the open literature (Zhong, et al., 2014; Zhao, et al., 2014; Chen, et al., 2013; Chen, et al., 2011). The process is reportedly capable of processing the titanomagnetite to produce the three commodities, namely; vanadium, iron and titanium. In one study, Chen et al. (2011) studied the thermodynamic behaviour of the as is and pre-oxidised Panzhihua titanomagnetite concentrate – the tests were conducted under reducing and isothermal (1000-1200°C) conditions with and without additives in the form of Na_2CO_3. The results of this study showed that pre-oxidation and additives played a considerable role in the metallisation efficiency of iron in the titanomagnetite concentrates. During pre-oxidation stage in air, it is reported that the particles of raw titanomagnetite concentrates formed pores, and that accelerated the reduction process in the subsequent stage. The addition of 1.5% Na_2CO_3 to the oxidative roast increased the metallisation degree of iron in the titanomagnetite to 96.4% after heating for 1 hour at 1200°C in the presence of pulverised coal. The reduced sample was composed of metallic iron, pseudobrookite solution and TiO_2 (Chen, et al., 2011).

In complementary work, Chen et al. (2013) proposed a novel process for processing titanomagnetite concentrates to recover vanadium, iron, and titanium using the same principles described above (Chen, et al., 2011). In this process, the titanomagnetite concentrate is directly reduced as discussed in the above work (Chen, et al., 2013). In the latter work (Chen, et al., 2013), the directly reduced titanomagnetite was subjected to magnetic separation to separate the metallic iron and the non-magnetic titanium-vanadium bearing fraction. The non-magnetic fraction was processed further as per the process flow diagram shown in Figure 5 (Chen, et al., 2013).

Zhao et al. (2014) altered the proposed novel process flowsheet by Chen et al. (2013). The altered process was more comprehensive as it included the extraction of vanadium, iron, titanium and chromium from a high-chromium titanomagnetite concentrate. The flowsheet of the latter process is shown in Figure 6 (Zhao, et al., 2014).

In another study, Zhong et al. (2014) embarked on a typical direct reduction, magnetic separation and double HCl leaching for the recovery of vanadium, iron and titanium. As shown in Figure 7, the process flowsheet produces a saleable titanium-enriched residue in addition to the vanadium and iron products (Zhong, et al., 2014).

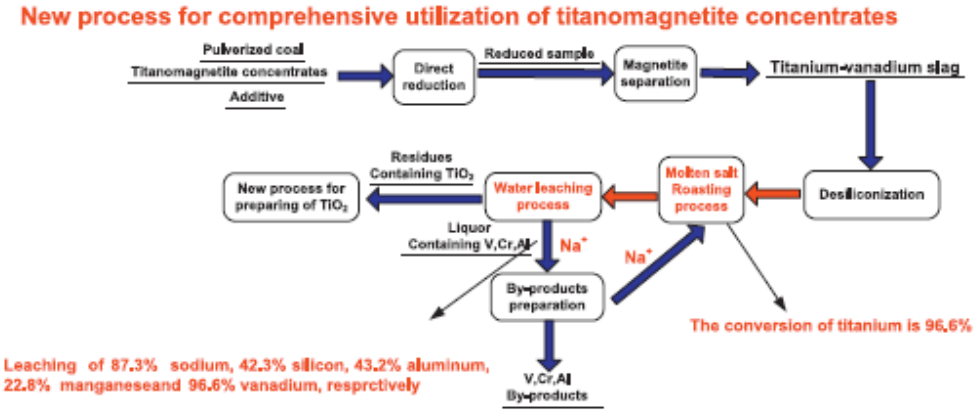

Figure 5: Proposed novel flow sheet for the processing of titanomagnetite concentrates (Chen, et al., 2013)

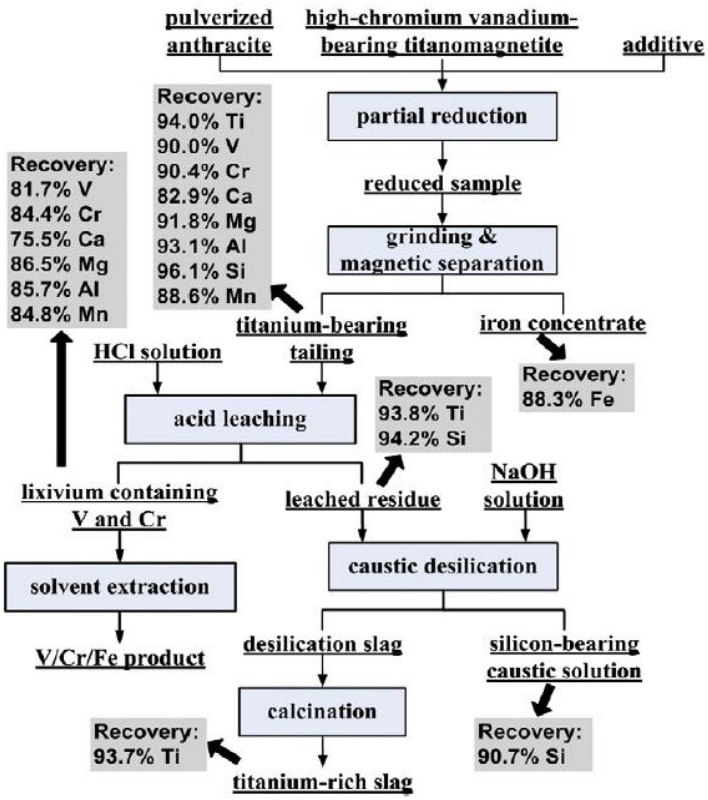

Figure 6: Proposed novel flow sheet for the processing of high chromium titanomagnetite concentrates (Zhao, et al., 2014)

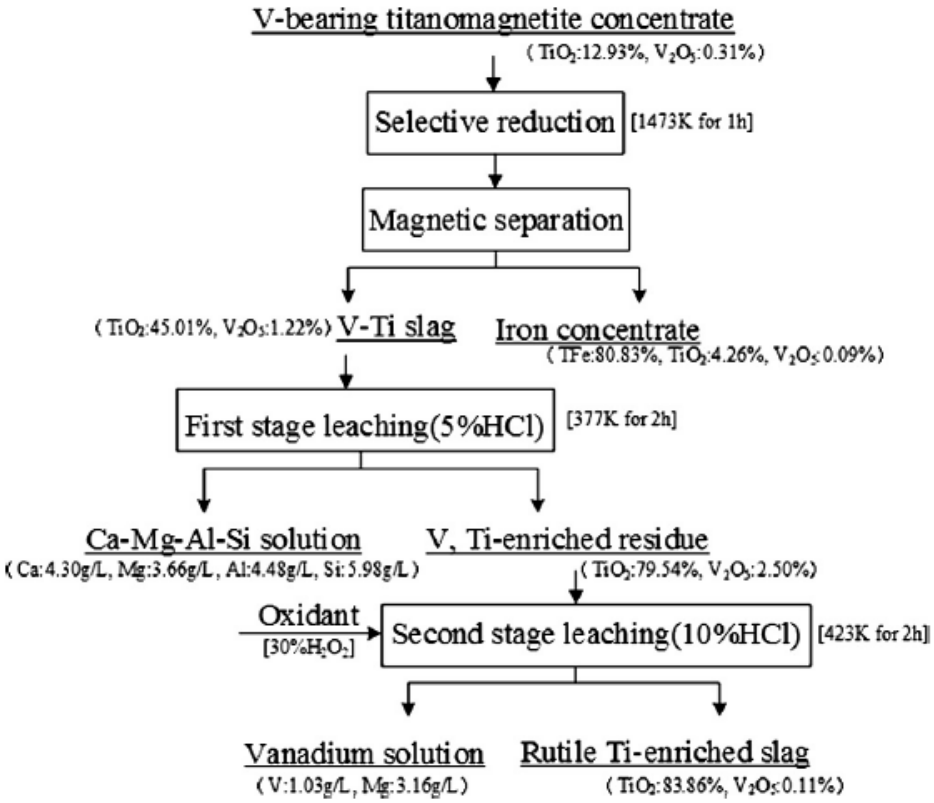

Figure 7: Proposed flow sheet for the recovery of Ti-enriched slag from titanomagnetite (Zhong, et al., 2014)

2.3.3 Smelting of titanomagnetite

In this context, the smelting of titanomagnetite refers to the pre-treatment and subsequent separation melting of titanomagnetite to produce pig iron and a titaniferous slag. In terms of smelting, the two approaches of smelting with high and low iron concentrations in the slags were reviewed.

In the past, it was believed that titanomagnetite could not be smelted using the cost effective iron making blast furnace technology, which is conventionally used for iron production, due to the high titanium content of above 10wt% in the ore. The direct processing of titanium rich ores typically result in the formation of titanium oxy carbides and nitrides that would block the hearth and tuyeres of the blast furnace (Steinberg, 2008). In 1949, Bleloch successfully demonstrated the use of submerged arc furnace (SAF) technology for the smelting of titanomagnetite (containing more than 12wt% TiO_2) which was mined from the

Bushveld Complex in South Africa. The proposed process by Bleloch (1949) entailed the addition of carbon for selective reduction of iron and vanadium while leaving behind a titania rich slag achieved from limestone-dolomite flux addition for lowering the slag liquidus temperature, the slag viscosity, and thus the process operating temperature (Bleloch, 1949).

The smelting of titaniferous magnetite to produce a vanadium bearing pig iron was started in the 1960s by EHSV and New Zealand Steel (NZS) using different technologies. EHSV adopted the submerged arc furnace (SAF) technology, whereas NZS opted to use the partially open slag bath furnace (OSBF) technology. Later, both EHSV and NZS converted their furnaces to full OSBFs (Steinberg, 2008).

The difference between SAF and OSBF smelting technologies is that the electrodes in the OSBF are arcing on top of the furnace contents, as opposed to being submerged in the burden as in the SAF. The OSBF arc phenomenon is also referred to as brush arc or open arc. The open arc technology offers many advantages over the submerged arc version – these include the opportunity of operating with finer feeds; and higher power inputs, thus higher operational temperatures, lower slag viscosity (can operate with lower flux addition), high V and Fe recoveries to metal, and subsequently high productivity.

After the development of a procedure to dilute titania in the titanomagnetite feedstock, a blast furnace operation for titanomagnetite smelting was successfully commissioned in China by Panzhihua Iron and Steel Limited (Pangang) and later adopted by Chengde Iron and Steel (Chengde), and in Russia by EVRAZ Nizhny Tagil Iron and Steel (NTMK) (Roskill, 2010; Zhang, et al., 2007; Taylor, et al., 2006; NTMK, 2003)

2.3.3.1 Pre-treatment

Titanomagnetite, a concentrate or a high grade ore, is generally subjected to one or more pre-treatment processes prior the subsequent smelting. Pre-treatment processes can include pelletisation of titanomagnetite with reductant, as well as a flux in case of fluxed smelting, prior to pre-heating and pre-reduction as well as sintering (NTMK, 2003). The pellets are generally subjected to solid state pre-reduction. In other operations, pelletisation was not included instead a lumpy material mixed with reductant and flux was subjected to pre-heating and pre-reduction, as for example in the recently closed EHSV operation. Pre-reduction provides significant electrical energy savings in the subsequent smelting operation

due to the fact that ideally most of the iron oxide is already reduced which means less reduction, if any, during smelting and also the hot pre-reduced charge provides an additional energy credit for the electric furnace smelting operation (Steinberg, 2008).

The pre-reduction kiln used by EHSV could typically be divided into two zones, namely the preheating and reduction zones. The pre-heating zone provided an effective devolatisation stage where some reduction was also achieved as a consequence of operating at high temperatures. In the reduction zone, iron oxide was reduced with char produced from the devolatilised coal (Steinberg, 2008). Ray et al. (1992) showed that the reduction kinetics of iron oxide by a carbonaceous reductant are dependent on temperature, carbon to iron oxide ratio, reducibility of iron oxide, the particle size distribution of the iron ore and carbonaceous reductant, and the reactivity of the carbonaceous reductant. High pre-reduction degrees at solid state are more favourable for the transit of the pre-reduced charge to the electric furnace. At EHSV, the highest pre-reduction degrees of iron oxide in the titanomagnetite were relatively low at about 45% (Steinberg, 2008). The low pre-reduction degrees were attributed to non-pelletisation. High pre-reduction degrees in the range of 90% are typically achieved from the pre-reduction of pellets (Taylor, et al., 2006; NTMK, 2003).

The study by Chen et al. (2011) of pre-reduction of pre-oxidised Panzhihua titanomagnetite concentrates in the temperature range of 1000-1200°C also demonstrated that the pre-reduced product has a potential to be used as feed in the smelting furnace other than being only used for selective leaching. The study showed that pre-oxidation and additives play a considerable role in the pre-treatment of titanomagnetite. Pre-oxidation forms pores in the particles of titanomagnetite – the pores are favourable for the acceleration of the succeeding reduction process. The best degree of metallisation of iron of 96.4% was achieved with the use of 1.5% Na_2CO_3 as an additive in the pre-reduction stage using a carbonaceous reductant at 1200°C for 1 hour (Chen, et al., 2011).

Halli et al. (2016) reported that the pre-reduction of titanomagnetite at solid state can also be achieved with methane gas. In the case of using methane as a reductant, the decomposition of methane into graphitic carbon and hydrogen gas, as shown in Equation [2.1], occurs at approximately 600°C. The produced graphitic carbon has got a very high activity and allows for high pre-reduction degrees to be achieved at lower temperatures compared to ordinary carbothermic reductions. The overall reaction of metal oxide, i.e. iron

oxide in the case of titanomagnetite, with methane can be presented by Equation [2.2]. The high activity of the produced carbon can result in the reduction of vanadium and adversely titanium (Halli, et al., 2016).

$$CH_{4(g)} = C_{(s)} + 2H_{2(g)} \quad [2.1]$$

$$4FeO_{(s)} + CH_{4(g)} = 4Fe_{(s)} + CO_{2(g)} + 2H_2O_{(g)} \quad [2.2]$$

2.3.3.2 Smelting with high iron in slag

Smelting titanomagnetite with high iron remaining in the slag operates on the same principles as in ilmenite smelting (Pistorius, 2008). As it is the convention in ilmenite smelting, fluxless smelting with high residual iron in the slag makes use of less reducing conditions such that about 10wt% FeO is left in the slag to act as a self-flux in preference to adding external fluxes (Zhong, et al., 2014; Taylor, et al., 2006; Jena, et al., 1994). As would be predicted from the Ellingham phase diagrams (Habashi, 2002), the low reducing conditions would result in the majority of the vanadium reporting to the slag. In this smelting approach, vanadium is recovered from the titaniferous slag. As described below, the technology of smelting with high iron in the slag is mainly at the development stage and has a significant potential.

The approach of smelting with high iron in the slag is described in several studies. In one study, a process is proposed which entails pelletisation, selective reduction of pellets in a rotary kiln using a mixture of lignite and anthracite as reductants. The reduced charge is melted in the electric furnace to separate pig iron from vanadium-titania slag. The next step entails the injection of Na_2CO_3 and Na_2SO_4 into the molten slag with oxygen, i.e. a carrier gas for the recovery of vanadium. Pig iron is processed further to produce steel products, whereas vanadium and titanium are recovered from the slag as V_2O_5 and TiO_2, respectively. The cumulative recovery of vanadium from titanomagnetite using this multi-stage process is estimated to be above 85% (Taylor, et al., 2006).

In another development work, Jena et al. (1994) subjected a titanomagnetite ore mined from Pipestone Lake, Manitoba, Canada, to a combination of pyro- and hydrometallurgical processes. This proposed process entails subjecting the ore (that contains 57.5wt% Fe, 0.66wt%V, and 16.6wt% TiO_2) to selective reduction smelting where iron primarily reports

to the pig iron phase while vanadium and titanium report to the slag phase. It is reported that the pig iron could have a purity of 99wt% Fe. The corresponding slag could contain 9-35wt% FeO, 31-46wt% TiO_2, and 1.2-1.6wt% V. In the smelting stage, the respective recoveries of titanium and vanadium to the slag phase were in excess of 98%. The slag was subjected to soda ash roasting at 950°C, followed by water leaching to recover vanadium in solution (for subsequent recovery by ammonia precipitation, and de-ammoniation to produce vanadium pentoxide). The vanadium leach residue was subjected to a titania upgrading process, which involved HCl leaching at 105°C in order to remove mainly iron, magnesium and aluminium. The upgraded titania slag contained 82.9wt% TiO_2, 1.5wt% FeO, 15.6wt% SiO_2, 1wt% MgO, 2wt% MgO, and 0.3wt% CaO. The cumulative titanium recovery was 90wt% (Jena, et al., 1994).

The Centre de Recherches Minerales (CRM) of Canada developed a process for the treatment of titanomagnetite mined from the Chibougamau deposit located in Quebec, Canada. The proposed process flowsheet entails crushing and grinding to -20 mesh, followed by magnetic concentration of the Chibougamau titanomagnetite from typically 9.80wt% to 9.11wt% TiO_2, 0.57wt% to 1.35wt% V_2O_5, and 34.5wt% to 60.8wt% Fe. The recoveries of V_2O_5 and Fe were 83.84% and 62.26%, respectively. The titanomagnetite concentrate is ground further to -325 micron before blending with a carbonaceous reductant of 0.26% by weight and pelletisation. The charge pellets are processed in electric arc furnaces in order to produce a high titania slag containing most of the vanadium. The vanadium content in the corresponding pig iron metal is typically kept below 0.07% (Taylor, et al., 2006). The titania slag is subjected to the conventional salt roast/ leach/ precipitation and calcination process in order to recover vanadium as V_2O_5. The corresponding pig iron is processed further to produce various steel products. In this process, the titania is not recovered (Taylor, et al., 2006; Gupta & Krishnamurthy, 1992).

2.3.3.3 Smelting with low iron in slag

Smelting with low iron in the slag means operating under strongly reducing conditions in order to essentially reduce the iron and vanadium to the metallic phase while the titanium is primarily deported to the slag phase. The reduction of titanomagnetite using a carbonaceous reductant, as it is typically used in the current option of titanomagnetite smelting, can be presented by chemical reactions shown in Equation [2.3] and [2.4]. In this smelting

approach, pre-reduced sinters, pellets or lumpy/ fine material are typically processed in blast or electric arc furnaces (Steinberg, et al., 2011; Zhang, et al., 2007; NTMK, 2003; Kelly, 1993).

$$Fe_3O_4 + 4C = 3Fe + 4CO \quad [2.3]$$

$$V_2O_5 + 5C = 2V + 5CO \quad [2.4]$$

This titanomagnetite smelting option can be conducted in the absence of a flux, i.e. fluxless smelting (Boyd, et al., 1993) or in the presence of a flux, i.e. fluxed smelting (Steinberg, et al., 2011; Zhang, et al., 2007; Kelly, 1993). The fluxed and fluxless titaniferous slags typically contain 20-40wt% TiO_2 and about 60wt% TiO_2, respectively. Boyd et al. (1993) reported high titania grades of 80wt% in the titaniferous slag produced through fluxless smelting of a clean titanomagnetite concentrate which was reduced using a low ash carbonaceous reductant during smelting. There are however indications that the attainment of high titania concentration in the titaniferous slag produced through fluxless smelting process would be restricted by the formation of reduced titanium species, i.e., Ti(O,C), when the TiO_2 content in the slag reaches 70wt% to 75wt% (Nell & McCullough, 2001).

In the smelting process with low FeO concentrations of typically below 3% in the slag, most of the vanadium from the feed (generally about 80%) reports to the pig iron because of the feasibility to apply strong reducing conditions. For these vanadium recoveries to the pig iron to be achieved, the pig iron would typically contain about 3.5wt% carbon and low levels of titanium of about 0.2wt% (Cox, 2013; Moolman, 2012; Steinberg, 2008; Zhang, et al., 2007; NTMK, 2003; Boyd, et al., 1993; Kelly, 1993). At EHSV, the Ti and C concentrations in the alloy were used as indicators of the intensity of reduction in the smelting furnace. High titanium concentration in the pig iron means high reducing conditions in the operational furnace. High titanium concentration in the pig iron is also unfavourable as it poses quality and safety risks during the subsequent ladle furnace operation for the recovery of vanadium as slag from the pig iron (Steinberg, 2008). Due to the need to strictly control the titanium concentration in the pig iron during the smelting of a relatively high grade vanadium titanomagnetite like the MML, some vanadium is inevitably lost to the titania bearing slag. Typically the MML titaniferous slag can contain as high as 0.9wt% V_2O_5 (Steinberg, 2008; Boyd, et al., 1993). A typical fluxed smelting flowsheet of the titanomagnetite is shown in Figure 8 (Steinberg, et al., 2011).

As detailed in the old Mintek patent (Boyd, et al., 1993), fluxless smelting of titanomagnetite is capable of extracting the three commodities, i.e. iron, vanadium and titanium, from a clean titanomagnetite concentrate. In this fluxless smelting approach, the liquidus temperature of the pig iron is lowered to below 1200°C if there is dissolution of about 3.5% carbon into the pig iron. The reduction and deportment of the iron to the metal phase result in an increase in the slag liquidus temperature such that the smelting operation is conducted at temperatures above 1650°C (Boyd, et al., 1993). This mismatch in the liquidus temperatures of the slag and metal results in superheated pig iron, which, while not impossible to operate, it increases smelting operational risks, namely; rapid refractory erosion and metal fuming risks. However some pyrometallurgical processes operate with superheated alloy/ matte phase; the PGM matte smelting industry is a prime example.

Recently, a number of large pilot plant campaigns were completed at Mintek to demonstrate the fluxless titanomagnetite smelting process for junior titanomagnetite resource owners (Edison, 2013; Waldeck, 2013; Whitman, 2013; Financial times, RNS number: 1649C, 2013; Cox, 2013; Moolman, 2012). Mintek's expertise and optimistic view in this smelting approach are still very strong. Despite successful demonstration of this process, no commercialisation has been accomplished as yet. It is believed that the challenges include the recent global decline of the price of steel and vanadium, as well as access to and high price of electricity in the prospective areas of operation.

Notwithstanding the above, the commercialisation of the demonstrated operations for the above referenced South African and Mozambican companies is still projected to occur in the near future – these companies include Tivani Ltd. (Moolman, 2012), Ironveld Ltd. (Cox, 2013), Bushveld Minerals Ltd. (Edison, 2013; Financial times, RNS number: 1649C, 2013; Waldeck, 2013), and Baobab Resources Plc (Whitman, 2013). These companies will in all likelihood operate in South Africa, except the latter which will be operating in Mozambique. The South African companies will process the titanomagnetite mined from the Bushveld complex. Baobab Resources Plc will process the titanomagnetite mined from the Tete mineral resource region. All four companies will in all likelihood process the titanomagnetite using the fluxless smelting technology.

A flowsheet of the fluxless titanomagnetite smelting operation was developed by Bushveld Minerals and is shown in Figure 9 (Edison, 2013).

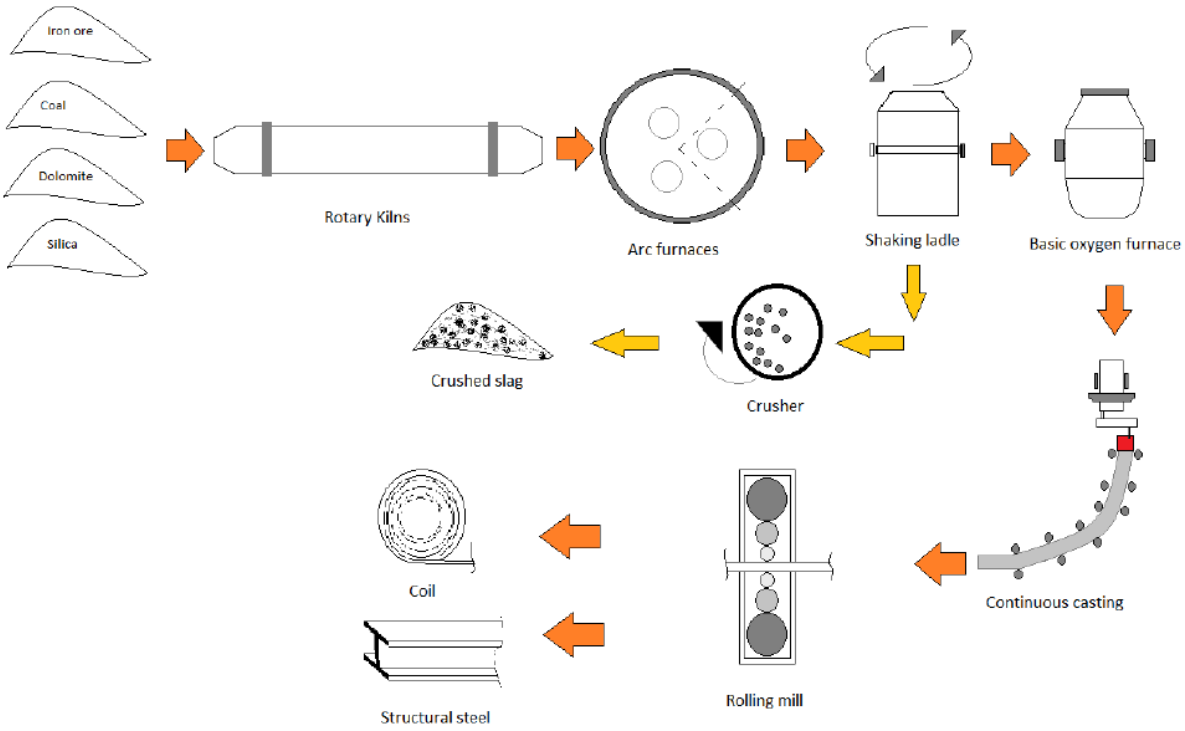

Figure 8: Typical flow sheet of the fluxed titanomagnetite smelting operation (Steinberg, et al., 2011)

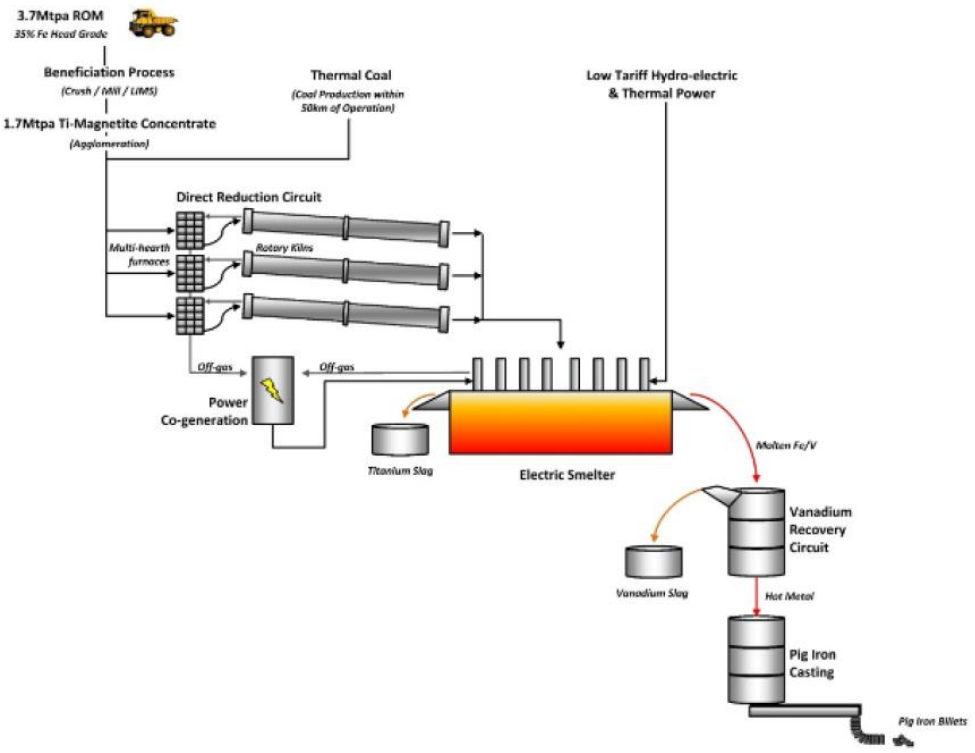

Figure 9: Typical flow sheet of the fluxless titanomagnetite smelting operation (Edison, 2013)

In both the fluxed and fluxless titanomagnetite smelting operations, the vanadium bearing pig iron is typically subjected to downstream processing to recover vanadium in the slag phase and high purity steelmaking pig iron. The vanadium bearing slag is generally processed further to produce the valuable vanadium pentoxide (V_2O_5) product which is used in catalysis for the production of sulfuric acid from sulfur dioxide. V_2O_5 is also a versatile intermediate product for other products like ferrovanadium and Fe-Ti-Al-V-Si alloys (Moskalyk & Alfantazi, 2003; Goldberg, et al., 1990). The corresponding high purity pig iron is generally subjected to casting to produce different steel products (Edison, 2013; Steinberg, et al., 2011).

The titania bearing slag produced during the production of the vanadium bearing pig iron, i.e. titaniferous slag, is generally discarded as waste, particularly in the case of fluxed smelting operations. For example, large titaniferous slag waste dumps exist from the recently closed EHSV operation in South Africa and Pangang operation in China (Steinberg, et al., 2011; Sui, et al., 2004). The size of the titaniferous slag dump generated from the recently closed EHSV operation is estimated to be about 45 million tons (Africa, Mining review, 2017; Fin24.com, 2017; Anderson, 2013). The titaniferous slag dump at Pangang is estimated to be increasing at a rate of about 3 million tons per annum and the overall dump was estimated to be above 50 million tonnes already in 2004 (Sui, et al., 2004). As stated above, these slags typically contain attractive titania grades.

The titaniferous slags are generally not beneficiated, particularly for the recovery of titanium. The reasons include that these slags typically contain low TiO_2 concentrations that they cannot be directly used as feedstocks in the production of titanium metal or titania pigment, and cannot be upgraded to feedstock grades because they comprise complex phase chemistries (Pistorius, 2011; Van Vuuren & Tshilombo, 2011). A typical complex structure of titaniferous slag is shown in Figure 10 (Pistorius, 2011). The desire for maximum exploitation of the valuable resources and to operate efficient metallurgical processes upholds that the titaniferous slag be processed further to extract titanium. However, to do so, fundamental understanding of the phase equilibria in these slags is essential.

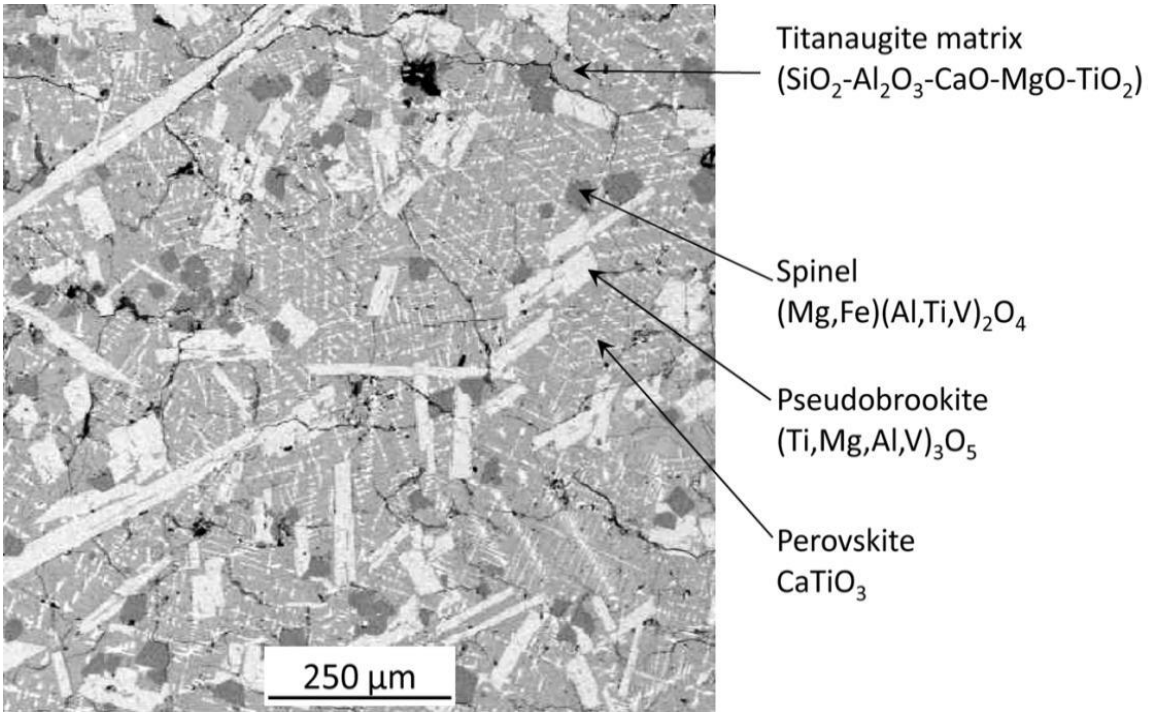

Figure 10: Backscattered electron image of a typical titaniferous slag with approximate composition: 32wt% TiOx, 22wt% SiO_2, 17wt% CaO, 15wt% MgO, 14wt% Al_2O_3 and 0.9wt% V_2O_5 (Pistorius, 2011)

2.4 Phase equilibria in titaniferous slags

Titaniferous slags are typically described by the Ca-Mg-Al-Si-Ti-O system because of the high concentrations of these components in the slags as detailed in Table 1. It should be noted that the fluxed titaniferous slags are characterised by the presence of TiO_2 in concentration ranges of 20wt% to 40wt%, except the blast furnace titaniferous slags produced by NTMK and CHMP in Russia which contain TiO_2 concentrations in the range of 8-10wt% (Hassell, et al., 2016).

The lack of interest in processing titaniferous slags to produce saleable titania materials is attributed to their low TiO_2 content that they cannot be used as direct feedstocks for the production of titania pigment, and the presence of the chemically inert spinel solid solution [$Mg(Al,Ti)_2O_4$] that cannot be handled by the available titania slag upgrading technologies (Pistorius, 2011; Van Vuuren & Tshilombo, 2011). There is a market for titania materials with 70wt% TiO_2 or more (Shijiazhuang Leveling import and export Co., Ltd., 2014); the first prize is however to produce a suitable feedstock for the preferred chloride pigment

production process (Van Dyk, 1999). To produce titania products from the titaniferous slags, it is essential that the cast slag from the primary smelting furnace contains little or no $Mg(Al,Ti)_2O_4$

The understanding of phase relations in titaniferous slags is thus important in order to be able to implement a suitable fluxing strategy for the production of a treatable titaniferous slag with little or no $Mg(Al,Ti)_2O_4$.

The general approach for studying phase relations in slags and drawing of phase diagrams is described in the open literature (Jung, et al., 2009; Jak & Hayes, 2004). As per the general approach, the components of the study of phase relations in the multicomponent Ca-Mg-Al-Si-Ti-O system applicable to titaniferous slags are listed below:

1. Evaluation of the available thermodynamic and phase equilibria literature in relation to the multicomponent Ca-Mg-Al-Si-Ti-O system,

2. Calculation and re-drawing of the equilibrium phase diagram using a thermochemical software

3. Equilibration-quench-(electron probe micro analysis) (EPMA) experiments to review and validate the calculated phase relations and diagrams

2.4.1 Evaluation of the Ca-Mg-Al-Si-Ti-O system

In order to understand equilibrium phase relations in a multi-component or higher order system like Ca-Mg-Al-Si-Ti-O system, subsystems or lower order systems are generally evaluated (Jung, et al., 2009). Some important lower order systems applicable to Ca-Mg-Al-Si-Ti-O system in air and reducing conditions are reviewed here.

The equilibrium phase relations are generally plotted in phase diagrams. A phase diagram is typically defined as the graphical representation of the set of thermodynamic parameters achieved when equilibrium amongst phases under specific conditions is established.

It should be noted that the typical titaniferous slags are characterized by the presence of TiO_2. Hence, the focus in the following subsections is subjectively limited to the phase relations of titania bearing subsystems.

2.4.1.1 Ca-Ti-O system

Phase relations in the Ca-Ti-O system have been studied extensively and are widely reported (Jacob & Gupta, 2009; Tulgar, 1976; Shultz, 1973; Jongejan & Wilkins, 1970; Roth, 1958; DeVries, et al., 1954). The eutectic point in the $CaO\text{-}TiO_2$ system occurs at about 1450°C. Perovskite ($CaO.TiO_2$) is the typical phase melting or crystallising at these temperatures (DeVries, et al., 1954; Tulgar, 1976). Roth (1958) and Jongejan and Wilkins (1970) reported the crystallisation of an additional phase with the composition $4CaO.3TiO_2$ at low TiO_2 concentrations than the stoichiometric requirement for $CaO.TiO_2$ crystallisation. Figure 11 shows the equilibrium phase diagram after the work completed by Tulgar (1976).

In some recent work, Jacob and Gupta (2009) studied the Ca-Ti-O system at 1200 K in pure oxygen and Ar. In this testwork, four ternary oxides without detectable range were identified: $CaO.TiO_2$, $4CaO.3TiO_2$, $3CaO.2TiO_2$ and $CaO.Ti_2O_3$. It is important to note that $CaO.Ti_2O_3$ contains trivalent titanium. Thus, in the system Ca-Ti-O, a combination of trivalent and tetravalent titanium species can co-exist under reducing conditions.

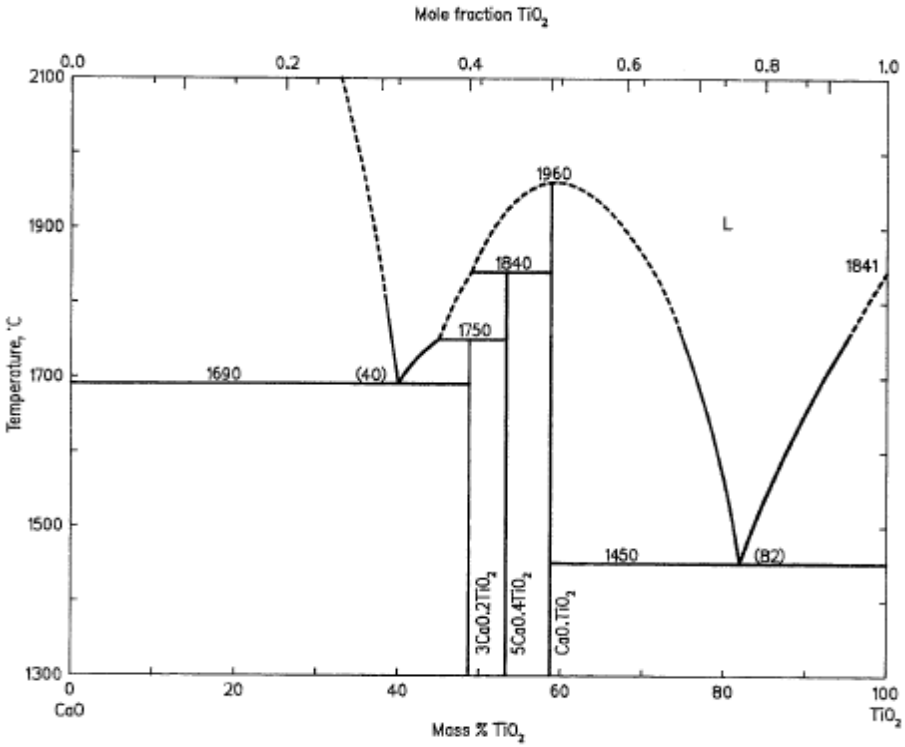

Figure 11: Phase diagram for the $CaO\text{-}TiO_2$ system (Tulgar, 1976)

2.4.1.2 Mg-Ti-O system

The MgO-TiO_2 system was investigated by many researchers in the past (Shindo, 1980; Rouf, et al., 1969; Woermann, et al., 1969; Massazza & Sirchia, 1958). The binary phase diagram in Figure 12 was established from the work conducted by Woermann et al. (1969). The minimum temperature of liquid formation is about 1600°C in relatively high TiO_2 mixtures. The typical phases that crystallise in the MgO-TiO_2 system are gandilite, with an inverse spinel structure (Mg_2TiO_4); geikielite, with an ilmenite structure ($MgTiO_3$); and karrooite, with a pseudobrookite structure ($MgTi_2O_5$).

In their work, Pelton et al. (1998) showed that under reducing conditions all three oxide phases observed in the MgO-TiO_2 system can incorporate trivalent titanium to form solid solutions with endmembers in the MgO-Ti_2O_3 and TiO_2-Ti_2O_3 systems. The MgO-Ti_2O_3 system reportedly resulted in the formation of $MgTi_2O_4$ with a spinel structure. The system TiO_2-Ti_2O_3 was investigated by Andersson et al. (1957). In addition to the rutile and several magneli (Ti_nO_{2n-1}, with $n \geq 4$) phases, Ti_3O_5 with a pseudobrookite structure and Ti_2O_3 with the rhombohedral corundum structure were reported as some of the phases with trivalent titanium which forms as a consequence of the reducing conditions (Andersson, et al., 1957). The $MgTiO_3$-Ti_2O_3 subsystem was also investigated by Reznichenko et al. (1979). In this work, the solubility studies of Ti_2O_3 in $MgTiO_3$ of as much as 33-35 mole% at 1100°C were reported (Reznichenko, et al., 1979). However, Vasyutinskii (1977) studied and characterised the $MgTiO_3$-Ti_2O_3 as a eutectic system with a composition close to the equimolar ratio of the $MgTiO_3$ and Ti_2O_3 (Vasyutinskii, 1977).

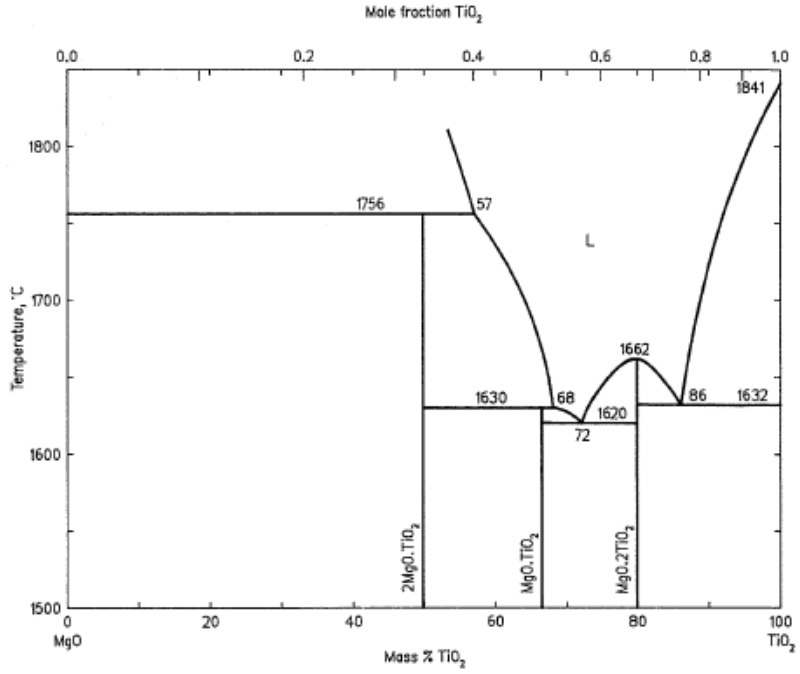

Figure 12: Phase diagram for the MgO-TiO_2 system (Woermann, et al., 1969)

2.4.1.3 Al-Ti-O system

The Al_2O_3-TiO_2 phase diagram is shown in Figure 13 (Kowalski, et al., 1995) as established from a combination of studies by many researchers (Azimov, et al., 1984; Goldberg, 1968; Lejus, et al., 1966; Lang, et al., 1952). A eutectic in the phase diagram is reported to be at about 1700°C with about 80 mol% TiO_2 in the mixture (Goldberg, 1968; Lang, et al., 1952). Goldberg (1968), and Lejus et al. (1966) showed the congruent melting of the tialite (Al_2TiO_5) phase in the temperature range of 1850°C to 1860°C. Al_2TiO_5 is generally reported as the intermediate compound in the Al_2O_3-TiO_2 system. However, Lejus et al. (1966) reported two new unidentified phases at point X and Y in the phase diagram, with the compositions of between 33 and 40 mol % TiO_2 in the temperature range between 1800°C and 1900°C. In the work conducted by Jung et al. (2009), the two compounds were approximated by a single compound Al_4TiO_8. The decomposition temperature of the Al_2TiO_5 to Al_2O_3 and TiO_2 reportedly occurs in the temperature range of 1260°C to 1280°C.

Since Ti has several stable oxidation states, it is important to evaluate the Al-Ti-O system under reducing conditions. The phase equilibria in the Al-Ti-O system under reducing conditions are reported by many researchers (Mizoguchi & Ueshima, 2005; Ohta & Morita, 2002; Remy, et al., 1988; Monnereau, et al., 1985; Glazova, 1965; Belon & Forestier, 1964;

McKee & Aleshin, 1963). The thermodynamic study of the phase equilibria in the Al-Ti-O system are also reported (Jung, et al., 2009; Rahmel & Spencer, 1991). A ternary phase containing a mixture of Ti oxidation states was reported by Monnereau et al. (1985) and Remy et al. (1988). The lowest liquidus temperature point in the reviewed system is in the range of 1695°C (Belon & Forestier, 1964) to 1720°C (Jung, et al., 2009).

Jung et al. (2009) calculated the ternary phase diagram for the system Al_2O_3-Ti_2O_3-TiO_2 – this is a case where Ti^{3+} and T^{4+} titanium valences co-exist in a mixture with Al_2O_3. In the systems: Al_2O_3-TiO_2 in air (Goldberg, 1968; Lang, et al., 1952), Al_2O_3-Ti_2O_3 at pO_2 of 10^{-15} bar (Jung, et al., 2009) and TiO_2-Ti_2O_3 (Anderson, et al., 1957; Krajewski, 1992), the existence of a liquid phase is not predicted. However, the calculated phase diagram shown in Figure 14 (Jung, et al., 2009) shows that a liquid phase in the Al_2O_3-Ti_2O_3-TiO_2 system at 1600°C is present in a large compositional range while at 1500°C the liquid is present in a small compositional range. Under the reducing conditions at 1600°C, the thermochemical calculation predicts the crystallisation of many primary phases depending on the composition and pO_2 - these include TiO_2, Ti magneli phases, Ti_3O_5 (pseudobrookite), ilmenite type phase(s), corundum type phase(s), and Al_2TiO_5 (tialite) (Jung, et al., 2009).

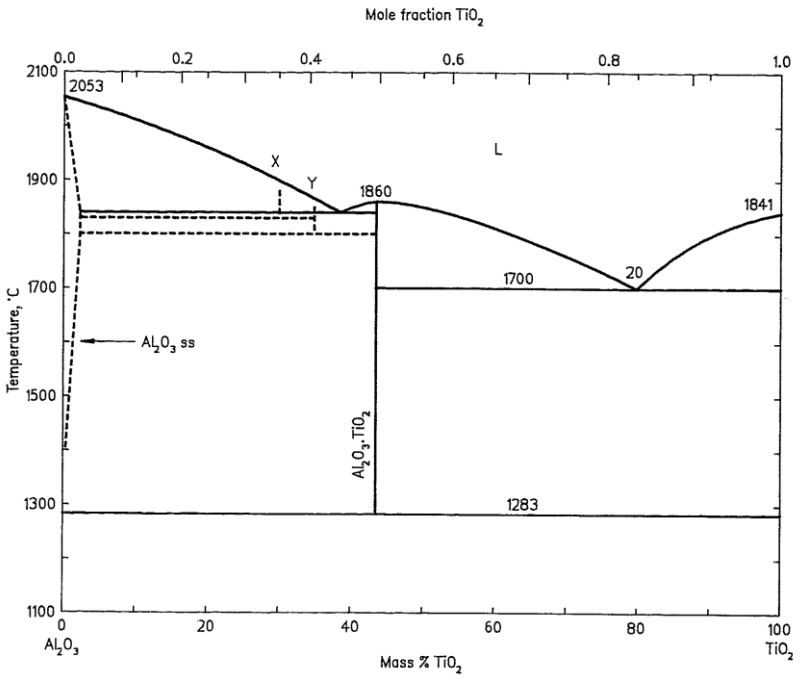

Figure 13: Phase diagram for the Al_2O_3-TiO_2 system (Eisenhuttenleute, Verlag Deutscher, 1995)

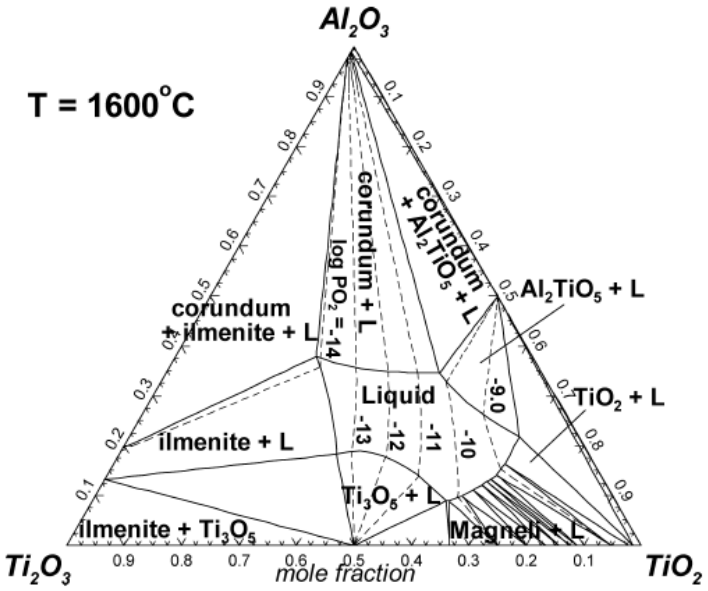

Figure 14: Calculated phase diagram for the Al_2O_3-Ti_2O_3-TiO_2 system at 1600°C with pO_2 isobars (Jung, et al., 2009)

2.4.1.4 TiO_2-Ti_2O_3 system

The calculated phase diagram for the TiO_2-Ti_2O_3 system is shown in Figure 15 (Jung, et al., 2009). The Iso-pO_2 lines show that the equilibrium amounts of Ti_2O_3 and TiO_2 in the liquid phase depends on the operation pO_2 and temperature. The oxidised tetravalent titanium species crystallise at high pO_2 approaching that of air at higher temperatures, whereas the nonstoichiometric titanium oxide phases, i.e. Magneli phases crystallise at similar pO_2 at low temperatures. At low pO_2, phases with reduced titanium species such as Ti_2O_3 and Ti_3O_5 are prevalent.

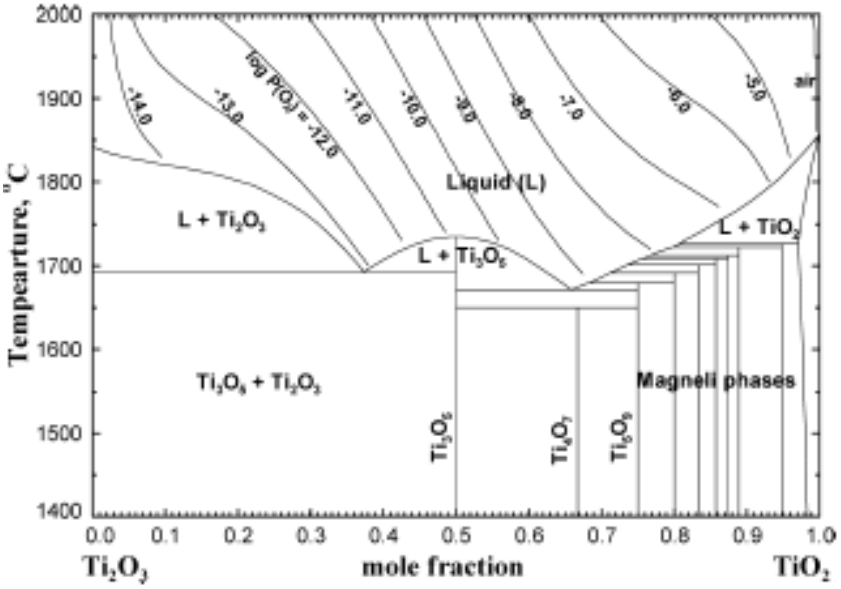

Figure 15: Calculated phase diagram for the TiO_2- Ti_2O_3 system with pO_2 isobars (Jung, et al., 2009)

2.4.1.5 Si-Ti-O system

The phase diagram for the SiO_2-TiO_2 system is shown in Figure 16 (Kowalski, et al., 1995) as established in the past (DeVries, et al., 1954). It appears in the phase diagram that no intermediate chemical phases or compounds are formed in the SiO_2-TiO_2 system. In addition, a eutectic between rutile and cristobalite occurs at about 1550°C with a content of TiO_2 of about 12wt% (Kirillova, et al., 2011; Massazza & Sirchia, 1958). However, Bunting (1953) and Evans (1970) reported that the eutectic occurs when the solubility of TiO_2 in the SiO_2 is 10.5% and 10.8%, respectively. The eutectic as predicted by Bunting (1933) is included in Figure 16.

Roy et al. (1952) studied the phase equilibria and thermodynamics in the Si-Ti-O system under reducing conditions. The intermediate phases forming in the system are Ti_2O_3 in corundum and ilmenite forms as well as pseudobrookite type phase, Ti_3O_5 (Roy, et al., 1952). These phases were also observed in the case of the Al-Ti-O system calculated under reducing conditions at 1600°C (Jung, et al., 2009).

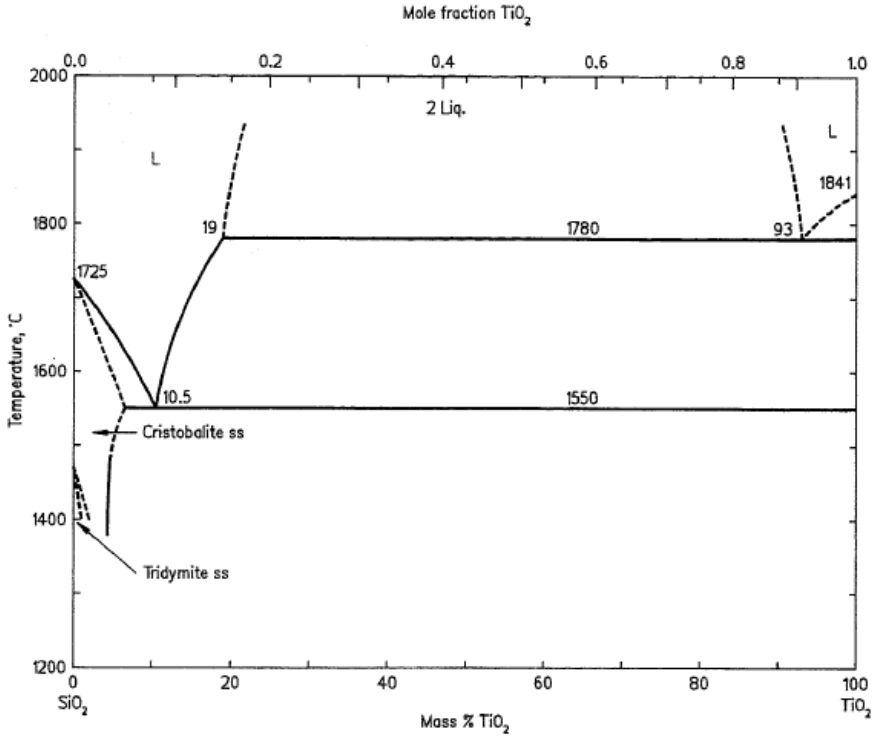

Figure 16: Phase diagram for the SiO_2-TiO_2 system (Eisenhuttenleute, Verlag Deutscher, 1995)

2.4.1.6 Mg-Al-Ti-O system

The Al_2O_3-MgO-TiO_2 subsystem is very important in the review of the high order Ca-Mg-Al-Si-Ti-O system. The phase diagram of this subsystem, shown in Figure 17, was drawn according to the results of Berezhnoi and Gulko (1955). In addition to the binary subsystems, this system is very important as it shows other possible phases that can be formed. The phases observed in the lower order binary subsystems are still observed in this ternary phase, namely; geikielite, with an ilmenite structure ($MgO.TiO_2$); gandilite, with an inverse spinel structure (Mg_2TiO_4); karrooite, with a pseudobrookite structure ($MgTi_2O_5$); and tialite (Al_2TiO_5). Additional phases are also observed in the ternary phase diagram, namely; spinel ($MgAl_2O_4$) and the pseudobrookite type karrooite-tialite solid solution ($MgTi_2O_5$- Al_2TiO_5) (Berezhnoi & Gulko, 1955).

Krajewski (1992) investigated the phase relations in the Al-Mg-Ti-O system under reducing conditions using the Mg-Ti-O and Al-Ti-O, Ti-O subsystems. As previously observed in the Mg-Ti-O and Al-Ti-O subsystems, only Ti has more than one valence states. Hence variation in composition is observed mainly on the reduction of Ti to a lower valence.

However, Krajewski (1992) reported significant higher substitutions of Al^{3+} to Ti^{3+} and Al^{3+} to Ti^{4+} in the corundum phase (Ti_2O_3) and rutile compared to previous literature data. Krajewski (1992) reported the maximum solubility of Ti^{3+} in rutile to be 2.7 mol% compared to 1.8 mol% reported by McKee and Aleshin (1966), and that of Ti^{4+} to be 0.7 mol% compared to 0.3 mol% reported by Lejus et al. (1966). Krajewski also reported that the maximum solubility of Al^{3+} in the Ti_2O_3 is about 5.7 mol% compared to the previously reported data (Rice & Robinson, 1977).

The additional phases observed in the phase relations of Al-Mg-Ti-O system under reducing conditions are spinel solid solution $Mg(Al,Ti)_2O_4$, Ti_3O_5, titanium magneli phases (Ti_nO_{2n-1} with $n \geq 4$) (Krajewski, 1992).

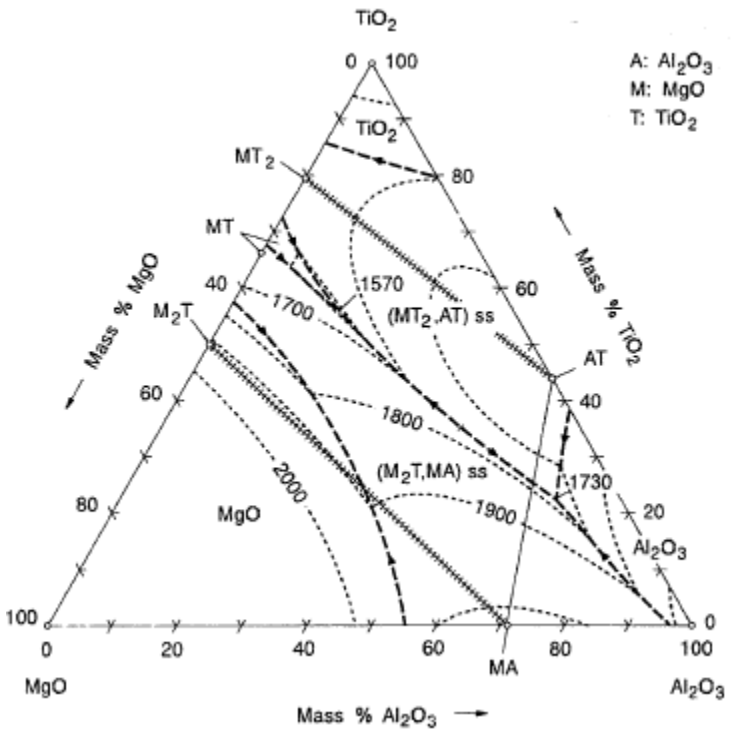

Figure 17: Phase diagram of the Al_2O_3-MgO-TiO_2 system (Eisenhuttenleute, Verlag Deutscher, 1995; Berezhnoi & Gulko, 1955)

2.4.1.7 Ca-Si-Ti-O system

The CaO-SiO_2-TiO_2 ternary system was investigated fully for the first time by Devries et al. (1955). The phase diagram in Figure 18 (Kowalski, et al., 1995) shows that along the CaO-TiO_2 binary, perovskite ($CaTiO_3$) phase crystalizes when there is about 60% and 40% of

TiO_2 and CaO in the slag, respectively. However, with an increase in SiO_2 concentration in the system, the liquidus temperature of the binary system is generally decreased in particular along the $CaTiO_3$ composition line where the content of more than 20% SiO_2 results in a liquidus temperature of 1365°C at point 'i'. Along the CaO-SiO_2 binary, an olivine phase, Ca_2SiO_4, is crystallized. There is no literature predicting the formation of the karrooite counterpart in terms of Ca, which would be $CaTi_2O_5$. There is however a calcium titanate, i.e. $3CaO.2TiO_2$, which was also identified by Jacobs and Gupta (2009) in their study of the binary CaO-TiO_2 system in air and argon atmospheres. Along the SiO_2-TiO_2 binary, the liquidus temperatures are generally high with no indication of the crystallization of phases below 1700°C (DeVries, et al., 1955).

Under reducing conditions, as stated previously, there is a potential for the production of reduced titanium species such as Ti_2O_3 in corundum and ilmenite forms, as well as pseudobrookite, Ti_3O_5 (Roy, et al., 1952).

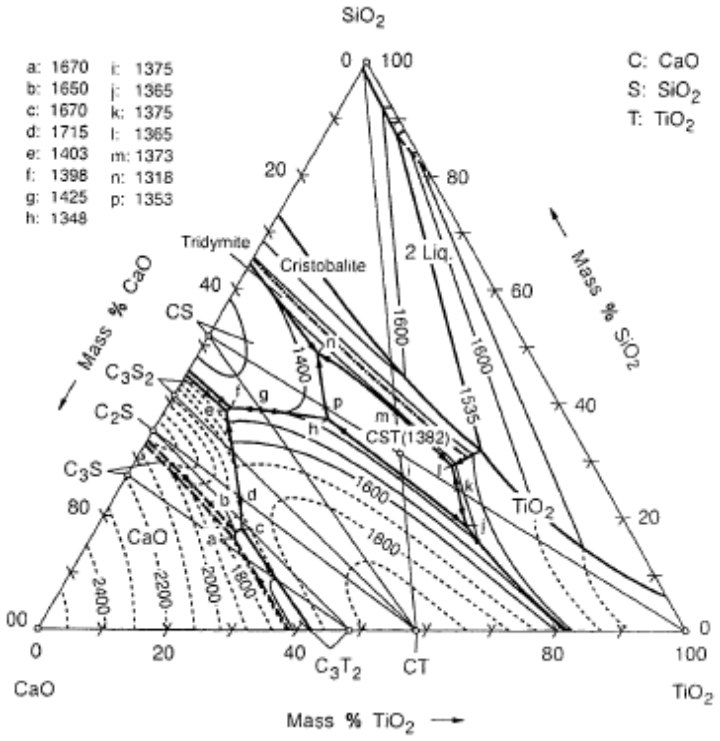

Figure 18: Ternary phase diagram of the CaO-SiO_2-TiO_2 system established in air (Eisenhuttenleute, Verlag Deutscher, 1995)

2.4.1.8 Ca-Al-Si-Ti-O system

Ohno and Ross (1963) conducted investigations in air to study the effect of the addition of 10-20% Al_2O_3 to a CaO-SiO_2-TiO_2 system with varying TiO_2 content on the crystallization of phases and the behaviour of the liquidus surface. The results of the study show that the liquidus temperature of the system decreased with increasing the TiO_2 content (Ohno & Ross, 1963). These results are contrary to the results reported by Fine and Arac (1980) who reported that the addition of TiO_2 increases the liquidus temperature. In terms of phase relations, crystallization of new phases in the form of tialite (Al_2TiO_5) and calcium aluminum silicate ($CaO.Al_2O_3.2SiO_2$) was observed when Al_2O_3 was added (Ohno & Ross, 1963).

2.4.1.9 Ca-Mg-Si-Ti-O system

Phase equilibria and liquidus surface of the CaO-MgO-SiO_2-TiO_2 quaternary system were studied in air (Kirschen & de Capitani, 1999; Kowalski, et al., 1995). The phase diagrams are presented in the form of subsystems showing numerous significant phases that form at elevated temperatures. These significant phases include perovskite ($CaTiO_3$), forsterite (Mg_2SiO_4), karrooite ($MgTi_2O_5$), magnesium silicate ($MgO.SiO_2$), and calcium titanium silicate ($CaO.TiO_2.SiO_2$).

2.4.1.10 Ca-Mg-Si-Al-Ti-O system

Several studies have been conducted to study equilibrium phase relations and liquidus temperatures in the multicomponent or higher order Ca-Mg-Al-Si-Ti-O system (Shi, et al., 2016; Zhao, et al., 2009; Datta, et al., 1993; Fine & Arac, 1980; McRae, et al., 1969; Jochens, et al., 1969; Osborn & Gee, 1969; Holmes, et al., 1968; Jochens, 1967; Devries, et al., 1955). The Ca-Mg-Al-Si-Ti-O system is typically used to describe titaniferous slags. In general, TiO_2 is added to blast furnace iron making slags to extend the lifespan of the industrial furnace (Morizane, et al., 1999). Hence, some researchers investigated the effect of the addition of TiO_2 to SiO_2-Al_2O_3-MgO-CaO system on the liquidus temperatures of the typical blast furnace slags. Fine and Arac (1980) reported that the addition of TiO_2 in the blast furnace slag conforming to the SiO_2-Al_2O_3-MgO-CaO system increases the liquidus temperature of the slag. However Detta et al. (1993), DeVries (1955) and Ohno and Ross (1963) reported that the liquidus temperatures are in fact decreased, whereas Shi et al. (2016)

suggested that the liquidus temperatures are not significantly influenced. The TiO_2 additions in these studies are generally lower than the fluxed titaniferous slags with a typical TiO_2 content of 20% and above. The TiO_2 contents studied by these researchers would be applicable to titaniferous slags with TiO_2 grades of 8-10% produced in Russia using blast furnaces (Hassell, et al., 2016).

Zhao et al. (2009) investigated the phase equilibria in the Ca-Mg-Al-Si-Ti-O system applicable to blast furnace ironmaking slags under carbon saturation. The investigated titaniferous slag had a TiO_2 grade of 10% (Zhao, et al., 2009), which is lower than the typical TiO_2 grades of 20-40wt% achieved in titaniferous slags produced in China, New Zealand and South Africa (Steinberg, et al., 2011; Zhang, et al., 2007; Kelly, 1993). However, the study provided valuable information regarding the crystallization of phases under reducing conditions – the pseudobrookite type phase containing reduced titanium species (Ti^{3+}) crystallised as a primary phase (Zhao, et al., 2009).

In a more relevant study in terms of TiO_2 grades, Holmes et al. (1968) investigated the liquidus temperatures in the CaO-MgO-Al_2O_3-SiO_2-TiO_2 system for titaniferous slags in air – the investigated compositional range included both low and relatively high titania bearing slags from 6% to 48% TiO_2. From this study, the following conclusions were established: (1) in the studied compositional range, the liquidus temperatures ranged between 1217°C and 1667°C, (2) the lowest liquidus temperature titaniferous slags are those with less than 12% difference between the contents of CaO+MgO and SiO_2, and (3) the liquidus temperatures were lowered when SiO_2 was substituted by TiO_2+Al_2O_3, in which case the CaO and MgO were kept constant (Holmes, et al., 1968). This work however lacks the primary and sub-liquidus phase crystallization information as well as sub-liquidus temperature data.

An important study of phase equilibria in titaniferous slags with constant TiO_2, SiO_2 and Al_2O_3 and varying ratios of CaO to MgO was conducted by Jochens (1967) and is also reported by Jochens et al. (1969), McRae et al. (1969) and Van Der Colf et.al (1979). The study of these phase equilibria was carried out using high purity chemical reagents to produce synthetic titaniferous slags in order to study phase equilibria in the target compositional range. The respective synthetic slag recipes made from oxide reagents were repeatedly fused in a muffle furnace, quenched in water and ground using agate mortar and

pestle. The test specimen were inserted into platinum capsules and heated up at isothermal equilibration conditions in a high temperature microscope. The equilibrated samples were subsequently quenched in water to preserve the phases that existed at equilibration conditions (Van der Colf & Howat, 1979; Jochens, et al., 1969; McRae, et al., 1969; Jochens, 1967).

The quenched samples were analysed by X-ray powder photography to determine the equilibrium phases for subsequent mapping to produce the equilibrium phase diagram in Figure 19 (Jochens, 1967). This equilibrium phase diagram shows that titaniferous slags have a very large phase crystallization range. In the phase diagram, the liquidus surface has a minimum temperature of about 1340°C in a system containing 18wt% CaO and 12wt% MgO. In addition, the liquidus surface in the phase diagram shows that the temperature difference between titaniferous slags comprising 0wt%MgO - 30wt%CaO, and 30wt% MgO - 0wt%CaO is small. However, at high MgO concentrations in the slag, the crystallization of the pseudobrookite solid solution (M_3O_5 ss), $4MgTi_2O_5$-Al_2TiO_5, as a primary equilibrium phase is favoured, whereas at high concentrations of CaO in the slag the crystallization of perovskite ($CaO.TiO_2$) as the primary equilibrium phase is favoured (Jochens, et al., 1969; McRae, et al., 1969; Jochens, 1967).

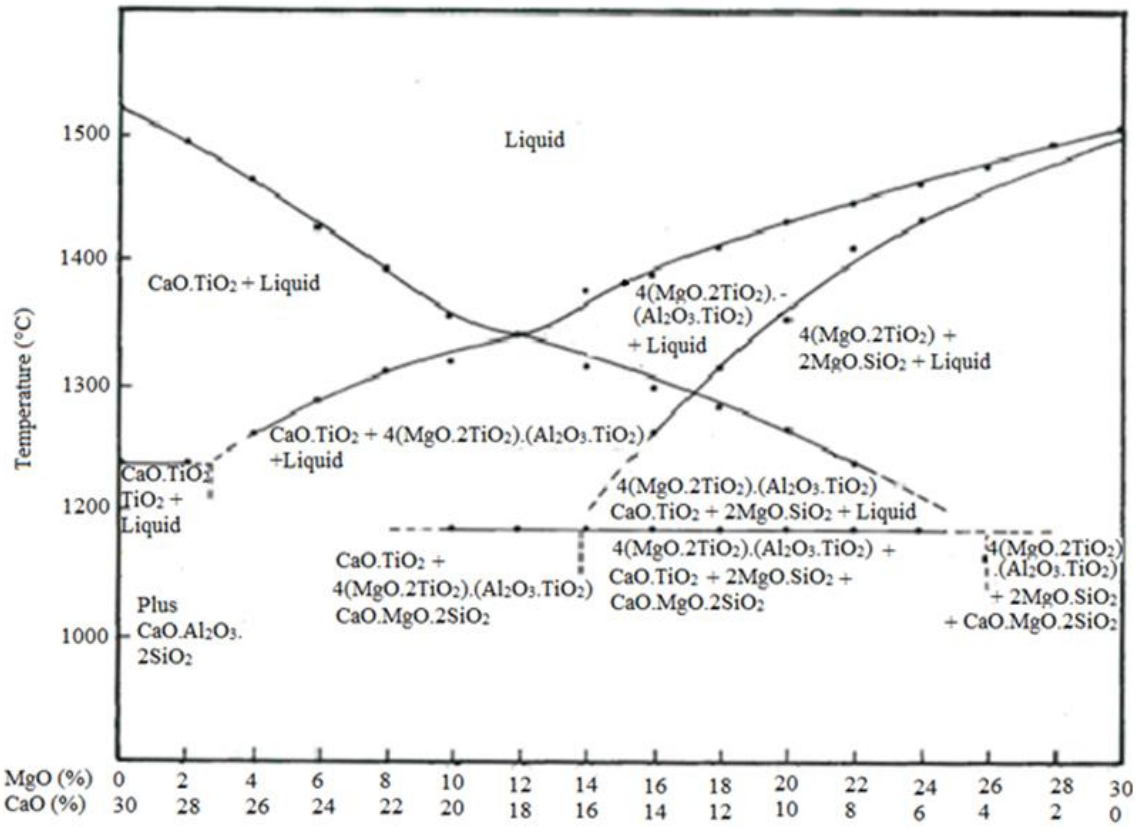

Figure 19: Phase diagram established in air for the slag system: TiO_2 = 37.19wt%, SiO_2 = 19.69wt%, and Al_2O_3 = 13.12, at varying proportions of CaO (30-0wt%) and MgO (0-30wt%) (Jochens, 1967)

This phase diagram was established in air. As a consequence of this, the crystallisation of phases that contain reduced Ti^{3+} species as reported by Zhao et al. (2009) cannot be predicted. In addition, contrary to the wide reporting of the crystallisation of spinel phase in real plant titaniferous slags (Pistorius, 2011; Steinberg, 2008) and in lower order systems (reviewed in the above subsections), the current phase diagram does not predict the crystallisation of a spinel phase. However, in his development work, Jochens (1967) reported some X-Ray diffraction patterns corresponding to those of spinel. The crystallisation of the spinel was however rejected because the patterns were faint and overlapped with those of the confirmed pseudobrookite solution. The reported phase equilibria established in air therefore need to be reviewed and validated or updated. In addition, the equilibrium phase diagram needs to be expanded and redrawn under low oxygen partial pressures (pO_2) applicable to titanomagnetite smelting operations in order to have a suitable phase diagram for correct prediction of crystallisation of phases in titaniferous slags.

2.4.2 Calculation of phase diagrams

In the current programme, FactSage thermochemical software was used to calculate the equilibrium phase diagrams applicable to titaniferous slags. However, evaluation of the available thermodynamic databases in the latest version of FactSage, i.e. FactSage 7.2, demonstrated that Al_2TiO_5 is not modelled as a component or an endmember in the existing pseudobrookite solid solution database. Hence, FactSage 7.2 would not be able to correctly calculate phase equilibria in the Ca-Mg-Al-Si-Ti-O system where an Al_2TiO_5 bearing pseudobrookite solid solution is anticipated to crystallise. It was therefore important that an Al_2TiO_5 bearing private pseudobrookite solid solution database is developed for correct calculation of the phase equilibria applicable to titaniferous slags.

It is important to note that that the private pseudobrookite solid solution database was developed using the optimised thermodynamic data available in literature (Centre for Research in Computational Thermochemistry, 2018; Bale, et al., 2016; Bale, et al., 2008; Bale, et al., 2002; Pelton, et al., 1998). Hence, experimentation and optimisation of the private pseudobrookite solid solution database were not conducted in the current study. Conventional thermodynamic modelling methodologies were followed to describe the pseudobrookite solid solution for the subsequent development of the database. The following subsections deal with literature pertinent to the thermodynamic modelling for the development of databases of solution phases.

2.4.2.1 Thermodynamic modelling

During high temperature operations, species typically dissolve into each other to form multicomponent phases such as slags, mattes, and alloys. The behaviour of solutions is complex; hence the calculation and drawing of phase diagrams for predicting the phase relations in these multicomponent systems require a combination of theory and experimentation to deal with the thermodynamics of these systems. Thermodynamic modelling coupled with thermochemical simulation is typically used for calculations of phase diagrams (Wulandari, et al., 2009; Jung, et al., 2009; Jak and Hayes, 2004).

In the past, phase diagrams were generally developed using data from experimental investigations. The experimentation typically becomes challenging and time consuming with an increase in the number of components in the system. In addition, the phase equilibria

and thermodynamic properties of the respective phase diagrams are generally determined from independent experiments and may be inconsistent if caution is not applied. The CALculation of PHase Diagram (CALPHAD) method was therefore established to address these challenges. The CALPHAD method is defined as the computer-based coupling of phase diagrams and thermochemistry. In the CALPHAD method, equations describing the Gibbs energy of the respective phases in the system are set up in terms of the state variables such as temperature, pressure and composition. In this way, the CALPHAD method is able to evaluate the model parameters into a self-consistent data-set which can be used to predict thermodynamic properties outside the reviewed range (Cacciamani, 2016; Pelton, 2006; Kattner, 1997; Kaufman & Bernstein, 1970).

In the CALPHAD method, the thermochemical data including the heat capacity and enthalpy of formation are directly used to determine the Gibbs energy function, whereas the phase equilibrium data including liquidus, solidus and phase fields provide information about the relative stabilities of phases. In cases of complex multicomponent and multiphase systems, the thermochemical and phase equilibrium data for binary and ternary subsystems are evaluated; for each phase, model equations are presented in terms of Gibbs energy given as a function of temperature and composition. The model equations for the binary and ternary subsystems are optimised using special optimisation models to within experimental error limits and subsequently stored in the databases. The databases are generally accessed by Gibbs energy minimisation software to calculate the thermodynamic properties, phase diagrams, and other properties for complex multicomponent systems (Cacciamani, 2016; Pelton, 2006; Kattner, 1997; Kaufman & Bernstein, 1970).

The technique of Gibbs energy minimisation is vital for determining phase equilibria. This technique starts with the determination of the Gibbs energy of the components of a phase – this technique works with the Gibbs energies of pure substances which can be extended to account for compounds and multicomponent phases (Eriksson , et al., 1993). In the Gibbs energy minimisation method, the free energy of all the equilibrium phases in the system needs to be thermodynamically at a minimum as shown in Equation [2.5] (Perrut, 2015; Wulandari, et al., 2009),

$$G = \sum_{i=1}^{p} n_i G_i^{\emptyset} = minimum \qquad [2.5]$$

Where n_i is the number of moles of species i, and $G_i^{\emptyset}$ is the Gibbs energy of species i in phase $\emptyset$. It is important that the n_i values are not negative. The Gibbs free energy of an element can be expressed using the Gibbs-Helmholtz equation as shown in Equation [2.6] (Perrut, 2015),

$$G(T_0) = H_{298} + \int_{298}^{T_0} C_p \, dT - T_0 \left(S_{298} + \int_{298}^{T_0} \frac{C_p}{T} dT \right) \quad [2.6]$$

Where H_{298} and S_{298} are the enthalpy and entropy of a pure element under atmospheric pressure conditions at a temperature of 298 K. C_p is the heat capacity of the pure element at constant pressure. Equations [2.6] and [2.7] show that the Gibbs free energy is temperature dependant; this dependence can be expressed as a power series as shown in Equation [2.7] (Perrut, 2015; Wulandari, et al., 2009).

$$G = a + bT + cT \ln T + \sum d_n T^n \quad [2.7]$$

Where a, b, c, and d_n are coefficients established as experimental parameters from thermodynamic and phase diagram data, and n are integers. These coefficients drive the temperature dependence of the Gibbs energy of the pure element in a particular phase.

The heat capacity of a pure substance at constant pressure can be determined using the expression in Equation [2.8] (Perrut, 2015; Wulandari, et al., 2009).

$$C_p(T) = -c - \sum (n-1) d_n T^{n-1} \quad [2.8]$$

Considering Equations [2.7] and [2.8], it appears that a and b are the only missing parameters that need to be optimised (Perrut, 2015). These parameters, i.e. a and b can be determined from the enthalpy and entropy data, respectively. In cases where the experimental data is lacking, first-principles calculations can be used to get the required thermochemical data (Liu, 2009; Kattner, 1997).

In the minimisation of Gibbs energy in real multicomponent and multi-phase systems, the Gibbs energy of each solution phase is calculated based on three main contributions as shown in Equation [2.9],

$$G^{\emptyset} = G^0 + \Delta G^{ideal} + \Delta G^{excess} \quad [2.9]$$

Where, G^0 is the contribution of the standard Gibbs energy of a pure substance in phase $\emptyset$, G^{ideal} is the contribution of the Gibbs energy of mixing in an ideal solution, and G^{excess} is the excess Gibbs energy of mixing of the real solution which takes into account the real behaviour of a solution (Wulandari, et al., 2009; Kattner, 1997).

Numerous thermodynamic models are available for predicting the properties of multicomponent solutions in terms of Gibbs free energy from the optimised binary and ternary parameters. This information is then stored in databases (Cacciamani, 2016; Pelton, 2006; Kattner, 1997; Kaufman & Bernstein, 1970). Literature on numerous thermodynamic models for multicomponent slags, fluxes and salts was reviewed and summarised by many researchers in the past (Wulandari, et al., 2009; Pelton, 2004; Ganguly, 2001). Some thermodynamic liquid and solid solution models applicable to slag systems are summarised in the following subsection – the current study is dedicated to the modelling of the pseudobrookite solid solution in titaniferous slags. More emphasis is thus placed on sublattice model coupled with Compound Energy Formalism (CEF) and Redlich-Kister Polynomial to account for interaction parameters as a function of composition and temperature. As informed by literature (Kang, et al., 2006; Bale, et al., 2002; Pelton, et al., 1998), this thermodynamic modelling approach is applicable in the current study for the development of a private pseudobrookite solid solution database for the calculation and simulation of phase equilibria of titaniferous slags.

Thermodynamic models:

Slags are defined as oxide-based ionic solutions which can be described by many thermodynamic models depending on the properties of the slag being reviewed. For example, liquid slag solutions, liquid-solid solutions and solid solutions are modelled using different thermodynamic models. Table 4 gives a summary of some thermodynamic models for solutions as they apply in slag systems (Povoden-Karadeniz, et al., 2012; Malakhov, 2010; Wulandari, et al., 2009; Jung, et al., 2009; Pelton, 2006; Pelton, 2004; Ganguly, 2001; Hillert, 2001).

As will be clear later, the sublattice model coupled with CEF and Redlich-Kister Polynomial are pertinent to the current study. The sublattice modelling was first established for use in molten salt solutions (Pelton, 1988). Sublattice models are generally used to model crystalline phases with different types of sublattices for the constituents. In the sublattice

model for the pseudobrookite type structure, the cations are placed in octahedral coordination, which is composed of two non-equivalent octahedral sites with fourfold (4c) and eightfold (8f) multiplicity (Buscaglia, et al., 1996; Navrotsky, 1975). Different constituents of the solution are placed on different sublattices: cations go to appropriate cation sublattices while the anions go to anion sublattices. The configurational entropy of mixing on each sublattice can be assumed (Pelton, 2006; Hillert, 2001; Shi, et al., 1992).

The CEF is typically coupled with the sublattice model in order to take into account the Gibbs energy of a phase that has two or more sublattices which show a variation in composition. CEF is able to reproduce the probability of site occupancy, and therefore it is able to reproduce the energy for the solution phase. Random mixing of species is assumed on respective sublattices. Sublattices take into account the long range order (LRO) when the atoms are regularly arranged on sublattices over large distances. Interaction parameters between constituents are generally expressed in the form of Redlich-Kister polynomial – Legendre expansions are also permitted for binary terms (Hillert, 2001). Extrapolation of binary parameters into ternary systems is performed using Muggianu's symmetric rule, whereas Kohler's rule can also be used. The ternary extrapolation systems containing data for the respective parameters are generally gathered to produce thermodynamic databases (Perrut, 2015; Pelton, 1988).

In a sublattice model where A and B mix in the first sublattice, and C and D mix in the second sublattice, the reciprocal mixing system, i.e. $(A,B)_a(C,D)_c$ can be used to represent the mixing on the sublattices. a and c are site ratios for the first and second sublattices, respectively. Any species, i.e. atom, molecule, ion or vacancy, can be represented in the sublattice model (Pelton, 2006; Hillert, 2001; Shi, et al., 1992).

Table 4: Summary of some thermodynamic solution models applicable in slags

Model	**Principle**	**Application**	**Model description**
Ideal solution	Example: A and B species making a binary solution – no difference in the interaction between like and unlike atoms (A-A=A-B=B-B) – no enthalpy of mixing and volume expansion.	Though the ideal solution model is not typically applicable in slag modelling; it is however a good starting point for the more comprehensive and complex models.	$G_m = G_A^0 n_A + G_B^0 n_B - T\Delta S^{conf}$ G_m is the molar Gibbs energy of the solution; G_A^0 and G_B^0 are standard Gibbs energies of components A and B, respectively; n_A and n_B are moles of A and B; and ΔS^{conf} is the configurational entropy. $\Delta S^{conf} = -R(n_A \ln n_A + n_B \ln n_B)$
Dilute solution with Henrian activities	This model works on the principle of Henry's law for activity of the solute and Raoult's law for the activity of the solvent.	This model is typically applied for calculating equilibrium between liquid alloy and inclusions.	$a_i = \gamma_i^0 x_i$ a_i activity of the solute, γ_i^0 is the Henrian constant, and x_i is the concentration of solute
Regular solution	There are interaction parameters between A and B species – the parameter is independent of the composition of the binary A-B solution	In solid solutions. If A and B atoms, occupy lattice sites, the energy of AB bond is related to that of AA and BB. If energy is negative, mixing occurs, if positive, de-mixing is favoured.	$G_m = G_A^0 n_A + G_B^0 n_B - T\Delta S^{conf} + G^E$ G^E is the excess Gibbs energy accounting for the interaction of real solution components in specific sublattices.

Model	**Principle**	**Application**	**Model description**
Associate solution (similar to Lin-Pelton)	Considers the existence of a random mixture of associates or molecules in the liquid. Equilibrium is assumed amongst associates.	Involves the modelling of a binary liquid system – for example MO-SiO_2 (M = Ca, Mg, Pb, etc.).	The main parameters are the energies associated with the formation of the associates: $$xMO + SiO_2 \rightarrow M_xSiO_{2+x}$$
Reciprocal ionic liquid	Takes into account the existence of two sublattices in liquid oxides; it however does not consider the short range ordering described in Quasichemical models.	For example ternary liquid solution CaO-MgO-SiO_2.	The liquid structure can be presented as: $(Ca^{2+}, Mg^{2+})_P(SiO_4^{4-}, O^{2-}, SiO_2^0)_Q$ Where, P and Q indicate numbers of sites as: (electron neutrality is maintained) $$P = 2y_{SiO_4^{4-}} + 2y_{O^{2-}}$$ $$Q = 2y_{Ca^{2+}} + 2y_{Mg^{2+}}$$
Modified Quasichemical	Takes into account Short-Range Ordering (SRO) by considering all possible pairs of atoms or molecules A and B which have common coordinate number. The formation of AB pairs from AA and BB pairs can be expressed as: $AA + BB \rightarrow 2AB$	Mainly used in molten oxides and silicates.	The Gibbs energy for the liquid: $G^{liq} = n_i G_i^{liq} + n_j G_j^{liq} - T\Delta S^{conf} + \frac{n_{ij}}{2} G^{ex,liq}$ Where n_i and n_j are the number of moles of components i and j, and n_{ij} is the number of $(i-j)$ pairs, and the ΔS^{conf} is the configurational entropy of mixing for random mixing of $(i-i)$, $(i-j)$, and $(j-j)$ pairs.

Model	**Principle**	**Application**	**Model description**
Sublattice and Compound Energy Formalism (CEF)	Sublattices are used to represent the more-than-one Wyck-off positions existing in most solid phases. Sublattices are used to describe long range order (LRO). Consider reciprocal mixing: $(A,B)_a(C,D)_c$ a and c are site numbers for the first and second sublattices, respectively.	Typically used to model multi component solid oxide solutions with two or more sublattices. The model has been used for solid solutions of spinel and pseudobrookite as well as silicates.	Gibbs energy expression for solution with i and j components: $G = \sum_i \sum_j y_i' y_j'' G_{ij}^0 - TS^{config} + G^{excess}$ y_i' and y_j'' are site fractions on first and second sublattices. G_{ij}^0 is the standard Gibbs formation of the compound $i_a j_c$, also called 'endmember' $S^{config} = -R[a \sum_i y_i' \ln(y_i') + c \sum_j y_j'' \ln(y_j'')]$ R is the gas constant
Redlich-Kister polynomial	Accounts for the excess Gibbs energy in the sublattice model.	Typically used in connection with sublattice and CEF modelling of multicomponent solid solutions with two or more sublattices.	Redlich-Kister polynomial: $G^{excess} = y_A' y_B' (y_C'' L_{A,B:C} + y_D'' L_{A,B:D}) + y_C'' y_D'' (y_A' L_{A:C,D} + y_B' L_{B:C,D}) + y_A' y_B' y_C'' y_D'' L_{A,B:C,D}$ L is the interaction parameter in the Redlich-Kister series

The molar Gibbs energy expression for the solution can be expressed as shown in Equation [2.10], which can be rearranged into Equation [2.10],

$$G_m = \sum_i \sum_j y_i' \, y_j'' G_{ij}^0 - TS^{config} + G^{excess} \quad [2.10]$$

Where y_i' and y_j'' are site fractions on first and second sublattices, and G_{ij}^0 is the Gibbs energy of formation of the compound ij, also called 'endmember'; thus the main parameters of the CEF model are the endmember Gibbs energies (Pelton, 2006; Hillert, 2001; Shi, et al., 1992).

For the reviewed sublattice model example, i.e. $(\mathrm{A,B})_\mathrm{a}(\mathrm{C,D})_\mathrm{c}$, there can be four endmembers for which the Gibbs energies are $G_{A:C}^0$, $G_{A:D}^0$, $G_{B:C}^0$, and $G_{B:D}^0$. The four possible endmember states of reference for a reciprocal solution are illustrated in Figure 20 (Povoden-Karadeniz, et al., 2012; Hillert, 2001; Shi, et al., 1992). It is shown in this figure that all possible compositions can be established by compositional space on the two axes, y_A' and y_C''. The Gibbs energy of the solution phase is described by considering the mixture of all the endmembers. On the base of Figure 20, the corners represent the four endmembers and the sides represent the four interaction parameters. The endmember Gibbs energies plotted at the top of Figure 20 are the parameters of the CEF. Some of these energies are related to the Gibbs energies of the real compounds (Sundman & Gueneau, 2015; Hillert, 2001; Shi, et al., 1992).

The molar Gibbs energy of the solution phase can be expanded as in Equation [2.11] (Hillert, 2001).

$$G_m = y_A' y_C'' G_{A:C}^0 + y_A' y_D'' G_{A:D}^0 + \; y_B' y_C'' G_{B:C}^0 + y_B' y_D'' G_{B:D}^0 - TS^{config} + G^{excess} \quad [2.1]$$

The ideal/ configurational entropy (S^{config}) can be expressed as shown in Equation [2.12] (Hillert, 2001),

$$S^{config} = -R[a(y_A' \ln(y_A') + y_B' \ln(y_B')) + c(y_C'' \ln(y_C'') + y_D'' \ln(y_D''))] \quad [2.12]$$

Where R is the gas constant.

The excess and physical contributions in the solution are described by the Redlich-Kister polynomial as in Equation [2.13] (Hillert, 2001; Shi, et al., 1992).

$$G^{excess} = y'_A y'_B\left(y''_C L_{A,B:C} + y''_D L_{A,B:D}\right) + y''_C y''_D\left(y'_A L_{A:C,D} + y'_B L_{B:C,D}\right) + y'_A y'_B y''_C y''_D L_{A,B:C,D}$$ [2.13]

$L_{A,B:C}$, $L_{A,B:D}$, $L_{A:C,D}$, and $L_{B:C,D}$ represent the binary interaction parameters with comma separating interacting elements in the same sublattice, whereas $L_{A,B:C,D}$ represents the interaction parameter of the simultaneous mixing. The interaction parameters L are generally functions of pressure, temperature and composition (Hillert, 2001; Shi, et al., 1992).

The thermodynamic model parameters are typically stored in databases of computer-based thermochemical software for subsequent calculation of phase equilibria and thermodynamic properties of reviewed systems at given sets of conditions (Perrut, 2015).

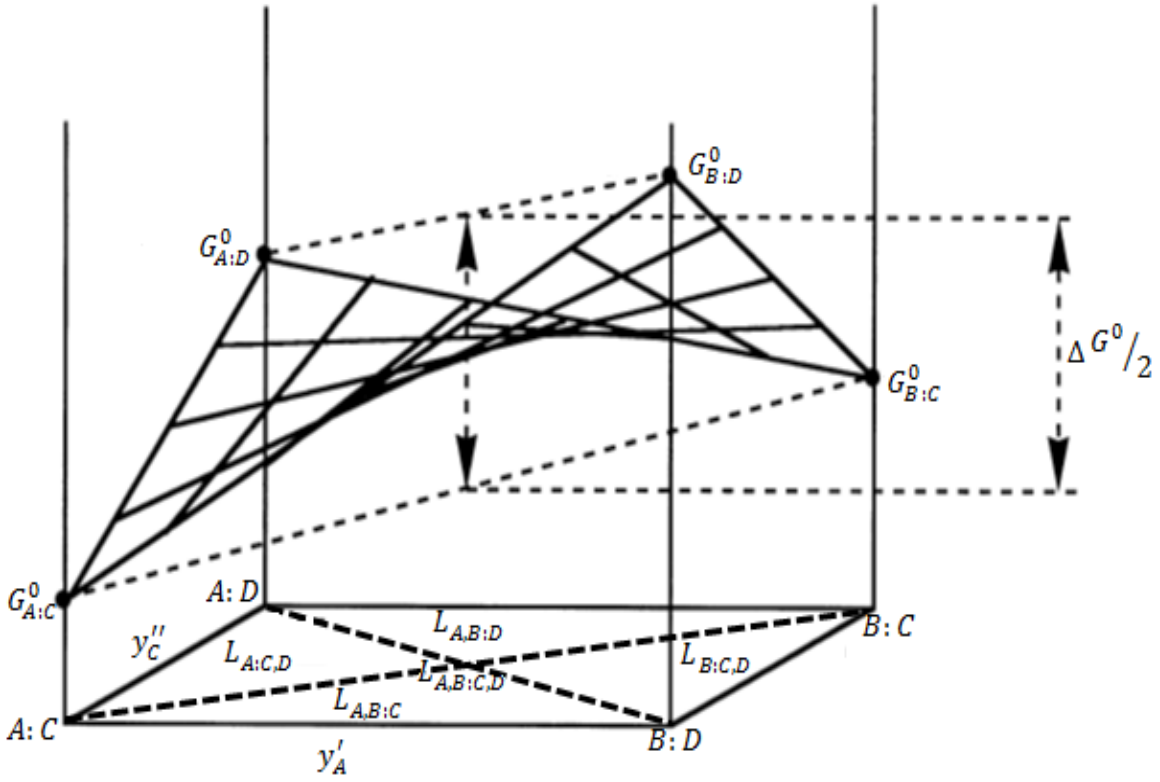

Figure 20: CEF illustration of the Gibbs energy of mixing, compositional space and interaction parameters in the reciprocal solution $(\mathrm{A,B})_a(\mathrm{C,D})_c$

Thermochemical software:

For the construction of phase diagrams of multicomponent and complex systems, it is challenging to conduct all the relevant experiments. Hence, the use of computer-based thermochemical software equipped with appropriate databases is typical for the calculation and simulation of multicomponent and complex phase diagrams (Jung, et al., 2009). There are several available commercial thermochemical software packages. These include Thermo-Calc of the Thermo-Calc group at KTH in Sweden, SGTE of Scientific Group Themoda Europe, THERMODATA of the THERMODATA group in France, Thermotech of Thermotech Inc. in the UK, MTDATA of the MTDATA group at NPL in the UK, Pyrosim of the pyrometallurgical group at Mintek in South Africa, and FactSage of the FACT group at Ecole Polytechnique in Canada.

The thermochemical databases developed by these groups are useful for the studies of phase equilibria of multicomponent and multiphase systems. The selection of an appropriate database for a given system is an important stage for the accurate thermochemical simulations. In any case, the database adopted for the study must have a thermodynamically self-consistent data-set (Pelton, 2004; Kaufman & Bernstein, 1970).

2.4.2.2 FactSage thermochemical software and databases

The thermodynamic calculations in the present study were conducted using FactSage thermochemical software – several versions were used during the course of this study, namely; FactSage7.0; FactSage7.1 and FactSage7.2. FactSage thermochemical software was introduced in 2001 as a fusion of the established software packages: Fact/ Fact-Win and ChemSage. The databases of FactSage are the largest set of evaluated and optimised thermodynamic databases for the inorganic systems in the world. The FactSage databases comprise consistently assessed thermodynamic data for numerous compounds and complex non-ideal solutions including those included in typical molten slags, alloys, salts, mattes and ceramics. Some oxide species are fully optimized from 25°C to above their liquidus temperatures at all compositions and oxygen partial pressures. The FactSage databases are regularly updated with new experimental data in order to always maintain high quality thermodynamic and phase equilibrium data for the compounds and solution systems for easy and correct attainment of model equations for the Gibbs energies of all phases as functions of temperature and composition (Bale, et al., 2002; Bale, et al., 2008; Bale, et al., 2016).

FactSage is equipped with several types of thermochemical databases including the compound databases, which account for the pure substances, and solution databases. The compound database contains thermochemical and phase equilibria data for over 4 400 compounds (Decterov, et al., 2004), 150 of which are solid stoichiometric compounds (Bale, et al., 2008). The solution databases contain over 120 non-ideal multicomponent solution phases (Decterov, et al., 2004).

The FactSage databases are included under 'FTsalt' for pure salts and salt solutions, 'FThall' for Hall aluminium pure substances and 17 solution phases formed among Al-Mg-Na-Li-Ca-F-O, 'FThelg' for 1400 aqueous solute species from GEOPIG-SUPCRT Helgeson database, 'FTmisc' for miscellaneous pure substances and solution phases, 'FTpulp' for pulp and paper database, and 'FToxid' for slags, glasses, minerals, ceramics, refractories, etc. which contain pure oxide substances and oxide solutions. The 'FToxid' database contain many components including Al_2O_3, As_2O_3, B_2O_3, CaO, CoO, CrO, Cr_2O_3, Cu_2O, FeO, Fe_2O_3, GeO_2, K_2O, MgO, MnO, Na_2O, NiO, PbO, SiO_2, SnO, TiO_2, Ti_2O_3, ZnO, and ZrO_2. The possible combinations of these components have not all been critically evaluated and optimised – in addition, not all composition ranges are covered (Bale, et al., 2016; Decterov, et al., 2004).

The 'FToxid' also contains many solid solution databases which include those listed below. It should be noted that for the modelling of the solid oxide solutions, for example pseudobrookite and spinel solid solutions, the sublattice model coupled with CEF and the Redlich-Kister polynomial were employed (Bale, et al., 2008; Pelton, 2006):

- Monoxide: CaO-MgO-MnO-CoO-NiO-FeO (+Fe_2O_3-Al_2O_3-ZnO-Cr_2O_3);
- Corundum: $A1_2O_3$-Cr_2O_3-Fe_2O_3;
- Wollastonite: $CaSiO_3$ (+$FeSiO_3$, $MgSiO_3$, $MnSiO_3$);
- ά-Ca_2SiO_4: ά-Ca_2SiO_4 (+Fe_2SiO_4, Mg_2SiO_4, Mn_2SiO_4);
- ά-Ca_2SiO_4: ά-Ca_2SiO_4 (+Fe_2SiO_4, Mg_2SiO_4, Mn_2SiO_4, Pb_2SiO_4, Zn_2SiO_4);
- Olivine: $[Ca^{2+}, Co^{2+}, Fe^{2+}, Mg^{2+}, Mn^{2+}, Ni^{2+}, Zn^{2+}]^{M2}(Ca^{2+}, Co^{2+}, Fe^{2+}, Mg^{2+}, Mn^{2+}, Ni^{2+}, Zn^{2+})^{M1}SiO_4$, where M1 and M2 represent the respective site fractions

- Ilmenite: (Fe^{2+}, Mg, Mn, Ti^{3+}) (Ti^{4+}, Ti^{3+})O_3
- Pyroxenes: (Ca, Fe^{2+}, Mg)^{M2} (Fe^{2+}, Fe^{3+}, Mg, Al)^{M1}(Fe^{3+}, Al, Si)$^{B}SiO_6$, where M1, M2, and B represent the respective site fractions
- Melilite: (Ca)2[Mg, Fe^{2+}, Fe^{3+}, Al, Zn] (Fe^{3+}, Al, Si)$_2O_7$
- Spinel: (Al^{3+}, Co^{2+}, Co^{3+}, Cr^{2+}, Cr^{3+}, Fe^{2+}, Fe^{3+}, Mg^{2+}, Ni^{2+}, Zn^{2+})^{T}[Al^{3+}, Co^{2+}, Co^{3+}, Cr^{3+}, Fe^{2+}, Fe^{3+}, Mg^{2+}, Ni^{2+}, Zn^{2+}, Va]$_2O_4$
- Pseudobrookite: (Fe^{2+}, Mg, Mn, Ti^{3+})(Ti^{4+}, Ti^{3+})$_2O_5$

The latest version of FactSage, FactSage 7.2 comprises all the essential compounds in the current study, including pseudobrookite-type compounds such as $MgTi_2O_5$, Ti_3O_5 and Al_2TiO_5, in its compound database (Centre for Research in Computational Thermochemistry, 2018). In the work conducted by Jochens et al. (1969) for the Ca-Mg-Al-Si-Ti-O system applicable to titaniferous slags in air, the $MgTi_2O_5$-Al_2TiO_5 solid solution phase was reported as a primary phase at MgO concentrations above 12wt% in the reviewed composition (Jochens, 1967). In addition, some literature reported in section 2.4.1 confirmed that the $MgTi_2O_5$-Al_2TiO_5 solid solution can crystallise as one of the phases in titaniferous slags. In addition, under reducing conditions, the pseudobrookite type solid solution would include reduced titanium species to form $MgTi_2O_5$-Al_2TiO_5-Ti_3O_5 solid solution (Krajewski, 1992; Berezhnoi & Gulko, 1955).

Nevertheless, the FactSage databases, particularly 'FToxid', do not have Al_2TiO_5 modelled as a component in the current pseudobrookite solid solution (Bale, et al., 2002; Bale, et al., 2008; Centre for Research in Computational Thermochemistry, 2018). Hence, the current FactSage 7.2 thermochemical software, would not be able to correctly model the Ca-Mg-Al-Si-Ti-O system with $MgTi_2O_5$-Al_2TiO_5-Ti_3O_5 as a possible pseudobrookite solid solution phases that can crystallise. A private pseudobrookite solution database capable of predicting the crystallization of the $MgTi_2O_5$-Al_2TiO_5-Ti_3O_5 solid solutions from compositions in the Ca-Mg-Al-Si-Ti-O system applicable to titaniferous slags needed to be developed and subsequently incorporated into FactSage. As said, the optimized thermodynamic data for the involved compounds is available in several publications and also included in the FactSage compound database (Centre for Research in Computational Thermochemistry, 2018; Bale, et al., 2016; Bale, et al., 2002).

In their study of the Mg-Ti-O system, Pelton et al. (1998) successfully developed a thermodynamic model for the $MgTi_2O_5$-Ti_3O_5 solid solution using the sublattice model coupled with CEF and Redlich-Kister polynomial. Thus in the current study, the binary thermodynamic models for the $MgTi_2O_5$-Al_2TiO_5 and Al_2TiO_5-Ti_3O_5 binaries were developed using the same principles. Fortuitously, the thermodynamic properties of the relevant compounds are available in literature (Pelton, et al., 1998) and also included in the FactSage compound database (Centre for Research in Computational Thermochemistry, 2018; Bale, et al., 2016; Bale, et al., 2002). These thermodynamic properties are included in Table 5 – the Gibbs free expressions of the endmembers are determined using Equations [2.14] to [2.16]. Experimentation for the validation and optimisation of the $MgTi_2O_5$-Al_2TiO_5-Ti_3O_5 private solid solution database was beyond the scope of the current research programme which only aimed to use the FactSage thermochemical databases to draw the phase diagram applicable to titaniferous slags.

Table 5: Optimised thermodynamic properties of the reviewed compounds relative to elements at 298.15 K

	A = Enthalpy ($Jmol^{-1}$)	B= Entropy ($Jmol^{-1}K^{-1}$)	a	b	c	d	e
TiO_2(s) (298-2130 K)	-944750	50.460	77.838		-33.678		4.0294
Ti_2O_3(β)[a] (470-2115 K)	-1519375	80.529	169.96		16.096	-750.22	-15.655
MgO(s) (298-3098 K)	-601500	26.951	61.110		-6.2115	-296.20	0.0584
Al_2O_3(s) (1200-2327 K)	-1656864	52.300	-787.52	0.06588	2638.2		0.0007
Ti_3O_5(s) (298-1991) K)	-2452465	157.617	158.99	50.20795			
$MgTi_2O_5$(s) (298-1930 K)	-2504887	137.34	232.58		-56.608	-755.50	5.8214
Al_2TiO_5(s) (298-2500 K)	-2577174	128.45	249.29		-48.061	-1350.1	5.1603

$$H(Jmol^{-1}) = A + \int_{298.15}^{T} C_p dT \quad [2.14]$$

$$S(Jmol^{-1}K^{-1}) = B + \int_{298.15}^{T} (C_p/T)\, dT \quad [2.15]$$

$$C_p(Jmol^{-1}K^{-1}) = a + b(10^{-3})T + c(10^{5})T^{-2} + dT^{-1/2} + e(10^{8})T^{-3} \quad [2.16]$$

2.4.3 Experimentation

Historically, the determination of phase diagrams was conducted using experimental data. In experimental testwork, specific properties and phenomena are measured and used to determine the phase equilibria in low and high order systems. These properties typically include chemical thermodynamic and physical properties of single and multi-phase systems. The typical chemical thermodynamic properties that can cause the disappearance or appearance of a phase include heat capacities, enthalpies, entropies, activities, Gibbs free energy, and partitioning parameter of elements. The typical properties used to detect the phase transitions and assemblages include optical, crystal structure, and phase compositions. These properties are generally used in the construction of a phase diagrams in which case they can be plotted as a function of composition, temperature and pressure. Before the execution of experimental studies, it is thus important to correctly identify the properties or phenomena that would provide the required information and the best experimental approach to obtain this (Jak & Hayes, 2004).

Various experimental techniques are available for the determination of chemical thermodynamic and physical properties of oxide systems. These experimental techniques for studying phase equilibria can be classified into static and dynamic techniques. Static techniques can be defined as the experimental techniques that involve the measurement of the property or observation of a system at a particular state with defined conditions – an example would be the measurement of a property at equilibrium state (Jak & Hayes, 2004). Examples of static techniques include electrochemical methods, X-Ray powder diffraction (XRD), hot stage microscopy, calorimetry and equilibration-quench-analysis techniques (Jak & Hayes, 2004; Jochens, et al., 1969; Belon & Forestier, 1963; Welch & Gutt, 1959; Lang, et al., 1952). The measurements carried out using the static techniques are typically conducted at constant temperature and pressure, or in a series of staged constant temperature-pressure experiments. The challenge facing the static techniques is the inability to address the error in high temperature measurements that may be brought about by the loss of sample components due to vapour phase reactions, or by reactions with containment materials. One of the main advantages of the static methods is the capability of accurate control of the temperature and oxygen partial pressure during the experimentation (Jak & Hayes, 2004).

The dynamic experimental techniques can be defined as those techniques that involve the measurement of property change as the system undergoes a phase transformation (Jak & Hayes, 2004). The typical dynamic techniques are based on thermal analysis, namely; thermal analysis (TA), differential thermal analysis (DTA), differential scanning calorimetry (DSC), and thermogravimetric analysis (TGA) (Haines, et al., 2002). The common disadvantage of dynamic techniques is that the measurements of properties of the system are inherently conducted under non-equilibrium conditions. In systems with poor phase transformation kinetics, the dynamic techniques generally produce inaccurate measurements. However, dynamic techniques are generally useful for measurements in highly fluid systems and in systems where reactions do not occur through diffusion mechanisms (Jak & Hayes, 2004).

Different approaches for studying the relationships between the phase equilibria in systems and chemical thermodynamic properties are established (Hillert, 1998). Several theoretical tools are available for the design and selection of process conditions as well as for the interpretation of data generated from phase equilibria experiments. These theoretical tools used in phase equilibria studies include Schreinemakers' rule, the lever rule and the phase rule. Schreinemakers' rule deals with the shapes of intersecting phase field boundaries – this rule is useful in the construction of phase diagrams of low and higher order systems (Jak & Hayes, 2004; Hillert, 1998).

The lever rule states that in a case of a bulk composition which is split into two phases, the compositions of the bulk phase and the two new phases are co-linear – the amounts of the two new phases have an inverse proportionality relationship to their distances to the bulk composition. The rule is typically used for the determination of the proportions of phases formed for a given bulk composition – this rule can be assessed in terms of the mass balance analysis of the components of the system. The rule can be extended to higher order or multicomponent systems (Jak & Hayes, 2004).

The phase rule can be described by Equation [2.17]. In the equation, F represents the degrees of freedom in any chemical system at equilibrium, C is the number of independent chemical components, P denotes the number of phases present for a given temperature and total pressure, and E represents the number of thermodynamic variables in the system at equilibrium. The phase rule is specifically useful in the evaluation and confirmation of

equilibrium phases in multicomponent systems including those in which some components can exist in more than one oxidation states. This rule is generally important for the interpretation of the phase equilibrium data (Jak & Hayes, 2004; Hillert, 1998).

$$F = C - P + E \quad [2.17]$$

The following subsections provide more information on experimental techniques that are relevant to the current study, i.e. the classical equilibration-quench-analysis. Hot stage microscopy and thermal analysis based techniques in the form of DSC and DTA were not used as a consequence of the unavailability of sufficiently high temperature systems. When selecting experimental techniques for phase equilibria studies, it is important to consider the thermodynamic property to be measured, the degrees of freedom of the system and reaction conditions to be controlled, the chemical and physicochemical properties of the system under study, and the reactivity of the system components with the containment or measurement materials (Jak & Hayes, 2004).

2.4.3.1 Classical equilibration-quench-analysis

The equilibration-quench-analysis technique is well established for the determination of phase equilibria in low and high order systems. This technique involves the equilibration of a small mass of the material of known composition under controlled conditions, usually under fixed temperature and pressure. The equilibrated sample is then subjected to rapid cooling to room temperature by quenching the hot material into a cold medium, usually ice/ cold water. The ideal to be achieved during quenching is to preserve the phase assemblage and phase composition that existed at equilibration temperature (Jak & Hayes, 2004). The properties of the material at room temperature are typically determined by a single or combination of analytical techniques – these examination techniques include electron probe microanalysis (EPMA) (Zhao, et al., 2009; Jak, et al., 1995) and/ or powder XRD (Jochens, 1967).

The equilibration-quench-analysis technique has been used successfully for the determination of solid solutions, solid-state phase relations and solid-liquid phase equilibria in which case the liquid phase can be quenched into glass or non-crystalline solid phase. The approach has been used to study high temperature phase relations in silicate slag systems – silicate systems are known for elongated equilibration times (Jak & Hayes, 2004).

For many years, the equilibration-quench-analysis technique has been a subjected of intensive research at the Pyrometallurgy Research laboratory (PYROSEARCH) of the University of Queensland in Australia (Hayes, et al., 2016; Jak & Hayes, 2010; Zhao, et al., 2009; Jak, et al., 1995). As established by PYROSEARCH, the equilibration-quenching-EPMA analysis technique can be described using the hypothetical illustration shown in Figure 21 (Jak & Hayes, 2004). A starting material with composition X, as shown in Figure 21, is prepared. Subsamples of sample X are subjected to equilibration at different temperatures of T_1 to T_4, followed by quenching. The phase assemblages and phase compositions of the respective quenched samples are typically determined by EPMA. For composition X, T_1 corresponds to the phase field of a complete liquid, while the liquidus temperature of composition X is between T_3 and T_4. T_2 falls within a primary phase field in which the primary phase is β. In this way, the phase diagram is constructed by testing different compositions at different equilibration temperatures followed mapping the equilibration temperatures at which various phases appear or disappear from the quenched samples (Jak & Hayes, 2010; Zhao, et al., 2009; Jak & Hayes, 2004; Jak, et al., 1995).

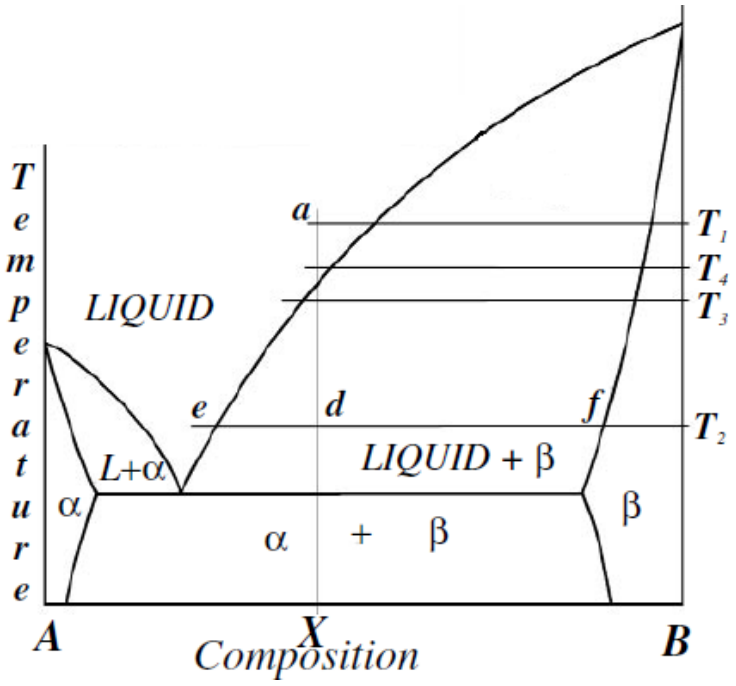

Figure 21: Hypothetical illustration of the equilibration-quench-EPMA analysis technique (Jak & Hayes, 2004)

The conventional equilibration-quench-analysis approach relies on a number of assumptions including that:

- Replicate experiments can be conducted accurately to identify the liquidus,
- Equilibration of the sample at isothermal test temperature can be achieved,
- The sample composition does not change during the equilibration process,
- No further crystallization occurs during quenching or the crystals formed during quenching can be distinguished and eliminated (by disregarding) from those formed during the equilibration at target temperature,
- A small quantity of the primary crystalline phase can be detected as soon as it forms – this has to be done within a small uncertainty range in terms of the equilibrium conditions, particularly the temperature.

The EPMA that is typically used for analysis in the equilibration-quench-analysis technique is essentially a dedicated scanning electron microscope (SEM) that is equipped with wavelength dispersive spectrometers for effective imaging of microstructures and determination of the compositions of the microstructures.

Experimental measurements are inherently associated with uncertainty. Hence the convention of the equilibration-quench-analysis technique is that experiments need to be taken in several cycles for confirmation purposes. In addition, some phase equilibria data and thermodynamic properties established during the equilibration-quench-analysis technique should be confirmed using other techniques; for example hot stage microscopy (HSM), differential scanning calorimetry (DSC) and differential thermal analysis (DTA) can be used to verify the established liquidus temperatures.

High temperature XRD systems are also useful for the identification of phases, including the liquidus temperatures.

However, due to unavailability of sufficiently high temperature systems of these techniques, the equilibration quench results were only cross checked against the thermochemical simulation data.

2.4.3.2 Hot stage microscopy

Hot stage microscopy (HSM) is a static technique which operates as a combination of microscopy and thermal analysis to study the properties of materials as a function of temperature and time. The visual examination of the test material during the HSM analysis gives valuable information with regard to liquidus temperature or melting point and other properties during heating. HSM is typically used to estimate the liquidus temperatures by direct or in-situ determination of the phase transformation temperature in simple and complex slag systems. In the past, this technique was successfully used by many researchers for the determination of the liquidus temperature of low vapour pressure systems with transparent liquid phases (Welch & Gutt, 1959).

HSM technique offers a unique opportunity of visual observation of the test sample to follow thermal changes throughout the test duration. This technique has the following general advantages (over the equilibration-quench-analysis technique): (1) it is free from the complications of quenching, (2) it allows for the straight-forward interpretation of results, and (3) it allows for the study to be conducted in a continuous temperature range. Some of the typical disadvantages of the technique include the relatively lesser availability of the instrumentation (experienced in the current study), more complex experimental set up, and more susceptibility to test material deterioration through evaporation, oxidation or other environmental interactions. The hot stage microscopy technique is ideal to complement the equilibration-quench-analysis technique, but cannot substitute it (Jak & Hayes, 2004; Haines, et al., 2002).

2.4.3.3 Differential scanning calorimetry

Differential scanning calorimetry (DSC) is a thermal analysis technique that operates by measuring the energy absorbed or emitted by a test material as a function of temperature and time. During heating of a sample in a DSC instrument, a phase transition occurs. The DSC technique typically determines the transition energy by the direct calorimetric measurement at the transition temperature. The transition energy is determined on a test material and inert reference material at identical temperatures in a controlled cooling or heating rate. DSC results typically show the heat transferred in arbitrary units, which can be interpreted in terms of enthalpy, entropy, and specific heat which are important for the determination of liquidus

and sub-liquidus temperatures. The DSC data is used to established liquidus-lines, solidus-lines and other phase transition points (Haines, et al., 2002).

There are two available setups of DSC systems, namely; the power-compensation and heat flux DSC systems. In the power compensation system, the test material and reference material are processed over a temperature range using separate but identical furnaces. In this set up, the temperatures of the test and reference samples are controlled in an identical range by varying the power input to the respective furnaces. The comparison of the energy requirements in the two furnaces gives the measure of the enthalpy and heat capacity differences in the test and reference materials. However, the heat-flux DSC system involves the heating of the test and reference materials in a single furnace. When the phase transitions occur in the test material, the enthalpy or heat capacity changes cause a difference between the temperatures of the test and reference materials (Haines, et al., 2002).

Just like in other dynamic experimental techniques, the challenge of the DSC technique is that measurements are conducted under non-equilibrium conditions – measurement uncertainties as a consequence of kinetic and metastability effects are thus common, especially in systems with slow phase transitions. However, the operation of the DSC system is less complicated compared to the manual equilibration-quench-analysis technique (Jak & Hayes, 2004). It is thus more sensible to use DSC and equilibration-quench-analysis technique for results verification and validation.

When a material is subjected to high temperatures, there may be a mass loss if the material contains volatile component or there is a chemical reaction. The mass loss as a function of temperature and time is typically measured by the Thermogravimetric Analysis (TGA) technique. The mass loss generally translates to a change in the material composition as well as in thermochemical and calorimetric properties. There can also be reactions that do not involve mass loss – the DSC becomes handy in the characterisation of the thermochemical and calorimetric properties of these reactions. Hence, modern DSC systems are coupled with a TGA component, to form a DSC-TGA hybrid, in order to acquire complementary information that would assist in the establishment of correct phase equilibria in low and high order systems.

2.5 Titania pigment production

Titanium is primarily used as TiO_2 (titania) pigment in, amongst others, paints, paper, plastic, foods and cosmetic industries. This is because TiO_2 pigment offers unprecedented properties such as high refractive index, opacity, brightness, whiteness, and resistance to discolouration under ultraviolet light (Roskill, 2003; Van Dyk, 1999).

Titania bearing minerals are typically processed directly or indirectly for the production of the pigment. These natural resources include rutile, anatase, ilmenite, perovskite and titanite (Gazquez, et al., 2014; Roskill, 2003). There are however other potential titania resources for the production of the pigment, namely; titanomagnetite (Gazquez, et al., 2014).

There are two main processes used for the production of the pigment, namely; the sulfate and chloride processes. The sulfate process entails the dissolution of the feedstock in sulfuric acid, followed by multiple stage purification and subsequently the controlled crystallisation of the titania to produce the pigment. The sulfate process offers some advantages over its counterpart, including that it uses a simpler technology and lower grade and cheaper raw materials to produce the special anatase pigment, which is preferred for use in the papers, ceramics and inks. However, the process generates a relatively high volume of hazardous sulfate waste that requires special treatment and disposal due to the use of relatively impure feedstock and the lack of an economic sulfuric acid recycling process. Moreover, the capital cost of a modern sulfate process is relatively high (Gazquez, et al., 2014; Roskill, 2003; Van Dyk, 1999).

The chloride process is generally preferred. In 2014, it was estimated that about 60% of the 4.5 million tons of titania pigment produced in the world was generated by the chloride process. In this process, the feedstock is subjected to carbo-chlorination in a fluidised bed at temperatures ranging between 900-1000°C in order to convert the TiO_2 to $TiCl_4$. The $TiCl_4$ is typically purified and oxidised back into a pure TiO_2 crystal that is further treated to produce a pigment of specific properties. The chloride process has relatively more stringent feedstock requirements compared to the sulfate process. However, the chloride process offers many advantages including the opportunity for a tighter product control, relatively less labour intensive, and more environmentally safer (Gazquez, et al., 2014; Roskill, 2003; Van Dyk, 1999).

As the details of the processing of titania resources to produce the pigment are different, the feedstock specifications also differ. These differences are discussed in the following subsections.

2.5.1 Feedstock for the sulfate process

In principle, the sulfate process can accommodate relatively low titania grade feedstock, provided that TiO_2 is not in the rutile structure, which is not soluble in sulfuric acid. However, the environmental restrictions on waste disposal have motivated for an increase in the demand for materials with high titania concentrations. As a second choice process, the feedstock to the sulfate process is generally what is deemed inadequate as feedstock for the preferred chloride process. The relegation of feedstock to sulfate process is generally based on the TiO_2 grade and the particle size distribution (PSD). The typical feedstock for the sulfate process include sulfate-grade ilmenite containing 44wt% to 57wt% TiO_2 and sulfate slag containing 75wt% to 80wt% TiO_2. Since the sulfate process operates by dissolution of the feedstock, it requires a large surface area; hence, the feedstock for the sulfate process is generally milled to fine particle sizes (Gazquez, et al., 2014; Roskill, 2003; Van Dyk, 1999).

2.5.2 Feedstock for the chloride process

The chloride process is the most preferred process for the production of the titania pigment. However, the feedstock properties for the chloride process are relatively more demanding. For example, because the chloride process is conducted in the fluidised bed, it can only process material with a PSD ranging between 850 and 106 µm. In some instances, there is also a D_{50} constraint. In typical feedstock production environment like the ilmenite smelting operations, titania slag with >85wt% TiO_2 is generally crushed and milled to -850 µm. A coarser fraction of -850 µm + 106 µm is generally recovered as feedstock for the chloride process and referred to as the 'chloride slag'. The fine -106 µm fraction is marketed as feedstock for the sulfate pigment production process and referred to as 'sulfate slag' or 'fine slag' (Gazquez, et al., 2014; Roskill, 2003; Van Dyk, 1999).

The nature of the chloride process allows it to process high grade TiO_2 feedstock with low levels of impurities. For example, a chloride feedstock with high MgO and CaO concentrations would compromise the stability of the fluidised bed due to the accumulation of the $MgCl_2$ and $CaCl_2$ that would form during chlorination. Thus, the fluidised bed

operation would need to be stopped and drained of the build-up. Impurities like V, Fe, Al, and Cr tend to form chlorides that contaminate the $TiCl_4$ product. Hence, it is important use the highest possible titania feedstock for the chloride pigment production. The typical feedstock for the chloride process include:

- Rutile with 95wt% TiO_2
- Synthetic rutile with 90wt% to 93wt% TiO_2
- Chloride-grade ilmenite with 60wt% TiO_2
- Leucoxene with 75wt% to 91wt% TiO_2
- Chloride slag with 86wt% TiO_2
- Upgraded slag (UGS) with 95wt% TiO_2

The typical specifications for the chloride slag produced from ilmenite smelting are summarised in Table 6 (Pistorius, 2008).

Table 6: Typical specifications for the chloride slag (wt%) (Pistorius, 2008)

Total TiO_2	>85
Ti_2O_3	<35
FeO	<12
SiO_2	<2
Al_2O_3	<1.5
CaO	<0.13
MgO	<1.2
MnO	<2
Cr_2O_3	<0.25
V_2O_5	0.60

Since the chloride feedstock has got a higher market value than the sulfate feedstock, the first prize is to produce the chloride feedstock. In the current study, the first prize was to produce a chloride feedstock from titaniferous slag.

2.6 Beneficiation of titaniferous slags

Titaniferous slags produced from high vanadium bearing titanomagnetite deposits may contain economically attractive titanium concentrations. As detailed in section 2.3, fluxed titaniferous slags may contain 20-40wt% TiO_2. Titanium in the titaniferous slags is primarily concentrated in the pseudobrookite solution, perovskite and non-crystalline phases with low concentration levels in the spinel solid solution [$Mg(Al,Ti)_2O_4$] (Pistorius, 2011; Steinberg, et al., 2011; Kelly, 1993).

Though titaniferous slags contain attractive TiO_2 concentrations, they are not beneficiated to produce feedstock for the production of the treasured titania pigment. The lack of beneficiation of titaniferous slags is attributed to the fact that these slags contain lower TiO_2 grades that the feedstock specifications for the production of the preferred chloride pigment. Moreover, these slags generally contain the refractory $Mg(Al,Ti)_2O_4$ and generally complex phase chemistry that cannot be handled using the available processes for upgrading titania bearing materials to feedstock grades (Van Vuuren & Tshilombo, 2011).

Secondary treatment or extension of current titanomagnetite smelting flowsheets to include the beneficiation of the titaniferous slags for the extraction of titanium is essential for the achievement of the principles of maximum exploitation of valuable resources, and can also result in the optimisation of the primary process economics. The beneficiation of titaniferous slags to produce titanium products would have an economic benefit. Perhaps, with titanium inclusion in the product scope of titanomagnetite processing, the recent closure of titanomagnetite smelting operation in a strategic country like South Africa could have been avoided. The closure of the Evraz Highveld Steel and Vanadium Corporation (EHSV) in South Africa occurred while the attractive titaniferous slag produced from their operations remained in a large dump site with an estimated size of about 45 million tons (Africa, Mining review, 2017).

The following subsections provide a review of available technologies and processes for the beneficiation of titania bearing materials.

2.6.1 Titania feedstock production technologies

Some ilmenite and lower grade ilmenite slags are effectively upgraded to typical chloride pigment process feedstock. The processes that can be used include:

- Chlorination: US patents: 4,629,607; 5,063,032: 5,384,355; and 4,933,153
- Sulfation of impurities: US patent: 4,362,557
- Salt roasting and caustic leaching: US patents: 2007/0110647 A1 and 4,038363
- Fluxing and leaching of impurities: US patent: 3,996,332 and SA patent: 93/5922
- Oxidative roast and leaching: US patent:3,060,002
- Becher process: The Becher process is an industrial process used to upgrade weathered ilmenite containing low concentrations of Cr and Mg to synthetic rutile of >90wt% TiO_2. This synthetic rutile is a suitable feed for the chloride pigment production process. The predominant synthetic rutile producing process, i.e. Becher process can be classified into main stages, namely; reduction, aeration and leaching. During reduction, the iron oxide in ilmenite is reduced in the presence of sulfur (for Mn removal) and carbonaceous reductant to metallic iron – an alternative synthetic rutile process, i.e. Benelite process only reduces to ferrous iron, followed by acid leaching removal of iron. The ilmenite containing the metallised iron is separated from the gangue materials by magnetic separation and screening.

  The reduced ilmenite is mixed with ammonium chloride solution and subsequently aerated and stirred in order to 'rust' the iron from the ilmenite and form a mixture of iron oxide and synthetic rutile. The synthetic rutile is separated from the iron oxide by a multi-stage hydrocyclone process. The synthetic rutile product is typically purified by leaching out of residual iron oxide and other impurities using sulfuric acid as lixiviant. The high purity rutile is separated from the acid leachate by spiral classifier and counter-current washing on a belt filter, followed by drying in a flash or fluidised bed dryer. The final synthetic rutile product typically contains between 90wt% and 96wt% TiO_2 and is generally marketed as a feedstock for the chloride pigment production process (Van Dyk, 1999).

- Phosphate process: The phosphate process was developed in the 1970s for the beneficiation of ilmenite resources to produce high purity rutile suitable for use as feedstock in the production of the chloride titania pigment. The process can be divided into three stages, namely; reduction of ilmenite ore, synthesis of rutile crystals in the slag, and liberation of the rutile crystals from the slag. The reduction of the ilmenite is conducted in an electric arc furnace (EAF) in the presence of lime and some residual ferrous oxide as fluxing agents. The resultant slag typically contains perovskite, ferrous pseudobrookite and glass phases.

  The synthesis of rutile crystals in the slag is accomplished by oxidation and fluxing with a phosphate compound such as P_2O_5 or TiP_2O_7. Rutile is then liberated from the phosphate glass matrix containing impurities through a combination of grinding and leaching using dilute phosphoric acid. The synthetic rutile product would typical have >94wt% TiO_2, and would be marketed as a feedstock for the chloride titania pigment production (Van Dyk & Pistorius, 1999).

- Oxidative-reductive roasting and HCl leaching process: This technology is generally referred to as the Upgraded Slag (UGS) process and was developed in the 90s (Doan, 1996; Borowiec, et al., 1998). A number of versions of the technology are disclosed in various publications, including; SA patent: 96/9772, US patent: 5,427,749; 5,830,420, and world patents: WO 91/13180, WO 97/19199 and WO 00/06786, Iscor's Beneficiated Titania Slag (BTS) process (Van Dyk, 1999). The conventional UGS process involves the sizing of the titania resource, generally a titania slag to a size suitable for use in a fluidised bed roaster, typically 106-850 µm (Borowiec, et al., 1998). The fundamental steps involved in the UGS process are described below (Borowiec, et al., 1998; Doan, 1996):

  - *Oxidative roasting:* During this stage of the process, Ti^{3+} and Fe^{2+} in the slag are converted to Ti^{4+} and Fe^{3+}, respectively, as shown in chemical reaction [2.18]. Rutile (TiO_2) and pseudobrookite (M_3O_5, where M can be Fe^{2+}, Fe^{3+}, Mg^{2+}, Ca^{2+}, V^{5+}, Al^{3+}, Ti^{3+} or Ti^{4+}) are the products of the oxidation stage:

$$(FeTi_2O_5)_{0.32}(MgTi_2O_5)_{0.33}(Ti_3O_5)_{0.35} + 0.25O_2 \rightarrow (Fe_2TiO_5)_{0.16}(MgTi_2O_5)_{0.33} + 1.53TiO_2 \quad [2.18]$$

During oxidation, the complex silicate structure is also decomposed. The iron species migrate to the boundaries of the grains. The iron migration facilitates access to iron during subsequent leaching for impurity removal (Van Dyk, 1999; Borowiec, et al., 1998).

- *Controlled reductive roasting:* The sparingly soluble Fe^{3+} is selectively reduced, without reducing Ti^{4+}, to Fe^{2+} or metallic Fe, which are readily leachable in HCl. The selective reduction can be represented by the chemical reactions shown in Equations [2.19] and [2.20] (Van Dyk, 1999; Borowiec, et al., 1998):

$$Fe_2O_{3(s)} + 3C_{(s)} \rightarrow 2FeO_{(s)} + 3CO_{(g)} \quad [2.19]$$

$$FeO_{(s)} + C_{(s)} \rightarrow Fe_{(s)} + CO_{(g)} \quad [2.20]$$

- *Leaching of detrimental species:* Mg, Al, Si, Ca and Fe from the roasted titania bearing slag are leached in HCl lixiviant (Borowiec, et al., 1998). In some work, a caustic leaching stage is added to remove SiO_2 from the HCl leach residue, as shown in equation [2.21] (Doan; Borowiec et al):

$$SiO_{2_{(s)}} + 2NaOH_{(aq)} \rightarrow Na_2SiO_{3_{(aq)}} + H_2O_{(l)} \quad [2.21]$$

- *Washing and calcination:* Washing and calcination of the leach residue are carried out to remove volatiles and species adsorbed onto the TiO_2 particles.

The waste from the UGS process generally includes soluble chloride salts of the alkali and alkali earth metals and other metals such as Fe. The other waste is a sodium silicate solution from caustic leaching. The aqueous solutions are typically subjected to waste treatment for neutralisation prior recovery of valuable by-products like vanadium and disposal of non-toxic waste (Borowiec, et al., 1998).

The UGS process is currently employed at Rio Tinto Fer et Titane (RTFT) in Canada for upgrading SORELSLAG® produced from Allard Lake ilmenite. The SORELSLAG® contains high concentration levels of alkaline earth metal impurities (Doan, 1996).

Titaniferous slags typically contain high levels of alkaline earth impurities like MgO and CaO from the gangue in the titanomagnetite, and from the flux in case of fluxed

smelting. Thus, the UGS process has a potential capability to upgrade the titaniferous slags to saleable titania materials by removing the alkaline earth (and other) impurities.

There are also dedicated processes for the production of titania materials from low grade or dilute titania resources like titaniferous slags. These processes have not been implemented because they are faced with many challenges including that they produce materials of still insufficient titania grades to qualify as high titania material and poor titania recoveries. There are however plans to use one of the potential processes for the treatment of EHSV titaniferous slag to produce marketable titania products – discussion on this development is given below.

Some of the proposed processes for treating low titania resources are described below:

- Selective Ti recovery by nitriding followed by chlorination (Van Vuuren & Tshilombo, 2011): This process was developed by the Council for Scientific and Industrial Research (CSIR) of South Africa. The process deals with selective extraction of TiO_2 from low TiO_2 bearing resources including titaniferous slags. The process entails the nitriding of titania in the low-grade resource in the presence of a carbonaceous reductant in a specialised reaction vessel, followed by chlorination to form liquid titanium tetrachloride ($TiCl_4$) while leaving behind the detrimental species in the solid residue. The liquid $TiCl_4$ is distilled and subsequently reacted with steam to form a high grade titania material. The chemical reactions involved in the process can be represented by Equations [2.22] and [2.23] (Van Vuuren & Tshilombo, 2011).

$$TiO_2 + 2C + {}^1/_2\, N_2 \leftrightarrow TiN + 2CO \qquad \Delta H=386 \text{ kJ/ gmol} \qquad [2.22]$$

$$TiN + 2Cl_2 \leftrightarrow TiCl_4 + {}^1/_2\, N_2 \qquad \Delta H=-477 \text{ kJ/ gmol} \qquad [2.23]$$

The challenges facing this process include: high temperature requirements of about 1300°C for nitriding, mass transfer limitations during nitriding, melting and accretions forming in the nitriding furnace, and the infeasibility to supply and maintain the necessary high temperatures for the nitriding reaction by partial combustion of the excessive reducing agent – this is because combustion to only

form carbon monoxide is insufficient for the process, and in case of complete combustion to form carbon dioxide, thus creating less reducing conditions, the nitriding reaction is unfavourable.

- Sulfation roasting and leaching of impurities (Fouad, 2005): The process involves sulfation roasting of low grade TiO_2 slag using SO_3 ($SO_2 + O_2$) at 800°C. The process relies on sulfation of the detrimental species in the slag, such as Mg, Al, Fe, and Ca, with a view of forming leachable metal sulfates. The reactions occurring during the process can be represented by the chemical reactions shown in Equations [2.24] to [2.29] (Fouad, 2005).

$$CaO + SO_2 + {}^1/_2\, O_2 \rightarrow CaSO_4 \quad [2.24]$$

$$MgO + SO_2 + {}^1/_2\, O_2 \rightarrow MgSO_4 \quad [2.25]$$

$$FeO + SO_2 + {}^1/_2\, O_2 \rightarrow FeSO_4 \quad [2.26]$$

$$C + O_2 \rightarrow CO_2 \quad [2.27]$$

$$2FeO + {}^1/_2\, O_2 \rightarrow Fe_2O_3 \quad [2.28]$$

$$Fe_2O_3 + 3SO_2 + {}^3/_2\, O_2 \rightarrow Fe_2(SO_4)_3 \quad [2.29]$$

The process produces gypsum, $CaSO_4$, which is chemically inert. Because of the inability to leach $CaSO_4$, the grade of the titania material that is produced is still very far from the synthetic rutile grade, i.e. TiO_2 content of more than 90wt%. The beneficiated slag had a titania grade of 82wt%. The proposed configuration of the sulfation process is unable to remove significant amounts of CaO, SiO_2, and Fe oxide from the titaniferous slag. There is currently no commercial application of this process in the titania industry, but it finds application in the base metals (BMs) industry where it is used to convert and recover BMs as soluble metal sulfates (Guntner & Hammerschmidt, 2012).

- Perovskite precipitation by oxidation: The process entails the blowing of air into molten slag to grow and precipitate a perovskite ($CaTiO_3$) phase in the slag (Zhang,

et al., 2007; Wang, et al., 2006; Zhang, et al., 2006). Titania is then recovered from perovskite (Wang, et al., 2010).

In order to induce the formation of the perovskite phase as shown in Equation [2.30], the activity of the TiO_2 and CaO should be increased. The oxidation of titaniferous slag ensures that low oxidation state titanium species and other titanium compounds are converted to produce TiO_2 as can be represented in Equations [2.31] to [2.34] (Zhang, et al., 2007).

$$TiO_2 + CaO \rightarrow CaTiO_3 \quad [2.30]$$

$$2TiO + O_2 \rightarrow 2TiO_2 \quad [2.31]$$

$$2Ti_2O_3 + O_2 \rightarrow 4TiO_2 \quad [2.32]$$

$$2TiN + 2O_2 \rightarrow 2TiO_2 + N_2 \quad [2.33]$$

$$TiC + 2O_2 \rightarrow TiO_2 + CO_2 \quad [2.34]$$

The kinetics and efficiencies of the activation of titania and the growth of the perovskite phase depend on the original slag chemistry. However, an additive in the form of Si-Fe powder is used to promote the titania activation and make the perovskite phase grow easily. The perovskite is recoverable from the slag by flotation (Zhang, et al., 2006; Wang, et al., 2006). The TiO_2 is then recovered from the perovskite concentrate by the alkaline roasting method followed by leaching removal of Ca and other impurities. The chemical reactions involved in the production of TiO_2 from $CaTiO_3$ concentrate are shown in Equation [2.35] to [2.39] (Wang, et al., 2010).

$$CaTiO_3 + 2NaOH \rightarrow Ca(OH)_2 + Na_2TiO_3 \quad [2.35]$$

$$Ca(OH)_2 \rightarrow CaO + H_2O \text{ (at temperatures above 600°C)} \quad [2.36]$$

$$Ca(OH)_2 + 2HCl \rightarrow CaCl_2 + 2H_2O \text{ (HCl leach option)} \quad [2.37]$$

$$Na_2TiO_3 + H_2O \rightarrow H_2TiO_3 + 2NaOH \text{ (water leach option)} \quad [2.38]$$

$$Na_2TiO_3 + 2HCl \rightarrow TiO_2 + 2NaCl + H_2O \text{ (HCl leach option)} \quad [2.39]$$

- Sulfate process: This version of the process was patented by EHSV for the recovery of titanium from the titaniferous slag (Becker & Dutton, 2002). The process entails:

  - Contacting sulfuric acid with finely ground (80% < 45 µm) low-grade titania EHSV titaniferous slag at elevated temperatures of about 180°C under constant stirring with compressed air to produce a filter cake containing sulfates of titanium, vanadium and aluminium. The cake is leached with water into solution, from which titanium oxide is separated by hydrolysis. Calcium remains in the solid substrate as gypsum. The titanium compounds that are produced in the leachate are shown in the chemical reaction given in Equation [2.40].

$$TiO_x + H_2SO_4 + H_2O \rightarrow TiO_2.xH_2O, TiOSO_4.H_2O, TiOSO_4.2H_2O, TiSO_4.H_2SO_4.2H_2O, Ti(SiO_4)_2 \quad [2.40]$$

  - Addition of ammonium sulfate in the titanyl sulfate solution to precipitate out impurities such as aluminium according to Equation [2.41]. A high purity titanyl sulfate solution is produced.

$$Al_2(SO_4)_3 + (NH_4)_2SO_4 + 24H_2O \rightarrow 2NH_4Al(SO_4)_2.12H_2O \quad [2.41]$$

  - Hydrolysis of the titanyl sulfate bearing solution with heated water which is seeded with nucleating or seeding agents to produce titanyl hydroxide. In case of titaniferous slags, like the EHSV slag produced from high vanadium bearing MML titanomagnetite, the titanyl sulfate solution would contain about 1wt% V_2O_5. Vanadium is extracted from the sulfate matrix through hydrolysis at a pH of about 3. Vanadium solution is generally heated with 25% ammonium solution to recover vanadium. However, the vanadium extraction efficiency is generally low at about 65% with the remainder going with the titanyl hydroxide.

  - Filtration of titanyl hydroxide bearing solution, and washing of the solids (to remove some of the vanadium impurity) followed by calcination to produce a >99.9wt% pure TiO_2 product.

  Another version of the titanyl sulfate process for the production of titania from low grade titania resources is currently under a patent owned by Avertana Limited, in

New Zealand (Hassell, et al., 2016). The Avertana invention provides a sulfation method for processing a low grade titania resource, particularly the titaniferous slag produced during ironmaking process, to recover titania and at least one other product which may be calcium, silica, alumina or magnesia. The invention is similar to the earlier titanyl sulfate formation process with the notable difference being on the additional product other than titania. The current invention is specific to the recovery of titania and another product, which is not vanadium – the EHSV procedure entailed the extraction of vanadium even though the extraction efficiencies were low.

The collection of hydrated titania in the Avertana invention may be conducted by filtration or centrifugation. The Avertana invention was successfully tested on titaniferous slags produced by NZS in New Zealand, EHSV in South Africa, Panzhihua Iron and Steel and Chengde steel in China, and NTMK in Russia (Hassell, et al., 2016).

Hatch successfully completed scoping and conceptual studies for the beneficiation of the EHSV titaniferous slag based on the sulfate process provided by Avertana. The SA government has committed about R4 billion for the development of a plant to process 10 million tons out of the plus 45 million tons of the titaniferous slag dump produced by EHSV. A photograph of this slag dump was taken by the author on the 15 May 2013 and is shown in Figure 22. The plant will be operated by Nyanza Light Metals (Nyanza) in Richards Bay, South Africa. The operation is projected to produce 50 thousand tons of titanium dioxide pigment annually. The production is expected to begin in late 2019. Nyanza is anticipated to be a low cost producer of TiO_2 pigment as it uses a waste material compared to the expensive conventional ilmenite and rutile (Africa, Mining review, 2017; Fin24.com, 2017; Anderson, 2013).

Figure 22: Photograph of the EHSV titaniferous slag dump

Conventionally, the titanyl sulfate formation process presents a safety hazard due to the reaction of the concentrated sulfuric acid with the particulate titania slag in air. Due to the refractory nature of TiO_2, the necessary high extraction efficiency of titanium inevitably results in the dissolution of other species which complicates the titanyl sulfate solution – this results in a multiple stage process to reject impurities, some of which can be recovered as by-products. The process generates high volume of hazardous sulfate waste as a consequence of processing low grade materials. This waste typically requires special treatment and disposal due to the lack of an economic sulfuric acid recycling process. The capital cost of a modern sulfate plant is high (Gazquez, et al., 2014; Roskill, 2003; Van Dyk, 1999).

2.6.2 Upgradability of titaniferous slags

Titaniferous slags have been produced in several plants around the world (Steinberg, et al., 2011; Zhang, et al., 2007; Kelly, 1993). Titania resources are typically processed to produce TiO_2 pigment and, to a lesser extent, titanium metal. TiO_2 pigment is produced via one of two processes, namely; the sulfate and chloride processes. The first prize is, therefore, to use the relatively new and cheaper chloride process. The technical requirements for the feedstock of the chloride process are relatively high, namely; TiO_2 grade of >85wt% and a particle size distribution (PSD) of 106-850 µm, which is suitable for use in the fluidised bed furnace that is used in the chloride process (Gazquez, et al., 2014; Pistorius, 2011).

Titaniferous slags are desirable for use as a feedstock for the preferred chloride pigment production process. Essentially, these slags need to be upgraded to the chloride process feedstock grade. There is also a market for a material with 70wt% TiO_2 (Shijiazhuang Leveling import and export Co., Ltd., 2014). The upgrading of titania materials typically involves the removal of impurities through the decomposition of chemical phases and leaching (Van Dyk, 1999; Borowiec, et al., 1998; Doan, 1996). Thus, the upgradability of titania resources depends on the phase composition. The main chemical phases contained in titaniferous slags are pseudobrookite, perovskite, and magnesium alumina spinel (Pistorius, 2011). Pseudobrookite is the primary TiO_2 bearing phase occurring in ilmenite slags – it is effectively handled by the UGS process (Doan, 1996). Perovskite, on the other hand, is upgradable to a high purity TiO_2 material by alkali roasting and acid leaching (Wang, et al., 2010).

Spinels, like magnesium alumina spinel ($MgAl_2O_4$) and solid solution spinel like [$Mg(Al,Ti)_2O_4$] are by definition a refractory material. It is typically used as refractory material for containment of molten materials during high temperature operations. It is also chemically inert in conventional acidic and basic environments. Dissolution of the spinels is possible under supercritical conditions involving the use of alkaline lixiviants such as NaF, KF, Na_3PO_4 or K_2CO_3 under a pressure of 2 kbar, at temperatures ranging between 390°C and 630°C over a period of 15 to 30 hours (Franke & Heimann, 1970). These conditions are complex and harsh, and have a potential of dissolving some of the titanium to the waste stream during the upgrading of titaniferous slags by the removal of impurities.

Some of the technologies reviewed in section 2.6.1, particularly the flux based processes like the phosphate process, have a potential to crack the spinel structure and beneficiate the typical titaniferous slags to suitable feedstock for the production of the preferred chloride titania pigment. However, most of these slag upgrading processes are still at development stages with the exception of the UGS process which is used commercially at RTFT in Canada for upgrading the SORELSLAG® slag which contains similar impurities to the titaniferous slags (Doan, 1996). The UGS process does not involve fluxing – as described above, it operates by manipulating the redox chemistry of iron and titanium. It may not be able to flux the refractory spinel structure for subsequent removal of impurities by leaching. Hence, a titaniferous slag that contains the spinel structure is undesirable for the purpose of

beneficiation of the slag to a marketable feedstock for chloride pigment production using the UGS process.

It is thus desirable to produce titaniferous slags with no spinel phase during the primary titanomagnetite smelting process for subsequent upgrading to marketable titania products using the established and industrially used UGS process (Rio Tinto, 2010; Doan, 1996). Hence, the current study focusses on the investigation of the best conditions for the production of spinel free titaniferous slags for subsequent beneficiation to marketable titania products using the UGS process – the first prize is to produce a feedstock for the chloride pigment production process.

2.7 Conclusions based on the literature

A literature survey was conducted to gather background information on the phase equilibria and beneficiation of titaniferous slags. The following aspects have been identified as possible development areas in order to facilitate the exploitation of titaniferous slags as titanium or titania resources.

- Though titaniferous slags contain attractive TiO_2 grades of 20-40wt%, there is currently no commercial operation for their exploitation, except the foretold Nyanza operation to be established to process the EHSV titaniferous slag in South Africa. This is attributed to the relatively low titania grades in these slags that they cannot be used directly as feedstock in the production of titanium products like the pigment and the metal. In addition, these slags comprise the inert spinel phase, which renders their upgrading to marketable titania products technically challenging. Hence, the understanding of phase equilibria of titaniferous slags needs to be developed in order to be able to implement suitable fluxing strategies to mitigate the crystallisation of the spinel phase for subsequent beneficiation or upgrading of the slags to feedstock grades for titania pigment and Ti metal production.

  Jochens (1967) established phase equilibria applicable to titaniferous slags typically produced from the smelting of the South African titanomagnetite. The phase equilibria were established in air. In the current literature review, it has been established that, by virtue of the phase equilibria having been established in air, the phase equilibria would not be able to predict the crystallisation of phases with

reduced titanium species. Evaluation of literature of the low and high Ca-Mg-Al-Si-Ti-O systems demonstrated that indeed reduced titanium species in the pseudobrookite solid solution would crystallise. Moreover, the established equilibrium phase diagram does not predict the crystallisation of the spinel structure, which is widely reported as one of the predominant phases crystallising in titaniferous slags (Pistorius, 2011; Steinberg, 2008; Zhang, et al., 2006). Jochens (1967) however observed some faint spinel lines on the X-Ray diffractograms during the development of the available equilibrium phase diagram. The presence of the spinel was rejected because the spinel lines on the diffractograms were overlapping with those of the confirmed pseudobrookite solid solution; hence, the omission of the spinel in the phase equilibria is attributed to the lack of high resolution analytical techniques such as EPMA in the 1960s.

As part of the current study, further work was proposed to re-draw the phase diagram in air to review and update the available phase diagram in air and at low pO_2 applicable to titanomagnetite smelting. The proposed development programme would include a combination of literature review, experimentation and thermochemical simulation. However, calculations of phase equilibria in the Ca-Mg-Al-Si-Ti-O system applicable to titaniferous slags cannot be completed using the latest version of the FactSage thermochemical software, i.e. FactSage 7.2 version. The reason for this is that tialite (Al_2TiO_5), one of the components of the pseudobrookite solution ($MgTi_2O_5$-Al_2TiO_5) predicted by Jochens (1967) in the available phase equilibria and in the literature (Berezhnoi & Gulko, 1955) is not modelled as an endmember in the customary pseudobrookite solid solution database of FactSage. Thus, a private pseudobrookite solution database for the $MgTi_2O_5$-Al_2TiO_5-Ti_3O_5 system needed to be developed using the established sublattice model coupled with CEF and Redlich-Kister polynomial theories. The phase equilibria of titaniferous slags would then be calculated using the customary and private solution thermodynamic databases.

- General technologies for upgrading low grade titania bearing resources to marketable titania materials are not able to handle titaniferous slags because of the complexity of their phase chemistry including the availability of the refractory spinel phase. In addition, the dedicated technologies to treatment of relatively low titania bearing

resources like the titaniferous slags are also considered in adequate (Pistorius, 2011; Van Vuuren & Tshilombo, 2011), except the version of the sulfate process proposed by Avertana which is earmarked for the treatment of the EHSV titaniferous slag. The presence of high concentrations of alkali earth metal impurities in the slag generally complicates the sulfate process because of the propensity to produce toxic sulfates that require special treatment and disposal arrangements.

The upgraded slag (UGS) process is stablished for the processing of titania bearing slags with high levels of alkali earth impurities (Doan, 1996), like the titaniferous slags. The UGS process has a potential for successful beneficiation of titaniferous slags to saleable titania products, preferably for use as feedstock in the production of pigment using the chloride process. The success of the UGS process to upgrade the titaniferous slags to marketable titania products will likely happen if the slags do not contain the spinel phase. Hence, the current study focussed on finding the best conditions for, and production of titaniferous slags with no spinel phase, followed by beneficiation to produce titania products using the UGS process.

CHAPTER 3:

MATERIALS AND EQUIPMENT

3.1 Introduction

The study of the phase equilibria in the Ca-Mg-Al-Si-Ti-O system applicable to titaniferous slags entailed the processing of synthetic titaniferous slags using numerous pieces of equipment including equilibration-quench-analysis setup and thermal analysis instrumentation. The investigations of the best Upgraded Slag (UGS) process conditions for the beneficiation of titaniferous slags were conducted using the titaniferous slag produced by Evraz Highveld Steel and Vanadium Corporation (EHSV). The best conditions were applied on titaniferous slags produced in the current work using conventional and cold crucible induction furnaces.

The present chapter of the thesis provides descriptions of the materials and equipment that were used in order to achieve the objectives of the project. In case of equipment, verification of intended test conditions and calibration information are also included in this chapter.

3.2 Materials

In order to prepare synthetic titaniferous master slags (MSs), analytical reagent grade powders of TiO_2, SiO_2, Al_2O_3, MgO and CaO with respective purities of 99.9wt% or above were purchased from Sigma-Aldrich. CaO was dried at 105°C overnight and subsequently stored in a desiccator in order to eliminate the prospect of hydration.

Platinum foil (99.9wt% pure) and wires (Pt/Rh 6% and Pt/Rh 30%) that were used to make the sample capsules used during equilibration-quench experiments and B-type thermocouples were supplied by Sigma-Aldrich and Heraeus, respectively. An Fe metal with a purity of 99wt% was supplied Sigma Aldrich for use as an induction susceptor during smelting in cold crucible induction furnace.

A real plant titaniferous slag was supplied by EHSV – the bulk chemical composition of the EHSV slag was determined by ICP-OES, and is shown in Table 7. The phase composition of the EHSV slag was determined by SEM-EDS and XRF results, and is reported in Figure 23. In order to produce another slag with a target chemical composition, a titanomagnetite material mined from the main magnetite layer (MML) of the South Africa's Bushveld

complex was also supplied by EHSV. With a desire of producing a titaniferous slag with low MgO content after smelting, the titanomagnetite ore was subjected to concentration by low intensity magnetic separation (LIMS). The bulk chemical composition of the titanomagnetite concentrate is included in Table 7.

A low sulfur carbonaceous material or Sasol carbon, with the trade name 'LS SASCARB', was supplied by Sasol and used as a reductant. Chemical grade MgO, Al_2O_3, SiO_2 and CaO were supplied by Associated Chemical Enterprise and used as synthetic fluxes during the smelting of the MML titanomagnetite concentrate.

CO and CO_2 gas cylinders with respective purities of 99.97wt% and 99.99wt% were supplied by Afrox for use to provide known oxygen partial pressures (pO_2) in selected phase equilibria tests.

The bulk compositions of the titanomagnetite materials, reductants, fluxes and other reagents used in the testwork programme are given in Table 7. For laboratory scale smelting testwork, 98wt% pure Al_2O_3 crucibles were purchased from Kayla Africa.

Table 7: Bulk compositions of the titanomagnetite materials, reductant, fluxes and other reagents (wt%)

	EHSV titaniferous slag	Titanomagnetite ore	Titanomagnetite concentrate	SASCARB	MgO	Al_2O_3	SiO_2	CaO
#FeO	3.59							
*Fe_3O_4		77.7	77.9					
MgO	14.3	1.48	1.34		99			
Al_2O_3	14.0	3.97	4.17			98		
SiO_2	21.6	1.34	1.25				98.5	
CaO	11.8	0.07	<0.05					96
TiO_2	33.0	13.3	13.2					
V_2O_5	0.82	1.67	1.86					
Cr_2O_3	0.16	0.20	<0.05					
MnO	0.78	0.24	0.30					
C				98.7				
Ash				0.33				
LOI				0.97				

#Fe species (mainly Fe and Fe^{2+}) expressed as FeO; *Total Fe expressed as Fe_3O_4; <0.05wt%: Analyte concentration is below the detection limit, which is 0.05wt%; $Titanium species ($Ti^{3+}$ and Ti^{4+}) expressed as TiO_2

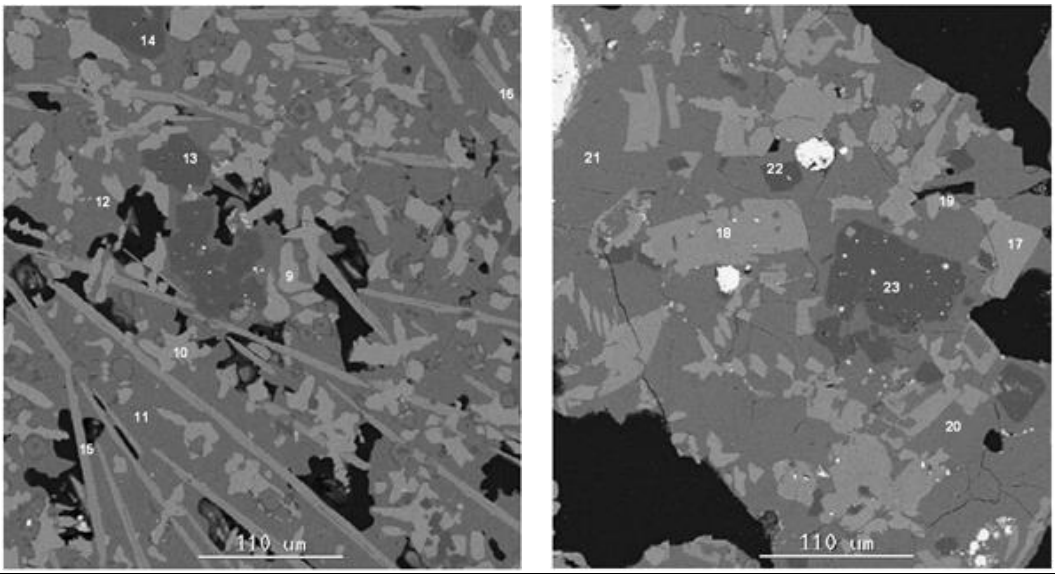

	MgO	Al_2O_3	SiO_2	CaO	TiO_2	V_2O_5	Cr_2O_3	MnO	FeO	Total	
	wt%	wt%	wt%	wt%	wt%	wt%	wt%	wt%	wt%	wt%	Phase
9	0.2	0.4	0.0	39.7	55.3	0.3	0.0	0.1	0.0	95.9	Perovskite
10	0.1	0.2	0.1	39.6	55.8	0.1	0.0	0.1	0.0	96.0	Perovskite
11	18.0	11.3	30.5	18.5	15.3	0.3	0.1	0.3	0.3	94.6	Titanaugite
12	13.9	8.2	38.7	22.1	12.6	0.1	0.1	0.4	0.2	96.3	Titanaugite
13	28.9	60.6	0.1	0.0	11.3	1.7	0.3	0.3	0.3	103.6	Spinel solid solution [$Mg(Al,Ti,V)_2O_4$]
14	28.9	63.0	0.2	0.1	8.0	2.3	0.5	0.4	0.2	103.7	$Mg(Al,Ti,V)_2O_4$
15	9.4	2.0	0.7	1.0	81.6	0.3	0.1	0.2	0.6	95.9	Pseudobrookite
16	8.9	2.1	0.3	0.7	82.3	1.1	0.1	0.3	0.2	96.0	Pseudobrookite
17	5.8	2.7	0.1	0.2	90.3	0.2	0.4	0.2	0.1	100.0	Pseudobrookite
18	9.3	1.8	0.3	0.3	86.6	1.9	0.1	0.3	0.0	100.6	Pseudobrookite
19	0.2	0.3	0.1	39.5	56.1	0.0	0.2	0.1	0.1	96.5	Perovskite
20	10.5	9.7	34.8	23.4	16.7	0.1	0.0	0.4	0.2	96.1	Titanaugite
21	9.6	10.1	34.3	23.9	18.6	0.4	0.3	0.4	0.2	97.7	Titanaugite
22	28.1	65.2	0.3	0.1	7.9	0.7	0.3	0.4	0.4	103.5	$Mg(Al,Ti,V)_2O_4$
23	27.6	62.5	0.5	0.2	9.2	1.4	0.4	0.5	0.4	102.8	$Mg(Al,Ti,V)_2O_4$

Figure 23: Backscattered electron image and EDS analysis results of a titaniferous slag produced by EHSV in South Africa

3.2.1 Preparation of master slags

The study of phase equilibria in the Ca-Mg-Al-Si-Ti-O system was conducted using synthetic titaniferous slag materials as adopted from the previous work conducted by Jochens (1967). In the current work, seven slag compositions were strategically selected and used to study essentially the entire range in the available phase diagram as shown in Figure 24 (Jochens, 1967) by dashed lines. Synthetic master slags were prepared in order to complete the intended phase equilibria studies.

The respective master slags (MSs) were prepared by weighing and mixing the individual high purity metal oxides in proportions suitable for the attainment of the target compositions. Each MS recipe had a total mass of 100 g. The individual MSs were blended in a mechanical mixer over 24 hours. The oxide mixture of each synthetic slag recipe was transferred into a steel hardened die pelletising equipment and pressed by 20 MPa to make a cylindrical pellet.

The pellet was placed onto a semi-circular high purity alumina boat which was made by cross-sectional cutting of an alumina tube. This positioning of the pellet on the boat restricted the contact between the pellet and the alumina boat to minimize contamination. The boat was placed inside the chamber of a furnace. The furnace was heated up at 10°C/ minute to 1200°C and kept at this temperature for 24 hours in air after which the furnace was allowed to cool down under normal laboratory conditions. The pre-heated pellet was recovered and the two edges that were in contact with the semi-circular alumina boat were cut off to avoid alumina contamination. The pellet was placed inside a clean plastic bag and carefully broken down into smaller pieces by gently hitting with a hammer. The sample pieces were ground into fine powder using an agate mortar and pestle.

The pelletising, pre-heating/ fusing, and grinding stages were replicated four times to reduce the respective activities and melting points of the individual metal oxide components in the MSs. Where possible, this pre-processing step ensured that the respective high liquidus temperature oxide components were reacted to form intermediate phases or compounds that have low liquidus temperatures. Otherwise, the direct processing of mixtures containing the high purity metal oxides, which individually have high liquidus temperatures, could lead to difficulties in the attainment of liquidus temperatures and equilibrium in the subsequent processing stage (Jak & Hayes, 2004; Jochens, 1967).

The pre-processed oxide recipes were used as MSs for the subsequent quenching testwork. The bulk and phase chemical compositions of the MSs were determined by a Varian Vista-PRO CCD simultaneous Inductively Coupled Plasma Optical Emission Spectrometer (ICP-OES) and a Bruker D8 advanced X-Ray Diffractometer (XRD), respectively. The bulk chemical compositions of the MSs are given in Table 8, whereas the phase compositions are shown in Figure 25. The chemical compositions suggest that the MSs were generally close to the target compositions. In cases where there were significant deviations, particularly on TiO_2 concentration, the totals also significantly deviated from 100%; hence, the deviation was mainly attributed to measurement uncertainty.

The results of the phase compositions show that the MSs generally formed some intermediate phases. However, all the MSs contained discrete quartz (SiO_2) phase. Replication of the pre-processing cycle did not help to include the SiO_2 into intermediate phases. In addition, increasing the fusing temperature was not ideal as it could result in substantial fusing of the slag and contamination by the alumina container. Instead, more evaluation was conducted during the subsequent processing to assess the ease of melting and attainment of equilibrium. All the MSs were stored for subsequent equilibration-quenching-analysis testwork.

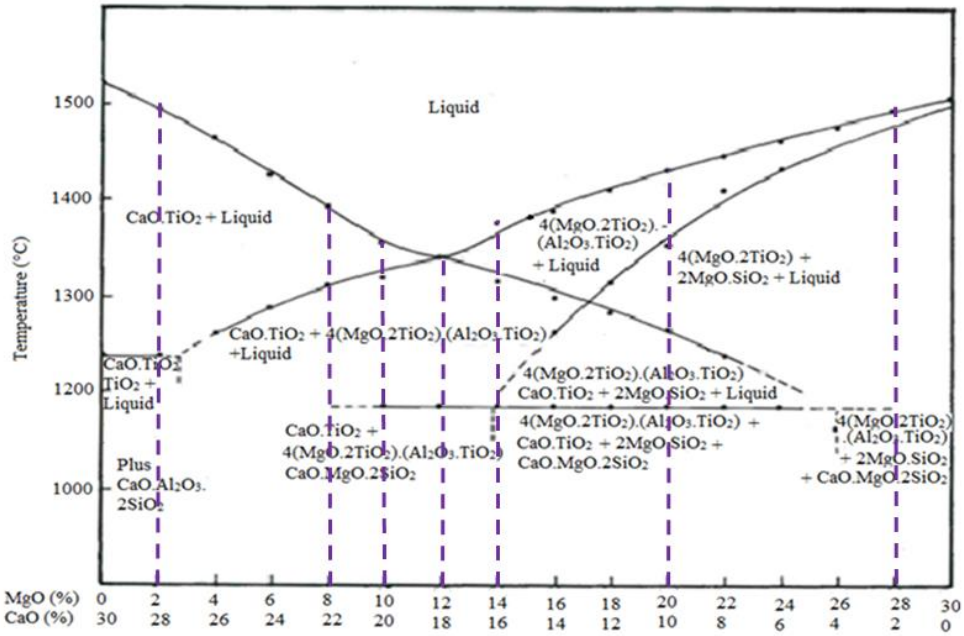

Figure 24: Available phase diagram established by Jochens (1967) with the selected compositions for the current study shown by purple dashed vertical lines

Table 8. Bulk chemical compositions of the MSs (wt%)

							Target	
	Al_2O_3	**CaO**	**MgO**	SiO_2	TiO_2	Total	**CaO**	**MgO**
MS 1	13.29	**28.42**	**2.14**	20.14	37.74	101.7	**28**	**2**
MS 2	13.40	**22.68**	**7.98**	20.18	38.58	102.8	**22**	**8**
MS 3	13.49	**20.30**	**9.76**	20.22	39.25	103.0	**20**	**10**
MS 4	12.85	**18.34**	**11.75**	19.86	38.91	101.7	**18**	**12**
MS 5	12.38	**15.82**	**12.90**	19.11	37.41	97.62	**16**	**14**
MS 6	13.00	**10.52**	**19.51**	19.84	40.00	102.9	**10**	**20**
MS 7	13.80	**2.62**	**28.88**	20.74	33.90	99.94	**2**	**28**

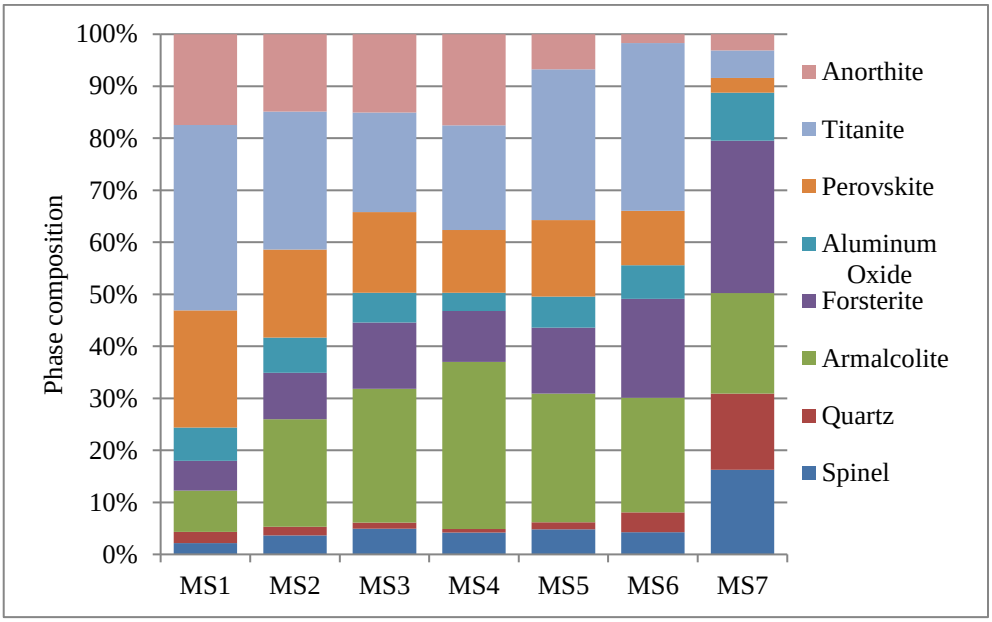

Figure 25: Phase chemical compositions of the MSs

3.3 Equipment

The equipment used in the current study is described in the following subsections. All the equipment calibrations and verifications of test conditions are also included in these subsections.

3.3.1 Equilibration-quench setup

A schematic representation of the equilibration-quench set up is shown in Figure 26. This figure also includes the details of the tests conducted at controlled partial pressure of oxygen (pO_2) provided by CO and CO_2 gas mixture. As shown in the diagram, the setup is equipped with (a) gas cylinders, (b) 'hydrosorb', (c) 'oxysorb', (d) mass flow controllers (MFCs), (e) gas pre-heating furnace, (f) vertical tube furnace, and (g) quenching water bath. The respective CO and CO_2 gases from the cylinders are conveyed through brass tubing to the 'hydrosorb' and oxysorb for the removal of residual moisture and oxygen, respectively. A typical appearance of unsaturated and saturated oxysorb is shown in Figure 27 – a new 'oxysorb' cylinder was on standby. The 'hydrosorb' cylinder was replaced after every six months – no frequent replacement was required as the CO and CO_2 gases were fairly high purity.

The gases were quantified according to the required proportions using Tylan mass flow meters and controllers. The CO-CO_2 mixture was also subjected to a secondary gas-conditioning stage. As shown in the setup, the respective measured gases are mixed and subsequently conveyed to a silica gel scrubber and gas pre-heating horizontal tube furnace equipped with Pt scrap for removal of trace level moisture and oxygen in order to achieve the desired pO_2. The gas pre-heating tube furnace was equipped with a 30 mm internal diameter quartz tube and operated at 500°C. The heating process in the pre-treatment horizontal tube furnace was controlled using separate RKc-REX-P90 controller.

The pre-heated gas was therefore fed into the vertical tube furnace for the equilibration-quench experiments under controlled pO_2. The furnace is equipped with U-shaped $MoSi_2$ heating elements and an alumina-sheathed B-type thermocouple (Pt-6% Rh/ Pt-30% Rh). This thermocouple, referred to as the control thermocouple, is located outside the furnace reactor tube and close to the heating elements to minimize the furnace control dead-time. The thermocouple is connected to a 'Eurotherm 902' programmable furnace controller.

The vertical tube furnace is equipped with a 99.8% pure alumina tube reactor with an internal diameter of 27 mm, external diameter of 35 mm, and a height of 1000 mm. The ends of the alumina tube are fitted with brass end-caps held in place and sealed with O-rings – the brass fittings are equipped with cooling water jackets to avoid overheating and damaging the O-rings. During experiments, the bottom end cap of the reactor was sealed using a plastic film – this end of the reactor was placed inside the water bath during the equilibration period. The top end cap was sealed by a rubber stopper with a hole for fitting an alumina sheath through which a Pt wire was passed to hold in position the test sample/ specimen contained in a Pt foil.

As it appears in Figure 26, the test gas enters the reactor from the bottom of the reactor tube through the side of the brass flange. The exit gas stream comes out through the side of the brass flange located at the top of the tube reactor – this stream was directed to the oil bubbler for monitoring whether a proper seal was maintained throughout the respective experiments. The equilibration-quench setup is equipped with a beaker at the bottom. The beaker contains cold water with glass beads placed at the bottom to avoid breaking the glass beaker during quenching. To quench a test sample, the Pt wire that was holding the sample inside a foil was released and slipped down the reaction tube, the foil containing the sample broke the plastic film at the bottom of the tube and fell into the cold water for quenching.

The internal diameter of the reaction tube is only 27 mm. Hence, it is impractical to have a working thermocouple and a pO_2 probe adjacent to the test sample throughout each experiment. The thermal profiling of the tube furnace and the pO_2 verification at specific temperatures were thus conducted without the test specimen and are reported in the following subsections.

It should be noted that for the equilibrium-quench testwork in air, the gas inlet and outlet connections on the tube furnace were left open throughout each experiment.

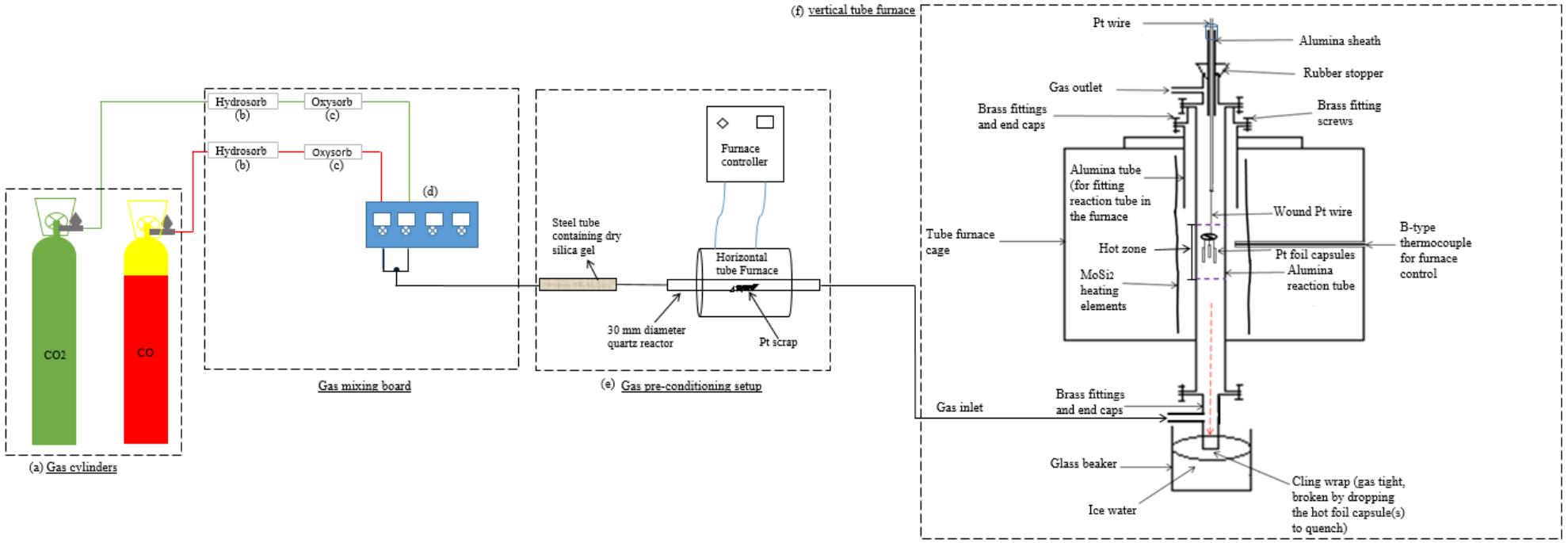

Figure 26: Schematic representation of the equilibration-quench setup

(a) (b)

Figure 27: Typical appearance of the (a) unsaturated and (b) saturated oxysorb systems

3.3.1.1 Operational temperature of the furnace

Temperature measurements in the furnace were conducted using thermocouples connected to a 34970A data acquisition unit supplied by Agilent Technologies, which is known today as Keysight Technologies. The data acquisition unit is calibrated annually by Keysight Technologies. Thermocouples consist of two wires made from dissimilar metals – the tips of the wires are typically welded together to form a junction, which is the temperature measurement point. In the current testwork, B-type thermocouples were made by connecting Pt-6% Rh and Pt-30% Rh wires. The B-type thermocouples have a maximum application temperature of 1700°C (Finn, 1980). It is common scientific practice that new thermocouples are calibrated to ensure that they read the correct temperatures. In addition, thermocouples can lose their accuracy when exposed to high temperatures for elongated period of times or when exposed to contaminating environments; hence, operating thermocouples also need to be calibrated from time to time.

In the current testwork, an operational or test thermocouple was calibrated against a primary standard thermocouple, i.e. ISOTECH 17977/1, which is traceable to a National Institute of Standards and Technology (NIST) standard as it was taken through the annual calibration

by the National Metrology Institute of South Africa (NMISA). The calibration procedure entailed the simultaneous temperature measurements using the standard and test thermocouples in a thermally equilibrated tube furnace at verification temperatures of 1100°C, 1200°C, 1300, 1400°C, 1500°C and 1600°C. The tested thermocouples, i.e. the primary standard and test thermocouple, were found to be accurate to ±2°C relative to the set point temperature. The details of the thermocouple calibration process are included in Appendix 1.1.

The position and length of the reaction/ hot zone in the vertical tube of the equilibration-quench furnace was determined by measuring the absolute temperatures at different depths inside the tube of the furnace. The measurements were done at a temperature of 1400°C. The results of the temperature measurements are shown in Figure 28. As measured from the top of the rubber stopper located at the top of the furnace, it can be seen on the curve that the hot zone at 1400°C is 17 cm long and is located between 40 and 57 cm.

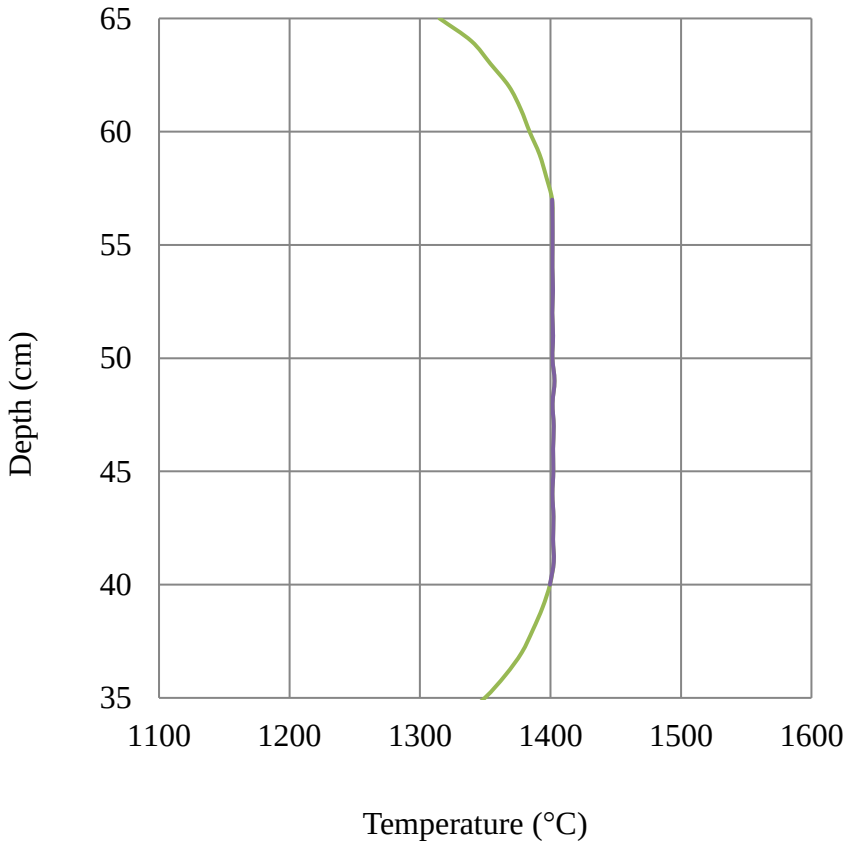

Figure 28: Temperature profile of the equilibration-quench furnace at 1400°C

3.3.1.2 Oxygen partial pressure in the tube furnace

Oxygen partial pressure (pO_2) data for commercial titanomagnetite smelting furnaces is not readily available in the open literature. The lack of the pO_2 data may be due to the perceived competitive advantage for stable furnace operations or it is simply not measured. The pO_2 in the smelting furnaces of the recently closed Evraz Highveld Steel and Vanadium Corporation (EHSV) was not directly measured; the intensity of reduction inside the furnace was however deduced from the C, V and Ti concentrations in the pig iron. The typical concentrations of C, V and Ti in a stable furnace operation were about 3.5wt%, 1.5wt%, 0.18wt%, respectively. When these concentrations were high, the conditions were regarded as very reducing; hence, a millscale correction material would be fed to lower the intensity of reduction inside the furnace. When the C, V, and Ti concentrations were lower than the specification, the operation was considered to be carbon deficient or operating with high pO_2; thus, more reductant would be added in the feed blend. When the desired pig iron chemistry was achieved, the process was said to be 'chemistry satisfactory' and stable (Steinberg, 2008).

Geldenhuis and Pistorius (1999) used a commercial oxygen probe to directly measure the pO_2 during pilot scale ilmenite smelting campaign. The lowest pO_2 measurements in the furnace were in the order of 10^{-12} atm (Geldenhuis & Pistorius, 1999). Ilmenite smelting furnaces for the production of high titania slags essentially operate with FeO concentrations of approximately 10wt% to provide the self-fluxing phenomenon (Pistorius, 2008). The fluxed titanomagnetite smelting operations typically produce a titaniferous slag with low FeO content of about 1wt% to ensure a typical vanadium recovery of 80% to the pig iron (Goso, et al., 2016; Steinberg, 2008). Hence, the pO_2 in the titanomagnetite smelting furnace is anticipated to be lower than 10^{-12} atm, which was measured in an ilmenite smelting furnace.

In the absence of direct pO_2 measurements in a titanomagnetite smelting furnace, the equilibrium pO_2 used in the current study was deduced from the Ellingham diagrams (Habashi, 2002) and FactSage 7.2 databases (Bale, et al., 2002; Bale, et al., 2016) for the reduction of V_2O_3 to metallic V at a titanomagnetite smelting temperature of 1500°C. This temperature is a close approximation to the tapping temperature of the titaniferous slag (Steinberg, 2008). It is understood that the pO_2 for the titanomagnetite smelting operation is not exclusively determined from the formation of a clean vanadium metal from V_2O_3.

However, the described approach would provide a fair estimation of the pO_2 in the furnace during the titanomagnetite in the absence of empirical data. Considering that not all the V is deported to the metal and that the reduction in the furnace would involve the Boudouard reaction (Steinberg, 2008), a pO_2 of 10^{-16} atm should be considered as a very rough estimation, which is used in the absence of empirical data. Nevertheless, FactSage thermochemical software simulations of the phase equilibria of titaniferous slags were conducted in regressive stages in terms of pO_2 levels from 0.21 (in air) to 10^{-16} atm.

The Gibbs free energy for the vanadium metal formation from V_2O_3 at 1500°C was estimated to be 521 460 J/ mol (Bale, et al., 2002). The equilibrium Gibbs energy expression shown in Equation [3.1] was used to calculate the required pO_2 at 1500˚C. As shown in Equation [3.2], the equilibrium pO_2 for the reduction of V_2O_3 to V at 1500°C is 4.353 x 10^{-16} atm.

$$\Delta G^{\circ} = -RT ln\, pO_2 \qquad [3.1]$$

Where: R, the gas constant, = 8.3144621 J/ mol.K, and T = 1500˚C + 273.15 = 1773.15 K

$$pO_2 = e^{-\frac{521\,460\ J/mol}{8.3144621 J/mol.K \times 1773.15 K}} = 4.353 \times 10^{-16}\ atm \qquad [3.2]$$

The required pO_2 in the reaction zone of the tube furnace used in the current testwork was provided by a mixture of CO and CO_2 gases. The target pO_2 was maintained by accurately controlling the flowrates of these gases using calibrated mass flow controllers. The gas flow controllers used in the current study were calibrated on nitrogen gas and subsequently validated using the bubble flow meter method. The validation was conducted by measuring the respective flowrates of CO and CO_2 at different controller set points. The procedure entailed the flowing of a set rate of CO or CO_2 gas into a soap bath connected to a marked burette, followed by the measurement of the velocity of a soap bubble moving through a known volume of the burette. The measured absolute volumetric flowrate of the respective gases were converted to standard flowrates and compared with the set standard flowrates on the Tylan mass flow meter. The calibration of the mass flow controllers is discussed in section 1.2.1 of Appendix 1.2.

The required pO_2 was provided by mixing CO_2 and CO. The ratio of CO_2 to CO for the control of the target pO_2 was calculated based on the equilibrium reaction in Equation [3.3].

$$CO + {}^{1}/_{2}\, O_2 = CO_2 \qquad [3.3]$$

The Gibbs energy of this reaction can be described as shown in Equation [3.4]. Thermodynamically, the Gibbs energy at equilibrium can also be expressed as shown in Equation [3.5] (Bale, et al., 2016; Bale, et al., 2002).

$$\Delta G^{\circ}_{rxn}(J/mol) = \Delta H^{\circ}_{rxn} - \Delta S^{\circ}_{rxn} \times T = -270951.6 + 80.970 \times T \qquad [3.4]$$

$$\Delta G^{\circ}_{rxn} = -RTlnK \qquad [3.5]$$

Equations [3.4] and [3.5] can be equated and expressed in terms of the equilibrium constant, K, as shown in Equation [3.6]. K for Equation [3.3] can also be expressed as shown in Equation [3.7]. Thus for the setting of the required pO_2 at specific temperature, the required ratio of CO_2 to CO was estimated by equating Equations [3.6] and [3.7] and rearranging to form the useful Equation [3.8].

$$K = e^{\frac{-270951.6+80.970\times T}{-RT}} \qquad [3.6]$$

$$K = \frac{P_{CO_2}}{P_{CO}\times\sqrt{P_{O_2}}} \qquad [3.7]$$

$$\frac{P_{CO_2}}{P_{CO}} = \sqrt{P_{O_2}}.\, e^{\frac{-270951.6+80.970\times T}{-RT}} \qquad [3.8]$$

The total gas flow into the tube furnace was maintained at 1000 standard cubic centimeters per minute (sccm). For the setting of a pO_2 of about 10^{-16} atm at 1500°C, 1000 and 10 sccm mass flow controllers were used to control the flows of CO and CO_2, respectively. The settings on the corresponding calibrated mass flow meters (MFMs) with respective maximum channels for CO and CO_2 of 1000 and 10 sccm are summarised in Table 9. The required CO_2 is very small that significant errors in the measurement of flowrates would occur. However, as also shown in the calibration information in section 1.2.1 of Appendix 1.2, the CO_2 flowrates were measurable. The quantification of error associated with the measurement of the flowrates of CO and CO_2 was not conducted as an oxygen probe was used to determine the absolute pO_2 in the reaction zone of the drop quench furnace.

Since the pO_2 inside the furnace was significantly smaller than the atmosphere surrounding the furnace, diffusion of oxygen into the furnace was highly possible. Hence all seals and connections in the tube furnace setup were checked for leakage using soapy water. The gas

outlet of the system was connected to a gas bubbler containing heating oil. The high positive pressure in the reaction tube during pO_2 monitoring was confirmed by continuous gas bubbling in the bubbler.

Table 9: pCO_2 and pCO proportions to set a pO_2 of about 10^{-16} atm at 1500°C

Target	From Equation [3.6]	Determined from simultaneous equations		Target settings on mass flow meter (conversion factors, CO_2 = 0.737, CO = 1)	
pO_2(atm)	$\frac{pCO_2}{pCO}$	pCO_2 (sccm)	pCO (sccm)	pCO_2 On channel 1 (sccm)	pCO On channel 4 (sccm)
4.353×10^{-16}	1.180×10^{-4}	0.118	999.882	0.2	999.9

Before the testwork under controlled atmospheres could be done, the pO_2 in the tube furnaces was verified by the reverse-equilibrium approach using the Fe/ FeO reaction at 1300°C with the pO_2 ranging between 10^{-10} and 10^{-11} atm. According to FactSage calculations, (Bale, et al., 2016; Bale, et al., 2002), the equilibrium pO_2 for the Fe/ FeO is 1.510 x 10^{-11} atm at 1300°C. Increasing the pO_2 to 10^{-10} atm at the same temperature resulted in the oxidation of all the Fe to FeO, while at lower pO_2 than 10^{-11} atm the FeO was converted to metallic Fe. The phase compositions of the test products were determined by a Bruker D8 advanced X-Ray Diffractometer (XRD). The reversal of the Fe to FeO and that of FeO to Fe around the equilibrium pO_2 were used as indicators of the correctness of the set pO_2 in the tube furnace.

The pO_2 was also verified regularly during the testwork programme using a DS-type oxygen probe supplied by Australian Oxytrol Systems (AOS). The oxygen probe incorporates a $SIRO_2$ oxygen sensor and a B-type thermocouple. This oxygen probe is suitable for measurements of pO_2 of 10^{-24} to 1 atm at temperatures from 550°C to 1700°C. Continuous use of the sensor at temperatures above 1300°C was avoided as it could reduce the lifespan of the sensor (Australian Oxytrol Systems Pty Ltd, 2017). In the vertical tube furnace of the equilibration-quench setup, the probe was inserted through the top end and held in place using a rubber stopper. The stopper also ensured gas tightness. Reference air was supplied to the oxygen probe at a rate of 10 sccm using a fish pond pump. The oxygen probe produced electromotive force (EMF) signal in DC millivolts which were measured by a data acquisition unit supplied by Keysight Technologies.

The relationship between pO_2 and EMF signal is described by the Nernst equation as detailed in section 1.2.2 of Appendix 1.2. The version of the Nernst equation used to determine the pO_2 from the EMF signal is given by Equation [3.9] (Australian Oxytrol Systems Pty Ltd, 2017).

$$E = \frac{RT}{nF} ln \left[\frac{pO_{2\ inside}}{pO_{2\ outside}}\right] \quad [3.9]$$

Where,

E = EMF of the sensor, (mV)

R = gas constant, 8.3145 $JK^{-1}mol^{-1}$

T = absolute temperature, (Kelvin)

n = number of charges, 4

F = Faraday constant, 96485 C mol^{-1}

$pO_{2\ inside}$ = oxygen partial pressure inside the probe, atm

$pO_{2\ outside}$ = oxygen partial pressure in the reaction tube of the furnace, atm

Since in the current study air was used as the reference gas flowing inside the oxygen probe, i.e. $pO_{2\ inside}$ = 0.209 atm, the Nernst equation for the determination of the $pO_{2\ outside}$ is simplified into Equation [3.10].

$$P_{O_2 outside} = 0.209 \times e^{\frac{-46.42 \times E}{T}} \quad [3.10]$$

The range of the EMF readings for the calibration of the $pO_{2\ outside}$ at 0.21 (in dry air) and 1×10^{-16} atm are summarised in Table 10. The measurement of pO_2 in air was conducted by opening the gas inlet and outlet, with continuous flow of the air reference gas inside the oxygen probe. The pO_2 of 4.353×10^{-16} atm in the reaction tube was produced using a mixture of CO_2 and CO.

As shown in Equation 3.9, pO_2 is a strong function of temperature. During equilibration quench experiments in atmosphere with a pO_2 of 10^{-16} atm at temperatures other than 1500°C, adjustments of the proportions of CO and CO_2 were conducted accordingly. pO_2 verifications using the DS-type probe were conducted sporadically in order to verify the effectiveness of the calculated CO and CO_2 mass flows. After the opening of the tube, for

introduction or removal of the test sample, the purging period of air using CO/CO_2 mixture to get the target pO_2 of 4.353×10^{-16} atm was 30 minutes.

Figure 29 shows the graphical representation of the relationship between $CO\text{-}CO_2$ and pO_2, expressed as oxygen fugacity (fO_2), with the shaded area showing the precipitation of carbon (Deines, et al., 1974). The data in this figure suggests that carbon would precipitate from the $CO\text{-}CO_2$ blend equivalent to a pO_2 of 10^{-16} atm when the temperature is about 1435°C. According to this data, the attainment of the target pO_2 of 10^{-16} atm using $CO\text{-}CO_2$ mixture at 1500°C would be unfeasible. However, measurement of the pO_2 using a probe showed that the target pO_2 of about 10^{-16} atm using $CO\text{-}CO_2$ mixture at 1500°C was attained. The ability to attain the target pO_2 nevertheless was attributed to that the working conditions are not too far off from the limit and that the referenced limits are on the edge of the carbon precipitation field where the measurement uncertainties are anticipated to be significant.

A calibrated CO monitor was placed inside the working laboratory to monitor the CO levels during the testwork. The monitor was set to activate an alarm when the CO concentration inside the laboratory reached 40 ppm. According to the CO handling guidelines (AFROX, 2015), the adverse effects of CO would manifest in humans after working for 8 continuous hours in an area with CO concentration of 50 ppm. However, extra precaution was taken in the current testwork – when the alarm was activated at 40 ppm, the laboratory was evacuated and the CO cylinder connections and lines were re-sealed.

Table 10: Verification of pO_2 in the reaction tube

Target pO_2 (atm)	CO_2 On channel 1 (sccm)	CO On channel 4 (sccm)	EMF readings (DC, mV)	Calculated pO_2 range (atm)
0.209	0	0	-0.601 – 1.206	0.212 – 0.203
4.353×10^{-16}	0.14	1000	1350 – 1323	$9.359 \times 10^{-17} - 1.898 \times 10^{-16}$

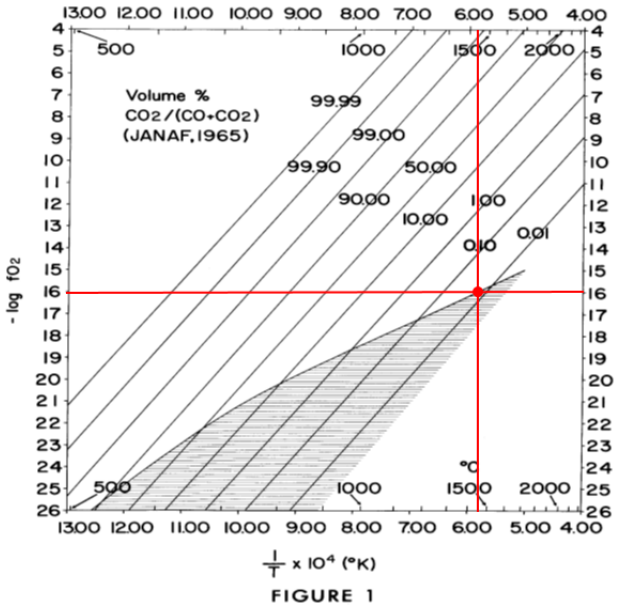

Figure 29: Graphical representation of the relationship between CO-CO_2 and fO_2 (Deines, et al., 1974)

3.3.1.3 Analysis

The MS samples that were processed using the equilibration-quench setup described above were analysed using Zeiss EVO® MA15 scanning electron microscope (SEM) coupled with a Bruker energy dispersive spectrometer (EDS) operated with Bruker Esprit software and Cameca SX50 electron probe X-ray microanalysis (EPMA). SEM-EDS was used to determine the backscattered electron images and X-ray mapping of the samples at a standard accelerating voltage of 20 kV.

EPMA operated with standard accelerating voltage of 15 kV with a probe current of 20 nA and a spot size of 5 µm. To complete the testwork in Ca-Mg-Al-Si-Ti-O system to determine the chemical compositions of the respective phases, the EPMA system was calibrated with discrete oxide reference standards for Ti, Mg, and Al, whereas wollastonite ($CaSiO_3$) was used to calibrate for Ca and Si. The oxygen associated with the respective elements was determined by stoichiometry. In the EPMA system, the wavelength dispersive spectrometers were used to measure peaks and two backgrounds adjacent to the peak. Mg, Al and Si were measured using thallium acid phthalate (TAP) crystals, whereas Ca and Ti were measured using the pentaerythritol (PET) crystals. The peak for each element was measured for 15 seconds with a 5 second measurement on each of the background positions, adjacent to the peak. A photographic image of the EPMA setup is shown in Figure 30.

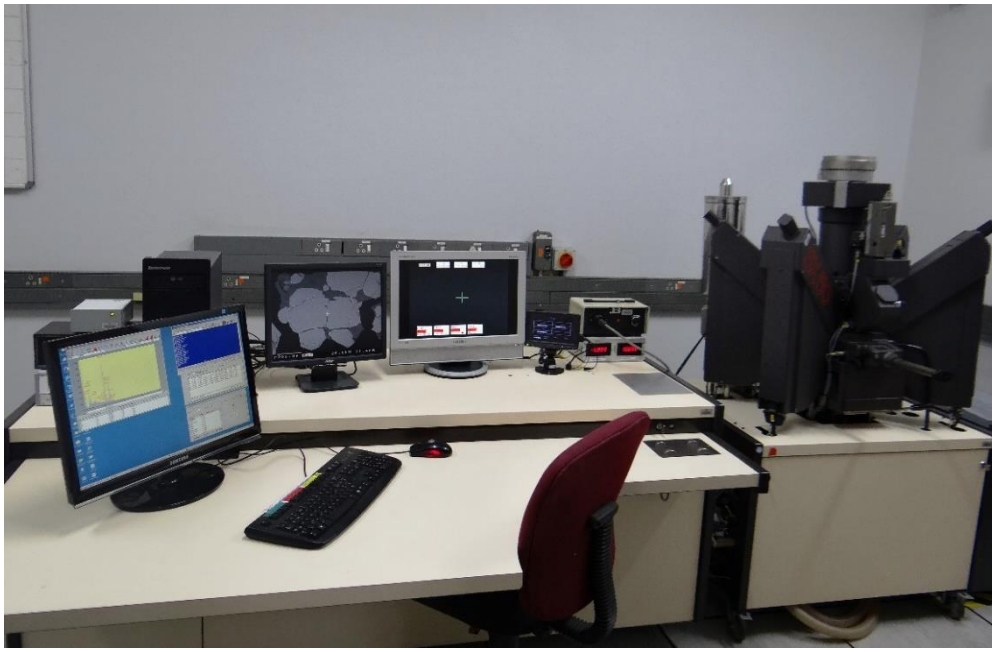

Figure 30: Photograph of the Cameca SX50 electron probe X-ray micro analyser

3.3.2 Conventional induction furnace

The smelting of titanomagnetite concentrate to produce a spinel free titaniferous slag for beneficiation studies was conducted in a 25 kW induction furnace which was setup by LH power. A schematic diagram showing the induction furnace set up is shown in Figure 31. In this set up, the smelting was conducted inside an alumina crucible. In each test, a charged crucible was placed inside the induction furnace chamber, i.e. a graphite susceptor crucible with the base covered with alumina bubbles. The graphite crucible was closed with a lid equipped with three holes: (1) for alumina sheath with one closed end used as a casing for the B-type thermocouple used for monitoring the sample temperature, (2) for an alumina tube used to flow in Ar gas to create an inert atmosphere inside the graphite crucible containing the test crucible, and (3) for off gas emissions. The top of the graphite susceptor crucible was thermally insulated using alumina bubbles and a fibre blanket. The thermocouple was connected to a data acquisition unit for sample temperature profiling throughout the duration of the test. The Ar gas flow was turned on to allow a continuous flow to run throughout the test.

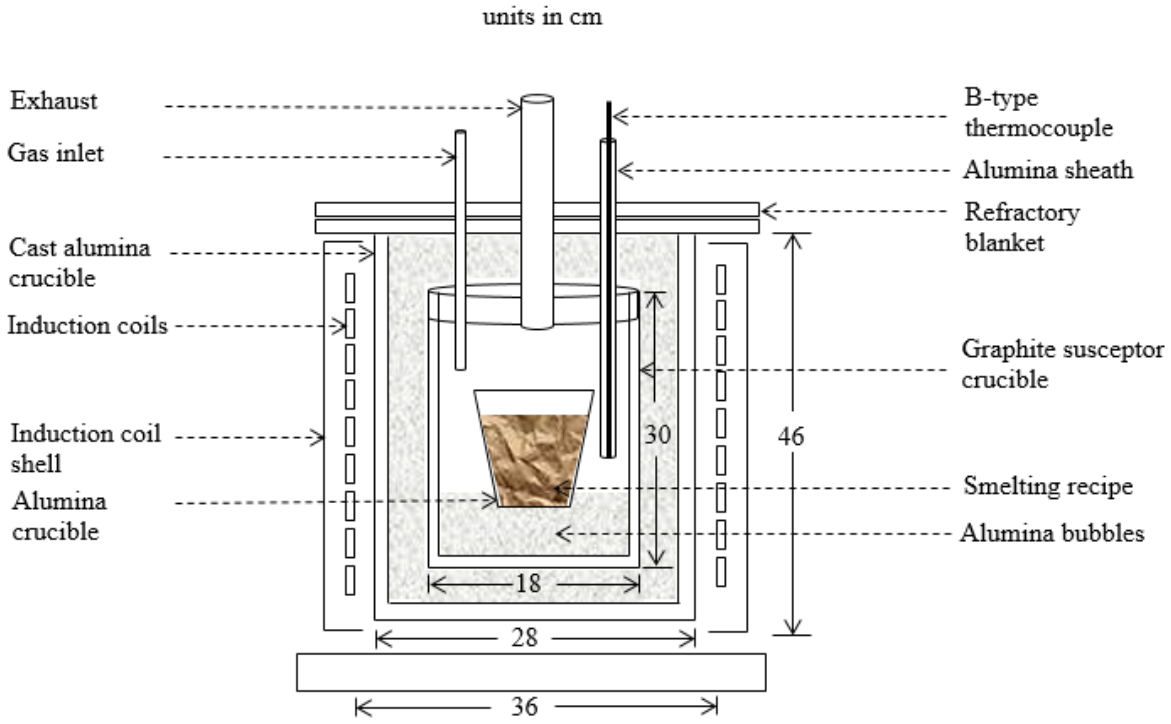

Figure 31: Schematic diagram of the 25 kW induction furnace setup

3.3.3 Cold crucible induction furnace

Since the titaniferous slag produced in the conventional induction furnace inside an alumina crucible also had a spinel solid solution phase, likely due to contamination of the slag by the alumina crucible wear, a contamination free slag was produced in cold copper crucible induction furnace at the Norwegian Institute of Science and Technology (NTNU) in Trondheim, Norway. This furnace facility is a creation of a combination of several components from different suppliers including, a power supply from Farfield Electronics (Pty) Ltd and a water cooled copper crucible from Australian Nuclear Science and Technology Organization (ANSTO). The power capacity of this induction furnace is rated at 75 kVA. Photographic images of the cold crucible induction furnace are shown in Figure 32. A schematic representation of the crucible setup is shown in Figure 33. The components of the cold crucible induction furnace setup are detailed in these figures.

The copper crucible is made up of finger-like segments for the prevention of induction in the crucible during the testwork. For the smelting testwork, boron nitride is sprayed inside the crucible in order to coat the crucible walls and fill the gaps between the segments or the fingers to avoid the leaking of the finely ground or molten charge. The boron nitride coating

also imparts wear and tear properties to the copper crucible and facilitates the removal of the charge from the crucible after the test. The contamination of the charge by the coating is generally low. This is a typical set of the crucible used in this laboratory facility.

Figure 32: Photographic images of the cold crucible induction furnace setup

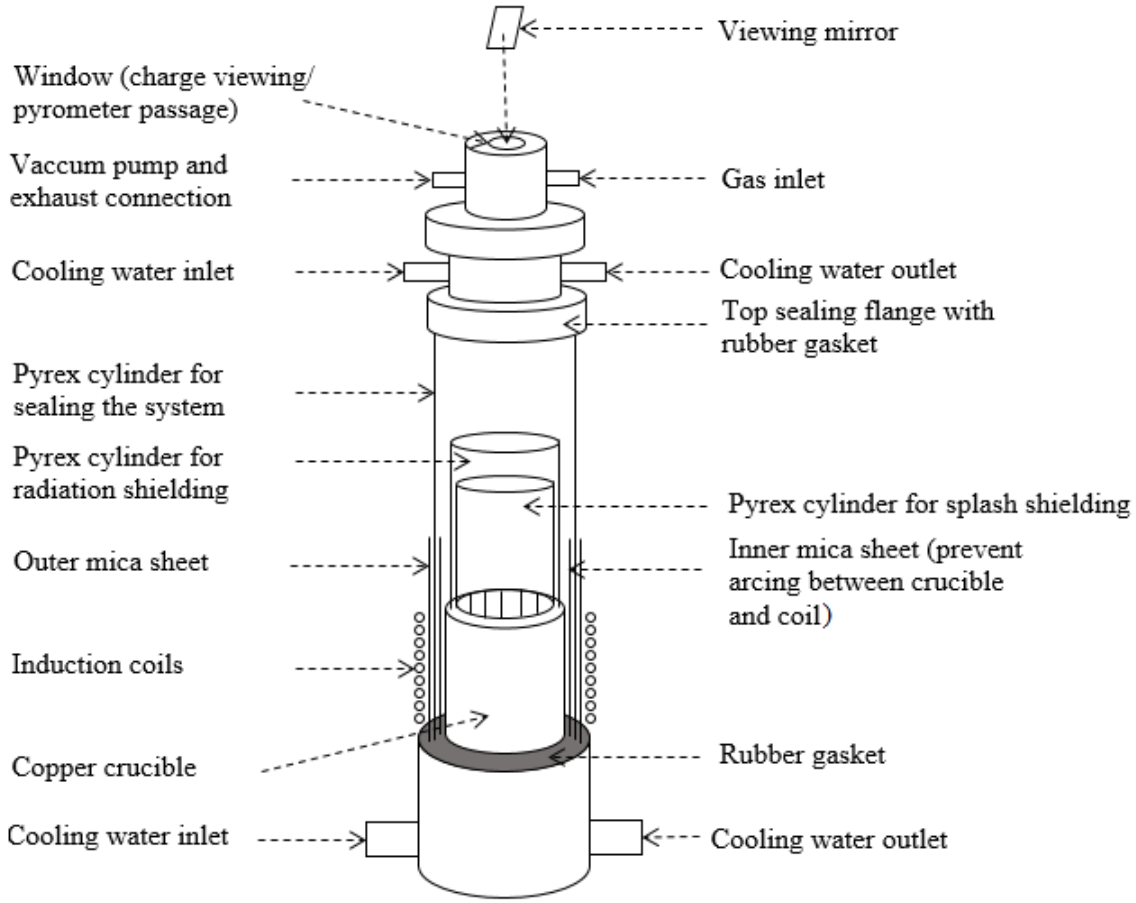

Figure 33: Schematic representation of the crucible setup in the cold crucible induction furnace

3.3.4 Smelting test evaluation

Generic material balance methodologies used by Maphutha et al. (2017) were adopted to assess the performance of the respective smelting tests conducted in the current study. A block diagram of the smelting process in the induction furnace is shown in Figure 34. The induction furnace smelting process can be described by the mass balance equation used for batch process as shown in Equation [5.3]. This equation is deemed appropriate as there is no accumulation in the process – the mass of the slag is determined by difference. However, in the case of cold crucible furnace there is also the freeze line product stream.

The recoveries of the components or elements of the feed to the respective product streams were calculated using Equation [5.4]. In this context, recovery refers to the quantity or percentage of the particular element contained in the feed that reports to, or is recovered to one of the product streams, i.e. off-gas, slag or alloy, after the smelting process.

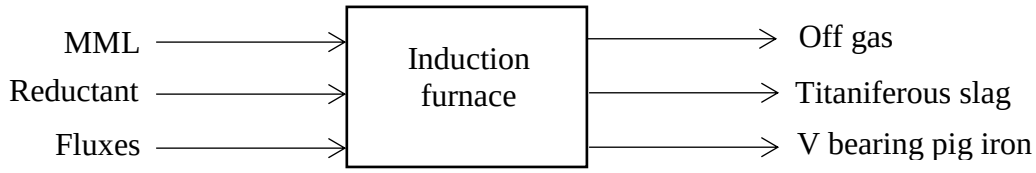

Figure 34: Block diagram of the smelting test in an induction furnace

$$\sum Mass\ in = \sum Mass\ out \qquad [5.3]$$

Where, '$\sum Mass\ in$' denotes the sum of the feed masses to furnace (MML, Reductant and fluxes), and '$\sum Mass\ out$' denotes the sum of the product masses from furnace (off-gas, titaniferous slag and V bearing pig iron).

$$\%Recovery\ of\ element\ i = \frac{M_i\ in\ a\ product\ stream}{M_i\ in\ the\ feed} \times 100 \qquad [5.4]$$

Where, 'M_i' is the mass of element i.

3.3.5 Fluidised furnace set up

A laboratory-scale fluid-bed furnace setup which was equipped with a quartz reactor with respective internal diameter and length of 3 cm and 110 cm was used during the roasting testwork to produce a UGS product from the titaniferous slags.

3.3.6 Thermochemical software

FactSage thermochemical software (Bale, et al., 2002) licenced to Mintek was used to simulate the phase equilibria of titaniferous slags. Three versions of the software, i.e. FactSage7.0, 7.1, 7.2, were used during the current study.

The Pyrometallurgical process simulation program, known as Pyrosim, developed by Mintek (Jones, 2001) was used in the current study. This program was used to simulate the conceptual process flowsheet for the production of vanadium, steel and titanium products from titanomagnetite.

CHAPTER 4

PHASE EQUILIBRIA OF TITANIFEROUS SLAGS

4.1 Introduction

Titaniferous magnetite (titanomagnetite) is typically smelted in the presence of a carbonaceous reductant and fluxes, such as silica, dolomite and/ or limestone, to produce a valuable vanadium bearing pig iron and a valueless TiO_2 (titania) bearing slag (Steinberg, 2008; Zhang, et al., 2007; Bleloch, 1949). This titania bearing slag is referred to as titaniferous slag. Titaniferous slags are typically described by the Ca-Mg-Al-Si-Ti-O system (McRae, et al., 1969; Jochens, 1967). These slags can contain between 20% and 40% TiO_2 (Pistorius, 2011; Steinberg, et al., 2011; Zhang, et al., 2007; Kelly, 1993). The TiO_2 content in these slags is low, so they cannot be used as direct feedstock for the production of titanium products. Moreover, titaniferous slags typically comprise complex phase chemistry, including the inert spinel solid solution phase that cannot be handled by the available titania slag upgrading technologies to beneficiate these slags to feedstock grades or final titanium products (Pistorius, 2011; Van Vuuren & Tshilombo, 2011). Fundamental understanding of the phase equilibria in the Ca-Mg-Al-Si-Ti-O system applicable to titaniferous slags is therefore essential in order to dictate the crystallisation of simple phases with no spinel phase.

Several investigations are reported on the study of equilibrium phase relations and liquidus temperatures in the multicomponent or higher order Ca-Mg-Al-Si-Ti-O system applicable to titaniferous slags (Shi, et al., 2016; Zhao, et al., 2009; Datta, et al., 1993; Fine & Arac, 1980; McRae, et al., 1969; Jochens, et al., 1969; Osborn & Gee, 1969; Holmes, et al., 1968; Jochens, 1967; Devries, et al., 1955). A review of the available literature on the Ca-Mg-Al-Si-Ti-O system applicable to titaniferous slags is covered extensively in section 2.4 of CHAPTER 2. The present section of the thesis adopted a holistic and general approach to reviewing available phase equilibria. The components of the current study included: (1) evaluation of the available thermodynamic and phase equilibria data pertinent to the Ca-Mg-Al-Si-Ti-O system applicable to titaniferous slags, (2) calculation of the phase equilibria in the Ca-Mg-Al-Si-Ti-O system covering a broad titaniferous slag compositional range using FactSage thermochemical software, and (3) equilibration-quench-(electron probe

micro analysis) (EPMA) and thermal analysis experiments as a way of reviewing and validating the calculated equilibrium phase relations and diagrams.

4.2 Critical evaluation of the Ca-Mg-Al-Si-Ti-O system

Substantial literature covering the thermodynamic and phase equilibria information pertinent to the multicomponent Ca-Mg-Al-Si-Ti-O system applicable to titaniferous slags is reviewed in section 2.4.1 of CHAPTER 2. The review includes that of selected important lower order systems involved in the high order Ca-Mg-Al-Si-Ti-O system. The current section provides a summary of the evaluation of the thermochemical and phase equilibria data for only the high order Ca-Mg-Al-Si-Ti-O system with a view of demonstrating the importance and activities of the current study.

Phase relations in the high order Ca-Mg-Al-Si-Ti-O system have been a subject of many investigations (Shi, et al., 2016; Zhao, et al., 2009; Datta, et al., 1993; Fine & Arac, 1980; McRae, et al., 1969; Jochens, et al., 1969; Osborn & Gee, 1969; Holmes, et al., 1968; Jochens, 1967; Devries, et al., 1955). Most of these studies evaluated the phase equilibria in systems with concentrations of less than 20% TiO_2 which are applicable to blast furnace (BF) titaniferous slags (Shi, et al., 2016; Zhao, et al., 2009; Morizane, et al., 1999; Datta, et al., 1993; Fine & Arac, 1980; Osborn & Gee, 1969; Devries, et al., 1955) – these compositions would cover the slags produced by NTMK in Russia (Hassell, et al., 2016; NTMK, 2003). Because of low TiO_2 grades, these titaniferous slags are less attractive as sources of Ti products.

Holmes et al. (1968) reported liquidus temperature results obtained from tests conducted in air for the Ca-Mg-Al-Si-Ti-O system applicable to low and relatively high TiO_2 bearing titaniferous slags in a compositional range spanning from 6% to 48% TiO_2. A wide liquidus temperature variability of 1217°C to 1667°C over the reviewed compositional range was reported. The lowest liquidus temperatures were achieved when the difference between the sum of CaO and MgO, and SiO_2 was less than 12%. At constant CaO and MgO concentrations, the liquidus temperatures were lowered when SiO_2 was substituted by TiO_2+Al_2O_3. This study lacks sub-liquidus temperature data as well as information on the primary and sub-liquidus phase crystallisation (Holmes, et al., 1968).

In his PhD research, Jochens (1967) undertook a comprehensive study to investigate the liquidus and sub-liquidus temperatures as well as the primary and sub-liquidus phase crystallisation phenomena in the Ca-Mg-Al-Si-Ti-O system applicable, particularly to fluxed titaniferous slags produced from the smelting of the main magnetite layer (MML) titanomagnetite mined from the South Africa's Bushveld Complex. In this study, conducted in air at constant concentrations of 37.19% TiO_2, 19.69% SiO_2, 13.12% Al_2O_3 and varying proportions of CaO (30-0%) and MgO (0-30%), the liquidus temperatures varied between 1340°C and 1520°C, where the ratios of CaO: MgO in the respective compositions were 18:12 and 30:0. The liquidus temperature difference between the two extreme compositions in terms of CaO and MgO, i.e. compositions with CaO: MgO ratios of 30:0 and 0:30, was only 15°C. In slag compositions with high CaO contents above 18%, perovskite ($CaTiO_3$) crystalized as the primary phase while at high MgO concentrations above 12% the pseudobrookite solid solution, i.e. $4MgTi_2O_5$-Al_2TiO_5 was the primary phase. The XRD powder patterns evaluated by Jochens (1967) only showed weak lines corresponding to the spinel structure; however, these XRD lines could not be distinguished from the confirmed primary $4MgTi_2O_5$-Al_2TiO_5 lines. Hence, the spinel was not included in the equilibrium phase diagram established from this work. The comprehensive data established in this work, which included numerous sub-liquidus temperatures and phases, are included in the equilibrium phase diagram in Figure 19. However, aspects that require further investigations in the established phase equilibria include the review of the crystallisation of the spinel and, if present the resolution of the primary phase between the pseudobrookite and spinel phases.

Zhao et al. (2009) investigated the phase equilibria in the Ca-Mg-Al-Si-Ti-O system applicable to BF titaniferous slag, <10% TiO_2, at carbon saturation. The results showed that the pseudobrookite primary phase contained reduced titanium species (Ti^{+3}). Thus, in previous work conducted by Holmes et al. (1968) and Jochens (1967), the crystallisation of phases with reduced species, like Ti^{3+}, from the Ca-Mg-Al-Si-Ti-O system could not be predicted as a consequence of that these studies were completed in air.

A summary of the results produced by Holmes et al. (1968) and Jochens (1967) is shown in Figure 35. The results show a significant variability in the liquidus surfaces of the two studies – the variability is more pronounced between the CaO: MgO ratios of 20:10 and 15:15. The source of variability is not obvious. It is however presumed that the reported experimental conditions could be different: in one extreme, one study could have been

completed in a closed system with no air circulation, in which case the partial pressure of oxygen (pO_2) would be lower than that of air (Schultz, et al., 2013), whereas in the other extreme, the experiment could have been completed in a continuous flow of air.

The titaniferous slags typically comprise complex phase chemistry that is composed of several phases including perovskite, pseudobrookite and spinel solid solutions (Pistorius, 2011). However, Jochens' phase diagram does not clearly predict the crystallisation of the spinel structure in the reviewed titaniferous slag compositional range. In addition, the presence of reduced titanium species, i.e. Ti^{3+}, in the pseudobrookite solution reported by Zhao et al. (2009) would not be included in Jochens' phase diagram as a consequence of the work having been completed in air. However, it should be noted that titaniferous slags are essentially produced under the highly reducing conditions necessary for the reduction of iron and vanadium, and not in air (Steinberg, 2008; Zhang, et al., 2007; NTMK, 2003; Kelly, 1993; Bleloch, 1949).

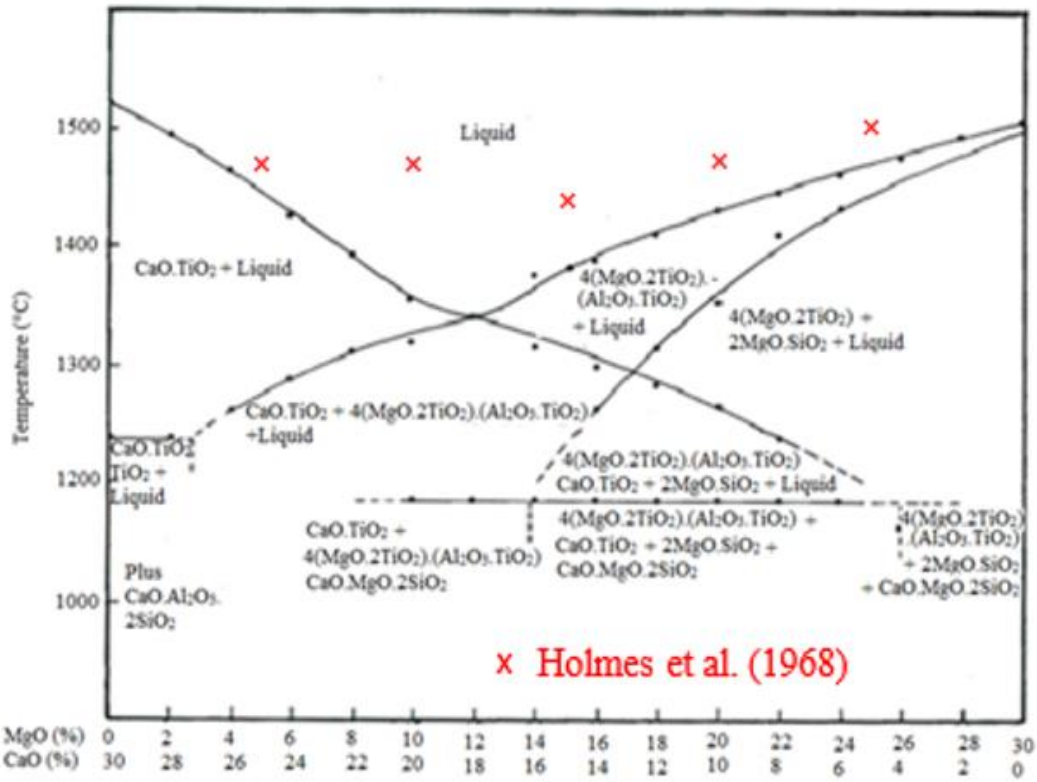

Figure 35: Equilibrium phase diagram established in air for the slag system: TiO_2~37wt%, SiO_2~20wt%, and Al_2O_3~13wt%, at varying proportions of CaO (30-0wt%) and MgO (0-30wt%) – a comparison of data produced by Jochens (1967) and Holmes et al. (1968)

4.3 Calculation of phase equilibria in the Ca-Mg-Al-Si-Ti-O system

The recent versions of the FactSage software, i.e. FactSage 7.0, 7.1 and 7.2, were used during the current research programme for the review of Jochens' phase equilibria established in air and calculations of updated phase equilibria covering a broad compositional range under pO_2 conditions applicable to titanomagnetite smelting. FactSage contains data for most compounds that can form in the Ca-Mg-Al-Si-Ti-O system, including pseudobrookite-type compounds such as titanium pentoxide (Ti_3O_5) karrooite ($MgTi_2O_5$) and tialite (Al_2TiO_5). It also contains many solid solution databases which include solution phase such as olivine $[Ca^{2+}, Co^{2+}, Fe^{2+}, Mg^{2+}, Mn^{2+}, Ni^{2+}, Zn^{2+}]^{M2}(Ca^{2+}, Co^{2+}, Fe^{2+}, Mg^{2+}, Mn^{2+}, Ni^{2+}, Zn^{2+})^{M1}SiO_4$, spinel: $(Al^{3+}, Co^{2+}, Co^{3+}, Cr^{2+}, Cr^{3+}, Fe^{2+}, Fe^{3+}, Mg^{2+}, Ni^{2+}, Zn^{2+})[Al^{3+}, Co^{2+}, Co^{3+}, Cr^{3+}, Fe^{2+}, Fe^{3+}, Mg^{2+}, Ni^{2+}, Zn^{2+}, Va]_2O_4$, and pseudobrookite: $(Fe^{2+}, Mg, Mn, Ti^{3+})(Ti^{4+}, Ti^{3+})_2O_5$ (Bale, et al., 2008; Pelton, 2006).

Al_2TiO_5 is not included as an endmember in the $(Fe^{2+}, Mg, Mn, Ti^{3+})(Ti^{4+}, Ti^{3+})_2O_5$ structure for pseudobrookite solid solution; thus, it appears that it was not modelled as a component of this solution. However, in the studies of the Ca-Mg-Al-Si-Ti-O system applicable to titaniferous slags in air, Jochens (1967) reported that $4(MgO.2TiO_2).Al_2O_3.TiO_2$ or stoichiometrically $4MgTi_2O_5$-Al_2TiO_5 crystallises as the primary phase at high MgO concentrations. The crystallisation of Ti_3O_5 in relevant lower order and high Ca-Mg-Al-Si-Ti-O systems is reported in previous investigations (Zhao, et al., 2009; Krajewski, 1992; Berezhnoi & Gulko, 1955). Hence, according to Jochens' (1967) phase equilibria, FactSage equipped with the customary pseudobrookite databases would not be able to correctly predict the equilibrium phase relations in the Ca-Mg-Al-Si-Ti-O system in which the $MgTi_2O_5$-Al_2TiO_5-Ti_3O_5 solid solution is anticipated to crystallise.

Therefore, a private pseudobrookite solution database for the $MgTi_2O_5$-Al_2TiO_5-Ti_3O_5 ternary system needed to be developed and subsequently incorporated into FactSage for the calculation of the phase equilibria in the Ca-Mg-Al-Si-Ti-O system. Then, the calculation of the equilibrium phase diagrams for the Ca-Mg-Al-Si-Ti-O system applicable to titaniferous slags could be conducted.

The development of the private pseudobrookite solid solution was conducted using the CALPHAD principles. The application of the CALPHAD in the current study included thermodynamic modeling and development of a private solution database in FactSage.

Optimized thermodynamic data were used during the development of the private pseudobrookite database (Bale, et al., 2002; Pelton, et al., 1998). The evaluation of the efficiency of the modelling approach entailed the comparison of one of the reviewed binary model, i.e. $MgTi_2O_5$-Ti_3O_5, against the binary system contained in the FactSage customary pseudobrookite solid solution database (Bale, et al., 2002).

4.3.1 Thermodynamic modelling of solid solution database

The development of the solid solution database for the $MgTi_2O_5$-Ti_3O_5-Al_2TiO_5 system was conducted through thermodynamic modelling of the binary systems and subsequent extrapolation to the ternary system. The $MgTi_2O_5$-Ti_3O_5 binary solution was modelled in the past (Pelton, et al., 1998). In the current study, the thermodynamic models for the $MgTi_2O_5$-Al_2TiO_5 and Al_2TiO_5-Ti_3O_5 binary solutions were developed using the sublattice modelling approach coupled with CEF and Redlich-Kister polynomial. Fortuitously, the optimized thermodynamic parameters of the relevant compounds involved in the $MgTi_2O_5$-Ti_3O_5-Al_2TiO_5 system are available in literature (Pelton, et al., 1998) and also included in the FactSage compound databases (Bale, et al., 2002). These optimized parameters are included in Table 11.

4.3.1.1 Case for assuming ideal solution mixing in $MgTi_2O_5$-Al_2TiO_5 and Al_2TiO_5-Ti_3O_5 systems

Thermodynamic modelling of pseudobrookite solid solution phases using the sublattice model coupled with CEF and Redlich-Kister polynomial was completed by several researcher in the past, including; Kang et al. (2006) for $MnTi_2O_5$-Ti_3O_5 system, Pelton et al. (1998) for $MgTi_2O_5$-Ti_3O_5 system, and Eriksson et al. (1996) for the $FeTi_2O_5$-Ti_3O_5. In these studies, the thermodynamic models were developed with the assumption of ideal solution mixing in the respective pseudobrookite binary systems, i.e. the excess Gibbs energy of mixing was zero ($G^E = 0$). Thermochemical calculations using these ideal solution thermodynamic databases provided 'very' good correlation between the calculated and experimental results (Kang, et al., 2006; Pelton, et al., 1998; Ericksson, et al., 1996). Hence, the ideal solution approximation in the $MgTi_2O_5$-Al_2TiO_5 and Al_2TiO_5-Ti_3O_5 systems was deemed satisfactory and adopted in the current study. Moreover, optimized thermodynamic model parameters were acquired from literature (Bale, et al., 2002; Pelton, et al., 1998) and used to develop a thermodynamic database for the $MgTi_2O_5$-Ti_3O_5-Al_2TiO_5 system.

Table 11: Optimised thermodynamic model parameters applicable to the development of the $MgTi_2O_5$-Ti_3O_5-Al_2TiO_5 solid solution database

$G_{MgTi_2O_5} = G^0_{MgTi_2O_5}$ $H^0_{298.15}\ (Jmol^{-1}) = -2\ 504\ 887.41$ $S^0_{298.15}(Jmol^{-1}K^{-1}) = 137.34$ $C_p(Jmol^{-1}K^{-1}) = 232.58 - 5\ 660\ 800.1T^{-2} - 755.50T^{-1/2} + 582\ 140\ 003T^{-3}$
$G_{Al_2TiO_5} = G^0_{Al_2TiO_5}$ $H^0_{298.15}\ (Jmol^{-1}) = -2\ 577\ 173.79$ $S^0_{298.15}(Jmol^{-1}K^{-1}) = 128.45$ $C_p(Jmol^{-1}K^{-1}) = 249.29 - 4\ 806\ 100.1T^{-2} - 1\ 350.1T^{-1/2} + 516\ 030\ 000T^{-3}$
$G_{Ti_3O_5} = G^0_{Ti_3O_5}$ $H^0_{298.15}\ (Jmol^{-1}) = -2452465.03$ $S^0_{298.15}(Jmol^{-1}K^{-1}) = 157.62C_p(Jmol^{-1}K^{-1}) = 158.99 + 0.05020785T$
<u>$MgTi_2O_5$-Al_2TiO_5 binary model:</u> $G^0_{Al_2TiO_5} = \frac{1}{2}\left(G^0_{Al_3O_5^-} + G^0_{AlTi_2O_5^+}\right) + 2RT\ln\left(\frac{1}{2}\right)$ $G^0_{Al_3O_5^-} = G^0_{AlTi_2O_5^+} = G^0_{Al_2TiO_5} - 2RT\ln\left(\frac{1}{2}\right)$
<u>$MgTi_2O_5$-Ti_3O_5 binary model:</u> $G^0_{Ti_3O_5} = \frac{1}{2}\left(G^0_{Ti_3O_5^-} + G^0_{Ti_3O_5^+}\right) + 2RT\ln\left(\frac{1}{2}\right)$ $G^0_{Ti_3O_5^-} = G^0_{Ti_3O_5^+} = G^0_{Ti_3O_5} - 2RT\ln\left(\frac{1}{2}\right)$

Ti_3O_5-Al_2TiO_5 binary model:

$$G^0_{Ti_3O_5} = \frac{1}{2}\left(G^0_{Ti_3O_5^-} + G^0_{Ti_3O_5^+}\right) + 2RT\ln\left(\frac{1}{2}\right)$$

$$\mathrm{G^0_{Ti_3O_5^-}} = \mathrm{G^0_{Ti_3O_5^+}} = \mathrm{G^0_{Ti_3O_5}} - 2\mathrm{RT}\ln\left(\frac{1}{2}\right) = \mathrm{G^0_{Ti_3O_5}} + 11.52565T$$

$$G^0_{Al_2TiO_5} = \frac{1}{2}\left(G^0_{Al_3O_5^-} + G^0_{AlTi_2O_5^+}\right) + 2RT\ln\left(\frac{1}{2}\right)$$

$$\mathrm{G^0_{Al_3O_5^-}} = \mathrm{G^0_{AlTi_2O_5^+}} = \mathrm{G^0_{Al_2TiO_5}} + 11.52565T$$

$$G^0_{Ti_3O_5^{2+}} = \frac{1}{2}\left(G^0_{Ti_3O_5} + G^0_{Al_2TiO_5}\right)$$

$$G^0_{AlTi_2O_5^-} = G^0_{Al_2TiO_5^-} = \frac{1}{2}\left(G^0_{Ti_3O_5} + G^0_{Al_2TiO_5}\right) + 11.52565T$$

4.3.1.2 $MgTi_2O_5$-Al_2TiO_5 solid solution model

Crystallographic studies have shown that $MgTi_2O_5$ has an octahedral structure in which the Mg^{2+} and Ti^{4+} cations occupy two non-equivalent sites, namely; sublattices A and B, respectively (Xirouchakis, et al., 2002; Navrotsky, 1975). Similarly, the octahedral structure of Al_2TiO_5 reportedly contains Al^{3+} and Ti^{4+} in the respective A and B sublattices (Epicier , et al., 1991). The $MgTi_2O_5$-Al_2TiO_5 solid solution is thus considered to be composed of three sublattices, namely; A and B cationic sublattices and C anionic sublattice constructed by the O^{2-}. Complete random distribution of Mg^{2+}, Ti^{4+} and Al^{3+} can be assumed to be present in the cationic sublattices of the solid solution at high temperatures (Buscaglia, et al., 1996; Navrotsky, 1975). The modelling of the $MgTi_2O_5$-Al_2TiO_5 solid solution followed a successful approach implemented by previous researchers in modelling similar pseudobrookite-type solid solutions (Kang, et al., 2006; Pelton, et al., 1998; Ericksson, et al., 1996). The same simplified model is adopted here, in which the occupancies of $MgTi_2O_5$ and Al_2TiO_5 are taken as $(Mg^{2+})_A(Ti_2^{4+})_BO_5$ and $(Al^{3+})_A(Ti^{4+}Al^{3+})_BO_5$, respectively. The occupancies in the $MgTi_2O_5$-Al_2TiO_5 solid solution are thus represented as $(Mg^{2+}_{1-x}, Al^{3+}_x)_A(Ti^{4+}_{2-x}, Al^{3+}_x)_BO_5$, with the assumption that the cations mix randomly on each sublattice. This assumption allows for the ideal entropy of the solid solution to be calculated using Equation [4.1] (Pelton, 2006; Hillert, 2001; Pelton, et al., 1998; Ericksson, et al., 1996; Shi, et al., 1992):

$$\Delta S^{ideal} = -R[(1-x)\,ln(1-x) + x\,ln\,x] - R\left[(2-x)\,ln\left(\frac{2-x}{2}\right) + x\,ln\left(\frac{x}{2}\right)\right] \quad [4.1]$$

Where $(1-x)$ and x represent the overall mole fractions of $MgTi_2O_5$ and Al_2TiO_5, respectively.

The interaction of cations and anions in the $MgTi_2O_5$-Al_2TiO_5 solid solution are such that there are four endmembers, namely; the real component $MgTi_2O_5$ and three pseudocomponents $Al_3O_5^-$, $AlTi_2O_5^+$, and $MgAl_2O_5^{2-}$. The molar Gibbs energy of the solution is therefore given by the expression in Equation [4.2] (Pelton, 2006; Hillert, 2001; Pelton, et al., 1998; Ericksson, et al., 1996; Shi, et al., 1992):

$$G = (1-x)\left(\frac{2-x}{2}\right)G^0_{MgTi_2O_5} + x\left(\frac{x}{2}\right)G^0_{Al_3O_5^-} + x\left(\frac{2-x}{2}\right)G^0_{AlTi_2O_5^+} + (1-x)\left(\frac{x}{2}\right)G^0_{MgAl_2O_5^{2-}} - T\Delta S^{ideal} + G^E \quad [4.2]$$

The optimized thermodynamic model parameters of the real compounds involved in the current model are included in Table 11 (Bale, et al., 2002; Pelton, et al., 1998; Ericksson, et al., 1996). This thermodynamic data is considered to be the most reliable and is also used in the FactSage thermochemical software (Bale, et al., 2002). The Gibbs energy of the real component $MgTi_2O_5$, i.e. $G_{MgTi_2O_5}$, in Equation [4.2] is obtained from Table 11. The thermochemical properties of the respective components of $MgTi_2O_5$-Al_2TiO_5 system are determined using Equations [4.3] to [4.6].

$$H(Jmol^{-1}) = A + \int_{298.15}^{T} C_p dT \quad [4.3]$$

$$S(Jmol^{-1}K^{-1}) = B + \int_{298.15}^{T} (C_p/T)\,dT \quad [4.4]$$

$$C_p(Jmol^{-1}K^{-1}) = a + b(10^{-3})T + c(10^5)T^{-2} + dT^{-1/2} + e(10^8)T^{-3} \quad [4.5]$$

$$G(T) = H_{298.15} + \int_{298.15}^{T} C_p\,dT - T\left(S_{298.15} + \int_{298.15}^{T}\frac{C_p}{T}dT\right) \quad [4.6]$$

The combination of the pseudocomponents is such that the $MgTi_2O_5$-Al_2TiO_5 solid solution is always electrically neutral. The pure Al_2TiO_5 compound is thus assumed to be an ideal equimolar mixture of $Al_3O_5^-$ and $AlTi_2O_5^+$. The Gibbs energy of Al_2TiO_5 is therefore given by Equation [4.7]:

$$G^0_{Al_2TiO_5} = \frac{1}{2}\left(G^0_{Al_3O_5^-} + G^0_{AlTi_2O_5^+}\right) + 2RT\ln\left(\frac{1}{2}\right) \quad [4.7]$$

$G^0_{Al_2TiO_5}$ is also obtained from Table 11. The Gibbs energies of the real components and pseudocomponents of the $MgTi_2O_5$-Al_2TiO_5 solid solution are further related by the exchange reaction shown in Equation [4.8]:

$$(Mg^{2+})_A(Ti_2^{4+})_BO_5 + (Al^{3+})_A(Al_2^{3+})_BO_5^- = (Al^{3+})_A(Ti_2^{4+})_BO_5^+ + (Mg^{2+})_A(Al_2^{3+})_BO_5^{2-} \quad [4.8]$$

The Gibbs free energy of the exchange reaction can be expressed as shown in Equation [4.9].

$$\Delta G_{MgTi_2O_5-Al_2TiO_5} = G^0_{AlTi_2O_5^+} + G^0_{MgAl_2O_5^{2-}} - G^0_{MgTi_2O_5} - G^0_{Al_3O_5^-} \quad [4.9]$$

In Equation [4.2], an additional excess Gibbs energy term, G^E, was included to account for solution non-ideality. However, as discussed in section 4.3.1.1, G^E is approximated by zero in the present study.

For demonstration purposes, G^E can be expressed as shown in Equation [4.10] (Pelton, et al., 1998).

$$G^E = cX_{Mg^{2+}(A)}X_{Al^{3+}(A)}X_{Ti^{4+}(B)} \quad [4.10]$$

Where $X_{Mg^{2+}(A)}$, $X_{Al^{3+}(A)}$ and $X_{Ti^{4+}(B)}$ denote the fractions of A or B sublattice sites occupied by Mg^{2+} Al^{3+} and Ti^{4+}, respectively. In terms of mole fractions, G^E would be as shown in Equation [4.11].

$$G^E = c(1-x)(x)(2-x)/2 \quad [4.11]$$

Where c is an empirical parameter, and $(1-x)$ and x represent the overall mole fractions of $MgTi_2O_5$ and Al_2TiO_5, respectively. G^E of the $MgTi_2O_5$-Al_2TiO_5 solid solution can also be described by the Redlich-Kister polynomial as in Equation [4.12] (Hillert, 2001; Shi, et al., 1992).

$$G^E = x(1-x)\left[(2-x)L_{Mg^{2+},Al^{3+}:Ti^{4+}} + xL_{Mg^{2+},Al^{3+}:Al^{3+}}\right] + x(2-x)\left[(1-x)L_{Mg^{2+}:Ti^{4+},Al^{3+}} + xL_{Al^{3+}:Ti^{4+},Al^{3+}}\right] + x^2(1-x)(2-x)L_{Mg^{2+},Al^{3+}:Ti^{4+},Al^{3+}} \quad [4.12]$$

$L_{Mg^{2+},Al^{3+}:Ti^{4+}}$, $L_{Mg^{2+},Al^{3+}:Al^{3+}}$, $L_{Mg^{2+}:Ti^{4+},Al^{3+}}$, $L_{Al^{3+}:Ti^{4+},Al^{3+}}$ represent the binary interaction parameters – the comma in the subscript separate the interacting elements in the

same sublattice while the other sublattice is occupied by the species appearing on the other side of the colon. $L_{Mg^{2+},Al^{3+}:Ti^{4+},Al^{3+}}$ represents the interaction parameter of the simultaneous mixing of the solid solution. The interaction in this solid solution can be approximated by the binary interaction of Mg^{2+} and Al^{3+} on the A-sublattice when the B-sublattice is occupied by Ti^{4+}, i.e. $L_{Mg^{2+},Al^{3+}:Ti^{4+}}$. The interaction parameters 'L' are generally functions of pressure, temperature and composition. Hence the interaction parameter applicable in the current study can be expressed as shown in Equation [4.13] (Hillert, 2001; Shi, et al., 1992).

$$G^E = L_{Mg^{2+},Al^{3+}:Ti^{4+}} = \acute{a} + \acute{b}T \qquad [4.13]$$

a' and b' are the adjustable empirical parameters of the model which account for the deviation from ideal mixing. These parameters are typically obtained from the optimisation of experimental results (Hillert, 2001; Shi, et al., 1992).

In consideration of letting $G^E = 0$, the main parameters of the CEF model used in the current study were then the endmember Gibbs energies described in Equations [4.2], [4.7] and [4.9]. In order to describe the Gibbs energies of the endmembers, the standard Gibbs energy of $G^0_{AlTi_2O_5^+}$ or $G^0_{MgAl_2O_5^{2-}}$ could be assigned an arbitrary value, following an acceptable approach in the literature (Kang, et al., 2006; Pelton, et al., 1998; Ericksson, et al., 1996). In the current study, $G^0_{AlTi_2O_5^+}$ was however set to be equal to $G^0_{Al_3O_5^-}$. $G^0_{MgAl_2O_5^{2-}}$ was then determined in a case when $\Delta G_{MgTi_2O_5-Al_2TiO_5} = 0$ as it is appropriate for Gibbs energy minimization principles – this approach is also acceptable (Kang, et al., 2006). The Gibbs energies of the four endmembers were then determined using equations [4.2], [4.7] and [4.9].

The endmember Gibbs energies were expressed in terms of the Gibbs energies of the real components $MgTi_2O_5$ and Al_2TiO_5. Following a procedure adopted in previous studies (Povoden-Karadeniz, et al., 2012; Hillert, 2001; Shi, et al., 1992), the mixing of the $MgTi_2O_5$-Al_2TiO_5 solid solution can be demonstrated on the CEF reciprocal solution as shown in Figure 36. Figure 37 shows a simplified schematic diagram of the composition of the sublattice model for the $MgTi_2O_5$-Al_2TiO_5 solid solution – the neutral composition is shown by the dashed line.

The $MgTi_2O_5$-Al_2TiO_5 solution model was incorporated into the FactSage software for the subsequent development of a private $MgTi_2O_5$-Ti_3O_5-Al_2TiO_5 solid solution database. The

procedure for incorporating a private solution database into the FactSage software using the 'solution' module is well described on FactSage notes (Bale, et al., 2002) and was also followed in the current study. The procedure includes entering the Gibbs energy functions of the four endmembers, i.e. $G^0_{AlTi_2O_5^+}$, $G^0_{MgAl_2O_5^{2-}}$, $G^0_{MgTi_2O_5}$, and $G^0_{Al_3O_5^-}$, into the Gibbs energy minimization system, i.e. Compound Energy Formalism (CEF).

The interaction of the components of the solid solution was determined using the Redlich-Kister polynomial included in FactSage software; however, the interaction parameter for the estimated $L_{Mg^{2+},Al^{3+}:Ti^{4+}}$ was set to zero to follow an ideal solution model.

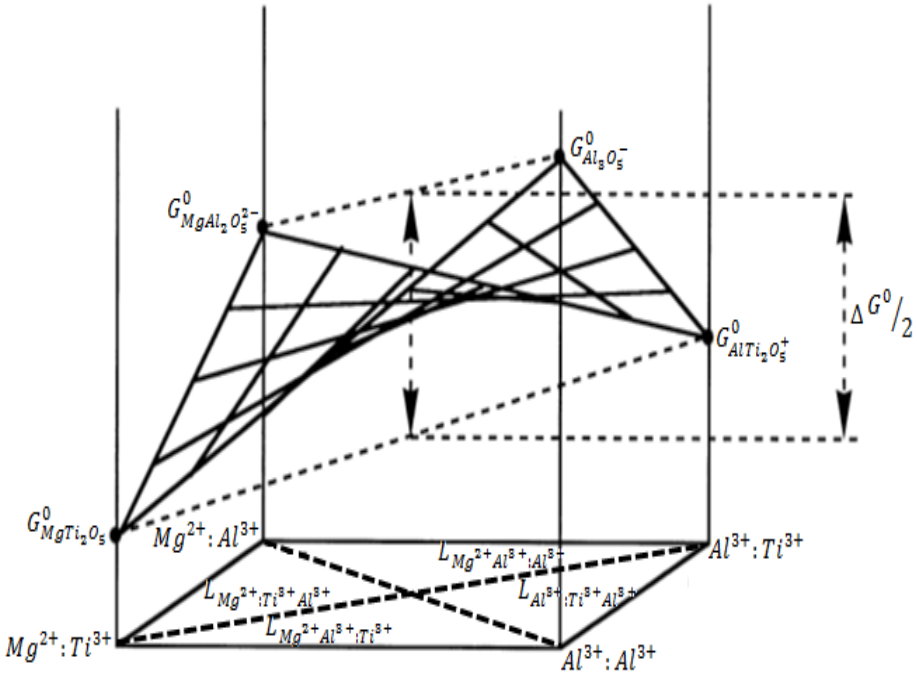

Figure 36: CEF illustration of the Gibbs energy of mixing, compositional space and interaction parameters in the reciprocal solution $(Mg^{2+}_{1-x}, Al^{3+}_x)(Ti^{4+}_{2-x}, Al^{3+}_x)O_5$

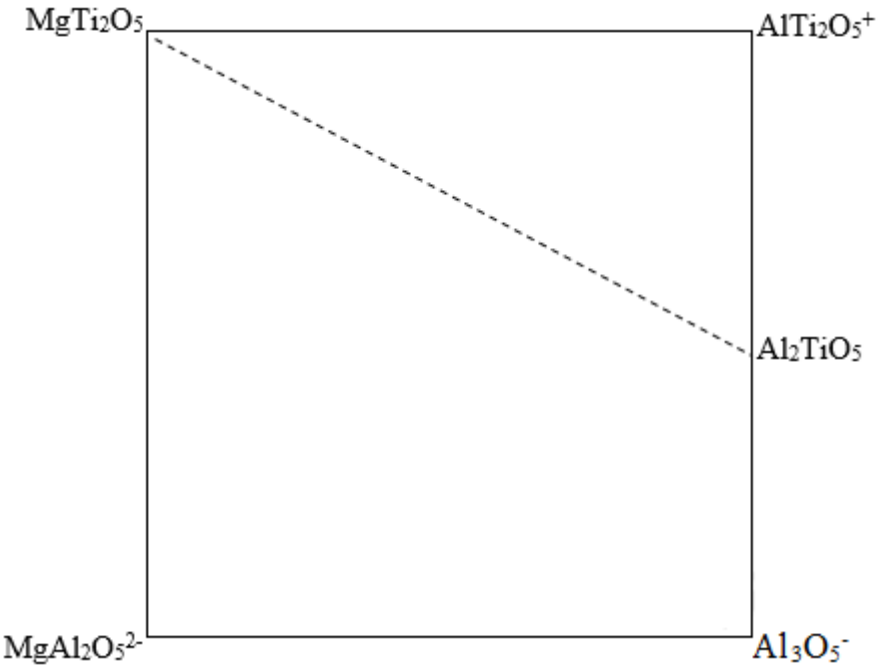

Figure 37: Schematic illustration of the composition of the sublattice model for the $MgTi_2O_5$-Al_2TiO_5 solid solution

4.3.1.3 $MgTi_2O_5$-Ti_3O_5 solid solution model

In their study of the Mg-Ti-O system, Pelton et al. successfully completed the thermodynamic modeling of the $MgTi_2O_5$-Ti_3O_5 solid solution using the sublattice model coupled with CEF and Redlich-Kister polynomial (Pelton, et al., 1998). The thermodynamic model information was uploaded onto FactSage solution database in order to produce a mini private $MgTi_2O_5$-Ti_3O_5 solution database for comparison with customary pseudobrookite solid solution. To achieve this, the Gibbs energy expressions of the four possible endmembers determined as described in 4.3.1.2 were entered into the CEF software and the Redlich-Kister polynomial on FactSage.

For calculations of the thermodynamic properties for the $MgTi_2O_5$-Ti_3O_5 solution, the temperature dependence of $\Delta G_{MgTi_2O_5-Ti_3O_5}$ was determined from experimental investigations and is shown in Equation [4.14] (Pelton, et al., 1998).

$$\Delta G_{MgTi_2O_5-Ti_3O_5} = 34776 + 44.615\,T \; in \; J/mol \qquad [4.14]$$

4.3.1.4 Ti_3O_5-Al_2TiO_5 solid solution model

The solution thermodynamics in the Ti_3O_5-Al_2TiO_5 system were investigated in different studies in the past (Vasyutinskii, 1977; Model, 1962). After experimental investigations, Vasyutinskii (1977) reported a restricted solubility in the Ti_3O_5-Al_2TiO_5 system, where the solubility of Al_2TiO_5 in Ti_3O_5 was reported to be about 20-25 mole%. However, Model (1962) postulated a mutual solubility in the Ti_3O_5-Al_2TiO_5 system, as in the case of the $MgTi_2O_5$-Ti_3O_5 system.

Following Model's (1962) postulation, it implies that the sublattice model coupled with CEF and Redlich polynomial can be used to describe the thermodynamic properties of the Ti_3O_5-Al_2TiO_5 solid solution. The solid solution is considered to be composed of three sublattices: A and B cationic sublattices and C anionic sublattice constructed by the O^{2-}. Both Ti_3O_5 ($Ti_2O_3.TiO_2$) and Al_2TiO_5 ($Al_2O_3.TiO_2$) fall in the category of the M_2TiO_5 pseudobrookite, where M = Ti^{3+} or Al^{3+} (Navrotsky, 1975). As described by Eriksson et al. (1996) and Pelton et al. (1998), Ti_3O_5 has the approximate ion occupancy of $(Ti^{3+})_A(Ti^{4+}Ti^{3+})_BO_5$. Hence, as also adopted in section 4.3.1.2, the approximate ion occupancy in Al_2TiO_5 is assumed to be $(Al^{3+})_A(Ti^{4+}Al^{3+})_BO_5$, which is similar to that of Ti_3O_5. The mixing of cations in the Ti_3O_5-Al_2TiO_5 solid solution would then take the substitutional model approach with the respective A and B sites occupied by mixing of Ti^{3+} and Al^{3+}. The neutral Ti_3O_5-Al_2TiO_5 solid solution can also be presented in terms of the cation distribution in the respective sublattices (Povoden-Karadeniz, et al., 2009), where Ti_3O_5 and Al_2TiO_5 sublattice occupancies in the M_2TiO_5 type pseudobrookite solid solution can be presented in four formations: $\left(Ti^{3+}_{\frac{4}{3}}Ti^{4+}_{\frac{2}{3}}\right)\left(Ti^{3+}_{\frac{2}{3}}Ti^{4+}_{\frac{1}{3}}\right)O_5$, $\left(Al^{3+}_{\frac{4}{3}}Ti^{4+}_{\frac{2}{3}}\right)\left(Al^{3+}_{\frac{2}{3}}Ti^{4+}_{\frac{1}{3}}\right)O_5$, $\left(Ti^{3+}_{\frac{4}{3}}Ti^{4+}_{\frac{2}{3}}\right)\left(Al^{3+}_{\frac{2}{3}}Ti^{4+}_{\frac{1}{3}}\right)O_5$ and $\left(Al^{3+}_{\frac{4}{3}}Ti^{4+}_{\frac{2}{3}}\right)\left(Ti^{3+}_{\frac{2}{3}}Ti^{4+}_{\frac{1}{3}}\right)O_5$. The solution can thus be presented as $\left[(Ti^{3+},Al^{3+})_{\frac{4}{3}}Ti^{4+}_{\frac{2}{3}}\right]\left[(Ti^{3+},Al^{3+})_{\frac{2}{3}}Ti^{4+}_{\frac{1}{3}}\right]O_5$, with an assumption that the ions are randomly mixing on each sublattice. The endmembers involved in the solution are: two real compounds Ti_3O_5 and Al_2TiO_5, and seven pseudocomponents $Ti_3O_5^-$, $AlTi_2O_5^-$, $Al_2TiO_5^-$, $Al_3O_5^-$, $Ti_3O_5^+$, $AlTi_2O_5^+$, and $Ti_3O_5^{2+}$. The molar Gibbs energy of the solution would take the form presented in Equation [4.15], with $(A,B)_a(C,D)_c$ solution used as a case demonstration (Hillert, 2001; Shi, et al., 1992).

$$G_m = y'_A y''_C G^0_{A:C} + y'_A y''_D G^0_{A:D} + y'_B y''_C G^0_{B:C} + y'_B y''_D G^0_{B:D} + RT[a(y'_A \ln(y'_A) + y'_B \ln(y'_B)) + c(y''_C \ln(y''_C) + y''_D \ln(y''_D)) + G^E] \quad [4.15]$$

Where R is the gas constant; a and c are site ratios for the first and second sublattices; y'_i and y''_j are site fractions on first and second sublattices; and G^0_{ij} is the standard Gibbs free energy of the endmember of the solution. As in section 4.3.1.2, G^E in Equation [4.15] was approximated to be zero. The main parameters of the model were then the endmember Gibbs energies. The Gibbs energies of the four possible combinations in the Ti_3O_5-Al_2TiO_5 solid solution are presented in Equations [4.16] to [4.19]. The overall Gibbs energy of the solution is thus given by Equation [4.20].

$$G_{solution1} = \frac{8}{9}G^0_{Ti_3O_5^-} + \frac{4}{9}G^0_{Ti_3O_5} + \frac{4}{9}G^0_{Ti_3O_5^+} + \frac{2}{9}G^0_{Ti_3O_5^{2+}} + 2RT\left[\frac{4}{3}ln\left(\frac{4}{3}\right) + \frac{2}{3}ln\left(\frac{2}{3}\right)\right] + RT\left[\frac{2}{3}ln\left(\frac{2}{3}\right) + \frac{1}{3}ln\left(\frac{1}{3}\right)\right] \quad [4.16]$$

$$G_{solution2} = \frac{8}{9}G^0_{Al_3O_5^-} + \frac{4}{9}G^0_{Al_2TiO_5} + \frac{4}{9}G^0_{AlTi_2O_5^+} + \frac{2}{9}G^0_{Ti_3O_5^{2+}} + 2RT\left[\frac{4}{3}ln\left(\frac{4}{3}\right) + \frac{2}{3}ln\left(\frac{2}{3}\right)\right] + RT\left[\frac{2}{3}ln\left(\frac{2}{3}\right) + \frac{1}{3}ln\left(\frac{1}{3}\right)\right] \quad [4.17]$$

$$G_{solution3} = \frac{8}{9}G^0_{AlTi_2O_5^-} + \frac{4}{9}G^0_{Ti_3O_5} + \frac{4}{9}G^0_{AlTi_2O_5^+} + \frac{2}{9}G^0_{Ti_3O_5^{2+}} + 2RT\left[\frac{4}{3}ln\left(\frac{4}{3}\right) + \frac{2}{3}ln\left(\frac{2}{3}\right)\right] + RT\left[\frac{2}{3}ln\left(\frac{2}{3}\right) + \frac{1}{3}ln\left(\frac{1}{3}\right)\right] \quad [4.18]$$

$$G_{solution3} = \frac{8}{9}G^0_{Al_2TiO_5^-} + \frac{4}{9}G^0_{Al_2TiO_5} + \frac{4}{9}G^0_{Ti_3O_5^+} + \frac{2}{9}G^0_{Ti_3O_5^{2+}} + 2RT\left[\frac{4}{3}ln\left(\frac{4}{3}\right) + \frac{2}{3}ln\left(\frac{2}{3}\right)\right] + RT\left[\frac{2}{3}ln\left(\frac{2}{3}\right) + \frac{1}{3}ln\left(\frac{1}{3}\right)\right] \quad [4.19]$$

$$G = G_{solution1} + G_{solution2} + G_{solution3} + G_{solution4} \quad [4.20]$$

$G^0_{Ti_3O_5}$ and $G^0_{Al_2TiO_5}$ for the real components are obtained from Table 11. From previous studies (Ericksson, et al., 1996; Pelton, et al., 1998), it can be accepted that the pure Ti_3O_5 compound is composed of an equimolar mixture of $Ti_3O_5^-$ and $Ti_3O_5^+$. The pure Al_2TiO_5 compound is also assumed to be an ideal equimolar mixture of $Al_3O_5^-$ and $AlTi_2O_5^+$. The Gibbs energies of Ti_3O_5 and Al_2TiO_5 are thus expressed as shown in Equation [4.21] and [4.22], respectively.

$$G^0_{Ti_3O_5} = \frac{1}{2}\left(G^0_{Ti_3O_5^-} + G^0_{Ti_3O_5^+}\right) + 2RT\ln\left(\frac{1}{2}\right) \quad [4.21]$$

$$G^0_{Al_2TiO_5} = \frac{1}{2}\left(G^0_{Al_3O_5^-} + G^0_{AlTi_2O_5^+}\right) + 2RT\ln\left(\frac{1}{2}\right) \quad [4.22]$$

To facilitate the description of all Gibbs energy of the endmembers in the solid solution, $G^0_{Ti_3O_5^-}$ was set to be equal to $G^0_{Ti_3O_5^+}$, while $G^0_{Al_3O_5^-}$ was set to equal to $G^0_{AlTi_2O_5^+}$. The endmembers in the solid solution are further related by the exchange reactions involved in $\left(Ti^{3+}_{\frac{4}{3}}Ti^{4+}_{\frac{2}{3}}\right)\left(Ti^{3+}_{\frac{2}{3}}Ti^{4+}_{\frac{1}{3}}\right)O_5$, $\left(Al^{3+}_{\frac{4}{3}}Ti^{4+}_{\frac{2}{3}}\right)\left(Al^{3+}_{\frac{2}{3}}Ti^{4+}_{\frac{1}{3}}\right)O_5$, $\left(Ti^{3+}_{\frac{4}{3}}Ti^{4+}_{\frac{2}{3}}\right)\left(Al^{3+}_{\frac{2}{3}}Ti^{4+}_{\frac{1}{3}}\right)O_5$ and $\left(Al^{3+}_{\frac{4}{3}}Ti^{4+}_{\frac{2}{3}}\right)\left(Ti^{3+}_{\frac{2}{3}}Ti^{4+}_{\frac{1}{3}}\right)O_5$, as shown in Equations [4.23] to [4.26]. The Gibbs energies of the respective reciprocal reactions are described in Equation [4.27] and [4.2].

$$(Ti^{3+}_2)_A(Ti^{4+})_BO_5 + (Ti^{4+}_2)_A(Ti^{3+})_BO_5^+ = (Ti^{3+}_2)_A(Ti^{3+})_BO_5^- + (Ti^{4+}_2)_A(Ti^{4+})_BO_5^{2+} \quad [4.23]$$

$$(Al^{3+}_2)_A(Ti^{4+})_BO_5 + (Ti^{4+}_2)_A(Al^{3+})_BO_5^+ = (Al^{3+}_2)_A(Al^{3+})_BO_5^- + (Ti^{4+}_2)_A(Ti^{4+})_BO_5^{2+} \quad [4.24]$$

$$(Ti^{3+}_2)_A(Ti^{4+})_BO_5 + (Ti^{4+}_2)_A(Al^{3+})_BO_5^+ = (Ti^{3+}_2)_A(Al^{3+})_BO_5^- + (Ti^{4+}_2)_A(Ti^{4+})_BO_5^{2+} \quad [4.25]$$

$$(Al^{3+}_2)_A(Ti^{4+})_BO_5 + (Ti^{4+}_2)_A(Ti^{3+})_BO_5^+ = (Al^{3+}_2)_A(Ti^{3+})_BO_5^- + (Ti^{4+}_2)_A(Ti^{4+})_BO_5^{2+} \quad [4.26]$$

$$\Delta G_1 = G^0_{Ti_3O_5^-} + G^0_{Ti_3O_5^{2+}} - G^0_{Ti_3O_5^+} - G^0_{Ti_3O_5} \quad [4.27]$$

$$\Delta G_2 = G^0_{Al_3O_5^-} + G^0_{Ti_3O_5^{2+}} - G^0_{AlTi_2O_5^+} - G^0_{Al_2TiO_5} \quad [4.28]$$

$$\Delta G_3 = G^0_{AlTi_2O_5^-} + G^0_{Ti_3O_5^{2+}} - G^0_{AlTi_2O_5^+} - G^0_{Ti_3O_5} \quad [4.29]$$

$$\Delta G_4 = G^0_{Al_2TiO_5^-} + G^0_{Ti_3O_5^{2+}} - G^0_{Ti_3O_5^+} - G^0_{Al_2TiO_5} \quad [4.30]$$

ΔG represents the Gibbs energy change for each reciprocal reaction. Since the Ti_3O_5-Al_2TiO_5 solid solution is primarily composed of stoichiometric compounds, ΔG was assumed to be zero in the current work as it was the case in previous studies of the pseudobrookite solid solution (Kang, et al., 2006). Considering the assumption stated above that $G^0_{Ti_3O_5^-} = G^0_{Ti_3O_5^+}$ and $G^0_{Al_3O_5^-} = G^0_{AlTi_2O_5^+}$, it appears that $G^0_{Ti_3O_5^{2+}}$ can be approximated by either $G^0_{Ti_3O_5}$ and $G^0_{Al_2TiO_5}$ for the respective reactions. In the current study, $G^0_{Ti_3O_5^{2+}}$ was thus

approximated by $\frac{1}{2}(G^0_{Ti_3O_5} + G^0_{Al_2TiO_5})$ to allow for the determination of the Gibbs energy of other endmembers. The Gibbs energy expressions for all endmembers involved in the Ti_3O_5-Al_2TiO_5 solid solution were established by simultaneous solution of Equations [4.16] to [4.22] and [4.27] to [4.30]. These Gibbs energies of the respective endmembers are included in Table 11.

4.3.1.5 Ternary thermodynamic database for $MgTi_2O_5$-Ti_3O_5-Al_2TiO_5 solid solution

The binary systems described in the above subsections were combined and extended to develop the multicomponent $MgTi_2O_5$-Ti_3O_5-Al_2TiO_5 solid solution database for incorporation into FactSage software. The extension procedure followed the sublattice modelling principles in the form of compound energy formalism (CEF), as used by previous researchers to model the customary pseudobrookite solid solution in FactSage software (Bale, et al., 2002; Pelton, et al., 1998).

During the development of the private database for the pseudobrookite solid solution with $MgTi_2O_5$, Ti_3O_5, and Al_2TiO_5 as endmembers, it was assumed that the solution is composed of three sublattices: the anionic sublattice constructed by the O^{2-} and the two cation sublattices corresponding to the non-equivalent 4c and 8f positions in the octahedral structure (Bale, et al., 2002; Pelton, et al., 1998; Buscaglia, et al., 1996). Following the assumptions adopted in the case of binary pseudobrookite structures described in the above sections, the sublattice occupancy of the multicomponent solution can be presented as $(Mg^{2+}Ti^{3+}Al^{3+}Ti^{4+})_A(Ti^{4+}, Ti^{3+}, Al^{3+})_B O_5$. The Gibbs energies of the endmembers and the solution were described to allow for the calculation of conditions for multiphase and multicomponent phase equilibria by means of Gibbs energy minimization software of FactSage. The developed private $MgTi_2O_5$-Ti_3O_5-Al_2TiO_5 solid solution database in FactSage was allocated a standard four-letter abbreviation of 'PSE1' with the full name of the database being Al-pseudobrookite to indicate the inclusion of Al_2TiO_5 endmember in the pseudobrookite solid solution.

The private PSE1 solid solution and other databases, as described in the following sections, were used to calculate the equilibrium conditions and phase diagrams for the Ca-Mg-Al-Si-Ti-O system applicable to titaniferous slags in air and under low oxygen partial pressure (pO_2) conditions attained during the titanomagnetite smelting operation. The calculated equilibrium conditions were compared with measurements from the experiments conducted

for the Ca-Mg-Al-Si-Ti-O system in air and at low pO_2 conditions applicable to titanomagnetite smelting.

4.3.1.6 Assessment of the private thermodynamic database

The private PSE1 database in FactSage was assessed by comparison with the FactSage customary pseudobrookite database, i.e. 'PSEU'. The comparison entailed the calculations of the phase equilibria on sections of the Mg-Ti-O system which are covered by both databases in terms of the pseudobrookite-type phase crystallisation. For the calculations, either PSE1 or PSEU, i.e. pseudobrookite or Al-pseudobrookite database was selected together with other appropriate databases to cover these phase equilibria in the sections of the Mg-Ti-O system. The additional databases that were selected from the FT oxide bank of databases included SlagA for liquid slag of all oxides, MeO_A for monoxide species, TiO_2 for rutile, ILMEA for ilmenite, and TiSp for titania spinel.

The binary equilibrium phase diagrams of the MgO-TiO_2 system were calculated in air using the FactSage customary PSEU and private PSE1 databases as shown in Figure 38 and Figure 39, respectively. The calculated phase equilibria were also compared with the MgO-TiO_2 data available in literature (Shindo, 1980; Rouf, et al., 1969; Woermann, et al., 1969; Massazza & Sirchia, 1958), which is shown in a binary phase diagram in Figure 12 (Woermann, et al., 1969). The calculated and literature phase equilibria data sets are fairly comparable particularly in terms of the crystallisation of the pseudobrookite solid solution.

The literature (Woermann, et al., 1969) and calculated equilibrium phase diagrams for the MgO-TiO_2 system, i.e. Figure 12, Figure 38 and Figure 39 show two different eutectic temperatures with the subsequent solid containing pseudobrookite as one of the eutectic phases. These data sets predict that at the first eutectic temperature of 1620°C ±5°C in a composition with a mole fraction of TiO_2 of 0.58±0.05, pseudobrookite and ilmenite would crystallise as the eutectic phases in the solid product. At the second eutectic temperature of 1640°C ±20°C in a composition with a mole fraction of TiO_2 of about 0.76, the eutectic phases in the solid would be pseudobrookite and rutile. Between the two eutectic temperatures and compositions at a composition with TiO_2 mole fraction of 0.66, karrooite or $MgTi_2O_5$ is identified by the vertical line as the pseudobrookite type phase that is formed from 1 mol of MgO and 2 moles of TiO_2, i.e. according to the mole fractions of TiO_2 and

MgO. Moreover, the calculated values and literature confirm that the $MgTi_2O_5$ has a congruent melting point of about 1660°C.

These results suggest that both the FactSage customary PSEU and private PSE1 databases are comparable to the literature data (Shindo, 1980; Rouf, et al., 1969; Woermann, et al., 1969; Massazza & Sirchia, 1958). The observation was thus accepted as a validation of the competency of the private PSE1 database for the calculation of phase equilibria in air.

The efficiency of the private PSE1 database was assessed further in a ternary MgO-Al_2O_3-TiO_2 system. This assessment allowed for the investigation of the effect of Al_2O_3 on the MgO-TiO_2 system. For this assessment, polythermal projections for the MgO-Al_2O_3-TiO_2 system were calculated using FactSage equipped with the private PSE1 databases. In this context, the polythermal projection is used as a representation of the ternary liquidus surface with all the invariant points of respective compositions and temperatures shown on the liquidus surface. The polythermal projections for the MgO-Al_2O_3-TiO_2 system calculated in the current study are depicted in Figure 40. The calculated liquidus projections using PSE1 databases for the Al_2O_3-MgO-TiO_2 system were evaluated against recent literature data studies (Ilatovskaia & Fabrichnaya, 2019; Ilatovskaia, et al., 2018; Boden & Glasser, 1973). The calculated liquidus surface reported by Ilatovskaia (2019) is shown in Figure 41. The temperatures and compositions of invariant points in the Al_2O_3-MgO-TiO_2 system produced in the current study and available literature are summarised in Table 12 (Ilatovskaia & Fabrichnaya, 2019; Ilatovskaia, et al., 2018; Boden & Glasser, 1973).

There was a general agreement between the calculated data in the current work and the literature data. However, on the transitional invariant point, the calculated temperature in the current study was more than 100 K lower than the literature data (there is also a variation of about 60°C between the data in the literature). This temperature difference corresponded with a difference in the compositions of invariant reactions. Considering that the private PSE1 database is preliminary in nature and requires further validation with experimental data, the comparison between the data generated in the current work was considered to be within an acceptable range. Hence, the private PSE1 database was accepted to be competent for calculations of phase relations in a high order Ca-Mg-Al-Si-Ti-O system applicable to titaniferous slags. The calculated higher order phase equilibria would, in any case, be reviewed and validated using experimental data.

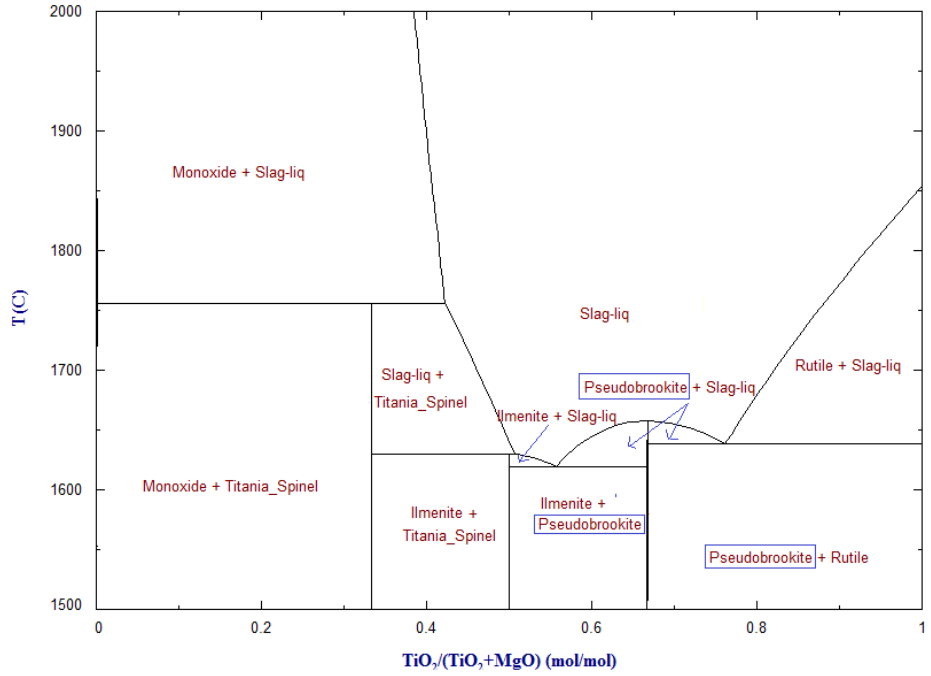

Figure 38: Calculated MgO-TiO_2 system with the selection of the FactSage customary PSEU database

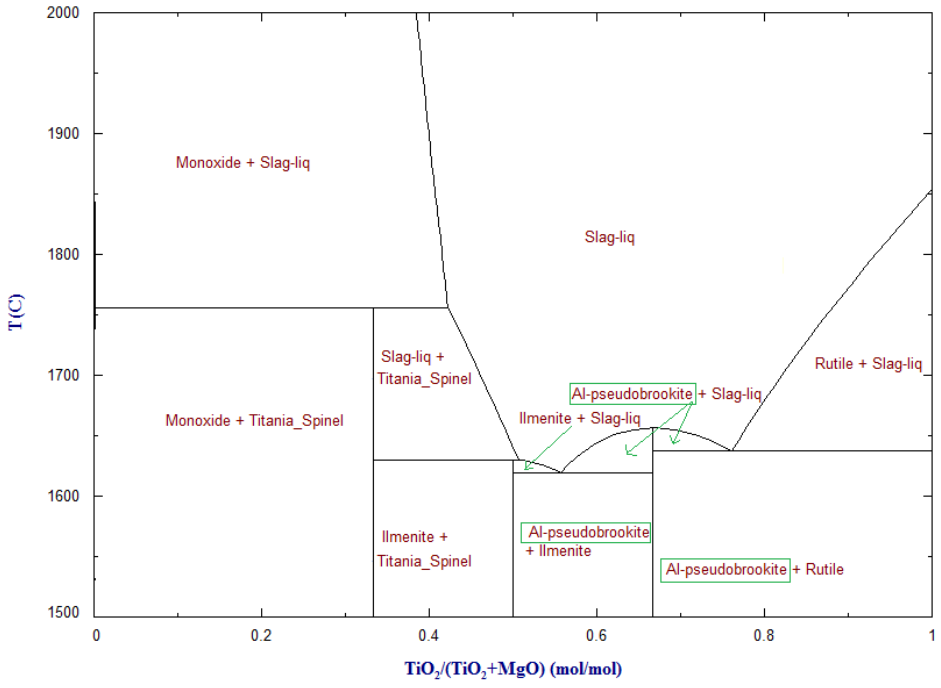

Figure 39: Calculated MgO-TiO_2 system with the selection of the private PSE1 database developed in the current work

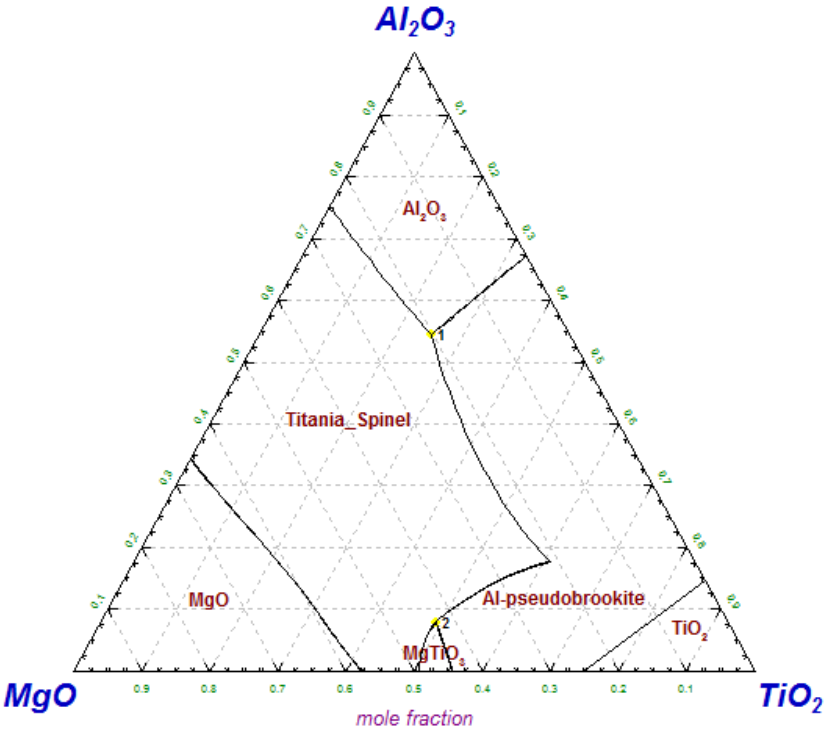

Figure 40: Calculated polythermal projections in the MgO-Al_2O_3-TiO_2 system using a private PSE1 database developed in the current work

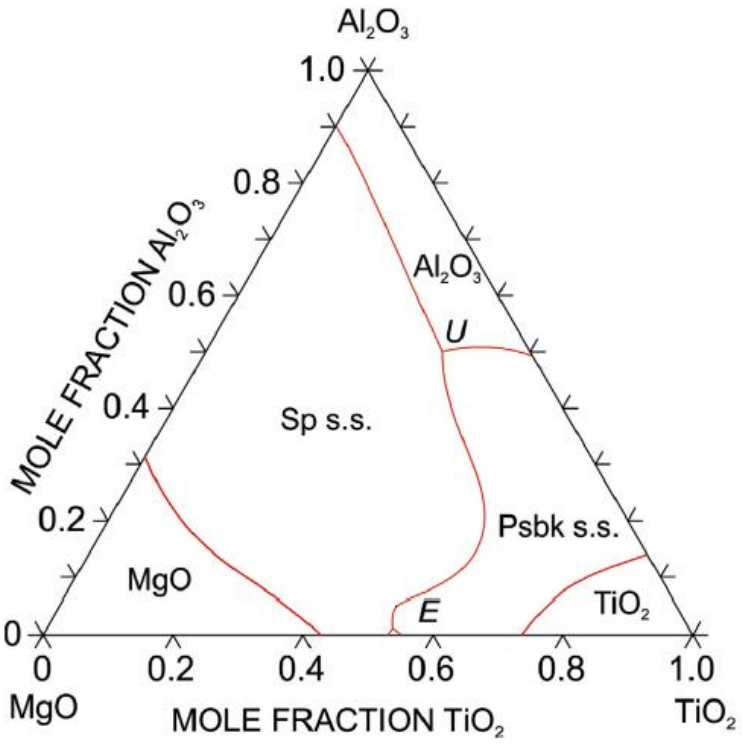

Figure 41: Polythermal projections in the MgO-Al_2O_3-TiO_2 system as presented in recent studies (Ilatovskaia & Fabrichnaya, 2019)

Table 12: Summary of the parameters of invariant points in the MgO-Al_2O_3-TiO_2 system

Temperature, K	Type	Composition (mol%)			Reference
		Al_2O	MgO	TiO_2	
Liquid ↔ $MgTiO_3$ + pseudobrookite ss + spinel ss					
1843	Eutectic	9.31	47.11	43.58	(Boden & Glasser, 1973)
1875		3.68	42.64	53.68	(Ilatovskaia, et al., 2018)
1893		1.36	45.43	53.21	(Ilatovskaia & Fabrichnaya, 2019)
1831		7.82	42.88	49.30	Current studies
Liquid + Al_2O_3 ↔ pseudobrookite ss + spinel ss					
2006	Transitional	-	-	-	(Boden & Glasser, 1973)
2065		50.08	13.50	36.42	(Ilatovskaia & Fabrichnaya, 2019)
1907		54.40	20.28	25.31	Current studies

ss: solid solution; - not specified

4.3.2 Calculation of phase equilibria in air

4.3.2.1 Methodology

The FactSage thermochemical software equipped with the private Al-pseudobrookite (PSE1) database for the $MgTi_2O_5$-Ti_3O_5-Al_2TiO_5 system was used to calculate the phase equilibria in air in the same compositional range as used by Jochens (1967). The phase equilibria calculations were conducted using the FactSage customary search databases, i.e. FactPS for pure substances and FToxid for oxide species, as well as the private PSE1 database developed in the current study as described in section 4.3.1. The equilibrium phase relations in air for the Ca-Mg-Al-Si-Ti-O system applicable to the titaniferous slags were calculated, and the results were processed using the 'Phase Diagram' and 'Equilib' modules of the FactSage software.

4.3.2.2 Results and discussions

As the first task of the current work, FactSage was employed to re-draw Jochens' phase diagram for titaniferous slags. The calculated equilibrium phase diagram is shown in Figure 42. This phase diagram shows that the liquidus temperatures of the titaniferous slags change from about 1540°C in a composition with 30wt% CaO and 0wt% MgO, to about 1480°C in a composition with 0wt% CaO and 30wt% MgO, passing through a minimum liquidus temperature of about 1305°C in a composition with 20wt% CaO and 10wt% MgO. The

calculated phase diagram in air suggests that the detrimental spinel solid solution will crystallise in the reviewed titaniferous slag compositions when the MgO concentration is 2.6wt% or more.

The calculated liquidus surface was compared with the experimentally obtained liquidus surfaces reported by Jochens (1967) and Holmes et al. (1968). Figure 43 shows a summary of the comparison between the calculated and experimental liquidus surface and phase equilibria. It appears that the liquidus surface predicted by Holmes et al. (1968) is generally higher than those of Jochens (1967) and current FactSage calculation. In terms of compositions, the slags of the compared systems are similar; hence, the composition is not anticipated to be the reason behind the significant difference of the reported liquidus surface by Holmes et al. (1968) from the other liquidus surfaces. The departure of the Holmes et al. data from the other data sets is more significant between the CaO: MgO ratios of 20:10 and 15:15. The variability of the results was attributed to a possible difference in the experimental conditions as one study could have been completed in a closed system with no air circulation, in which case the partial pressure of oxygen (pO_2) would be lower than that of air (Schultz, et al., 2013), whereas the other experiment could have been completed in a continuous flow of air. The actual experimental set up is not clear in the two studies.

Nevertheless, the liquidus surfaces on Jochens' (1967) and the calculated phase diagrams are fairly comparable as shown in Figure 43. The noticeable difference is that in Jochens' phase diagram the minimum liquidus temperature is at about 1340°C in a composition with 18wt% CaO and 12wt% MgO, whereas in the calculated phase diagram it is at about 1305°C in a composition with 20wt% CaO and 10wt% MgO. These results will be reviewed further in section 4.4.5.4 in conjunction with the experimental data of the current study.

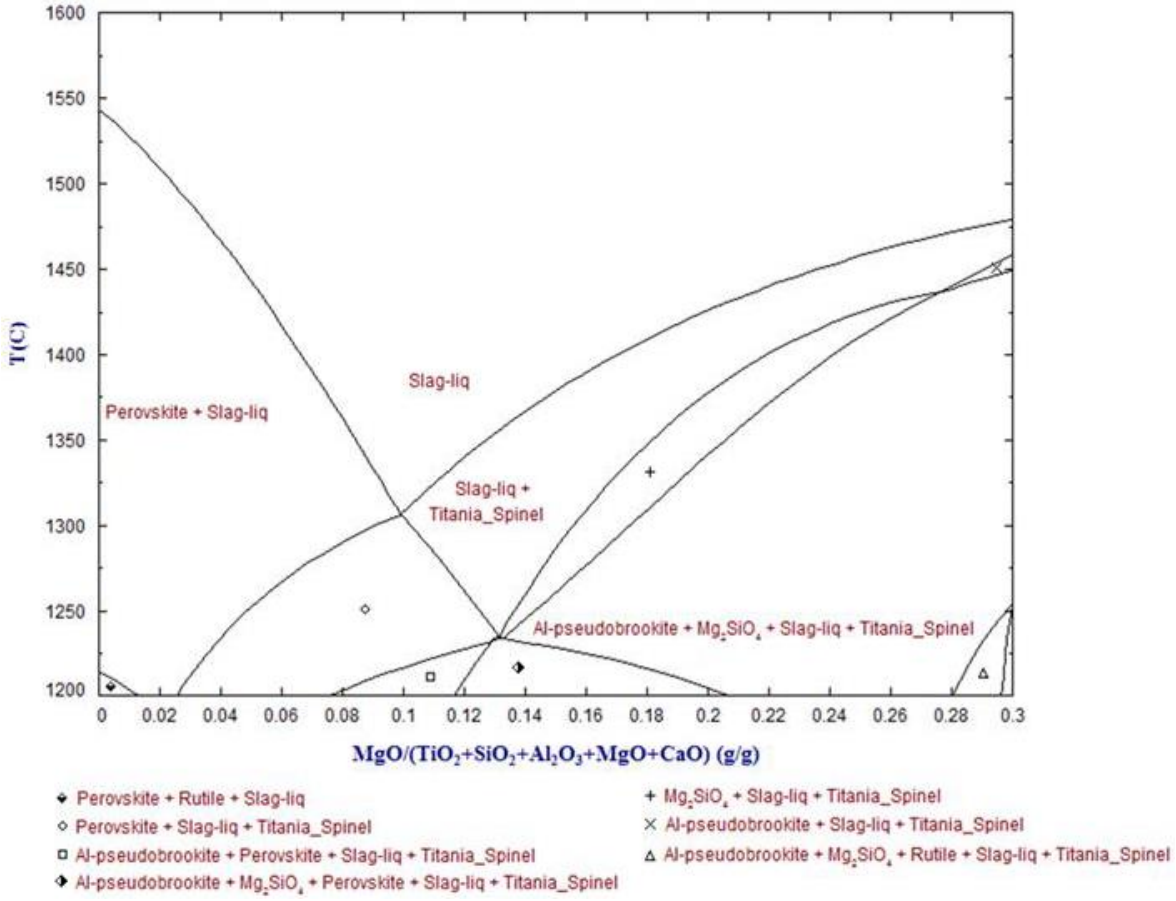

Figure 42: Calculated equilibrium phase diagram at pO_2 = 0.21 atm for the slag system: TiO_2 = 37.19wt%, SiO_2 = 19.69wt%, and Al_2O_3 = 13.12wt%, at varying proportions of CaO (30-0wt%) and MgO (0-30wt%)

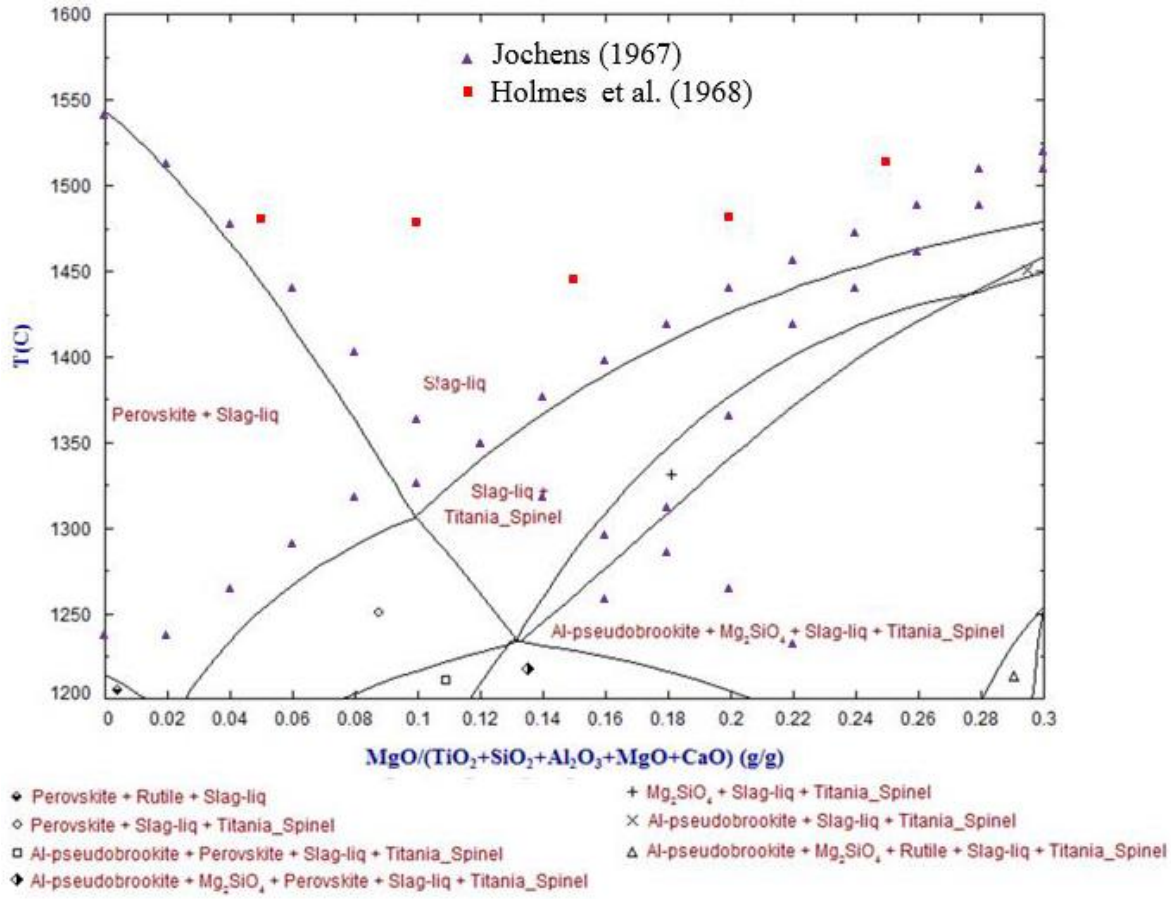

Figure 43: Phase equilibria in the system TiO_2 = 37.19wt%, SiO_2 = 19.69wt%, and Al_2O_3 = 13.12wt%, at varying proportions of CaO (30-0wt%) and MgO (0-30wt%) produced in air: comparison of phase equilibria from calculation using FactSage, and Jochens' and Holmes' experimental work.

In terms of the phase equilibria, it appears that both Jochens' and the calculated phase diagrams predict that at high CaO levels before the minimum liquidus points, $CaO.TiO_2$ (perovskite) crystallises as the primary phase. There is however a difference in the prediction of the crystallisation of the primary phase at high MgO contents above the liquidus point: Jochens' phase diagram predicts the crystallisation of the pseudobrookite solid solution, i.e. $MgTi_2O_5$-Al_2TiO_5, whereas the FactSage calculation suggests that at higher MgO levels the primary phase is a titania spinel, i.e. a spinel solid solution of $Mg(Al,Ti)_2O_4$. According to Jochens' phase diagram, the secondary phase after the primary $MgTi_2O_5$-Al_2TiO_5 solid solution is an olivine, i.e. forsterite (Mg_2SiO_4). However, FactSage calculation predicts that the secondary phase to the primary $Mg(Al,Ti)_2O_4$ phase can either be Mg_2SiO_4 or $MgTi_2O_5$-Al_2TiO_5 depending on the ratio of MgO to CaO – for example,

Mg_2SiO_4 is generally the secondary phase except at MgO concentration of 27wt% and above in the reviewed compositional range where $MgTi_2O_5$-Al_2TiO_5 is the secondary phase. At higher MgO concentrations, the FactSage calculation predicts a big phase region where equilibrium exists between four phases, namely; liquid slag, $Mg(Al,Ti)_2O_4$; Mg_2SiO_4; and $MgTi_2O_5$-Al_2TiO_5.

It should be noted that Jochens' phase diagram does not predict the crystallisation of the spinel solid solution, i.e. $Mg(Al,Ti,V)_2O_4$ (Jochens, 1967; Jochens, et al., 1969; McRae, et al., 1969). Though Jochens in his PhD studies observed some X-Ray diffraction patterns corresponding to those of the spinel, the crystallisation of the spinel was rejected because the suspected patterns were faint and overlapped with those of the confirmed pseudobrookite solution. Pistorius (2011) noted that titaniferous slags typically contain spinel solid solution [$Mg(Al,Ti,V)_2O_4$] as one of the phases. In addition, the crystallisation of the spinel structure at high MgO concentrations in Al_2O_3 bearing matrices in air is reported in other literature (Berezhnoi & Gulko, 1955). Thus, the thermochemical calculation provides more realistic phase equilibria in terms of the spinel crystallisation in the Ca-Mg-Al-Si-Ti-O system in air.

The phase equilibria are further reviewed using the results of experimental investigations conducted in the current study and reported in section 4.4.5.4.

4.3.3 Calculation of phase equilibria at pO_2 conditions applicable to titanomagnetite smelting

4.3.3.1 Methodology

The calculations of phase relations in the Ca-Mg-Al-Si-Ti-O system applicable to titaniferous slags in terms of compositions and pO_2 were conducted using FactSage equipped with its customary search databases, i.e. FactPS database for pure solids and oxides database FToxid, as well as a private PSE1 database for the $MgTi_2O_5$- Ti_3O_5-Al_2TiO_5 solution, which was developed in the current study as described in section 4.3.1. The phase equilibria and thermodynamic data relating to the titaniferous slags were plotted using the 'Phase Diagram' and 'Equilib' modules of the FactSage software.

4.3.3.2 Results and discussions

Effect of pO_2 on liquidus surface and phase equilibria

The effect of pO_2 on the liquidus surface of titaniferous slags was investigated across the compositional range investigated by Jochens (1967). Figure 44 shows liquidus temperature plotted as a function of CaO/ MgO ratio at varying pO_2 levels. The results show that the liquidus surface in the Ca-Mg-Al-Si-Ti-O system with the composition applicable to a fluxed titaniferous slag increases with decreasing the pO_2. This observation concurs with the findings of Nityanand and Fine (1983) who studied the effect of TiO_2 additions and pO_2 on liquidus temperatures of some $CaO\text{-}Al_2O_3$ melts, and found that at low pO_2 and high TiO_2 contents there is a continuous increase of the liquidus temperatures. Decreasing the pO_2 to 10^{-14} atm resulted in the shift of the minimum liquidus composition from a CaO: MgO ratio of 20:10 to 18:12. However, at pO_2 of 10^{-16} atm, FactSage predicts that the minimum liquidus composition goes back to a CaO: MgO ratio of 20:10. Decreasing the pO_2 beyond 10^{-16} atm resulted in a shift of the minimum liquidus temperature from a composition with a CaO: MgO ratio of 20:10 towards 22:8.

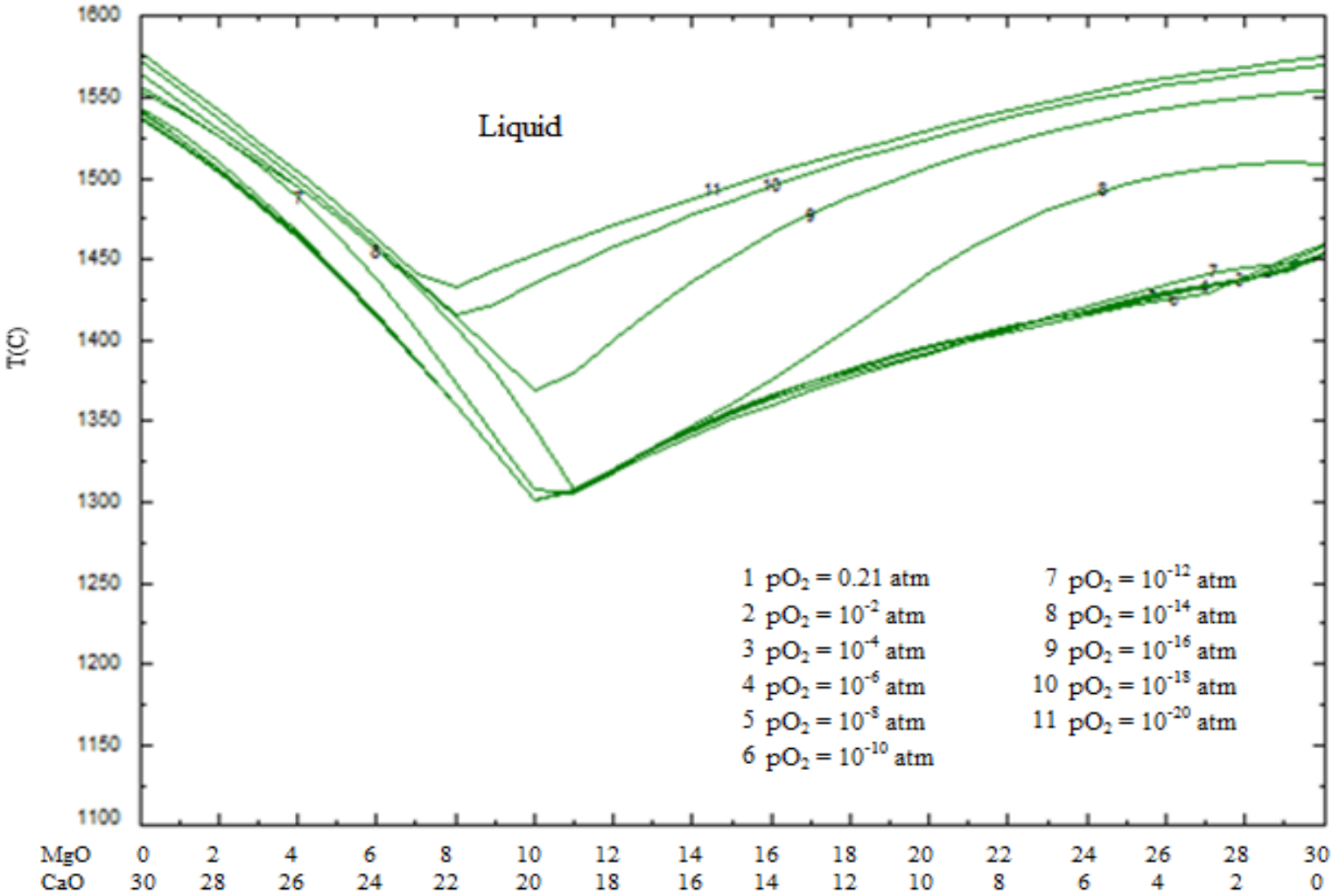

Figure 44: Effect of pO_2 on the liquidus surface of the titaniferous slag of the composition: TiO_2 = 37.19wt%, SiO_2 = 19.69wt% and Al_2O_3 = 13.12wt%, with varying proportions of CaO (30-0wt%) and MgO (0-30wt%)

The effect of pO_2 was investigated further on the dolomite fluxed titaniferous slag composition, which was employed by the defunct EHSV operation. Figure 45 shows the change of liquidus temperatures as a function of pO_2 at fixed composition of the slag: TiO_2 = 37.19wt%, SiO_2 = 19.69wt%, and Al_2O_3 = 13.12wt%, MgO = 14wt% and CaO = 16wt%. The results on the figure show that the spinel solid solution $[Mg(Al,Ti)_2O_4]$ generally crystalizes as a primary phase throughout the reviewed pO_2 range, with Al-pseudobrookite and perovskite crystallizing as secondary or ternary phases depending on the pO_2.

Oxidized titanium species, i.e. Ti^{4+}, is readily reduced to lower oxidation state titanium species when subjected to reducing and high temperature conditions as relevant in the ironmaking process (Zhao, et al., 2009). The reduction of the Ti^{4+} has the potential of affecting the phase equilibria. The effect of pO_2 on the phase equilibria was therefore simulated by monitoring the reduction of titanium species – the assessment was conducted by monitoring the Ti^{3+}/ Ti^{4+} mass fraction ratio with variations of the pO_2. Figure 46 shows Ti^{3+}/ Ti^{4+} mass fraction ratio plotted as a function of pO_2 in the range of 0.21 to 10^{-16} atm. The results in the figure show an increase in Ti^{3+}/ Ti^{4+} mass fraction ratio with decreasing pO_2. This implies that by decreasing the pO_2 to the range applicable in titanomagnetite smelting, the phase equilibria of the slag would deviate from the phase equilibria that were determined in air by Jochens (1967).

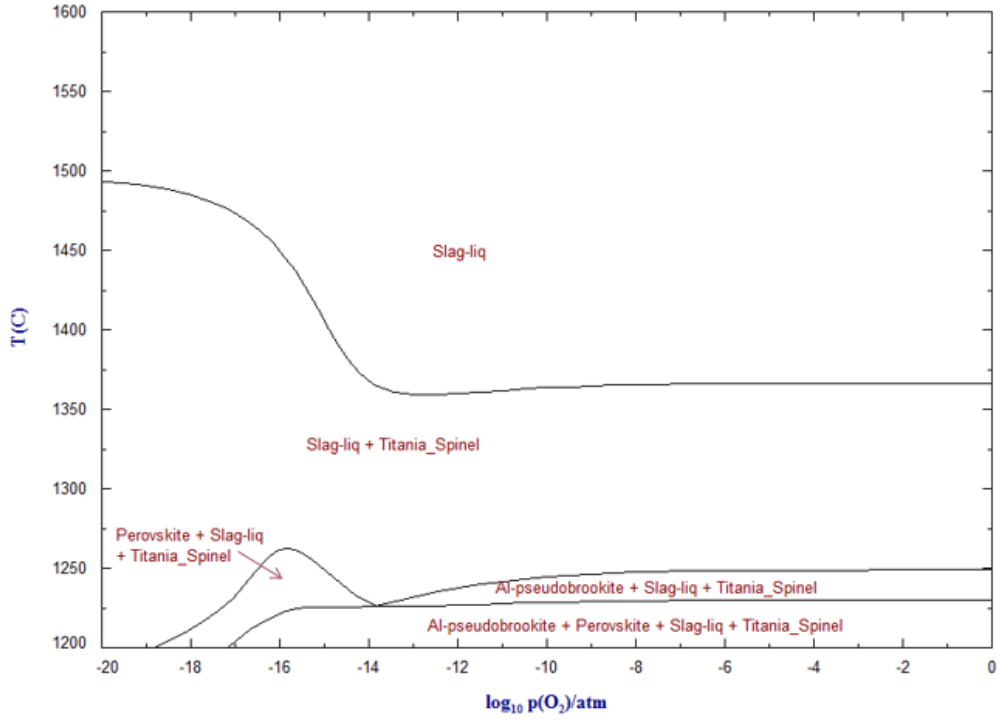

Figure 45: Effect of pO_2 on the liquidus surface and phase equilibria of the dolomite fluxed titaniferous slag with the composition: TiO_2 = 37.19wt%, SiO_2 = 19.69wt%, and Al_2O_3 = 13.12wt%, MgO = 14wt% and CaO = 16wt%

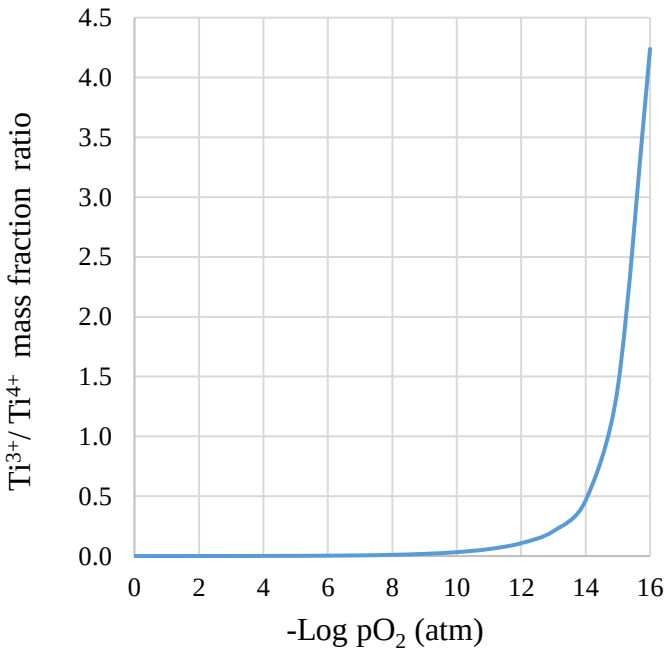

Figure 46: Effect of pO_2 on the titanium reduction in the dolomite fluxed titaniferous slag with the composition: TiO_2 = 37.19wt%, SiO_2 = 19.69wt%, and Al_2O_3 = 13.12wt%, MgO = 14wt% and CaO = 16wt%

Calculated equilibrium phase diagrams for titaniferous slags

Figure 47 to Figure 50 were calculated at respective pO_2 of 10^{-10} to 10^{-16} atm using FactSage thermochemical software equipped with the private PSE1 databases for predicting phase equilibria of fluxed titaniferous slags that conform to a typical composition: 37.19wt% TiO_2, 19.69wt% SiO_2, 13.12wt% Al_2O_3, and 30.00wt% of various ratios of CaO+MgO. The liquidus surfaces in these figures show that, as also reported above, the liquidus temperature increases with decreasing pO_2.

The calculated equilibrium phase diagram at 10^{-16} atm in Figure 50 shows that the liquidus temperatures of the titaniferous slags with extreme compositions in terms of CaO: MgO ratio, i.e. compositions with CaO: MgO ratios of 30:0 and 0:30, are similar at about 1570°C. The liquidus surface passes through a minimum of 1370°C in a composition with 20wt% CaO and 10wt% MgO.

In terms of phase equilibria, there is no significant difference between those produced at 10^{-10} to 10^{-16} atm. In general, the phase equilibria show that at high CaO levels before the minimum liquidus point, the primary phase is perovskite ($CaTiO_3$), whereas at high MgO levels after the minimum liquids point, the primary phase is a spinel solid solution, i.e. $Mg(Al,Ti)_2O_4$. In comparison with the calculated and Jochens' phase equilibria in air, the calculated phase equilibria at low pO_2 of 10^{-16} atm show that perovskite and $Mg(Al,Ti)_2O_4$ primary phases crystallise at higher temperatures. This was attributed to the reduction of Ti^{4+} to Ti^{3+}. Moreover, the calculated phase equilibria at pO_2 of 10^{-16} atm show that the detrimental $Mg(Al,Ti)_2O_4$ phase will crystallise in the reviewed titaniferous slag compositions for as long as the MgO concentration is 2wt% or more. At lower MgO concentrations than 2wt%, the pseudobrookite solid solution is host to MgO. These results show that the probability of the crystallisation of the $Mg(Al,Ti)_2O_4$ phase increases with decreasing the pO_2.

The calculated phase equilibria at pO_2 of 10^{-16} atm were evaluated further in section 4.4.5.5 using equilibration-quench-EPMA analysis results.

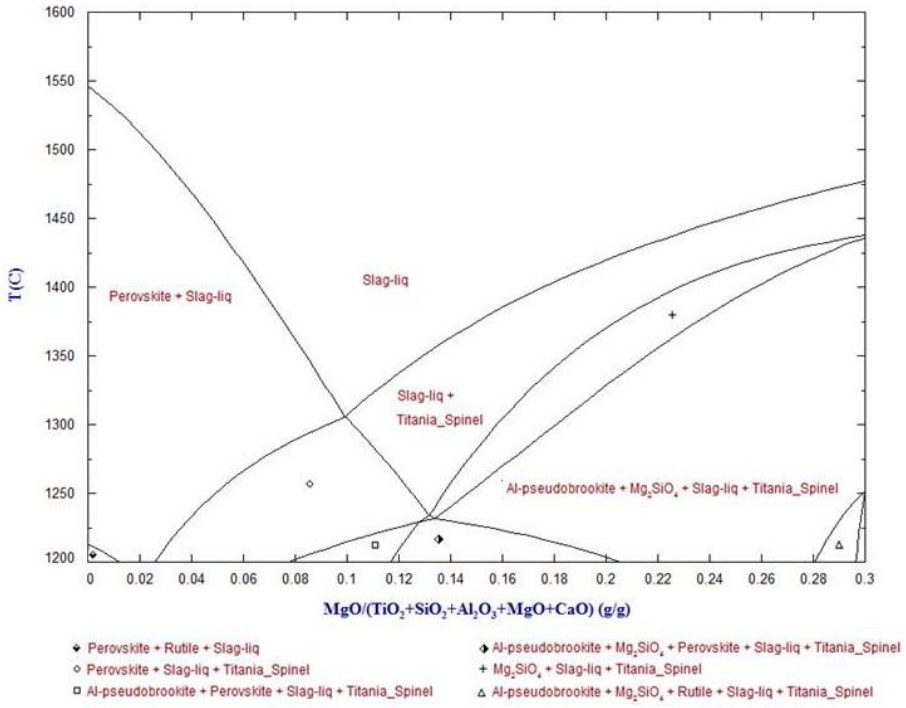

Figure 47: Calculated equilibrium phase diagram at pO_2 of 10^{-10} atm for the fluxed titaniferous slags that conform to the reviewed composition

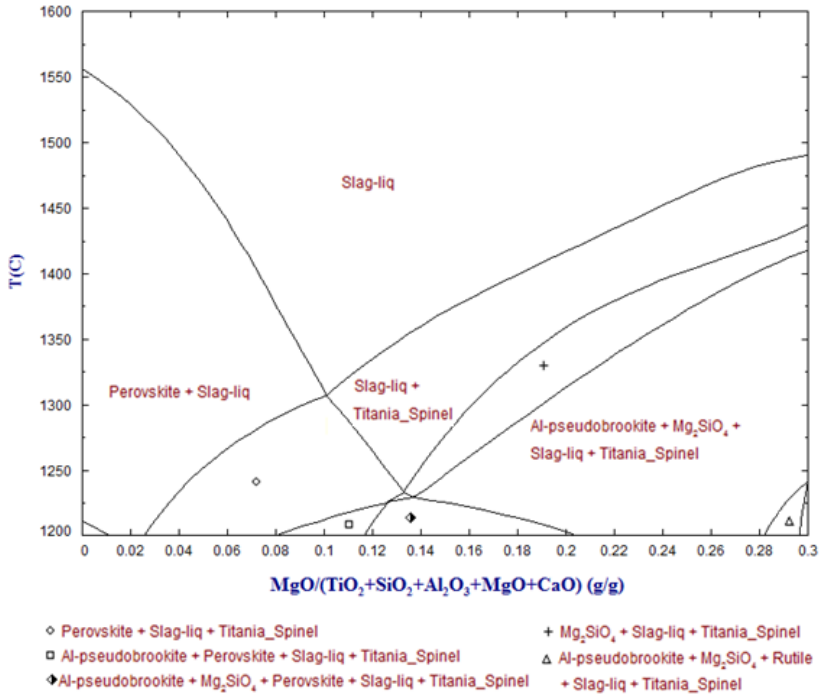

Figure 48: Calculated equilibrium phase diagram at pO_2 of 10^{-12} atm for the fluxed titaniferous slags that conform to the reviewed composition

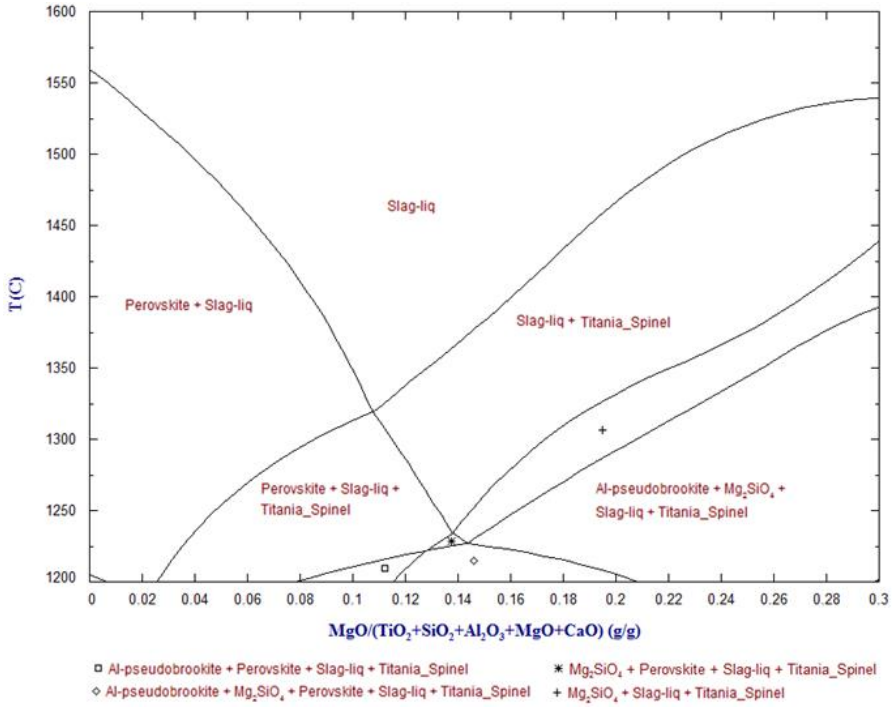

Figure 49: Calculated equilibrium phase diagram at pO_2 of 10^{-14} atm for the fluxed titaniferous slags that conform to the reviewed composition

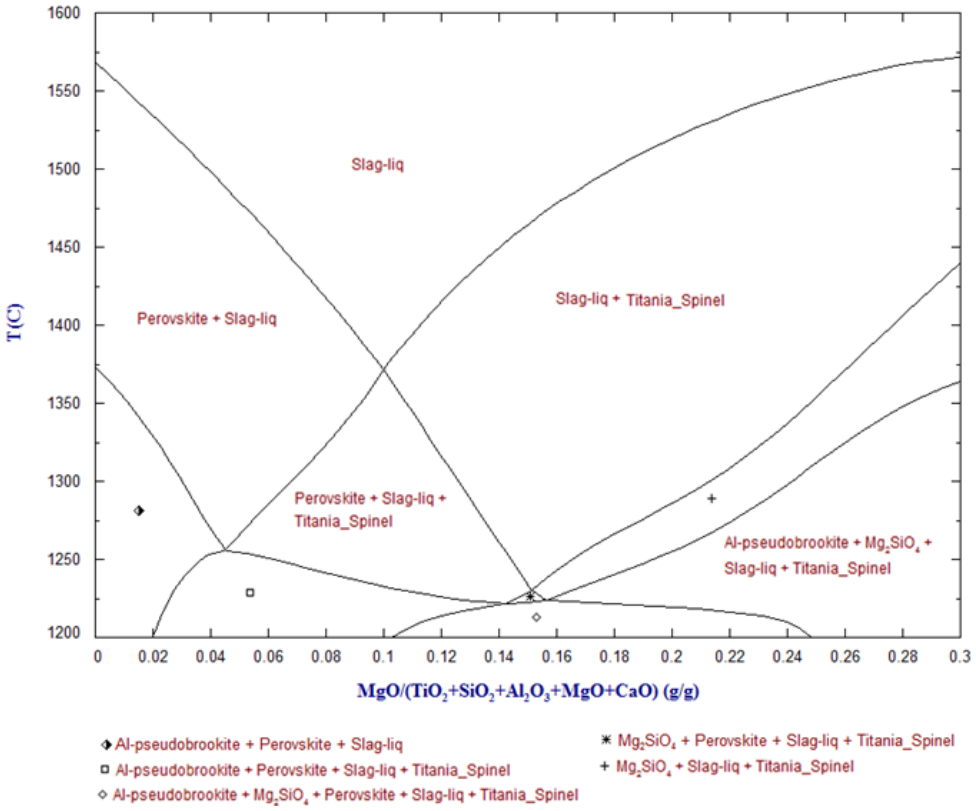

Figure 50: Calculated equilibrium phase diagram at pO_2 of 10^{-16} atm for the fluxed titaniferous slags that conform to the reviewed composition

Phase equilibria were also calculated for when the TiO_2 concentration in the slag is 30wt%, 25wt% and 20wt%, while keeping the sum of MgO + CaO constant at 30wt%, and increasing SiO_2 and Al_2O_3 in a 1:1 ratio from the amount with which the TiO_2 content was decreased from the starting 37wt% TiO_2 adopted in Jochens' composition. This approach allows for the evaluation of indicative phase equilibria in cases of titaniferous slags with as low as 20wt% TiO_2 content, and varying SiO_2 and Al_2O_3 concentrations. To complete these calculations using FactSage 7.2, all the databases, including the private PSE1 database, and the data processing modules that were used in the original calculations were adopted. The calculated phase equilibria at pO_2 of 10^{-16} atm under decreasing TiO_2 concentrations in the compositions are given in Figure 51, Figure 52, and Figure 53.

The results show that the phase equilibria of the reviewed titaniferous slag compositions are generally similar, especially in terms of the crystallisation of primary phases. There are visible deviations in sub-liquidus regions. For example, at high CaO concentrations, the pseudobrookite secondary phase is replaced with corundum (Al_2O_3-Ti_2O_3) solution when the TiO_2 and (Al_2O_3 + SiO_2) concentrations are decreased and increased, respectively. The crystallisation of corundum in Al_2O_3-Ti_2O_3-TiO_2 under reducing conditions is reported in literature (Jung, et al., 2009). As the TiO_2 concentration is lowered and (Al_2O_3 + SiO_2) concentrations are increased in the titaniferous slags, the sub-liquidus phase fields with the pseudobrookite solution shrink, and some subsequently disappear, i.e. (Al-pseudobrookite + Perovskite + Slag-liq + Titania_Spinel) and (Al-pseudobrookite + Mg_2SiO_4 + Perovskite + Slag-liq + Titania_Spinel) – at the same time, the phase fields that contain spinel solid solution and Mg_2SiO_4 phases in the sub-liquidus region grow in size.

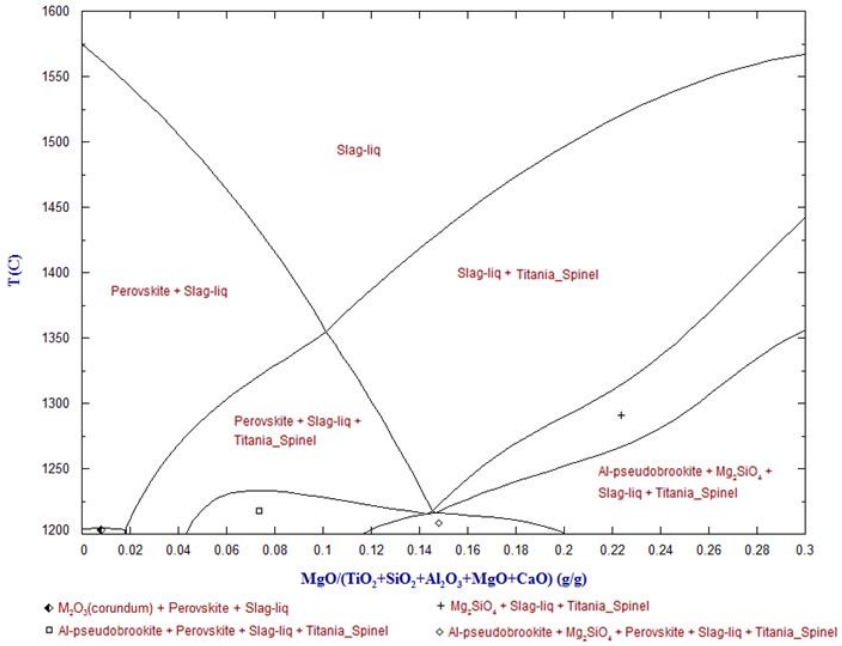

Figure 51: Calculated equilibrium phase diagram developed at pO_2 of 10^{-16} atm for the fluxed titaniferous slags with composition: TiO_2 = 30.00wt%, SiO_2 = 24.00wt% and Al_2O_3 = 16.00wt%, with varying proportions of CaO (30-0wt%) and MgO (0-30wt%)

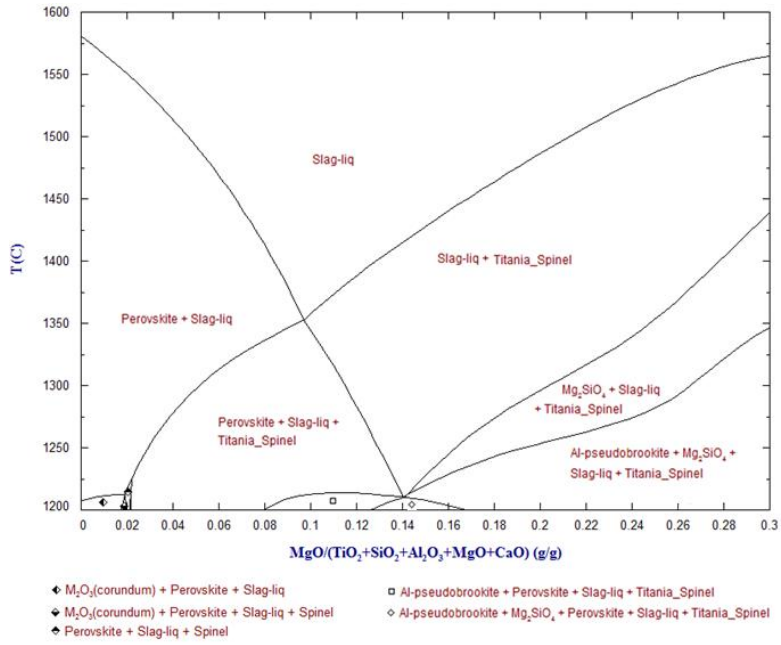

Figure 52: Calculated equilibrium phase diagram developed at pO_2 of 10^{-16} atm for the fluxed titaniferous slags with composition: TiO_2 = 25.00wt%, SiO_2 = 27.01wt% and Al_2O_3 = 17.99wt%, with varying proportions of CaO (30-0wt%) and MgO (0-30wt%)

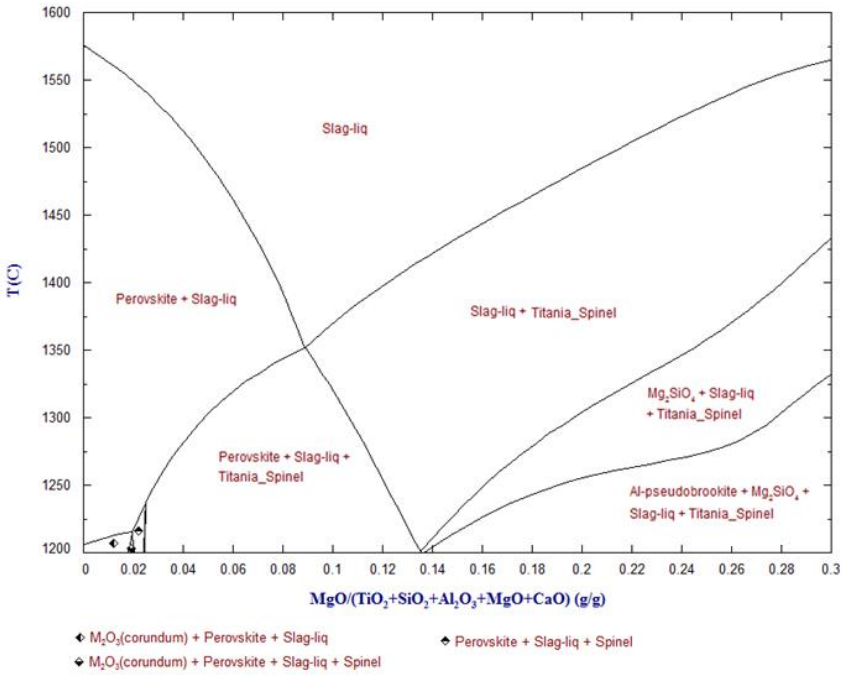

Figure 53: Calculated equilibrium phase diagram developed at pO_2 of 10^{-16} atm for the fluxed titaniferous slags with composition: TiO_2 = 20.00wt%, SiO_2 = 30.01wt% and Al_2O_3 = 19.99wt%, with varying proportions of CaO (30-0wt%) and MgO (0-30wt%)

4.4 Experimental review of phase equilibria of titaniferous slags

The isothermal equilibration, quenching and EPMA analysis method was adopted in the current investigation. The method is comprehensively described in the literature following developments at the Pyrometallurgy Research Group of the University of Queensland (Hayes & Jak, 2012; Jak & Hayes, 2004). Thus, only specific experimental conditions pertinent to the current investigation are described in the following subsections.

4.4.1 Experimental plan

A series of experiments were conducted as detailed in the following points. The experiments were conducted using the seven master slags (MSs) that were prepared as detailed in section 3.2.1 of CHAPTER 3. The setting up and verification of equilibration-quench test conditions are also discussed in section 3.3.1 of CHAPTER 3.

- Equilibration-quench experiments using selected MSs with a fixed composition to determine the equilibration time. The experiments were conducted at a fixed and specific equilibration temperature while varying reaction times. This was conducted prior to experimentation in air and at controlled pO_2 of 10^{-16} atm.

- Equilibration-quench experiments using the respective MSs to determine the equilibrium phases, typically between 1200°C and 1600°C. The first set of experiments were conducted in air to review and validate the phase equilibria reported by Jochens (1967), and those calculated in the current study and reported in section 4.3.2.2. The latter experiments were conducted at a controlled pO_2 of about 10^{-16} atm in order to review and validate the equilibrium phase diagram calculated and drawn in Figure 50. This phase diagram is deemed applicable for the correct prediction of phase equilibria of titaniferous slags.

- Analysis of real plant titaniferous slag for the review and validation of the applicability of the proposed calculated phase equilibria at low pO_2 conditions.

4.4.2 Experimental procedures: Equilibration-quench and EPMA analysis

Equilibration-quench and EPMA analysis testwork was conducted on all seven selected MSs in air and on MSs 1, 3, 4, 5, and 7 under controlled pO_2 of 10^{-16} atm. The selection of test MSs was strategic in order to verify specific areas in the calculated equilibrium phase

diagrams. To complete each experiment, the equilibration-quench furnace set up described in section 3.3.1 of CHAPTER 3 was heated up at 5°C/ minute to a pre-heat temperature of 1200°C. This temperature was maintained as the minimum operating temperature of the furnace during these studies.

As deduced from the work of Jochens (1967) and Holmes et al. (1968), the liquidus and solidus temperatures of the titaniferous slags in the reviewed compositional range are between 1200°C and 1600°C. The equilibration drop quench experiments were therefore conducted in this temperature range.

To complete the equilibration-quench experiments, each MS sample was placed in a capsule made from a platinum foil with a thickness of 0.127 mm. The typical masses of the test MS specimen ranged between 200 and 500 mg – the choice of using small sample masses was to allow for rapid attainment of equilibration time (Hume-Rothery, et al., 1952). In addition, the entire sample would be analysed, thus eliminating the sampling uncertainties in the phase equilibria.

4.4.2.1 Determination of equilibration time

The equilibrium time for the respective MSs was investigated at reactions times ranging between 0.5 and 24 hours using MS5 and MS3 at a target equilibration temperature of 1350°C. The procedure, as was also followed for actual equilibration-quench experiments, entailed sliding the sample capsule from the top (over 30 minutes) to the hot/ reaction zone of the tube furnace using a wound Pt wire supported by an alumina sheath. The MS5 or MS3 sample was then heated up at 5°C/ min from 1200°C to 1550°C where, according to Jochens data (Jochens, 1967), the sample would be completely liquid. The furnace temperature was then lowered to an equilibration temperature of 1350°C. The reasons for this experimental approach are described in section 4.4.2.2.

For the equilibration time studies in air, MS5 was used and the respective holding times at 1350°C were 0.5, 1, 3, 4, and 24 hours. At the end of the equilibration time, the capsules were dropped into a bath of ice water to quench as a way of preserving the phases that existed at equilibrium test temperatures. The quenched sample was embedded in an epoxy resin and polished for subsequent EPMA analysis to determine the morphology of the phases and the composition of the individual phases in sample. The suite of compositions was compared between the samples produced under different holding times. As reported in section 4.4.5.1

below and in Jochens work (Jochens, 1967), an equilibration time of 1 hour was generally more than enough to establish equilibrium state in air. The use of small sample sizes allowed for rapid attainment of equilibrium for the current silica rich compositions. An equilibration time of 1 hour was therefore adopted during the equilibration-quench experiments in air.

The equilibrium time at controlled pO_2 was studied using MS3 between the holding times of 1, 4, 8, 16, 24 and 48 hours. Following the same sample preparation and analysis procedures described above, it was established that, as also reported in section 4.4.5.1, a minimum holding time of 16 hours is required to achieve equilibrium state at pO_2 of 10^{-16} atm. Hence, the equilibration-quench experiments at pO_2 of 10^{-16} atm were conducted for a minimum holding time of 16 hours.

4.4.2.2 Experiments in air

Equilibration-quench experiments in air were conducted as described in section 4.4.2.1. However, in some instances, three capsules containing the same MS were processed at the same time to evaluate the homogeneity of the MS powders. To complete the experiments in air, the gas inlet and outlet connections on the equilibration-quench tube furnace set up were left open.

In consideration of the phase diagram established by Jochens (1967), before equilibration at specific temperatures, the samples were pre-melted at higher temperatures. The relatively high liquidus temperature MSs, i.e. MS1 and MS7 were pre-melted at 1600°C whereas the rest of the lower liquidus temperature MSs were pre-melted at 1550°C – the duration of the pre-melting stage was 30 minutes. The pre-melting ensured that the MSs were homogenized prior to the formation of equilibrium phases at respective temperatures, and that the equilibrium crystals grew into clear equilibrium shapes rather than irregular shapes of undissolved particles (Jak & Hayes, 2004).

The selection of equilibration test temperatures was strategic in that at first larger temperature ranges were selected after which a decision was made to fine-tune the equilibrium crystallization temperature in the range or, if the phase composition had not changed, to expand the equilibration temperature range. The equilibration temperatures were fine-tuned by 5°C to 10°C. The MSs were equilibrated at temperatures between the pre-melting temperature and 1200°C, which is a typical solidus temperature in the phase equilibria established by Jochens (1967). At the end of the equilibration time of 1 hour, the

capsules were dropped into a bath of cold water to quench as a way of preserving the phases that existed at equilibration test temperatures.

The quenched samples were recovered, mounted in epoxy resin, polished and then examined using EPMA. In the current testwork, an acceleration voltage of 15 kV and a probe current of 15 nA were used on the EPMA instrument. The standards that were used to calibrate the EPMA included the primary oxides of the MS components, i.e. rutile, quartz, corundum, periclase, with the exception of CaO which is very hydroscopic – in this case, wollastonite ($CaSiO_3$) was used as a calibration standard. The determination of the elements contained in respective phases, and subsequently chemical phase compositions of the sample using EPMA had a general accuracy of 1wt% or better. As the EPMA measured the elemental concentrations in the phases, the respective phase compositions were therefore deduced using stoichiometric calculations in full view of the anticipated phases based on literature – this is because the titanium speciation was not conducted due to inaccessibility of suitable analytical technique for analysing small samples of <0.1 g. The crystallized phases were subsequently identified. The experimental approach can be summarised as illustrated in Figure 54 (Jak & Hayes, 2004).

The experimental equilibration temperatures and compositions were plotted in the same axis as in the phase diagram developed in previous studies (Jochens, 1967; Jochens, et al., 1969).

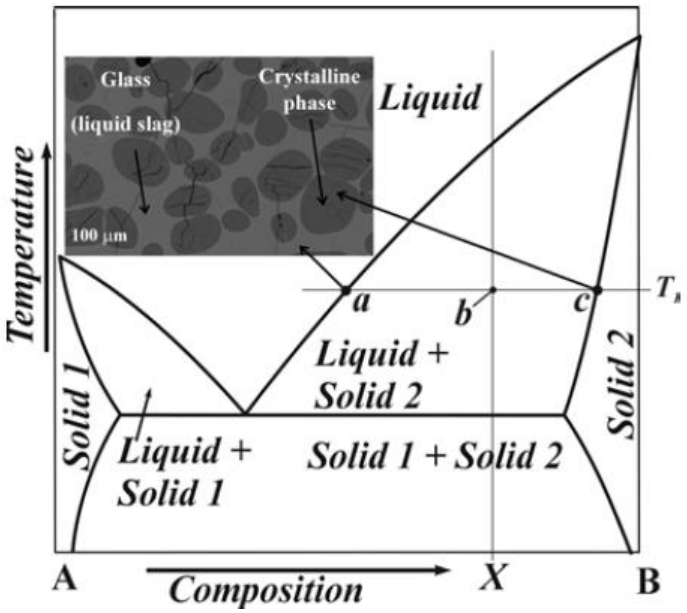

Figure 54: Hypothetical diagram illustrating the experimental approach of the classical equilibration-quench-EPMA analysis method

4.4.2.3 Experiments at pO_2 of 10^{-16} atm

For the experiments at pO_2 of 10^{-16} atm, the procedure detailed in section 4.4.2.2 for the preparation and introduction of MS specimen in the equilibration-quench tube furnace set up was followed. The difference is that the gas inlet and outlet were connect to the CO/ CO_2 supply and exhaust, respectively. Because the tube of the equilibration-quench furnace setup is small and cannot fit the test specimen, the pO_2 probe, and the thermocouple at the same time, the specimen bearing capsule was introduced to the pre-heating temperature of 1200°C followed by sealing of the furnace. The test conditions of a flow of 1000 sccm of CO/ CO_2 were turned on to purge the air out of the tube. The purging period was 30 minutes – this was determined during the pO_2 verification process reported in section 3.3.1.2 of CHAPTER 3 as the equilibrium time for the attainment of the set pO_2 conditions at high temperatures.

The temperature of the reaction zone and the pO_2 were periodically verified, typically after 5 tests, using the respective B-type thermocouple and pO_2 probe to ensure that the samples were tested at the correct target equilibration temperatures and pO_2.

4.4.3 Phase equilibria of real plant titaniferous slag

The relevance of the available phase equilibria (Jochens, 1967) and the established phase equilibria in the current testwork was evaluated using a real plant titaniferous slag. The titaniferous slag obtained from the defunct EHSV waste dump was used as a case study. The real slag was subjected to bulk chemical characterization by a Varian Vista-PRO CCD simultaneous inductively coupled plasma optical emission spectroscopy (ICP-OES). The samples was also subjected to respective phase and morphological characterisations by Bruker D8 advanced X-Ray Diffractometer (XRD) and Zeiss EVO® MA15 scanning electron microscope (SEM) coupled with a Bruker energy dispersive spectroscopy (EDS). The phase relations in the real plant slag were therefore evaluated against the phase equilibria in the available (Jochens, 1967) and newly established phase equilibria in the current study. This exercise was qualitative in nature as the influence of the residence time during processing and the different cooling mechanisms on the real titaniferous slag and the synthetic slags used to develop the available and new data was not considered.

4.4.5 Experimental results and discussions

4.4.5.1 Equilibration time

As the first task, equilibration-quench testwork in air and at pO_2 of 10^{-16} atm were conducted using the selected MSs to determine the time required for the MSs to reach equilibrium in the respective environments.

The tests conducted at pO_2 of 10^{-16} atm generally resulted in the deterioration of the strength of the Pt capsules. During the opening of the capsule to recover the processed sample, the foil would break into pieces that contaminated the sample. SEM-EDS analysis was conducted to roughly investigate the mechanism of the Pt foil weakening by determining the new Pt compounds that could form. Figure 55 shows the backscattered electron micrographs illustrating the interaction of the Pt foil and the MS5 after equilibration-quench test at 1350°C for 1 hour in an atmosphere with a pO_2 of 10^{-16} atm. EDS analysis on the Pt-slag interface did not show the formation of new Pt compounds. However, the Pt capsule was able to contain most of the MSs for the longest evaluated equilibration time of 48 hours without contamination of the slag. In general, the capsule made from Pt foil became rigid and brittle after processing at temperatures above 1250°C in an atmosphere of pO_2 of 10^{-16} atm – it was challenging to fold a thinker Pt foil than 0.127 mm to make a capsule. Selman et al. (1970) reported that hardness and cracking occur on Pt (and Pd) when subjected to carbonaceous and high temperature conditions. The solubility of carbon into Pt is estimated to be less than 0.02% at 1700°C. The hardening and cracking of Pt was however attributed to the diffusion of carbon at high temperatures (Selman, et al., 1970). Hence in the current study, the hardening and embrittlement of the Pt foil was attributed to the diffusion of carbon into it. In the test products, small pieces of Pt metal were observed, presumably generated during the recovery of the process slag from the capsule.

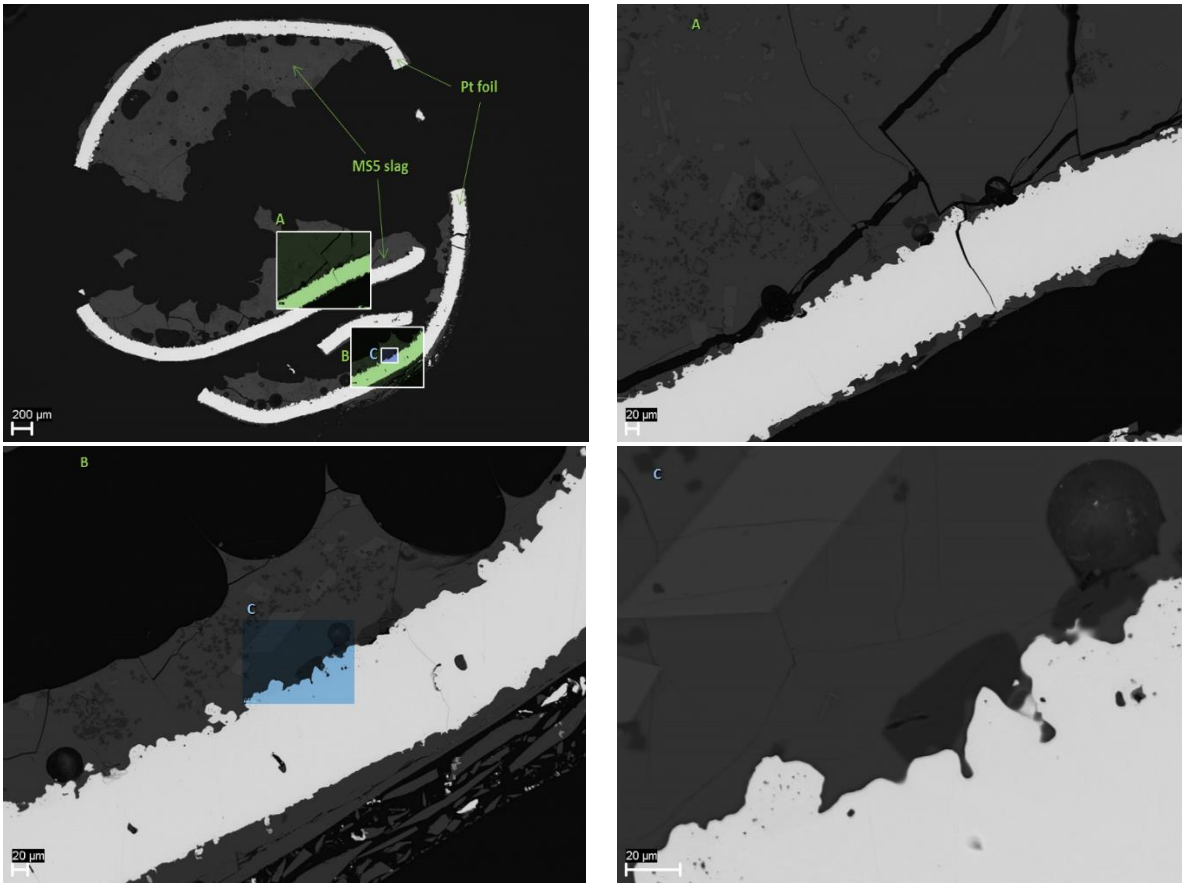

Figure 55: Backscattered electron micrograph showing the interaction of the MS5 slag with the capsule made from a high purity Pt foil

Equilibration time in air

The results of the equilibration-quench experiments using MS5 at 1350°C in air at different times are summarised in Table 13. These results show that a consistent set of phases of liquid, $MgTi_2O_5$-Ti_3O_5-Al_2TiO_5 and $Mg(Al,Ti)_2O_4$ was obtained in all the holding times that were tested, i.e. 0.5 to 24 hours. In the original work, Jochens used an equilibration time of 1 hour (Jochens, 1967). The current investigation confirms that an equilibration time of 1 hour is sufficient to attain equilibrium conditions. Hence, in the current study, an equilibration time of 1 hour was also adopted for the testwork conducted in air. Jochens cautioned that an equilibration time of 1 hour may not necessarily be sufficient to establish absolute equilibrium conditions, especially below solidus temperatures where the kinetics of solid phase transformations are anticipated to be slow (Jochens, 1967). The scope of the current investigations did not include tests at temperatures below 1200°C, i.e. well above the solidus at all conditions.

Table 13: Summary of phases established at different holding times for the determination of the equilibration time for the experiments conducted in air

Holding time, (hours)	Phases
0.5	liquid, $MgTi_2O_5$-Ti_3O_5-Al_2TiO_5 and $Mg(Al,Ti)_2O_4$
1	liquid, $MgTi_2O_5$-Ti_3O_5-Al_2TiO_5 and $Mg(Al,Ti)_2O_4$
3	liquid, $MgTi_2O_5$-Ti_3O_5-Al_2TiO_5 and $Mg(Al,Ti)_2O_4$
4	liquid, $MgTi_2O_5$-Ti_3O_5-Al_2TiO_5 and $Mg(Al,Ti)_2O_4$
24	liquid, $MgTi_2O_5$-Ti_3O_5-Al_2TiO_5 and $Mg(Al,Ti)_2O_4$

Equilibration time at pO_2 of 10^{-16} atm

The results of the investigation of the minimum equilibration time using MS3 at 1350°C in an atmosphere with pO_2 of 10^{-16} atm are summarised in Table 14. These results show that after 1 hour of operation there were no crystalline phases. Liquid, $CaTiO_3$, and $Mg(Al,Ti)_2O_4$ phases were observed after 8 hours of operation under these conditions. However, after 16 hours of operation, a set of four phases, i.e. liquid, $CaTiO_3$, $Mg(Al,Ti)_2O_4$, and $MgTi_2O_5$-Ti_3O_5-Al_2TiO_5, was observed. The same set of phases remained even when the test duration was increased to 24 hour and subsequently to 48 hours. After the 48 hour test, the Pt capsule was very brittle – only a very small sample could be attained for EPMA analysis.

A minimum holding time of 16 hours for the testwork in an atmosphere with pO_2 of 10^{-16} atm was deemed necessary for the attainment of the equilibrium conditions. It is possible that the sample holding time of 16 hours may not have been sufficient to establish absolute equilibrium conditions for all the MSs and towards the solidus temperatures of the respective MSs. The proposed minimum equilibration time was accepted with a full view of this possibility – these results were deemed sufficient as they were used to verify the calculated phase equilibria using the FactSage thermochemical software. However, the tests at pO_2 of 10^{-16} atm on respective MSs were conducted for the longest possible time, which was typically 24 hours. Equilibration times in excess of 24 hours generally resulted in the deterioration of the Pt capsule that in some cases the sample was completely lost and the test needed to be repeated. Hence, an equilibration period of 24 hours was generally maintained in the testwork programme at pO_2 of 10^{-16} atm.

Table 14: Summary of phases established at different holding times for the determination of the equilibration time for the experiments conducted at pO_2 of 10^{-16} atm

Holding time, (hours)	Phases
1	Liquid
8	Liquid, $CaTiO_3$, and $Mg(Al,Ti)_2O_4$
16	Liquid, $CaTiO_3$, $Mg(Al,Ti)_2O_4$, and $MgTi_2O_5$-Ti_3O_5-Al_2TiO_5
24	Liquid, $CaTiO_3$, $Mg(Al,Ti)_2O_4$, and $MgTi_2O_5$-Ti_3O_5-Al_2TiO_5
48	Liquid, $CaTiO_3$, $Mg(Al,Ti)_2O_4$, and $MgTi_2O_5$-Ti_3O_5-Al_2TiO_5

4.4.5.2 Equilibration-quench EPMA analysis in air

As the first task of the current programme, equilibration-quench experiments were conducted to review and validate Jochens' equilibrium phase diagram (Jochens, 1967). The equilibrium phase diagram drawn in the current study is shown in Figure 56, and the EPMA data that is converted to oxides is included in Appendix 1.3. This phase diagram shows that the liquidus surface of the reviewed slags changes from 1410°C at 28wt% CaO and 2wt% MgO, to 1515°C at 2wt% CaO and 28wt% MgO, passing through a minimum of 1300°C at 20wt% CaO and 10wt% MgO.

In Figure 56, phase field V and VII are most likely contiguous; in that case, the primary phase field would be composed of the spinel solid solution [$Mg(Al,Ti)_2O_4$]. These results agree with the results shown in the backscattered electron image of the plant slag produced at EHSV (Figure 23), with a composition similar to the data point separating phase field V and VIIM, that the crystallisation temperatures of spinel and pseudobrookite solutions are very close. Thus, the temperature resolution of the equilibration quench experiments of ±5°C did not suffice to provide the required temperature resolution to explicitly indicate the $Mg(Al,Ti)_2O_4$ as the primary phase.

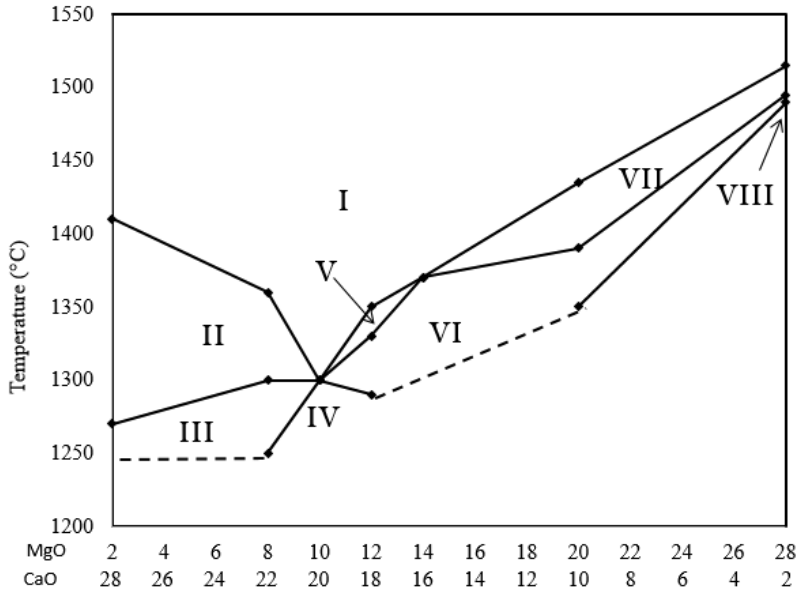

I	Liquid (L)	V	$Mg(Al,Ti)_2O_4$ + L
II	$CaTiO_3$ + L	VI	$MgTi_2O_5$-Ti_3O_5-Al_2TiO_5 + $Mg(Al,Ti)_2O_4$ + L
III	$CaTiO_3$ + $MgTi_2O_5$-Ti_3O_5-Al_2TiO_5 + L	VII	$Mg(Al,Ti)_2O_4$ + L
IV	$CaTiO_3$ + $MgTi_2O_5$-Ti_3O_5-Al_2TiO_5 + $Mg(Al,Ti)_2O_4$ + L	VIII	$Mg(Al,Ti)_2O_4$ + $MgTi_2O_5$-Ti_3O_5-Al_2TiO_5 + Mg_2SiO_4 + L

Figure 56: Equilibrium phase diagram established in air for the slag system: TiO_2 = 37wt%, SiO_2 = 20wt%, and Al_2O_3 = 13wt%, at varying ratios of CaO (30-0wt%) and MgO (0-30wt%)

4.4.5.3 Evaluation of equilibration-quench results using phase rule

The established phase diagram was evaluated using an established theoretical tool, i.e. Gibbs Phase Rule (phase rule). As previously stated, the phase rule is defined by Equation [4.31].

$$F + P = C + 2 \quad [4.31]$$

Where, F = number of degrees of freedom, i.e. minimum number of intensive variables (temperature, pressure and composition) that can be changed independently without disturbing the phases in equilibrium

C = minimum number of independent components

P = number of phases, i.e. number of homogeneous distinct and separate components of the system (liquids, solids and/ or gases)

In the current study of the TiO_2-SiO_2-Al_2O_3-MgO-CaO system in air, the pressure was assumed to be constant. The phase rule thus changed to the condensed version as shown in Equation [4.32].

$$F + P = C + 1 \quad [4.32]$$

The compositions were fixed in terms of the concentrations of TiO_2, SiO_2 and Al_2O_3 or in simply terms, the ratio of (CaO+MgO) to (TiO_2 + SiO_2 + Al_2O_3) was fixed. The pO_2 was also fixed at 0.21 atm (i.e. in air). With these considerations, the phase rule changes further to Equation [4.33].

$$F + P = C + 1 - 2 = C - 1 \quad [4.33]$$

The number of components of the system is 5 (TiO_2-SiO_2-Al_2O_3-MgO-CaO). Hence the phase rule simplifies to Equation [4.34].

$$F + P = 5 - 1 = 4 \quad [4.34]$$

The evaluation of the number of possible phases in respective phase fields as a function of the degrees of freedom is simplified in Table 15.

Table 15: Review of the variations of F and P in the TiO_2-SiO_2-Al_2O_3-MgO-CaO system

	F + P = 4			
P	1	2	3	4
F	3	2	1	0

As shown in this table:

- When F = 3, P = 1. This corresponds to the phase field at temperatures (T) above the liquidus surface, i.e. phase field 'I' on the phase diagram. This implies that T and the 2 ratios [CaO/(MgO + TiO_2 + SiO_2 + Al_2O_3) and MgO/(CaO + TiO_2 + SiO_2 + Al_2O_3)] can be changed within the limits of the liquid phase field.

- When F = 2, P = 2. The three primary phase fields, i.e. 'II', 'V', and 'VII', satisfy these conditions. This implies that T and CaO/MgO ratio can be changed independently within the respective primary phase regions.

- When F = 1, P = 3. These conditions correspond to two phase fields, i.e. 'III' and 'VI'. Thus, T or one of the ratios can be changed independently without changing the number of phases in these fields.

- When F = 0 and P = 4, invariant point 'IV' is satisfied. Under these conditions, changing any variable, i.e. T or any ratio, will result in the disturbance of equilibrium phases.

There are no gross inconsistencies between the acquired experimental and theoretical data. The phase rule and the current results agree that the maximum number of phases that can exist under the tested conditions in TiO_2-SiO_2-Al_2O_3-MgO-CaO system, i.e. specific T and component ratios in air, is 4. It appears that the solidus conditions will also have a maximum of 4 phases – thus, the sub-solidus fields with 4 phases already will self-transform into a maximum of 4 solid phases under solidus conditions.

4.4.5.4 Comparison of current experimental results with FactSage calculated and literature phase equilibria

The phase equilibria established in the current experimental work were compared with those available in the open literature, i.e. the results reported by Holmes et al. (1968) and Jochens (1967), and the calculated results in section 4.3.2.2. A comparison of the current experimental results and the other available data is shown in Figure 57. Holmes et al. (1968) only studied the liquidus temperatures of the reviewed system and those were consistently higher than those established in the current and Jochens' (Jochens, 1967) work. The deviation of liquidus temperatures of Holmes et al. (1968) from the other data sets is more pronounced around the minimum liquidus temperature. The general deviation of Holmes et al. (1968) results from the other data sets can be attributed to the possible difference in the actual experimental conditions. Though all the tests were supposedly completed in air, in which the absolute pO_2 is generally not measured, the closing of the system at high temperatures may result in a decrease in the pO_2 such that the actual pO_2 is lower that the basic air pO_2 of 0.21 atm (Schultz, et al., 2013). As previously shown in Figure 44, the liquidus surface in the Ca-Mg-Al-Si-Ti-O system increases with decreasing pO_2. Hence it is possible that the work of Holmes et al. (1968) was conducted at lower pO_2 than that of air.

In terms of the liquidus surface, the current and Jochens' experimental data are fairly comparable. A clear deviation in the liquidus temperatures of the current equilibration-quench results from the other data sets is observed in compositions with high CaO concentrations. For example, for the composition with 28wt% CaO and 2wt% MgO, the current equilibration-quench work reports a liquidus temperature of about 1410°C, whereas

the other data sets, i.e. Holmes et al. (1968), Jochens (1967), as well as current FactSage calculation agree that the liquidus temperature is about 1500°C. Several repeat tests of the equilibration-quench experiments using the MS composition with 28wt% CaO and 2wt% MgO (MS1) still showed that the liquidus temperature of the perovskite in this matrix is about 1410°C.

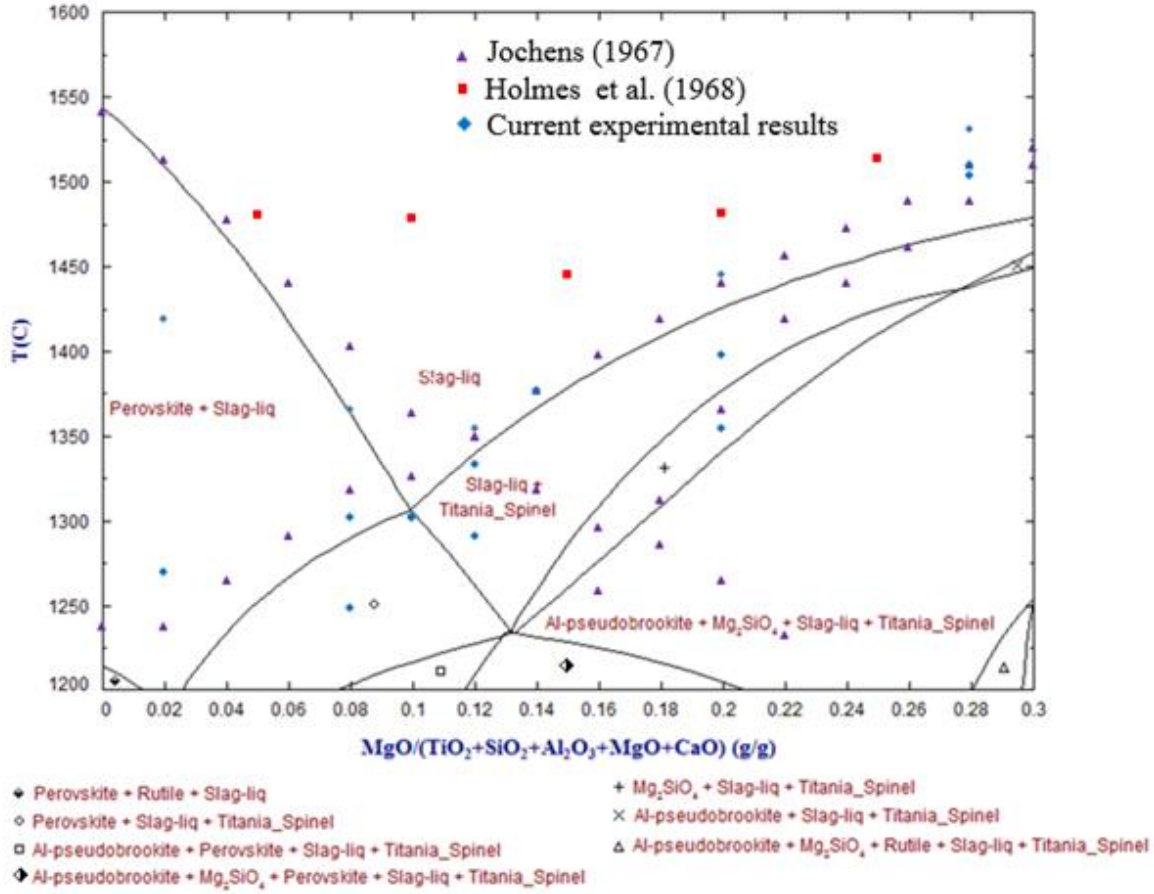

Figure 57: Comparison of phase equilibria in air established from current experimental and calculated results and available literature data (phase diagram calculated using FactSage software)

The anomaly of the low liquidus temperature for MS1 in current equilibration-quench experiments compared to other data sets was investigated further by putting as seed $CaTiO_3$ crystal in the melt. The $CaTiO_3$ crystals were synthesized using the conventional method of mixing stoichiometric amounts of CaO and TiO_2, followed by heating at 1300°C over 24 hours – the X-ray diffractogram of the synthetic $CaTiO_3$ crystals is shown in Figure 58. Few granules of $CaTiO_3$ (a primary phase in this composition) were placed at the bottom of the Pt capsule for seeding the primary phase – the granules had to be very small to avoid the

modification of the synthetic slag composition. Thereafter, the MS1 material was placed on top of the granules. The sample arrangement that was made in this way was processed at 1450°C, which is between the two reported liquidus temperatures of 1490°C and 1410°C. The testwork was conducted to determine the likely liquidus temperature of the MS1 between the reported temperatures. If the $CaTiO_3$ crystals are observed or not observed at the end of the test duration at 1450°C, the liquidus temperature is likely 1490°C or 1410°C, respectively. The sample was heated in two ways to complete two tests: 1) heating from 1200°C to 1600°C and holding for 30 minutes, followed by lowering the temperature to 1450°C and equilibration for an hour, and subsequently quenching in cold water (this is the normal procedure followed in the testwork), and 2) heating the sample to 1450°C and equilibrating for an hour, followed by quenching in cold water.

The samples were subjected to SEM-EDS analysis and the respective micrographs are shown in Figure 59. The crystals on the micrographs are clear. It appears that the current experimental results may be wrong in that at 1450°C the slag is completely glass. Follow up chemical analysis of the MS1 showed that there is no contamination. The results suggest that the nucleation kinetics of $CaTiO_3$ crystals in MS1 are slow. It is thus possible that the adopted holding time of 1 hour may not be a suitable equilibration time for MS1. In previous work by Jochens (1968), $CaTiO_3$ nucleation challenges were not specified. Hence it is believed that the intermediate phases in the feeds to the equilibration experiments were different between the current and Jochens' work. The pre-treatment process prior to equilibration in air may not be consistent between the two studies. Intermediate phases in the equilibration test feeds are not specified in Jochens' work (1967).

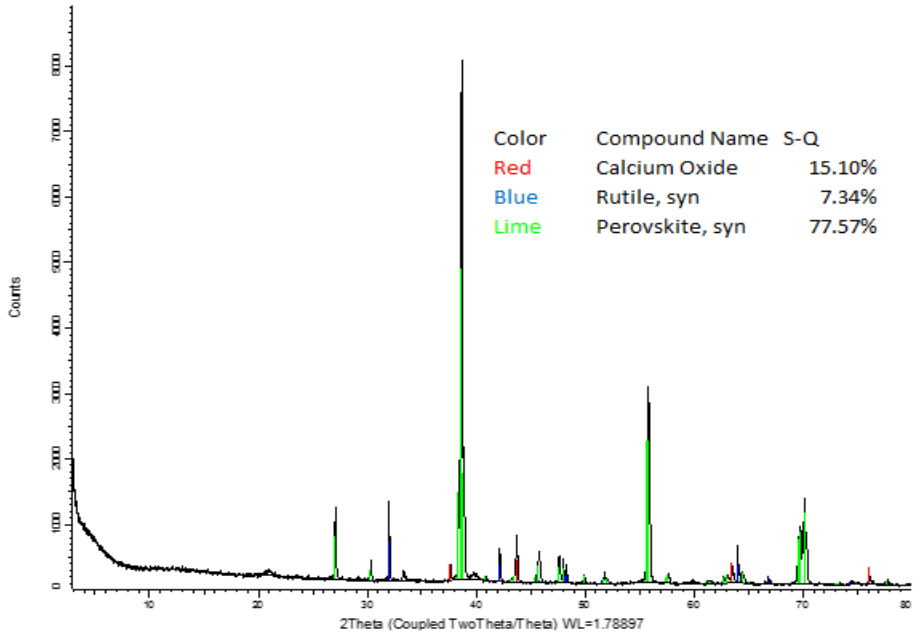

Figure 58: X-Ray diffractogram of the synthetic $CaTiO_3$ crystals

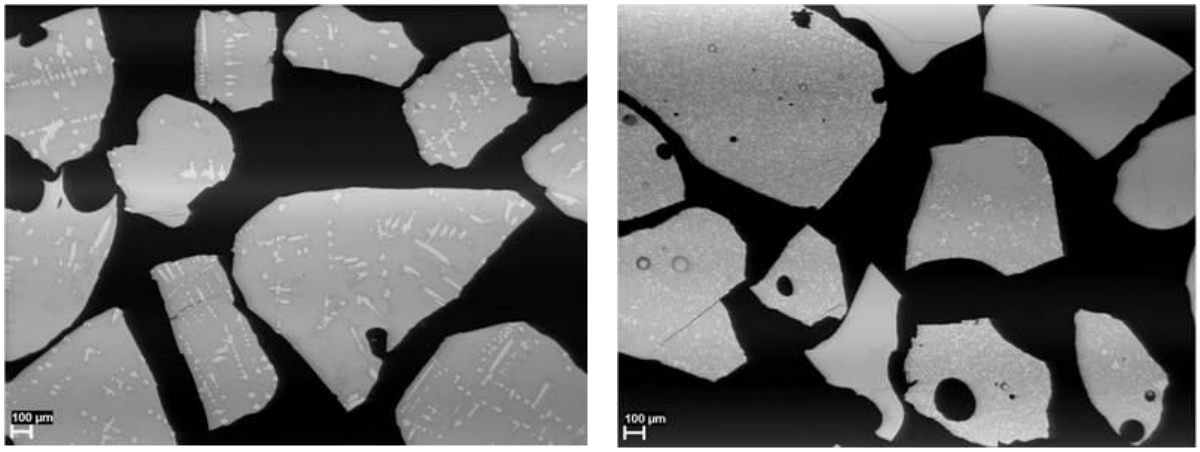

Pre-melted at 1600°C, equilibrated at 1450°C Direct equilibration at 1450°C

Figure 59: Backscattered electron micrographs of the MS1 samples processed with $CaTiO_3$ seeding crystals

Another deviation is observed in the minimum liquidus temperatures and compositions: Jochens (1967) reported the liquidus temperature to be at 1345°C with a composition of 18wt% CaO and 12wt% MgO, whereas the current results of equilibration-quench testwork and FactSage calculation reported it to be at about 1300°C with a composition of 20wt% CaO and 10wt% MgO. Considering that two independent data sets agree about the liquidus temperature and composition, it is plausible that Jochens' data (1967) may be unreliable in this case. It is not clear what could have led to this uncertainty in Jochens measurements.

In terms of the phase relations, Jochens (1967), and current equilibration-quench and FactSage calculations agree that at high CaO levels before the minimum liquidus temperature point, perovskite ($CaTiO_3$) is the primary phase. At higher MgO levels after the minimum liquidus temperature point, Jochens (1967) reported that $4(MgO.{}_2TiO_2).Al_2O_3.TiO_2$, or stoichiometrically pseudobrookite solution ($4MgTi_2O_5$-Al_2TiO_5) crystallises as the primary phase until a composition with a maximum MgO concentration of 30wt%. However, the current equilibration-quench and FactSage calculation results agree that the spinel solid solution [$Mg(Al,Ti)_2O_4$] crystallises as a primary phase from the minimum liquidus composition with 10wt% MgO concentration until a composition with a maximum MgO concentration of 30wt%.

Jochens (1967) reported forsterite (Mg_2SiO_4) as the secondary phase in compositions above the minimum liquidus composition containing 12wt% MgO concentration – the crystallisation of the spinel phase is not reported at all. The ternary and solidus phase fields in Jochens' (1967) work typically contain perovskite and olivine solution $(Mg,Ca)_2SiO_4$ depending on the composition. However, the ternary phase observed in the current equilibration and calculation work is Mg_2SiO_4.

The phase relations observed in the current study agree to some extent with literature data reported by Berezhnoi and Gulko (1955) in their study of the Al-Mg-Ti-O sub-system. They reported that in air the phases that can crystallise include geikielite, with an ilmenite structure ($MgO.TiO_2$); gandilite, with an inverse spinel structure (Mg_2TiO_4); spinel ($MgAl_2O_4$) and the pseudobrookite type karrooite-tialite solid solution ($MgTi_2O_5$-Al_2TiO_5) (Berezhnoi & Gulko, 1955). In the current equilibration-quench and calculation work, spinel and pseudobrookite solid solution are reported. However, the crystallisation of geikielite was not observed. The absence of geikielite is attributed to the presence of significant SiO_2 concentration in the system studied in the current programme – hence, Mg_2SiO_4 is crystallised instead.

4.4.5.5 Equilibration-quench EPMA analysis at pO_2 of 10^{-16} atm

The phase equilibria of titaniferous slags were studied at pO_2 of 10^{-16} atm using the typical Ca-Mg-Al-Si-Ti-O system. The phase transformation points determined in the current study were connected into an equilibrium phase diagram as shown in Figure 60 – the EPMA data that is converted to oxides is included in Appendix 1.3. The liquidus surface in this phase

diagram changes from 1480°C in a composition with 28wt% CaO and 2wt% MgO, to 1550°C in a composition with 2wt% CaO and 28wt% MgO, passing through a minimum of 1370°C in a composition with 20wt% CaO and 10wt% MgO.

This equilibrium phase diagram was also evaluated using the phase rule. Following the approach adopted in the case of the phase equilibria established at pO_2 of 0.21 atm (in air), the generic expression for the phase rule for the phase equilibria established at pO_2 of 10^{-16} atm can also be expressed as in Equation [4.21], i.e. F+P = 4. When F = 3, P = 1; thus phase filed 'I', which is a complete liquid field, corresponds with these conditions. Temperature (T) and the 2 ratios [CaO/(MgO + TiO_2 + SiO_2 + Al_2O_3) and MgO/(CaO + TiO_2 + SiO_2 + Al_2O_3)] can be changed within the limits of the liquid phase field.

In a case where F = 2, P = 2, the two primary phase fields, i.e. 'II' and 'V' satisfy these conditions. Thus, T and CaO/MgO ratio can be changed independently within the respective primary phase fields. However, if F = 1, P = 3, - this is the case that satisfies the phase fields 'III' and 'VI'. Thus, T or one of the ratios can be changed independently without changing the number of phases in these fields. When F = 0 and P = 4, invariant points 'IV' and 'VII' are satisfied. At invariant points, changing any variable, i.e. T or any ratio, would result in the disturbance of equilibrium phases.

The acquired experimental and theoretical data generally agree that the maximum number of phases that can exist under the tested conditions in Ca-Mg-Al-Si-Ti-O system, i.e. specific T and component ratios in air, is 4. The solidus conditions will also have a maximum of 4 phases. The sub-solidus fields with 4 phases already will self-transform into a maximum of 4 solid phases under solidus conditions.

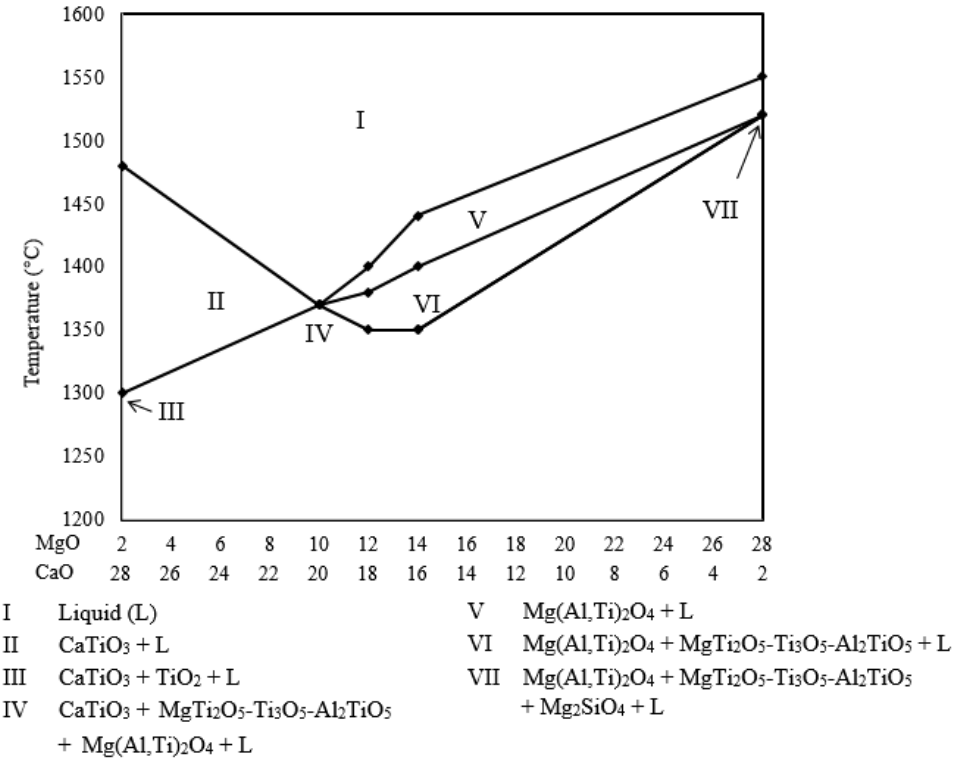

Figure 60: Equilibrium phase diagram established at pO_2 of 10^{-16} atm for the slag system: TiO_2 = 37wt%, SiO_2 = 20wt%, and Al_2O_3 = 13wt%, at varying ratios of CaO (30-0wt%) and MgO (0-30wt%)

The effect of pO_2 on the phase equilibria of titaniferous slags was further studied by evaluating the established experimental data in the current work for the Ca-Mg-Al-Si-Ti-O system in air and at pO_2 of 10^{-16} atm, i.e. phase relations in Figure 56 were compared to those in Figure 60. The liquidus surface and sub-liquidus boundaries of the two equilibrium phase diagrams established in the current testwork were superimposed as shown in Figure 61. This figure shows a general trend of an increase in the liquidus temperatures with decreasing the pO_2. The general increase in the liquidus and sub-liquidus temperatures with decreasing pO_2 in the system can be attributed to the differences in the phase relations. In high CaO compositions in both equilibrium phase diagrams, i.e. Figure 56 and Figure 60, $CaO.TiO_2$ crystallises as the primary phase. In high MgO compositions, the phase equilibria established in air show that $MgTi_2O_5$-Al_2TiO_5 crystallises as a primary phase until a composition with 14wt% MgO concentration. Thereafter, the spinel solid solution [$Mg(Al,Ti)_2O_4$] crystallises as the primary phase until a composition with a maximum MgO concentration of 30wt%. However, the phase equilibria established at pO_2 of 10^{-16} atm show $Mg(Al,Ti)_2O_4$ as the only primary phase in high MgO compositions.

The differences in terms of the phase relations and (sub-) liquidus temperatures in the Ca-Mg-Al-Si-Ti-O system depending on the composition and pO_2 were reported in some sub-systems in literature (Jung, et al., 2009; Krajewski, 1992). For example, in their calculation of the phase equilibria in the Al_2O_3-Ti_2O_3-TiO_2, Jung et al. (2009) reported a difference in the crystallisation of the primary phases, which mainly depended on the composition and pO_2 in the reaction zone. In addition, Krajewski (1992) reported crystallisation of different phases in the Al-Mg-Ti-O system depending on the composition and pO_2 in the reaction zone. The composition of the system in the current study was kept constant. The difference in crystallisation of phases in relation to lowering the pO_2 can be brought about by the reduction of oxidised Ti^{4+} to Ti^{3+}. Thus, the typical phases that crystallised in the subsystems included $Mg(Al,Ti)_2O_4$, Al_2TiO_5, $MgTi_2O_5$, Ti_3O_5, and titanium magneli phases (Ti_nO_{2n-1} with $n \geq 4$) (Jung, et al., 2009; Krajewski, 1992; Rice & Robinson, 1977; Vasyutinskii, 1977; McKee & Aleshin, 1963; Anderson, et al., 1957). Jung et al. (2009) further reported that in the Al_2O_3-Ti_2O_3 system studied at 10^{-15} atm, the liquid range would be significantly larger at 1600°C compared to 1500°C.

These studies agree with the results of the current study in that the phase relations and (sub-) liquidus temperatures would be dependent on the composition and pO_2 in the reaction zone. The current study shows that in the compositional range with 10wt% to 30wt% MgO concentration in a reaction atmosphere with a pO_2 of 10^{-16} atm, the $Mg(Al,Ti)_2O_4$ distinctly crystallises as a primary phase while $MgTi_2O_5$-Ti_3O_5-Al_2TiO_5 is the secondary phase. Ideally, the determination of Ti^{3+} in samples would serve as a good validation for the existence of phases containing reduced titanium species. The Ti^{3+} determination in the MS samples processed at pO_2 of 10^{-16} atm was not conducted due to the limitation in the quenched sample size. However, the lack of Ti^{3+} validation was considered acceptable as the study was conducted in parallel with computational simulation for validation.

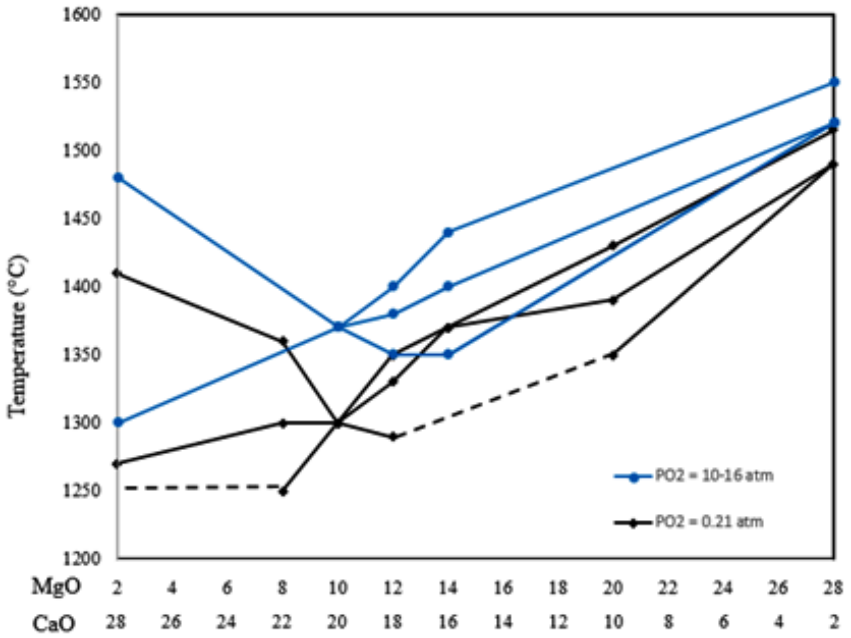

Figure 61: Comparison of phase equilibria established from experimental investigations at pO_2 of 0.21 and 10^{-16} atm for the slag system: TiO_2 = 37wt%, SiO_2 = 20wt%, and Al_2O_3 = 13wt%, at varying ratios of CaO (28-2wt%) and MgO (2-28wt%)

The experimental results of the phase equilibria established at a pO_2 of 10^{-16} atm were compared with those obtained from thermochemical simulation using FactSage software. These two sets of data are shown in Figure 62 – FactSage software was used to calculation the equilibrium phase diagram, in which the equilibration-quench results are also plotted. In general, the liquidus surfaces in the calculated and equilibration-quench phase equilibria are similar. There is however a clear deviation in the two results in that the equilibration-quench experiments and FactSage calculation predict that MS1 with CaO: MgO wt% ratio of 28:2 has a liquidus temperature of 1480°C and 1535°C, respectively. The same anomaly was observed and investigated during the investigations conducted in air and reported in section 4.4.5.4. As it transpired in the case of testwork in air, the equilibration quench experimental results may be inaccurate because of the possibly poor nucleation kinetics of the $CaTiO_3$ primary phase in the MS1 composition. The holding time of a minimum of 16 hours may be too short to achieve equilibrium for the MS1 material. As stated previously, extended holding times beyond 24 hours were generally problematic in that the Pt capsule would be severely worn-out, and a substantial amount of slag would be lost such that the test would need to be repeated. Hence, the pre-treatment process of the synthetic slag may need to be optimised.

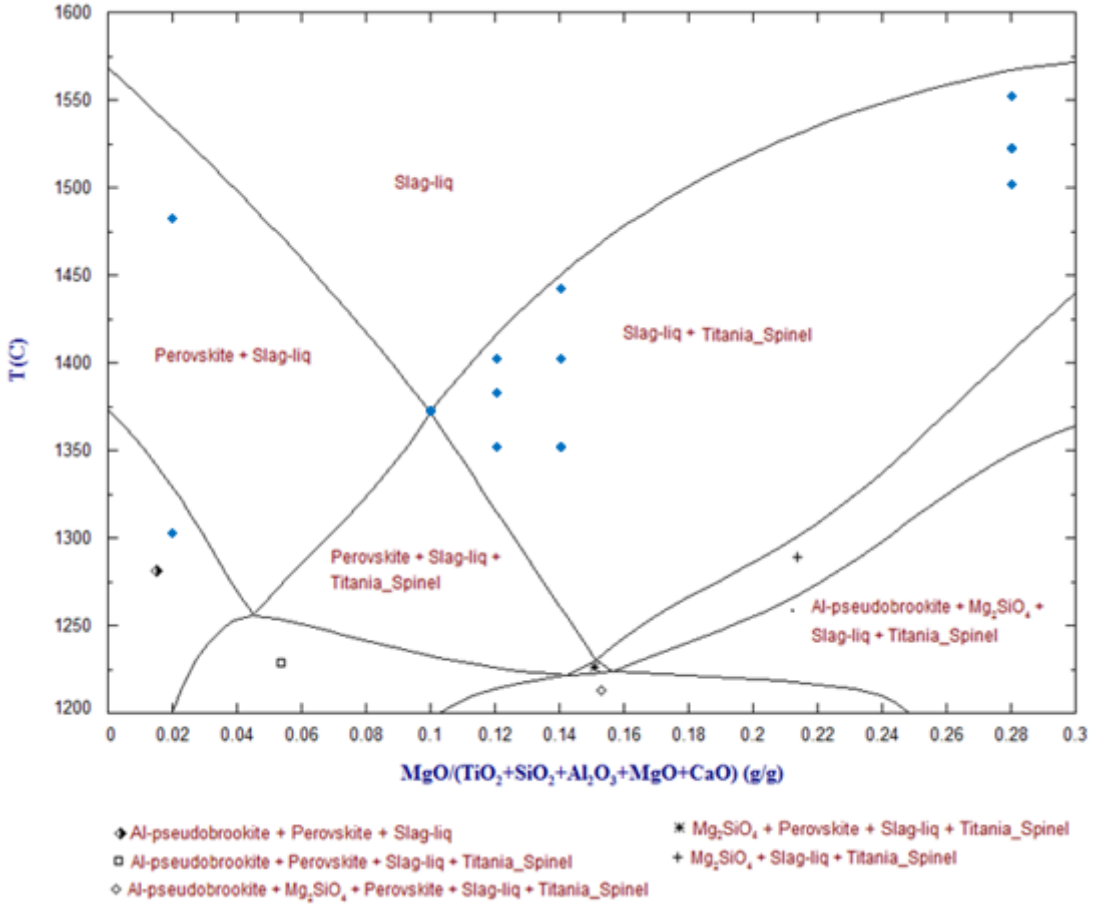

Figure 62: Comparison of phase equilibria at pO_2 of 10^{-16} atm established from current experimental work and calculation using FactSage software: TiO_2 = 37wt%, SiO_2 = 20wt%, and Al_2O_3 = 13wt%, at varying ratios of CaO (28-2wt%) and MgO (2-28wt%)

In terms of the phase relations, there is a general agreement that $CaTiO_3$ and $Mg(Al,Ti)_2O_4$ are two primary phases that crystallise at high CaO concentrations before and after the minimum liquidus temperature compositions, respectively. In both sets of data, $MgTi_2O_5$-Ti_3O_5-Al_2TiO_5 solid solution crystallises as the secondary phase before and after the minimum liquidus compositions – the low MgO regions, i.e. before the minimum liquidus temperature point, the pseudobrookite solid solution is low in the $MgTi_2O_5$ component.

The FactSage calculation predicts that the minimum point on the liquidus surface is an invariant point where the liquid, $CaTiO_3$ and $Mg(Al,Ti)_2O_4$ co-exist in equilibrium. The phase region where liquid, $CaTiO_3$ and $Mg(Al,Ti)_2O_4$ are in equilibrium is fairly small. Thereafter, the next phase boundary signals the start of a four phase equilibrium region of liquid, $CaTiO_3$, $Mg(Al,Ti)_2O_4$ and $MgTi_2O_5$-Ti_3O_5-Al_2TiO_5. However, the invariant point

at the minimum liquidus temperature in the equilibration-quench results indicates an outright equilibrium point for the four phases, namely; liquid, $CaTiO_3$, $Mg(Al,Ti)_2O_4$ and $MgTi_2O_5$-Ti_3O_5-Al_2TiO_5. Since the selection of temperature during the equilibration testwork was in stages, the equilibration-quench data may have omitted the small three phase region observed in the FactSage phase equilibria before the minimum point on the liquidus surface. Around the minimum point on the liquidus surface, the two sets of data agree about the equilibrium of liquid, $CaTiO_3$, $Mg(Al,Ti)_2O_4$ and $MgTi_2O_5$-Ti_3O_5-Al_2TiO_5.

After the minimum liquidus temperature point there is general agreement between the two sets of data that the order of phase crystallisation from the liquid is: $Mg(Al,Ti)_2O_4$], $MgTi_2O_5$-Ti_3O_5-Al_2TiO_5, and Mg_2SiO_4. However, FactSage calculations predict that at high MgO concentrations between 27wt% and 30wt%, Mg_2SiO_4 would crystallise before $MgTi_2O_5$-Ti_3O_5-Al_2TiO_5. In addition, there is a general disagreement in terms of the sub-liquidus crystallisation temperatures. This disagreement may be attributed to the challenges relating to the complexities associated with the completion of the tests at pO_2 of 10^{-16} atm – the test failure rate was high, and thus there was a natural desire to minimise the tests conducted under these challenging conditions.

4.5 Evaluation of established phase equilibria against real plant titaniferous slag

The phase equilibria data available in the open literature (Jochens, et al., 1969; McRae, et al., 1969; Jochens, 1967) and the ones established in the current study in air and at pO_2 of 10^{-16} atm were evaluated further against real plant titaniferous slags. The titaniferous slag produced by EHSV was used as a case study. The bulk chemical composition of the EHSV titaniferous slag is included in Table 7. Backscattered electron images and EDS analysis results of the EHSV titaniferous slag are shown in Figure 23. The differences in the cooling mechanisms between the EHSV slag, which was relatively slow cooled, and the slags evaluated in the current development work were ignored for the purpose of the current study.

The intensities and shapes of the crystals of spinel and pseudobrookite solution phases in Figure 23 suggest that any of these phases could have crystallized first directly from a complete liquid. From this data, it is still not clear which of the two phases is a primary phase. The other phases are perovskite and diopside. The set of phases reported in Figure 23 is similar to that reported for typical titaniferous slags in Figure 10 (Pistorius, 2011).

The chemical composition of the EHSV slag is noticeably different in terms of Ti, MgO and CaO from that used in the development of Jochens' and the updated equilibrium phase diagrams. However, with consideration of CaO+MgO in the current slag analysis, indicative phase stabilities could still be attained from Jochens' phase diagram or updated phase diagram shown in Figure 53. The chemical composition of the EHSV slag suggests that the phase stability in the slag can be approximated by that of the composition with MgO: CaO wt% ratio of about 16:14 on the equilibrium phase diagrams.

Jochens' equilibrium phase diagram predict the crystallisation of pseudobrookite solid solution as the primary phase under the reviewed slag composition; however, it does not predict the crystallization of spinel solid solution. The updated phase equilibria shown in Figure 53 established in the current work from thermochemical simulation using FactSage and validated using experimentation at pO_2 of 10^{-16} atm predict that in the reviewed composition of the EHSV slag, the spinel solid solution would crystallise as the primary phase, followed by crystallisation of the pseudobrookite solution. Hence, the phase equilibria established in the current study at pO_2 of 10^{-16} atm were accepted as the best available for predicting the crystallisation of phases in titaniferous slags.

Phase equilibria using the exact chemical composition of the EHSV slag shown in Table 7 were also calculated using the FactSage software that was equipped with the updated Al-pseudobrookite thermodynamic database. Figure 63 shows the ccalculated equilibrium phase diagram at varying pO_2 for the EHSV slag with the chemical composition: TiO_2 = 33.0wt%, SiO_2 = 21.6wt%, and Al_2O_3 = 14.0wt%, MgO = 14.3wt%, CaO = 11.8wt%, and FeO = 3.59wt%. These results show that the $Mg(Al,Ti)_2O_4$ crystalizes as a primary phase throughout the reviewed pO_2 range, followed by $MgTi_2O_5$-Ti_3O_5-Al_2TiO_5 solid solution. Perovskite is crystallised as a ternary phase around a pO_2 of 10^{-16} atm, which was estimated as the operational pO_2 during titanomagnetite smelting.

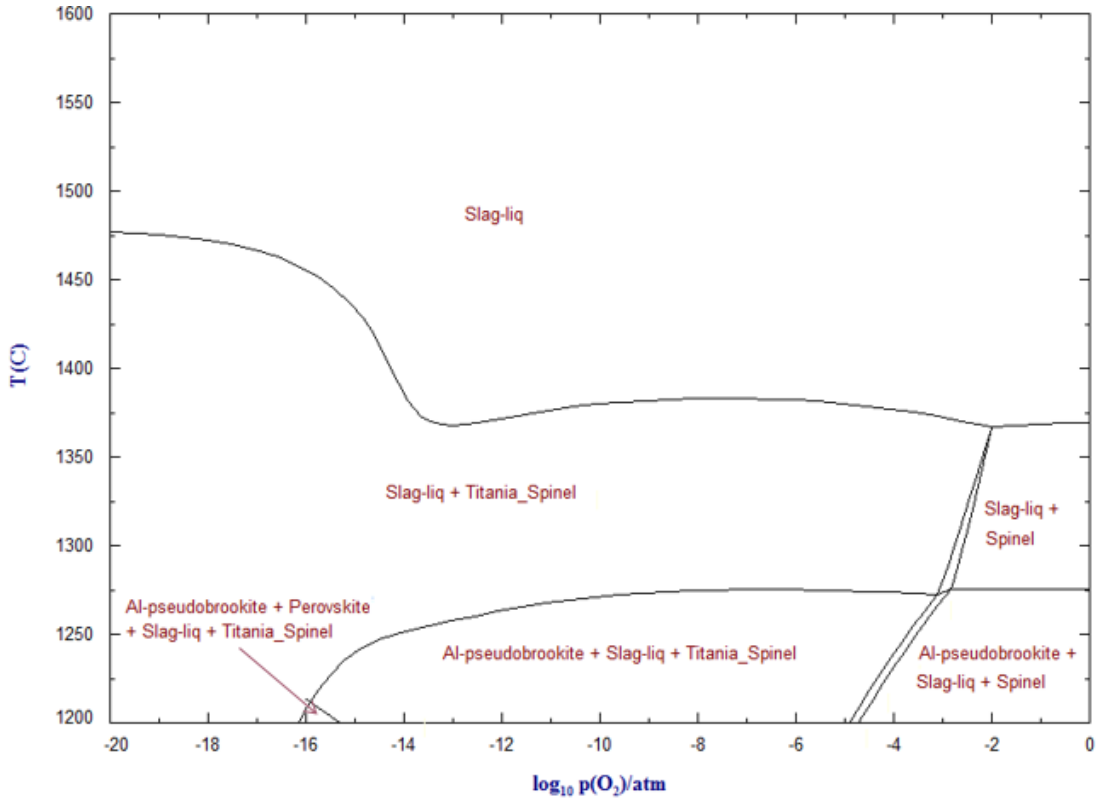

Figure 63: Calculated equilibrium phase diagram at varying pO_2 for the EHSV slag with the chemical composition: TiO_2 = 33.0wt%, SiO_2 = 21.6wt%, and Al_2O_3 = 14.0wt%, MgO = 14.3wt%, CaO = 11.8wt%, and FeO = 3.59wt%

4.6 Evaluation of the best titaniferous slag composition for beneficiation

As discussed above, the phase equilibria calculated at pO_2 of 10^{-16} atm using FactSage software equipped with a private Al-pseudobrookite solid solution database provide the best approximation of the crystallisation of phases in titaniferous slags. The objective of the original work by Jochens (1967) was to provide phase equilibria data in titaniferous slags that would be fluxed with limestone, limestone-dolomite, dolomite-magnesite, and magnesite. With a better understanding of the phase equilibria after the current study, the calculated phase equilibria were used to identify a suitable slag chemistry with no crystallisation of the spinel solution phase for subsequent beneficiation to produce titanium products. The updated phase equilibria show that the crystallisation of the spinel solid solution occurs over a significant compositional range. An increase in the MgO concentration in the slag increases the tendency of the crystallisation of the $Mg(Al,Ti)_2O_4$. However, the updated phase equilibria show that a spinel-free titaniferous slag would contain a maximum of about 2wt% MgO. Thus, the fluxed titanomagnetite smelting would need to

be conducted using an MgO free limestone flux. A slag with such a low MgO concentration would have a relatively high liquidus temperature. The costs of operational process temperature increase would be compensated by the sales of the titanium products.

As it will be clear in CHAPTER 5, the smelting of a titanomagnetite, using the South African MML titanomagnetite as a case study, in the presence of an MgO-free limestone flux and low ash reductant can produce titaniferous slag with about 4wt% MgO concentration. The MgO in the titaniferous slag would come from the feed titanomagnetite concentrate.

The effect of pO_2 and temperature on the crystallisation of phases in the titaniferous slag with 4wt% MgO concentration was investigated further by calculation using FactSage. The calculation was conducted in order to evaluate that the produced slag would contain a spinel structure. The calculated phase equilibria suggest that the $Mg(Al,Ti)_2O_4$ will indeed crystallise in the titaniferous slag with 4wt% MgO concentration. Stoichiometrically, the slag can crystallise a maximum of 14.1wt% $MgAl_2O_4$ – this assumes the worst case scenario where all the MgO crystallise as spinel. However, as shown in the phase diagram, some MgO will crystallise into the $MgTi_2O_5$-Ti_3O_5-Al_2TiO_5 solid solution, particularly around the estimated operational pO_2 of 10^{-16} atm. To minimize the crystallisation of the detrimental $MgAl_2O_4$ in titaniferous slags, it is best to reduce the MgO in the matrix. It would however be possible to produce a saleable titania material with more than 80wt% TiO_2 from a titaniferous slag fluxed with MgO-free limestone.

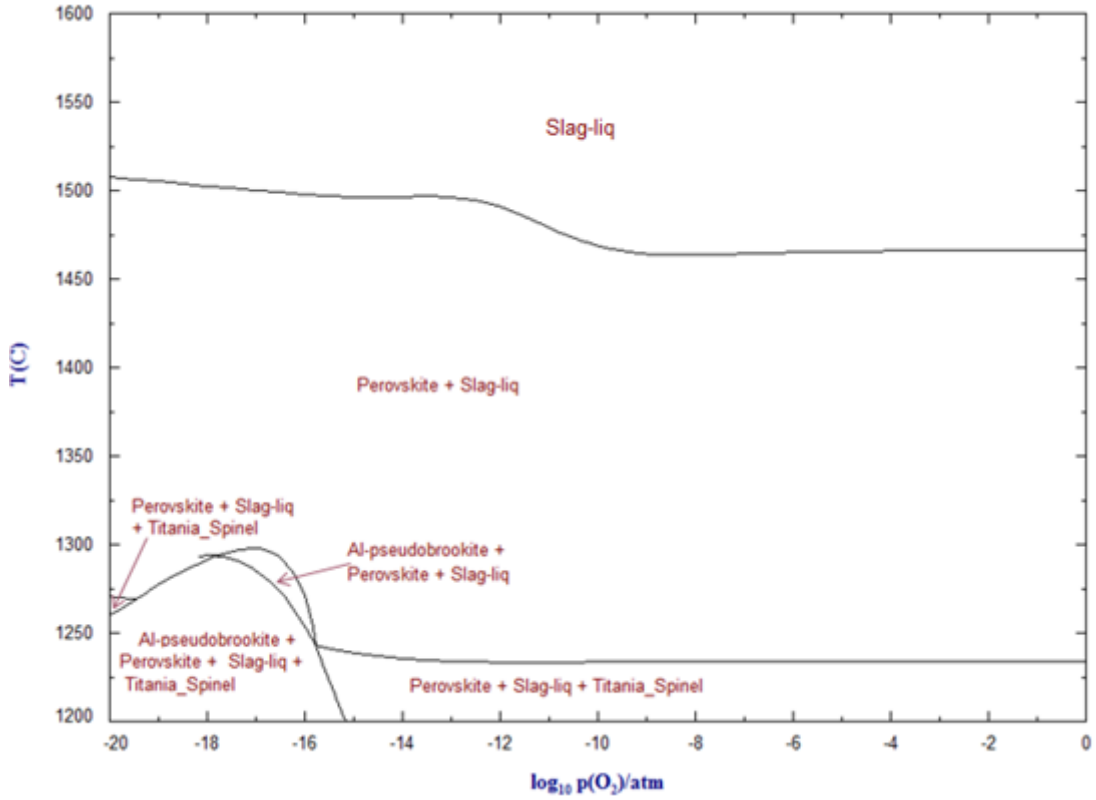

Figure 64: Effect of pO_2 and temperature on the phase equilibria of the limestone fluxed titaniferous slag with the composition: TiO_2 = 37.19wt%, SiO_2 = 19.69wt%, and Al_2O_3 = 13.12wt%, MgO = 4wt% and CaO = 26wt%

4.7 Conclusions

Thermodynamic modelling and experimentation have been conducted to study the phase equilibria of titaniferous slags with a view of identifying a treatable slag chemistry for subsequent beneficiation to produce titanium products. The following conclusions were formulated from this study of the Ca-Mg-Al-Si-Ti-O system applicable to titaniferous slags:

- A private $MgTi_2O_5$-Ti_3O_5-Al_2TiO_5 (Al-pseudobrookite) thermodynamic database was developed using the CALPHAD principles and subsequently incorporated into FactSage to facilitate the calculation of phase equilibria of titaniferous slags. The database was successfully validated by comparing the modelled $MgTi_2O_5$-Ti_3O_5 binary with that of the customary pseudobrookite in FactSage.

- The FactSage software equipped with updated databases was used to calculate phase equilibria in air for Ca-Mg-Al-Si-Ti-O system in the compositional range of

titaniferous slags in order to review and update the available phase equilibria in literature (Jochens, 1967). The updated phase equilibria were validated using results of equilibration-quenched-EPMA analysis method.

- The FactSage software equipped with the updated databases was also used to calculate phase equilibria in the Ca-Mg-Al-Si-Ti-O system in the compositional range of titaniferous slags at low pO_2 applicable to titanomagnetite smelting. The liquidus surface of titaniferous slags increased with decreasing the pO_2. Moreover, the Ti^{3+} content in the titaniferous slags also increased with decreasing pO_2 – the rate of increase is exponential and became significant at pO_2 between 10^{-10} to 10^{-16} atm. Phase equilibria calculated at 10^{-16} atm were successfully validated using equilibration-quench results and the phase chemistry of a real plant titaniferous slag. The validated phase equilibria confirmed that $Mg(Al,Ti)_2O_4$ crystallises as a primary phase in titaniferous slags with high MgO concentrations - the Al-pseudobrookite generally crystallised as a secondary phase.

- The established phase equilibria at 10^{-16} atm show that $Mg(Al,Ti)_2O_4$ has a very large crystallisation range in the reviewed titaniferous slag compositional range. However, it is feasible to produce a titaniferous slag with no spinel crystallisation when the MgO content in the slag is below 2wt%. To produce the spinel-free titaniferous slag for subsequent beneficiation, an MgO free limestone flux and low ash reductant would be required during the smelting of titanomagnetite – the South African MML titanomagnetite concentrate would typically produce a titaniferous slag with about 4wt% MgO. Thus some spinel will be crystallised in the titaniferous slag produced from the smelting of the MML titaniferous magnetite.

CHAPTER 5

BENEFICIATION OF TITANIFEROUS SLAGS

5.1 Introduction

Titaniferous slags produced as by-products in the smelting of titanomagnetite are typically described by the Ca-Mg-Al-Si-Ti-O system. The fluxed titaniferous slags generally contain attractive TiO_2 grades of 20-40wt% (Hassell, et al., 2016; Steinberg, 2008; Taylor, et al., 2006; Sui, et al., 2004). However, they are not beneficiated because they comprise complex phase chemistry, including the chemically inert spinel solid solution [$Mg(Al,Ti)_2O_4$] that cannot be handled by the available titania slag upgrading technologies (Pistorius, 2011).

Low grade titania resources are effectively upgraded to marketable titania feedstock grade through one of many technologies published in the open literature (Van Vuuren & Tshilombo, 2011; Fouad, 2005; Van Dyk, 1999; Borowiec, et al., 1998). Amongst these processes, the upgraded slag (UGS) process is established for upgrading low grade Titania slags containing high levels of alkaline earth impurities (Borowiec, et al., 1998; Doan, 1996). This technology is in use at a commercial scale in Canada for upgrading the SORESLAG^{TM} produced from the Allard Lake ilmenite that contains high levels of alkaline earth impurities (Doan, 1996). In the UGS process, the impurity bearing phases in the slag are decomposed, followed by leaching of impurities (Borowiec, et al., 1998). It is thus very important that the phase chemistry of the slag is suitable for subsequent beneficiation.

The phase equilibria studies of titaniferous slags reported in CHAPTER 4 revealed that titaniferous slags have a varying phase crystallisation range depending on the smelting recipe. Most importantly, the updated phase equilibria of the Ca-Mg-Al-Si-Ti-O system in the compositional range of titaniferous slags at low pO_2 applicable to titanomagnetite smelting showed that titaniferous slags that are free from the detrimental $Mg(Al,Ti)_2O_4$ can be produced when the MgO concentration in the reviewed compositions is below 2wt%.

The current section of the thesis reports on production of titaniferous slag with little or no spinel, followed by beneficiation using the UGS process. The best UGS conditions were investigated using both the produced titaniferous slag and the readily available titaniferous slag produced by the defunct Evraz Highveld Steel and Vanadium Corporation (EHSV).

5.2 Experimental

5.2.1 Experimental plan

A series of experiments were conducted according to the following themes:

- Smelting production of spinel-free titaniferous slags using conventional and special cold crucible induction furnaces.
- Beneficiation testwork of the EHSV titaniferous slag using the UGS process
- Beneficiation testwork of the titaniferous slags with little or no spinel phase using the UGS process

5.2.2 Smelting tests

The MML titanomagnetite concentrate with the composition shown in Table 7 was smelted in the presence of SASCARB reductant and synthetic flux to target a titaniferous slag with minimum or no spinel phase crystallisation. The reductant addition was calculated using Equations [5.1] and [5.2]. Based on previous testwork conducted at Mintek (Maphutha, et al., 2017; Sitefane, et al., 2017) , the stoichiometric reductant addition in the smelting recipe was maintained at 110%.

$$Fe_3O_4 + 4C = 3Fe + 4CO \quad [5.1]$$

$$V_2O_5 + 5C = 2V + 5CO \quad [5.2]$$

The fluxing strategy adopted in the testwork aimed to achieve a titaniferous slag with minimum or no crystallisation of the spinel solid solution. In order to be able to relate to the new phase diagram established at pO_2 of 10^{-16} atm shown in Figure 50, the amounts of SiO_2 and Al_2O_3 in the smelting recipe and the overall flux size (for TiO_2 control) were adjusted such that the subsequent titaniferous slag would have an approximate chemical composition of: SiO_2 = 19.69wt%, Al_2O_3 = 13.12wt% and TiO_2 = 37.19wt%.

Titania bearing slags are known to be corrosive to typical alumina and magnesia based refractories; thus the contamination of the slag by the crucible is inevitable (Maphutha, et al., 2017; Pistorius, 2004). With the desire of producing an uncontaminated titaniferous slag for the subsequent beneficiation testwork, the titanomagnetite smelting was conducted in a

graphite crucible. The use of a graphite crucible was discontinued because in the first test, a product with poor separation between the slag and the metal was produced. The poor separation of the products was attributed to the reduction of Ti to form high melting Ti(OC) species which increased the slag viscosity (Steinberg, 2008).

The titaniferous slags with clear separation from the corresponding alloys were produced in a conventional induction furnace equipped with a ceramic crucible and in a special induction furnace equipped with water cooled copper crucible. For the purpose of the current study in which the MgO addition would result in the formation of the chemically inert spinel phase, it was deemed undesirable to use a magnesia crucible during the smelting in a conventional induction furnace. In the previous study of the effect of crucible wear on the chemistry of titaniferous slag with MgO to CaO ratio of 14:16 (typical EHSV slag), Maphutha et al. (2017) found that the MgO dissolution from the crucible into the slag results in the alteration of the phase composition of the slag, whereas Al_2O_3 contamination from the crucible did not significantly change the phase composition of the slag. Hence, alumina crucibles were used during the smelting testwork.

5.2.2.1 Production of titaniferous slags for beneficiation tests

Based on the updated phase equilibria reported in Figure 50, laboratory scale smelting testwork was conducted to produce a titaniferous slag with minimum possible spinel for subsequent beneficiation using the UGS process. Without adding the MgO as part of the flux in the smelting recipe (and maintaining the flux size), it is anticipated that a titaniferous slag with MgO: CaO mass ratio of 4:26 would be produced. According to the updated phase equilibria, this slag composition would crystallise a little bit of $Mg(Al,Ti)_2O_4$. The titaniferous slags with minimum possible $Mg(Al,Ti)_2O_4$ were produced using the conventional and special cold crucible induction furnaces.

To test the UGS process on a slag with a considerably high $Mg(Al,Ti)_2O_4$ content, the EHSV titaniferous slag with a typical MgO: CaO ratio of 14:16 was used.

A summary of the smelting recipes and conditions is given in Table 16. The scale of the smelting test in the conventional induction furnace was based on 1000 g of MML in order to produce sufficient sample for the subsequent slag beneficiation testwork. However, the tests in the cold crucible induction furnace were conducted at 300 g scale because of a limitation in the crucible size – there was an additional mass of 20 g of the Fe metal

susceptor. The respective smelting recipes, without the Fe susceptor in the case of smelting in a cold crucible, were mixed by milling in a ring mill to produce a homogeneous blend.

Table 16: Summary of the normalised smelting recipes (wt%) and some test conditions

Test	MML	SASCARB	CaO	Al_2O_3	SiO_2	Fe metal Susceptor	MgO:CaO	Induction Furnace	Crucible
1	73.58	13.80	7.68	0.44	4.49		4:26	Conventional	graphite
2	73.62	13.80	7.65	0.44	4.49		4:26	Conventional	alumina
3	68.53	12.81	7.12	0.42	4.17	6.94	4:26	Cold crucible	Copper
4	68.51	12.77	7.11	0.42	4.19	7.01	4:26	Cold crucible	Copper
5	68.57	12.81	7.14	0.42	4.18	6.88	4:26	Cold crucible	Copper

Conventional induction furnace smelting

For tests in the conventional induction furnace, the recipes were quantitatively weighed and densely packed in respective graphite and alumina crucibles – holes were made on the packed material to open a passageway for the flow of anticipated CO and other emissions during the smelting process. The respective charged crucibles were placed onto the conventional induction furnace as shown in Figure 31.

Incremental power input to the induction furnace were applied to heat up the sample to 1600°C and kept at this temperature for an hour before allowing it to cool down to room temperature in an Ar atmosphere – the products were cooled down by switching off the induction furnace power while the cooling water circuit was left open during cooling. The heating profiles of the samples are shown in Figure 65.

On completion of testwork, each crucible was collected from the furnace chamber, weighed and subsequently broken down to recover the alloy and slag. Alloy and slag samples were prepared and analysed by ICP-OES and LECO. The slag samples were also analysed by SEM-EDS and XRD.

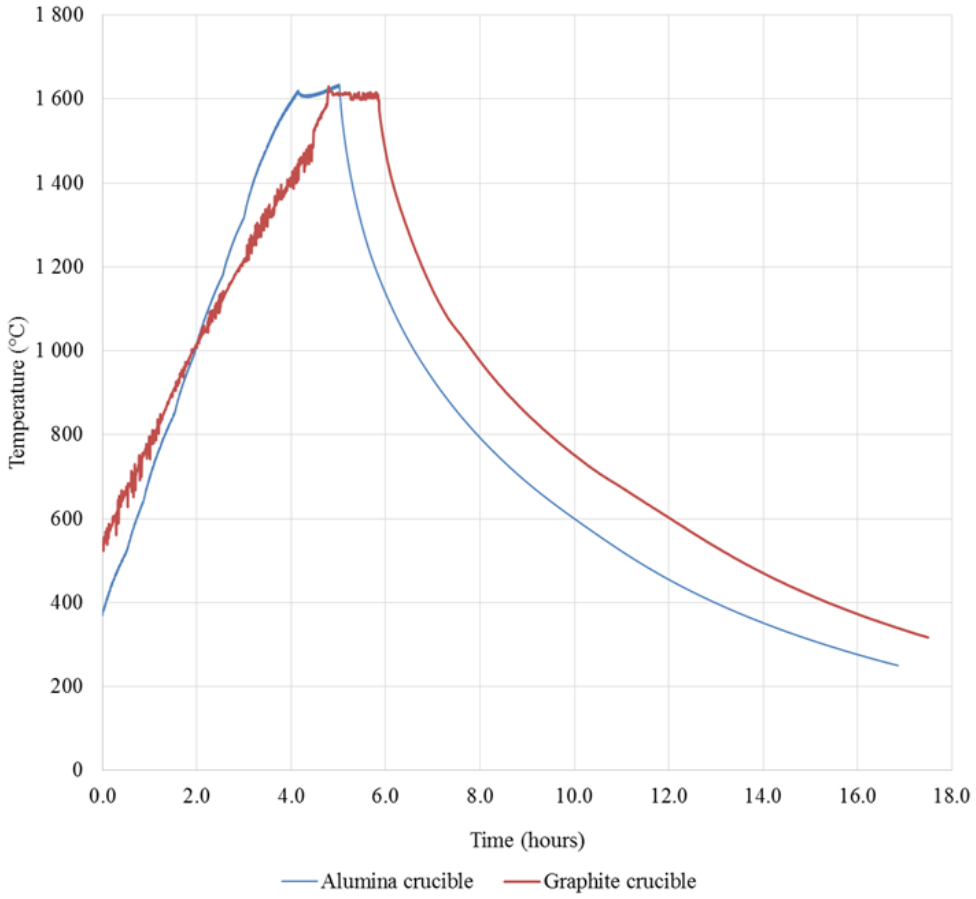

Figure 65: Heating profiles of the samples during the respective smelting tests in the conventional induction furnace

Cold crucible induction furnace smelting

The titaniferous slag produced in the conventional induction furnace was contaminated by Al_2O_3 from the crucible wear, and that resulted in substantial crystallisation of the detrimental $Mg(Al,Ti)_2O_4$. Hence, a titaniferous slag with minimum possible $Mg(Al,Ti)_2O_4$ was produced in the cold crucible induction furnace.

The production of the titaniferous slag in the cold crucible induction furnace was replicated in order to assess the repeatability of results and also produce sufficient sample for subsequent beneficiation. To complete each test, the recipe was quantitatively transferred into the boron nitride coated copper crucible. The Fe metal susceptor was placed on top of the smelting recipe. The crucible was placed onto the induction furnace setup described in section 3.3.3 of CHAPTER 3 – the water flows were opened in order to start with the testwork.

The Pyrex cylinder enclosing charged copper crucible was evacuated to a range of 0.6-1 kilopascal (kPa). The atmospheric air in the cylinder was replaced with Ar gas, after which the system was opened to allow a continuous flow of Ar at a rate of 1.7 normal litres per minute (NL/min). The smelting test was then completed by raising the input power of the induction furnace to 80% and allowed the test to continue for 10 minutes. The reactions inside the crucible were typically vigorous in the first 5 minutes and subsequently slowed down until there was no activity after 8 minutes. The test was left for an additional 2 minutes to ascertain that all reactions have completed. During the smelting test, the Fe metal susceptor would melt and sink to the bottom of the crucible while heating and melting the charged mixture underneath. Typically, the recipe melted and produced a titaniferous slag and a vanadium bearing pig iron which was diluted by the settling susceptor iron metal. It is inherent to the cold crucible induction furnace smelting that not all the charge reacts because of the formation of an instant freeze lining on the walls of the copper crucible. These phenomena make the mass balance and the simulation of real process dynamics challenging. However, for the purpose of producing a titaniferous slag to demonstrate the feasibility of producing a marketable titania product, the produced slag was deemed acceptable.

There was no available option for the measurement of the melt temperature during the execution of these experiments. However, visual inspection of the melt inside the cold crucible were deemed satisfactory for the purpose of the production of the titaniferous slag for subsequent beneficiation testwork.

At the end of the test duration, the power to the furnace was shut off. The water circuits on the setup were left open for a duration of 30 minutes in order to allow the products to solidify. The titaniferous slag and alloy products were collected and subjected to characterisation as described in the case of the smelting products of the conventional induction furnace above. For the subsequent UGS processing, the respective titaniferous slags were composited.

5.2.3 Scoping UGS process testwork on the EHSV slag

The conventional upgraded slag (UGS) process entails the following steps: sampling and sizing of the slag, oxidation of the sized slag, strictly controlled reduction of the oxidised slag, HCl leaching of the oxidised-reduced slag to remove impurities and calcination of the solid residue to produce a high purity TiO_2 product (Borowiec, et al., 1998; Doan, 1996). In

cases of titania slags containing high silica concentrations, a penultimate caustic soda leaching stage is added to remove silica (Doan, 1996).

In the current testwork, indicative conditions of the UGS process for the production of a saleable titania product from titaniferous slags were investigated using the abundant waste EHSV titaniferous slag as a case study.

5.2.3.1 Sample sizing

The bulk lumpy EHSV slag of 5 kg in mass was crushed using a laboratory jaw crusher. The crushed sample was split into 20 subsamples using a rotary splitter. Subsamples making a total of about 2 kg in mass were combined and subsequently screened and classified to a typical fluidised bed size range of 150-600 µm, which is within the literature size range of 106-850 µm (Borowiec, et al., 1998), using conventional sieves.

The bulk chemical and mineralogical characteristics of the EHSV slag are included in section 3.2 of CHAPTER 3.

5.2.3.2 Oxidative and reductive roasting

The oxidative and reductive roasting conditions were not optimised in the current testwork programme. Instead, the established conditions available in the open literature were adopted (Doan, 1996). The procedure entailed the measurement of 400 g of the sized EHSV titaniferous slag and quantitative transfer into a quartz tube reactor of the laboratory scale fluidised bed furnace setup. The charged quartz tube reactor was fitted in the fluidised bed furnace setup. The argon gas flow was opened on the cylinder and rotameter to flow at 10 NL/ min in order to fluidise the sample. The furnace power was switched on in order to heat up the sample at 10°C per minute to 875°C. At this temperature, the Ar gas flow was replaced with air to oxidise the sample for 2 hours before changing back to Ar and cooling the sample to room temperature by switch off the power of the fluidised bed furnace. A small sample of oxidised slag was withdrawn from the reactor and subsequently subjected to XRD and SEM analyses.

The remaining oxidised material was subjected to reduction as per the heating cycle used during oxidation, except that the flow of air at the holding temperature was replaced with carbon monoxide (CO) which operated for 0.5 hours. The oxidative-reductive roast was

collected from the reactor. A subsample was subjected to ICP-OES, XRD and SEM-EDS analyses.

5.2.3.3 HCl leaching

The objective of the HCl leaching testwork was to investigate the basic combination of leaching parameters for the removal of detrimental species from the oxidative-reductive roasted EHSV slag to produce a high grade titania product – these conditions would be transferred to processing the other titaniferous slags with little or no $Mg(Al,Ti)_2O_4$. The main parameters in the testwork were pulp density studied at solid to liquid (s: l) ratios of 1:2 (50 weight-volume percentage or w/v%) and 1:4 (25 w/v%); leaching test duration (8 and 24 hours); and HCl lixiviant concentration which was studied at 20wt%, 25wt% and 30wt%.

To complete each leaching test, a suitable volume of the HCl lixiviant solution (100 mL or 200 mL depending on the target pulp density) was measured and transferred into a batch leach reactor (a round-bottomed flask), followed by addition of a 50 g mass of the oxidative-reductive roasted EHSV slag into the same reactor. A magnetic stirrer bar was put in the reactor for agitation of the slurry during leaching. The reactor was immersed into an oil bath in a container which was placed on a magnetic hotplate. The magnetic hotplate was switched on to reflux the slurry at 110°C (measured in the slurry) under constant stirring at a speed of 250 rotations per minute (rpm) for the duration of the test before cooling down to room temperature.

The slurry was filtered through a Whatman 542 hardened ashless filter paper fitted onto a Buchner funnel. The residue was washed by re-slurrying in 200 mL of warm de-ionised water at 60°C and re-filtered. The filter cake was washed further with 50 mL of de-ionised water. A subsample of the residual sample was dried overnight at 105°C using a conventional oven. The dry sample was subjected to particle size distribution (PSD) analysis using sieves to assess the effect of HCl leaching on the PSD.

The dry residue was subjected to bulk chemical analysis by ICP-OES for the subsequent determination of the recovery of species to the leachate and residue product streams. The evaluation of the recovery of TiO_2 between the two product streams was based only on the residue analysis – the recovery to the leachate was determined by difference. The TiO_2 recovery to the residue was calculated using Equation [5.5].

$$\%\ \mathrm{TiO_2}\ recovery\ to\ residue = \frac{\%\mathrm{TiO_2}_{residue} \times Mass_{residue}}{\%\mathrm{TiO_2}_{feed} \times Mass_{feed}} \times 100 \quad [5.5]$$

5.2.3.4 NaOH leaching

The aim of caustic soda (NaOH) leaching was to remove SiO_2 from the HCl leach residue. The investigation of the best combination of process parameters included the study of the effect of pulp density, which was studied at a s: l ratio of 1:1, 1:2, and 1:4.

To complete each leaching test, a volume of 20 mL, 40 mL, or 80 mL of the 2.15 M NaOH solution was measured and transferred into a caustic soda resistant polytetrafluoroethylene (PTFE) reactor (beaker), followed by the addition of a 20 g mass of the HCl leach residue into the same reactor. A magnetic stirrer bar was inserted into the reaction unit. The reactor was closed using a PTFE lid and placed on a magnetic hotplate. The magnetic hotplate was switched on for respective heating and stirring of the slurry at 100°C (measured in the slurry) and 250 rpm for 3 hours before cooling down to room temperature. The slurry was then filtered through a Whatman 542 hardened ashless filter paper fitted onto a Buchner funnel. The filter cake was washed by re-slurrying in 80 mL of warm de-ionised water (60°C) and re-filtered. The filter cake was further washed with 20 mL of de-ionised water while on the Buchner funnel.

5.2.3.5 Calcination

The wet NaOH leach residue was transferred into an alumina crucible and calcined in a muffle furnace at 900°C for 3 hours to remove the volatile matter, crystalline water and other species that might be adsorbed onto the TiO_2 particles. The calcines were subjected to PSD analysis and bulk chemical analysis by sieve classification method and ICP-OES, respectively. Calcines from the best conditions in terms of chemistry were further analysed by XRD and SEM-EDS to determine the phase and morphological characteristics of the upgraded slag.

5.2.4 Beneficiation of a titaniferous slag produced using the conventional induction furnace

The results of the testwork reported in section 5.3.2 showed that the UGS process is unable to decompose $Mg(Al,Ti)_2O_4$ spinel structure in order to upgrade the titaniferous slag to synthetic rutile grade, i.e. to >90wt% TiO_2, that can be used to produce a pigment using the preferred chloride process. Hence, the current testwork was conducted on the titaniferous slag product that, according to the established phase diagram, would contain little or no spinel solid solution, i.e. $Mg(Al,Ti,V)_2O_4$. The titaniferous slag produced in section 5.2.2.1 using the conventional induction furnace was subjected to beneficiation using the best combination of UGS process conditions established in section 5.2.3 using the EHSV slag. The characteristics of the feed slag to the current testwork are included in section 5.3.1.1. However, this slag also contained some $Mg(Al,Ti,V)_2O_4$ due to contamination by the alumina crucible.

The best combination of UGS process conditions that were used to process the titaniferous slag product included sizing the slag to 150-600 µm PSD, fluidised bed roasting of the sized slag of 100 g in mass in an oxidising atmosphere of air at 875°C for 2 hours and later reduction in an atmosphere of CO at 875°C for 0.5 hours, leaching with 20wt% HCl lixiviant under refluxing at 110°C for 24 hours in a pulp density with s: l ratio of 1:4, caustic leaching with 2.15 M NaOH lixiviant at 100°C for 3 hours at a pulp density with s: l ratio of 1:4, and calcination at 900°C for 3 hours. Bulk chemical and mineralogical analyses using ICP-OES, XRD and SEM-EDS as well as PSD examination were conducted at various stages during the UGS processing of the produced titaniferous slag with hypothetically no spinel structure.

5.2.5 Beneficiation of a titaniferous slag produced using the cold crucible induction furnace

The characteristics of the feed slag to the current testwork are included in section 5.3.1.2. The three batches of titaniferous slags produced in the cold crucible induction furnace were blended to make a composite sample. This sample was prepared and processed using the same procedure as for the slag produced in a conventional induction furnace. However, during HCl and caustic leaching of the current titaniferous slag, samples were withdrawn after specific intervals of 4, 24, and 48 hours in case of HCl leaching, and 1, 3, and 24 hours in case of NaOH leaching in order to determine the kinetic behaviour of the system.

5.3 Experimental results and discussion

This section gives a summary of the results and discussion pertaining to the production and beneficiation of titaniferous slags using the modified UGS process.

5.3.1 Smelting test results

The smelting test results are divided into two: smelting testwork in conventional and cold crucible induction furnaces.

5.3.1.1 Smelting in a conventional induction furnace

Titaniferous slags were produced in the current section for beneficiation testwork – two tests to produce slags with the target MgO: CaO ratio of about 4:26 were conducted in graphite and alumina crucibles. Based on the established phase diagram, significant crystallisation of the spinel structure was not anticipated in these tests.

Product appearance and masses

There was no separation between the alloy and slag in the test conducted in the graphite crucible. The poor separation was attributed to the reduction of high oxidation titanium species by graphite to Ti(O,C) species which generally have high liquidus temperatures (Steinberg, 2008). Test 1 products were therefore not processed further.

The typical appearance of the smelting test products produced using an alumina crucible are shown in Figure 66. There was a good separation between the slag and the pig iron. Thus, the fluxing and operating temperatures were adequate. The masses of the products are summarised in Table 17. The mass loss is attributed to the emission of CO as per Equations [5.1] and [5.2]. The mass distributions in the products are similar to theoretical masses.

Table 17: Smelting product masses in the conventional induction furnace (wt%)

Crucible	Loss	Slag	Alloy
Graphite	32.53	67.47	0.00
Alumina	30.67	23.77	45.56

*Failed test due to the poor separation between slag and alloy

Figure 66: Typical appearance of the bulk smelting products

Bulk chemical compositions

The chemical compositions of the pig irons produced in the current study and in the past by EHSV are given in Table 18 (Steinberg, et al., 2011). As reported in the table of results, the totals of the chemical composition of the pig iron produced in the current study are low. The low totals can be attributed to measurement uncertainty.

At EHSV, the furnace control system involved the monitoring of the concentrations of C, V and Ti in the pig iron. The furnace operation was regarded as stable when the desired alloy chemistry was achieved, i.e. the concentrations of C, V and Ti were about 3.5wt%, 1.5wt% , 0.18wt%, respectively – under these conditions, the process was said to be 'chemistry satisfactory'. The C and Ti concentrations in the pig iron produced in the current study are significantly higher indicating that the operational environment was highly reducing. At EHSV, very highly reducing environments were unfavoured as they proved to be energy intensive due to the reduction of unintended components in the melt into the pig iron. This challenge was solved by increasing the feed rates of a correction material used to dilute the intensity of the reducing conditions and control the furnace energy input (Steinberg, 2008).

Under the highly reducing conditions suggested here, Fe and V would be mostly metalized – the Fe and V contents in the pig iron should be above that of EHSV. However, this is not the case in the current results, particularly in the case of Fe. These results thus support the possibility of measurement uncertainty in the determination of Fe and possibly other components of the pig iron. For the purpose of the current study which is aimed at producing a titaniferous slag for downstream beneficiation processing, the alloys are accepted as suitable for co-production of a titaniferous slag.

The pig iron analysis results also show that the concentrations of the slag forming species, i.e. Mg, Al, Si, Ca and Ti, are very high in the pig iron – this is a suggestion of a possible mixing of the slag and pig iron in the analysed samples. Mg, Al, Si, Ca and Ti are more stable as oxides and readily deport to the slag phase during smelting. Higher Si and Ti in the pig iron could also be due to strong reducing conditions in the furnace.

Table 18: Chemical compositions of the bulk test alloys (wt%)

	Mg	Al	Si	Ca	Ti	V	Cr	Mn	Fe	C	Total
EHSV	-	-	0.20	-	0.20	1.29	0.34	-	94.50	3.20	99.70
Current	0.07	0.41	1.37	0.54	1.70	0.94	0.45	0.34	87.69	4.17	97.80

The bulk chemical compositions of the titaniferous slags produced in the current study and the target slag are given in Table 19. The Al_2O_3 concentration in the produced titaniferous slag is high. This is an indication of a severe contamination by Al_2O_3 from the crucible erosion as anticipated from previous studies (Maphutha, et al., 2017; Pistorius, 2004). Thus, the concentrations of the other components of the slags were diluted by Al_2O_3. The chemical composition of the produced slag was calculated to evaluate the would-be chemical composition if there was no Al_2O_3 contamination. The calculated chemical composition of the titaniferous slag is given in Table 20. The calculated chemical species are still significantly different from the target – particularly in the case of SiO_2, CaO and TiO_2. The deviation was attributed to the uncharacteristically high iron content under the excessive reducing conditions (confirmed by high Ti and C in pig iron). From a chemical thermodynamics point of view presented by the Ellingham diagrams (Habashi, 2002), the metallisation of titanium species would occur after the metallisation of the iron species. Hence, the high iron content in the titaniferous slag is attributed to pig iron entrainment. The slags were however processed further to test the efficiency of the UGS process.

Table 19: Chemical compositions of the bulk test slags (wt%)

	MgO	Al_2O_3	SiO_2	CaO	TiO_2	V_2O_5	Cr_2O_3	MnO	FeO	Total
Target	4.00	13.12	19.69	26.00	37.19	0.00	-	-	0.00	100.00
Current	3.43	29.63	12.83	20.73	24.37	0.23	0.06	0.26	7.49	99.05

Table 20: Calculated chemical composition of the slag after correction of Al_2O_3 contamination (wt%)

	MgO	Al_2O_3	SiO_2	CaO	TiO_2	V_2O_5	Cr_2O_3	MnO	FeO	Total
Target	4.00	13.12	19.69	26.00	37.19	0.00	-	-	0.00	100.00
Current	4.25	13.12	15.89	25.67	30.16	0.28	0.07	0.33	9.28	99.05

The distribution of the elements between the product streams is evaluated in terms of the recoveries to the alloy, slag and overall elemental accountabilities as shown in Table 21, Table 22, and Table 23, respectively. Accountability was calculated as the sum of the respective elemental recoveries to alloy and slag, assuming that none of the elements reported to the off gas, which is presumably composed of CO and other volatile matter. The recoveries of Mg, Ca and Ti to the pig iron are uncharacteristically high. However, the V recovery to the pig iron is lower than a minimum of 70% which would be anticipated under such reducing conditions (Goso, et al., 2016; Steinberg, 2008). Moreover, the overall accountability of V is low. The low V recoveries to alloy and poor overall accountabilities can be attributed to the apparent metal entrainment in the titaniferous slag which led to a low pig iron collection, and possibly measurement uncertainty. The determination of minor elements are generally associated with considerable measurement uncertainties because of limitations in the detection limit of typical analytical techniques and methods (Berreda, et al., 2016).

Table 21: Elemental recoveries to the pig iron (wt%)

Mg	Al	Si	Ca	Ti	V	Mn	Fe
5.36	10.08	25.00	4.69	13.30	55.84	90.57	89.68

Table 22: Elemental recoveries to the slag (wt%)

Mg	Al	Si	Ca	Ti	V	Mn	Fe
102.39	89.00	70.69	83.04	73.77	4.94	35.08	3.85

Table 23: Elemental accountabilities (wt%)

Mg	Al	Si	Ca	Ti	V	Mn	Fe
107.7	99.1	95.7	87.7	87.1	60.8	125.6	93.5

Mineralogical compositions

The backscattered electron microstructure, EDS and XRD results of the titaniferous slag produced in the current section are given in Figure 67. A set of phases crystallised in the slag, namely; perovskite, rutile, pseudobrookite solid solution, gehlenite, and spinel solid solution. The decomposition of perovskite phase for the upgrading of TiO_2 can be achieved by NaOH roasting followed by HCl leaching (Wang, et al., 2010). In the modified UGS process with the NaOH leaching stage at high temperatures (Doan, 1996), it is anticipated that the Ca contained in perovskite will be removed as in the case of EHSV slag as demonstrated in section 5.3.2.

Other chemical phases in the slag are not known to be problematic in terms of chemical decomposition, except the $Mg(Al,Ti,V)_2O_4$. Although the bulk chemical composition of the produced slag contains a significant content of iron, the observed microstructure does not show iron bearing chemical phases. In addition, the expected pig iron entrainment in the titaniferous slag is also not observed in the microstructure of the slag. The absence of the iron bearing phases on the microstructure can be attributed to the slag inhomogeneity.

According to the phase diagram in Figure 50, the produced titaniferous slag with an MgO content of 4.25wt% (achieved with no MgO addition in the flux) should have some spinel solution crystals as long as the MgO concentration is more than 2wt%. However, the current slag seems to be crystallizing $Mg(Al,Ti,V)_2O_4$ as one of the major phases. The excessive crystallisation of the $Mg(Al,Ti,V)_2O_4$ in the produced titaniferous slag is attributed to the abundant Al_2O_3 in the melt which is attained from the wear of the test crucible. With an MgO content of 4.25wt%, the spinel content in the titaniferous slag would be about 15wt% if it is assumed that all the MgO would be contained in the magnesia alumina spinel structure. It is further assumed that excess Al_2O_3 in the spinel stoichiometry is deported to other phases such as gehlenite and pseudobrookite. With these assumptions, it is anticipated that the upgrading of the produced titaniferous slag using the UGS process would result in the final titania product containing more than 80wt% TiO_2.

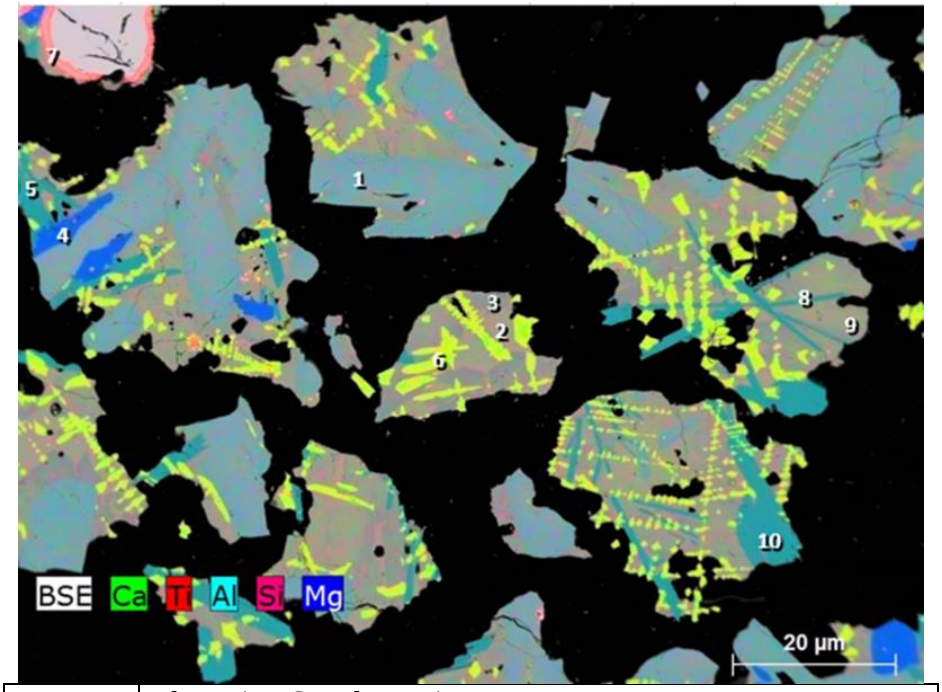

	Phase (EDS and XRD)
1	Titanaugite
2	Gehlenite
3	Titanaugite
4	Spinel solid solution [$Mg(Al,Ti,V)_2O_4$]
5	Pseudobrookite
6	Perovskite
7	Rutile
8	Pseudobrookite
9	Titanaugite
10	Pseudobrookite
	Quartz

Figure 67: Backscattered electron microstructure, EDS and XRD results of the titaniferous slag produced in an alumina crucible using the conventional induction furnace

5.3.1.2 Smelting in a cold crucible induction furnace

In order to eliminate the contamination of the titaniferous slag by the Al_2O_3 crucible wear, titanomagnetite smelting was conducted in a cooled copper crucible induction furnace, which is described in section 3.3.3 of CHAPTER 3.

Product appearance and masses

The typical appearance of the smelting test products in the cold copper crucible is shown in Figure 68. Not all the charge inside the crucible reacted to form the pig iron and the target titaniferous slag – some of the feed recipe formed a freeze lining inside the crucible as a

consequence of the continuous cooling on the surface of the copper crucible. Hence, the smelting test in the cold crucible induction furnace essentially produced four products, namely; (1) the off gas that is primarily composed of CO produced as a consequence of the reduction reactions shown in Equations [5.1] and [5.2]), (2) the freeze lining, (3) the pig iron that is made up of the Fe metal added for induction purposes and, Fe and V produced according to Equations [5.1] and [5.2], and (4) the titaniferous slag.

The slag contained some alloy entrainments. For the direct measurements of the masses of the freeze lining, alloy and slag, efforts were made to separate these materials the best way that is practically possible. The masses of the products are summarised in Table 24. The alloy masses suggest that there was about 80% metallisation of Fe from the titanomagnetite – this view assumes that the starting 20 g of the Fe susceptor was quantitatively recovered. Based on this estimation, the reported freeze lining contents of about 13% are lower than the anticipated contents of about 20%. Some of the unreacted recipe was ejected out of the copper crucible, as it appears on the brim of crucible shown in Figure 68 – the ejection of the unreacted sample was attributed to the violent nature of the smelting reaction in the cold crucible induction furnace. The mass losses presumably due to CO emissions were determined by difference; hence, the mass losses were consequently overestimated.

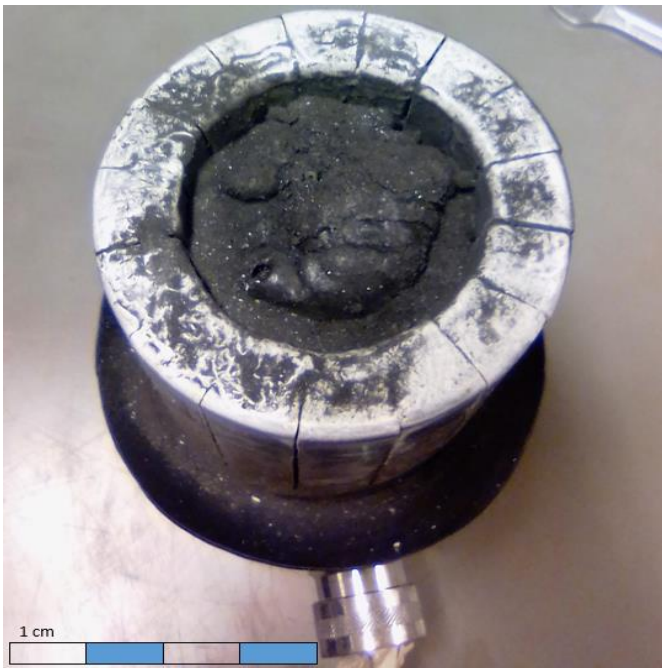

Figure 68: Typical appearance of the smelting test products in the cold copper crucible

Table 24: Smelting product masses in the cold crucible induction furnace (wt%)

Replicate tests	Loss	Freeze lining	Alloy	Slag
3	28.48	13.13	36.04	22.34
4	30.27	12.62	35.60	21.51
5	28.53	13.03	36.05	22.39

Bulk chemical compositions

The chemical compositions of the pig irons produced in the replicate testwork and in the past by EHSV are given in Table 25. These results show that the C and V concentrations in the replicate tests were significantly lower than the 'chemistry satisfactory' composition achieved by EHSV. These results suggest that the smelting conditions were not adequately reducing and/ or the reduction reactions were far from reaching equilibrium. The presence of a substantial freeze lining material and low Fe metallisation degrees of 80% support the view that the conditions were definitely not at equilibrium. The smelting in the cold crucible induction furnace stopped as soon as the induction metal settled at the bottom of the crucible. The suspended slag and freeze lining material were not effective for suscepting the energy from the induction coils. Hence, the smelting testwork was inevitably stopped far from the equilibrium state.

Table 25: Chemical compositions of the pig iron produced in the replicate tests (wt%)

Test	Mg	Al	Si	Ca	Ti	V	Cr	Mn	Fe	C	Total
EHSV	-	-	0.20	-	0.20	1.29	0.34	-	94.50	3.20	99.70
3	0.01	0.03	<0.025	0.01	0.04	0.08	0.10	0.10	98.03	1.54	99.94
4	0.02	0.03	<0.025	0.02	0.04	0.08	0.11	0.11	98.13	1.54	100.08
5	0.02	0.04	<0.025	0.09	0.14	0.02	0.03	0.02	97.95	1.46	99.77

The chemical compositions of the titaniferous slags produced in the replicate tests and the target slag are given in Table 26. The FeO content in the replicate titaniferous slags are consistently higher than the target composition. The high FeO concentrations in the slags support the assumption that the respective smelting tests did not reach equilibrium state. The concentrations of other components of the slags were significantly diluted by the high iron

concentration. Moreover, it appears that the chemical compositions of the produced titaniferous slags, particularly the FeO content, is not comparable to typical titaniferous slags. The properties of the slag may also be distorted from that of the typical titaniferous slag. However, in the absence of a better option, the respective slags were processed further for the purpose of testing the efficiency of the UGS process for the beneficiation of titaniferous slags. The respective product slags were combined to make one composite sample for the downstream processing. The chemical composition of the composite sample is included in Table 26.

Table 26: Chemical compositions of the titaniferous slags produced in the replicate tests (wt%)

Test	MgO	Al_2O_3	SiO_2	CaO	*TiO_2	V_2O_5	Cr_2O_3	MnO	#FeO	Total
Target	4.00	13.12	19.69	26.00	37.19	0.00	-	-	0.00	100.00
3	3.16	7.95	12.40	17.30	22.00	2.90	0.59	0.43	34.20	100.93
4	3.13	7.97	12.30	17.20	22.00	2.90	0.56	0.43	34.30	100.79
5	3.14	7.98	12.50	17.40	22.00	2.93	0.57	0.43	34.40	101.35
Composite	3.14	7.97	12.39	17.29	22.00	2.91	0.57	0.43	34.30	101.01

*Total Ti species (Ti^{3+} and Ti^{4+}) expressed as TiO_2, #Total Fe species (Fe^0 and Fe^{2+}) expressed as FeO

The smelting characteristics of titanomagnetite were evaluated using the distribution of major elements between the product phases. The recoveries of the major elements to the freeze lining, pig iron and slag reported in Table 27, Table 28 and Table 29, respectively. The overall elemental accountabilities are reported in Table 30. In general, the recoveries to respective product phases, and subsequently the overall accountabilities, appear to be distorted. The distortion was attributed to the challenges faced during the separation and quantitative measurements of the product phases – there is a potential of cross contamination between the samples of the product phases. Moreover, the accountabilities of minor elements are considerably incorrect due to measurement uncertainties associated with the determination of minor elements (Berreda, et al., 2016).

Of particular interest is that the recovery of Fe to the slag is in the order of 15%. Thus, the high Fe recovery in the slag phase supports the alleged incompletion of smelting reactions.

Table 27: Elemental recoveries to the freeze lining (wt%)

Test	Mg	Al	Si	Ca	Ti	V	Cr	Mn	Fe	C
3	13.99	12.46	15.21	13.20	12.64	13.13	5.60	14.85	15.45	13.10
4	12.08	12.64	18.12	12.71	12.18	13.26	4.85	14.27	14.87	12.62
5	13.07	13.45	17.48	13.17	13.11	14.59	3.33	13.90	15.30	13.03

Table 28: Elemental recoveries to the pig iron (wt%)

Test	Mg	Al	Ca	Ti	V	Cr	Mn	Fe	C
3	0.65	0.29	0.07	0.27	4.04	153.73	22.64	91.52	4.39
4	1.29	0.29	0.15	0.26	3.99	167.07	24.60	90.51	4.35
5	1.30	0.39	0.66	0.93	1.01	46.11	4.53	91.43	4.16

Table 29: Elemental recoveries to the titaniferous slags (wt%)

Test	Mg	Al	Si	Ca	Ti	V	Cr	Mn	Fe
3	76.88	25.56	217.29	56.54	54.33	50.83	384.68	46.73	15.38
4	73.35	24.63	208.87	54.25	52.34	48.96	351.70	45.01	14.86
5	76.50	25.68	219.36	56.85	54.41	51.43	372.18	46.79	15.50

Table 30: Elemental accountabilities (wt%)

Test	Mg	Al	Ca	Ti	V	Cr	Mn	Fe	C
3	91.52	38.32	69.82	67.24	68.00	544.02	84.21	122.35	17.49
4	86.72	37.56	67.11	64.78	66.21	523.62	83.88	120.24	16.97
5	90.88	39.52	70.68	68.45	67.03	421.62	65.22	122.22	17.19

Mineralogical compositions

The results of the backscattered electron microstructure combined with EDS and XRD data for the composite of the titaniferous slags produced in the cold crucible induction furnace are given in Figure 69. These results show that the titaniferous slag composite was composed

of many phases including perovskite, pseudobrookite, olivine, Fe oxide and iron rich ulvospinel phases. The content of the spinel phase in the slag can be approximated by the MgO concentration in the slag – this is for estimation purposes only. Assuming that most of the MgO crystallise in the magnesia alumina spinel, the titaniferous slag composite can thus be beneficiated to a titania product with about 90wt% TiO_2.

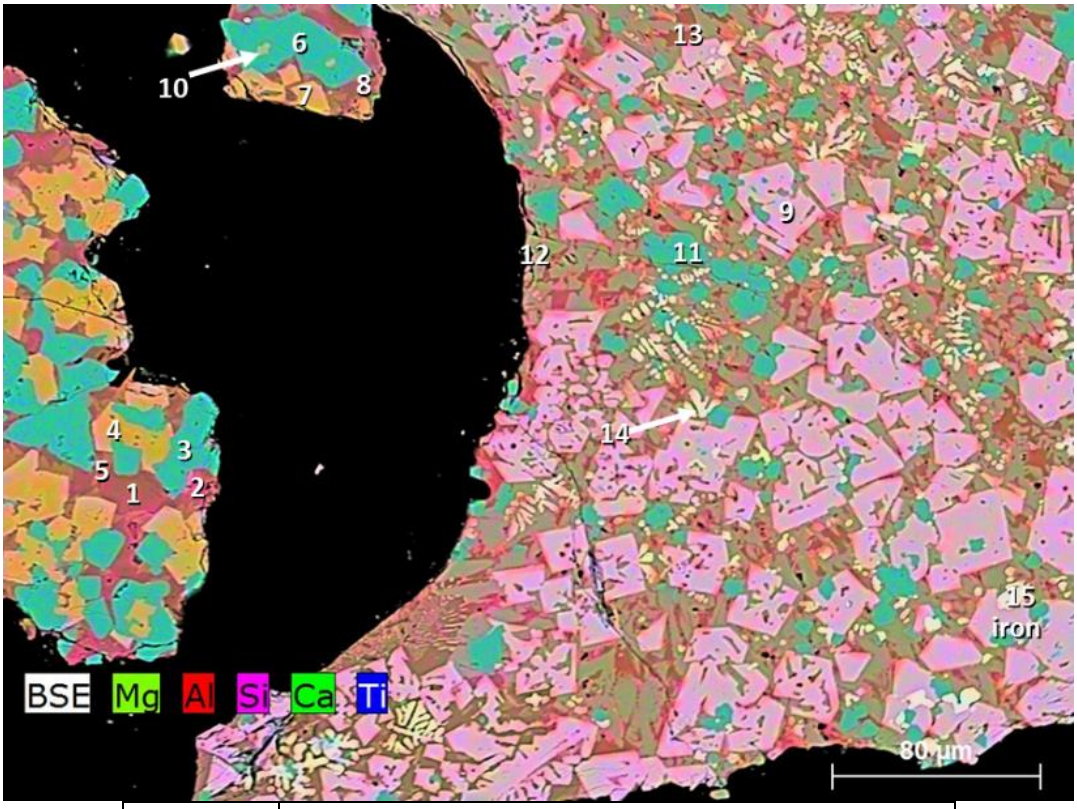

	Phases (EDS and XRD)
1	Titanaugite
2	Titanaugite
3	Perovskite
4	Ulvospinel
5	Titanaugite
6	Perovskite
7	Ulvospinel
8	Titanaugite
9	Ferrous pseudobrookite
10	Perovskite
11	Perovskite
12	Olivine
13	Titanaugite
14	FeO
15	FeO

Figure 69: Backscattered electron microstructure, EDS and XRD results of the composite of the three titaniferous slags produced in the cold crucible induction furnace

5.3.2 Beneficiation of the EHSV titaniferous slag using UGS process

The bulk and phase chemical compositions of the EHSV titaniferous slag that was used as feed in the UGS upgrading testwork are presented in Table 7 and Figure 23, respectively. The backscattered electron micrograph and phase chemical composition of the EHSV slag show that this slag is mainly composed of pseudobrookite solid solution, spinel solid solution [$Mg(Al,Ti,V)_2O_4$], perovskite and non-crystalline species. Titanium is incorporated in all three crystalline phases that are distributed throughout the grains. However, the analysis of the dark phases representing $Mg(Al,Ti,V)_2O_4$ spinel solid solution suggest that the spinel structure primarily host magnesia and alumina. The phase composition of the EHSV slag is similar to the typical titaniferous slag composition reported in literature (Pistorius, 2011).

The XRD and SEM-EDS analysis results of the oxidative and reductive roasted EHSV slag are shown in Figure 70. These results show that there was no significant phase transformation after oxidation of the EHSV slag. The micrograph for the oxidised slag show some bright regions, which can be attributed to metallic iron. The results suggest that the oxidative roasting conditions were non-equilibrium. In any case, the objective of the oxidative roasting is to convert Ti^{3+} species to refractory Ti^{4+} - titanium losses during leaching would be indicative of the severity of the incomplete oxidation stage. As shon in the micrograph for the reduced slag, reductive roasting of the pre-oxidised slag resulted in more metallisation of iron. There is no evidence in the phase chemistry that the metallisation of iron may have been accompanied by the reduction of the HCl inert Ti^{4+} to the relatively soluble Ti^{3+}.

An investigation of the best combination of the UGS conditions was conducted on the roasted EHSV slag. Several parameters were investigated during the HCl and NaOH leaching stages of the modified UGS process. As explained in the experimental procedures, the other parameters were adapted from literature (Borowiec, et al., 1998; Doan, 1996).

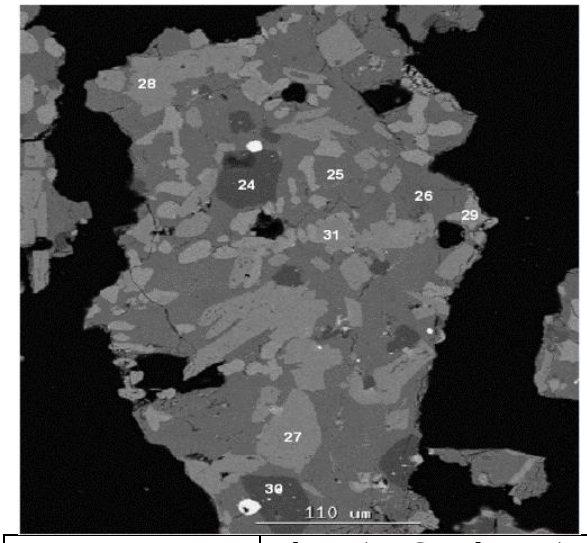

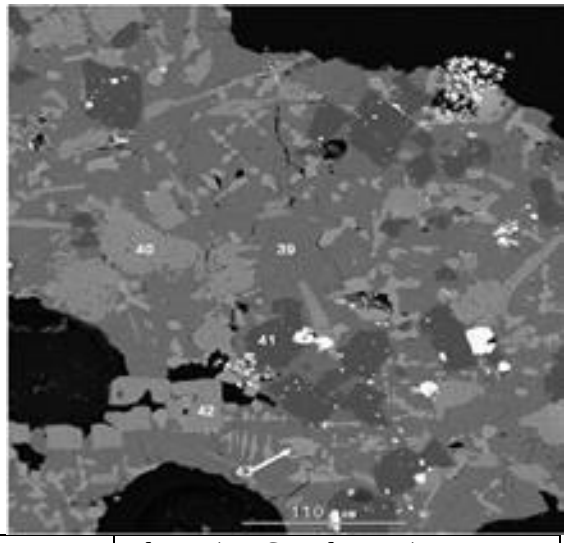

	Phase (EDS and XRD)		Phase (EDS and XRD)
24	$Mg(Al,Ti,V)_2O_4$	39	Non-crystalline
25	Non-crystalline	40	Pseudobrookite
26	Non-crystalline	41	$Mg(Al,Ti,V)_2O_4$
27	Pseudobrookite	42	Pseudobrookite
28	Pseudobrookite		Perovskite
29	Perovskite		Fe
30	$Mg(Al,Ti,V)_2O_4$		
31	Pseudobrookite		
Oxidised EHSV slag		Reduced EHSV slag	

Figure 70: Backscattered electron microstructure, EDS and XRD results of the roasted EHSV slag

5.3.2.1 Effect of HCl lixiviant concentration

The effect of HCl lixiviant concentration on the upgrading of TiO_2 in the EHSV slag was studied. During these studies, the pulp density and the leaching time were kept constant at 25 w/v% (or a solid to liquid ratio of 1: 4) and 24 hours, respectively. The HCl lixiviant concentration was investigated at 20wt%, 25wt% and 30wt%. The results are presented in Figure 71. These results show that the variation of the HCl lixiviant concentration between 20wt% and 30wt% resulted in an upgrade of only 3.2wt% TiO_2 in the leach residues of the EHSV slag. However, the TiO_2 recoveries to the residues were generally high at 90wt% and above.

The chemical compositions of the respective slags are reported in Table 31. These results show that the HCl leaching exercise effectively leached out iron and calcium species in the EHSV slag - there was only limited leaching of Mg, Al and Si species from the slag. It appears that these slightly leached species are contained in phases that are refractory in the HCl lixiviant. These refractory phases are further discussed below in section 5.3.2.3.

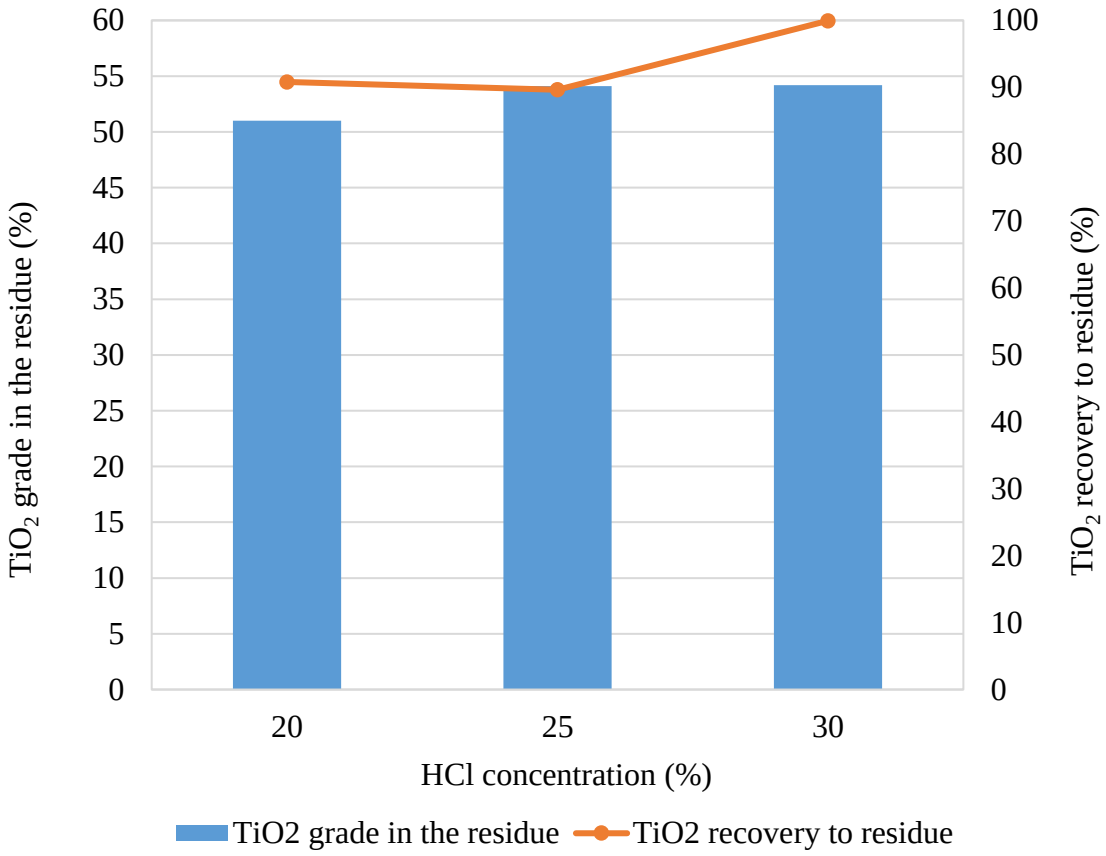

Figure 71. Effect of HCl lixiviant concentration on the TiO_2 upgrading and recovery to residue (product).

Table 31: Chemical compositions of EHSV slag leach residues at different HCl concentrations (wt%)

	MgO	Al_2O_3	SiO_2	CaO	TiO_2	V_2O_5	Cr_2O_3	MnO	FeO
EHSV slag	14.3	14.0	21.6	11.8	33.0	0.82	0.16	0.78	3.59
20wt% HCl lixiviant	7.29	9.75	27.5	3.20	51.0	<0.05	0.19	0.26	0.87
25wt% HCl lixiviant	6.98	10.1	27.3	0.11	54.1	0.90	0.16	0.38	<0.05
30wt% HCl lixiviant	7.59	11.0	25.7	0.10	54.2	0.92	0.18	0.40	<0.05

5.3.2.2 Effect of pulp density during NaOH leaching

Silicon species remained in the leach residue as part of the refractory species during the HCl leaching. Silicate phases are generally dissolved in caustic soda (Doan, 1996). Hence, the caustic soda (NaOH) leaching was adopted in the current study for the dissolution of silicon bearing phases. The NaOH leaching study was conducted on the 20wt% HCl leach residue of the EHSV slag. The effect of NaOH leaching on the upgrading of TiO_2 in the EHSV slag was studied at pulp densities of 25 w/v% (s: l ratio of 1:4), 50 w/v% (s: l ratio of 1:2) and 100 w/v% (s: l ratio of 1:1). The concentration of the NaOH lixiviant concentration and leaching time were adapted from previous studies (Doan, 1996), and were kept constant at 2.15 M and 3 hours, respectively.

The results of the effect of the pulp density during NaOH leaching on the TiO_2 grades and recoveries as a consequence of SiO_2 removal are given in Figure 72. The bar graph shows that the upgrading of TiO_2 in the EHSV titaniferous slag increased with decreasing pulp density. A lower degree of TiO_2 upgrading by 2.3wt% (from 72.3wt% to 74.6wt%) was recorded when the pulp density was lowered from 50 w/v% to 25 w/v%. Further, the TiO_2 recovery to the leach residue generally increased with increasing pulp density. These results show that the highest TiO_2 grade was achieved with the lowest recovery of 83.3%. Further optimization testwork is required to validate these results. A repeat test is reported in section 5.3.2.3.

The bulk chemical compositions of the EHSV slag leach residues after HCl leaching followed by NaOH leaching at different pulp densities are given in Table 32. The results summarised in this table show that the NaOH is indeed capable of removing silicon bearing phases from the EHSV slag. These results concur with those reported in literature (Doan, 1996). The removal efficiency of Si from the EHSV titaniferous slag improves with decreasing the pulp density – the best TiO_2 grade of 75wt% was achieved with the lowest pulp density corresponding to a s: l ratio of 1:4. In addition, these results show that the NaOH leaching is also not able to leach out Mg and Al species. The phases of existence of Mg and Al are reported below in section 5.3.2.3.

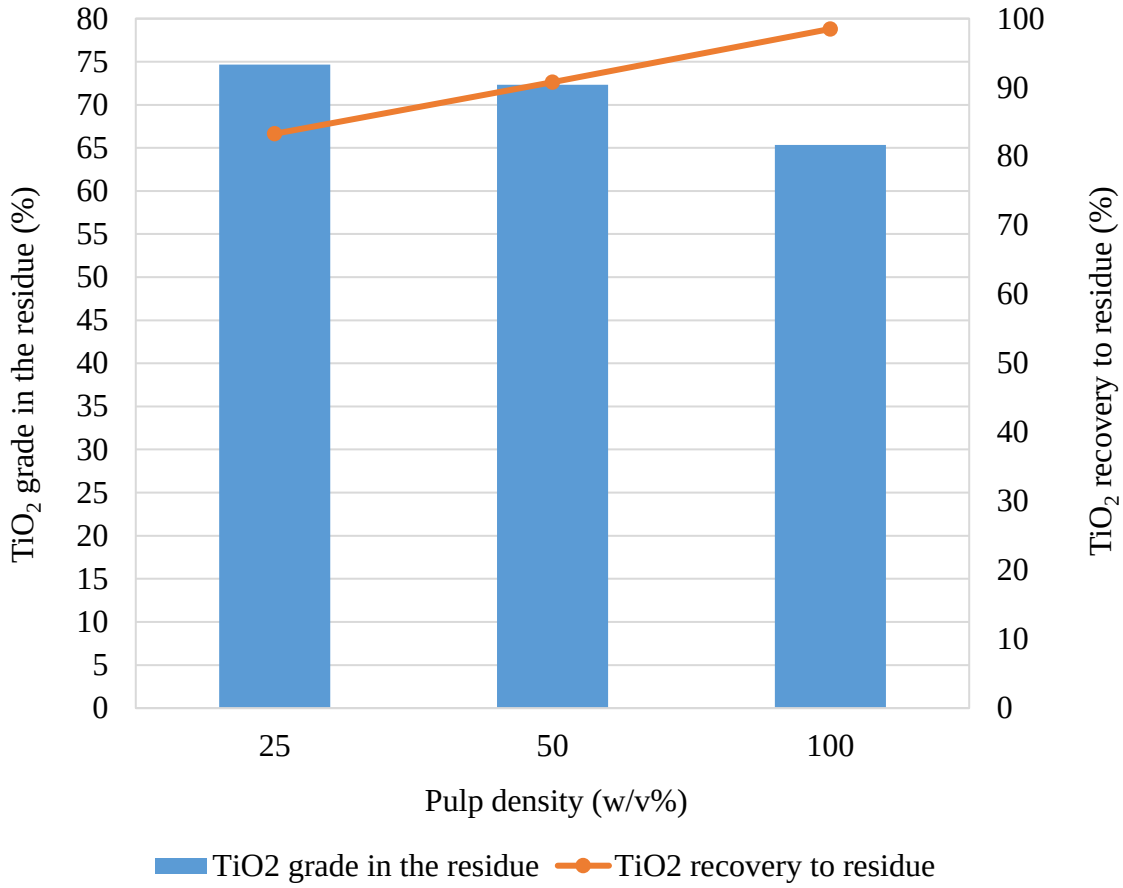

Figure 72. Effect of caustic leaching pulp density on the TiO_2 upgrading and recovery to EHSV slag leach residues.

Table 32: Chemical compositions of EHSV slag leach residues after HCl leaching coupled with NaOH leaching at different pulp densities (wt%)

	MgO	Al_2O_3	SiO_2	CaO	TiO_2	V_2O_5	Cr_2O_3	MnO	FeO
S: l of 1:1	9.62	13.13	5.98	4.14	65.34	<0.05	0.24	0.33	1.23
S: l of 1:2	8.61	13.91	1.60	1.13	72.31	1.08	0.26	0.25	0.84
S: l of 1:4	8.05	12.96	1.10	0.95	74.65	0.97	0.21	0.24	0.86

<0.05wt%: Analyte concentration is below the detection limit which is 0.05wt%

5.3.2.3 Final UGS product from the EHSV titaniferous slag

The best combination of UGS conditions for the processing of the EHSV titaniferous slag were deduced from the results of the preliminary development work reported above, and literature data (Borowiec, et al., 1998). These conditions are: sizing the slag to PSD range of +150-600 µm; fluidised bed roasting at 875°C for 2 hours in air; fluidised bed roasting at

875°C for 0.5 hours in CO; leaching with 20wt% HCl lixiviant under refluxing at 110°C for 24 hours in a s: l ratio of 1:4; and caustic leaching with 2.15 M NaOH lixiviant at 100°C for 3 hours in a s: l ratio of 1:4. The respective residues from the acid and caustic soda leaching stages were subjected to calcination at 900°C for 3 hours. A single pass test was conducted using the best combination of UGS conditions in order to validate the previous results.

The bulk chemical compositions of the HCl and NaOH leach residues are reported in Table 33. As reported in the development work above, these results show that the concentrations of the detrimental species in the EHSV titaniferous slag were lowered significantly, except Mg and Al. Through the un-optimised UGS process, the TiO_2 content in the EHSV titaniferous slag can be upgraded from about 33wt% to 75wt%. The cumulative recoveries of TiO_2 to the final leach residue was in excess of 80%. The rest of the titanium dissolved into solution during the HCl and NaOH leach stages – this titanium should have been in the Ti^{3+} oxidation state, which is fairly soluble in both HCl and NaOH lixiviants (Doan, 1996). The TiO_2 grade in the upgraded EHSV leach residue was still lower than the typical feedstock grade for the preferred chloride pigment production, which is typically 85wt% TiO_2 or above (Pistorius, 2011).

The backscattered electron micrographs and phase compositions of the HCl and NaOH leach residues of the EHSV titaniferous slags produced in the single pass test are shown in Figure 73 and Figure 74. After HCl leaching, it appears that Mg and Al are incorporated in the main titania bearing phase, i.e. pseudobrookite solid solution ($MgTi_2O_5$-$FeTi_2O_5$-Al_2TiO_5), and spinel solid solution [$Mg(Al,Ti,V)_2O_4$], whereas Si is contained in quartz. Pseudobrookite is the main phase occurring in ilmenite slags – ilmenite slags with suitable particle size distribution and TiO_2 grade of >85wt% are established feedstocks for the chloride pigment production process (Pistorius, 2008).

The $Mg(Al,Ti,V)_2O_4$ and quartz were also not leached out during the HCl leaching stage. The spinel structure is by definition inert to chemical treatment (Franke & Heimann, 1970). Quartz was leached during the follow up NaOH leaching stage; however, the spinel and the pseudobrookite solution could not be leached out. In the final leach residue, it appears that the detrimental species, i.e. Mg and Al, are primarily incorporated in a refractory spinel structure – the contents of the detrimental species in the pseudobrookite phase are relatively low. Phase equilibria experimental results at low pO_2 of 10^{-16} atm, i.e. Table 43 in Appendix 1.3, show that the dissolution of Ti into the spinel solid solution is below 5wt%.

A new phase in the form of Na-Ti-Si-O was also observed in the NaOH leach residue. The presence of sodium bearing phases in the upgraded titaniferous slag was attributed to inadequate washing of the residue.

Table 33: Chemical compositions of the final UGS product produced from EHSV titaniferous slag

	MgO	Al_2O_3	SiO_2	CaO	TiO_2	V_2O_5	Cr_2O_3	MnO	FeO
HCl leach residue	4.49	9.50	29.60	0.07	54.60	0.73	0.16	0.19	0.65
NaOH leach residue	8.67	12.84	1.65	0.12	74.14	0.98	0.21	0.26	1.13

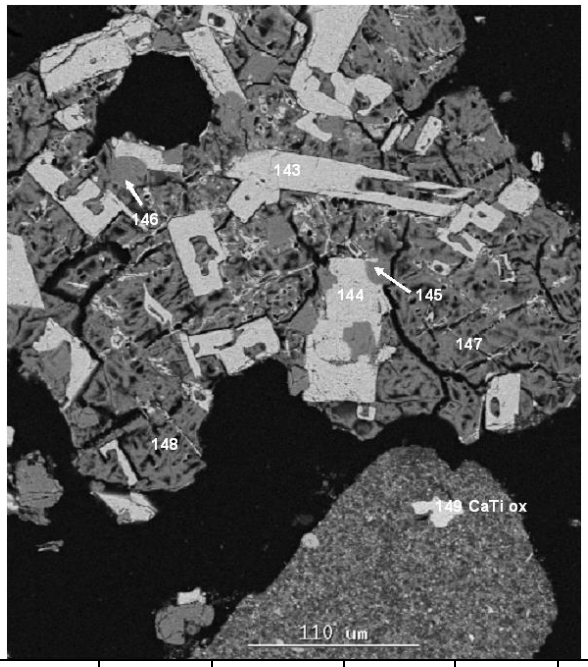

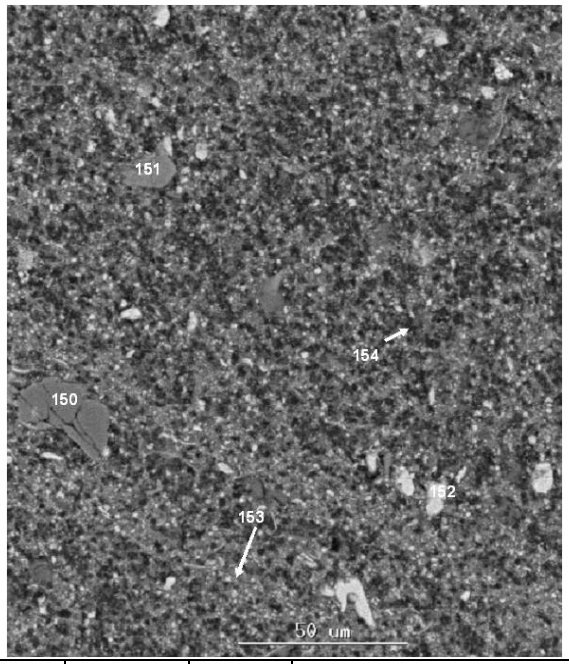

	MgO	Al_2O_3	SiO_2	CaO	TiO_2	V_2O_5	FeO	Phase
143	12.70	4.30	0.10	0.00	78.38	3.04	1.47	Pseudobrookite
144	7.82	4.39	0.32	0.00	82.44	3.53	1.50	Pseudobrookite
145	24.00	62.70	0.00	0.00	6.40	5.70	1.20	$Mg(Al,Ti,V)_2O_4$
146	24.80	66.40	0.00	0.10	4.74	2.57	1.38	$Mg(Al,Ti,V)_2O_4$
147	0.00	0.00	96.72	0.23	2.83	0.23	0.00	Quartz
148	0.10	0.00	97.93	0.10	1.66	0.10	0.10	Quartz
149	0.11	0.53	0.32	40.87	57.76	0.42	0.00	Perovskite
150	24.74	64.47	0.38	0.00	9.84	0.38	0.19	$Mg(Al,Ti,V)_2O_4$
151	23.94	52.71	0.59	0.20	16.65	5.71	0.20	$Mg(Al,Ti,V)_2O_4$l
152	13.85	2.73	0.42	0.00	81.64	0.94	0.42	Pseudobrookite

Figure 73. Microstructure, EDS and XRD results of the HCl leach residue of the EHSV titaniferous slag

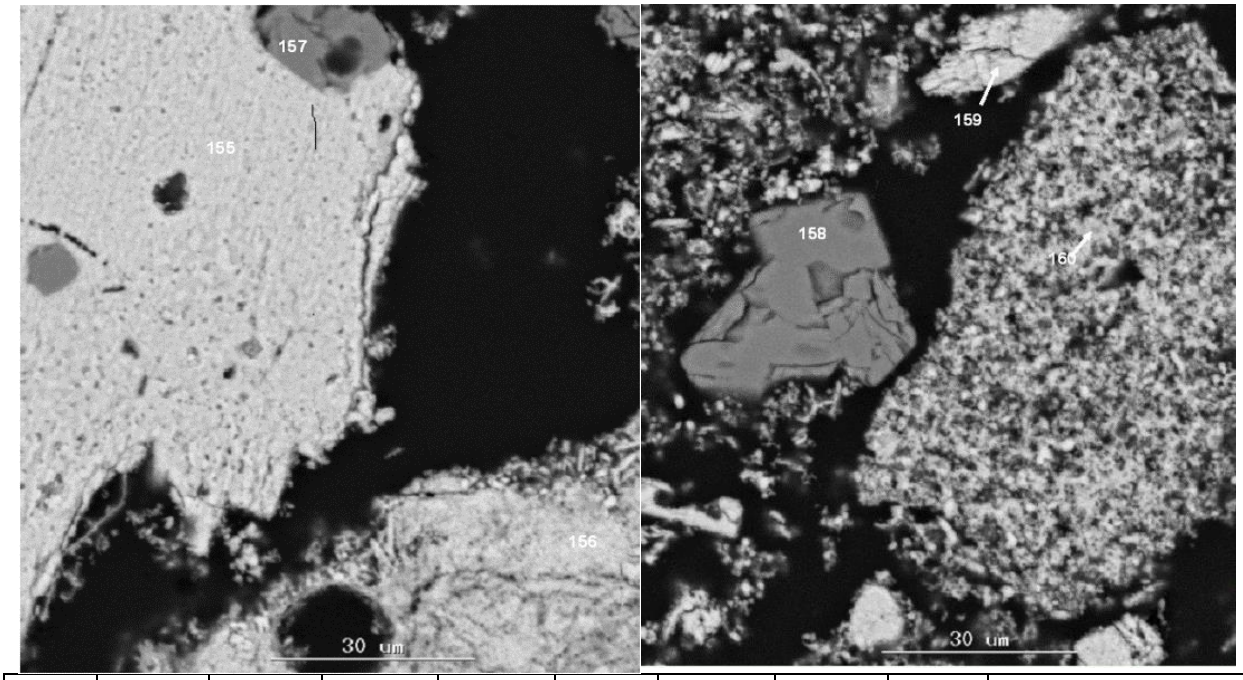

	Na_2O	MgO	Al_2O_3	SiO_2	CaO	TiO_2	V_2O_5	FeO	Phase
155		7.23	2.09	0.21	0.10	89.42	0.10	0.84	Pseudobrookite
156		0.22	1.20	2.72	0.11	95.54	0.00	0.22	Rutile
157		26.21	63.74	0.00	0.00	9.26	0.69	0.10	$Mg(Al,Ti,V)_2O_4$
158		24.44	63.93	0.10	0.00	5.87	4.30	1.37	$(Mg,Fe)(Al,Ti,V)_2O_4$
159		7.57	1.37	0.63	0.11	87.91	1.05	1.37	Pseudobrookite
160	11.95	0.94	0.31	10.75	0.52	72.82	1.98	0.73	Na-Ti-Si-O

Figure 74. Microstructure, EDS and XRD results of the final NaOH leach residue of the EHSV titaniferous slag

Evaluation of particle size distribution during UGS processing

Graphical representation of the particle size distribution (PSD) of the EHSV titaniferous slag as it was processed through the different stages of the UGS process is shown in Figure 75. These curves show that, after the two stage roasting, the PSD of the slag adversely got finer such that over 10% of the particles were below 150 µm. The HCl leaching stage resulted in a significant deterioration of the PSD such that approximately the D_{60} of the residue was below 150 µm (60% of the particles had a diameter of below 150 µm). Further processing of the slag through the NaOH leaching resulted in a further deterioration of the PSD such that the leach residue had a D_{90} of 150 µm as opposed to the starting slag with a D_{100} of +150 µm.

In addition to the unsuitability of the TiO_2 grade in the upgraded EHSV slag for use as feedstock in the preferred chloride process for pigment production, the PSD is also unsuitable as it falls outside the specified PSD of 106-850 µm for application in the fluidized bed used in the chloride pigment production process (Gazquez, et al., 2014; Van Dyk, 1999). If the chemical grade for the chloride process could be met through the UGS upgrading of a titaniferous slag with minimum or no spinel structure, the problem of the UGS product with finer PSD than the specification could be addressed by micro-pelletisation before feeding into the fluidized bed furnace operation. The concept would need further investigation.

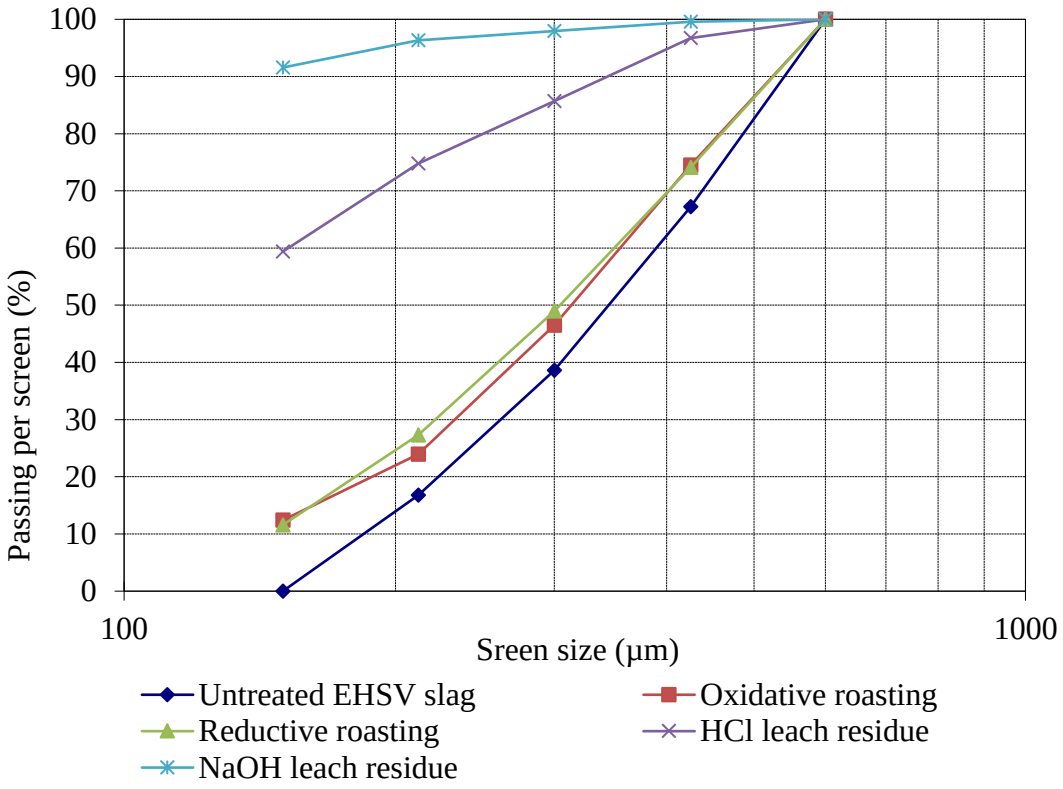

Figure 75. Particle size distribution of the EHSV titaniferous slag after treatment using the UGS process

5.3.3 Beneficiation of titaniferous slag produced using a conventional induction furnace

The bulk and phase chemical characteristics of the titaniferous slag produced in the conventional induction are included in Table 19 and Figure 67, respectively. The slag was processed using the best combination of UGS conditions established above and literature information. The conditions are detailed in section 5.3.2.3. The intermediate and final products were analysed for: bulk chemistry by ICP-OES, morphological characteristics and phase chemistry by SEM-EDS and XRD, and particle size distribution using conventional sieves.

5.3.3.1 Bulk chemical compositions

The bulk chemical compositions of the untreated and, processed intermediate and final products from the UGS processing of the titaniferous slag produced in the current work are given in Table 34. The results show that the produced titaniferous slag could only be upgraded from about 24wt% to 67wt% TiO_2 using the combination of UGS conditions established on the EHSV titaniferous slag in section 5.3.2.3. The detrimental species in the upgraded titaniferous slag were MgO and Al_2O_3, which typically existed in a chemically inert spinel structure. However, the remaining Al_2O_3 in the upgraded titaniferous slag was in excess of the stoichiometrical requirement in the spinel structure. The properties of the current UGS product does not meet the specifications of the feedstock for the chloride process that are described in section 2.5.2.

The results in Table 34 also show that the cumulative recoveries of the MgO and Al_2O_3 to residue were adversely significant in excess of 20%. The cumulative recovery of TiO_2 in the beneficiated slag was 76%. It is assumed that in a large scale operation smelting process, there will be no Al_2O_3 contamination. Hence, the UGS process is anticipated to perform better in terms of beneficiating the titaniferous slags to marketable titania products, preferably for use as feedstock for the production of the chloride pigment.

Table 34: Chemical compositions of the untreated and processed titaniferous slags produced in the current study (wt%)

Sample	Treatment Conditions		Al_2O_3	CaO	Cr_2O_3	FeO	MgO	MnO	SiO_2	TiO_2	V_2O_5
Cast slag	Sized to a range: +150 – 600 µm		29.63	20.73	0.06	7.49	3.43	0.26	12.83	24.37	0.23
Oxidised slag	Oxidation in a fluidized bed, air at 875°C for 2 hours	After	28.65	19.96	0.06	7.96	3.35	0.26	12.66	24.21	0.23
	Recovery to residue		98%	97%	101%	107%	99%	101%	100%	100%	101%
Reduced slag	Reduction in a fluidized bed, in CO at 875°C for 0.5 hours	After	28.54	19.96	0.06	7.96	3.35	0.26	12.66	24.72	0.23
	Recovery to residue		99%	99%	99%	99%	99%	99%	99%	101%	99%
HCl leach residue	Leach in 20% HCl under reflux at 110°C for 24 hours in s: l of 1:4	After	25.05	4.74	0.00	0.33	4.48	0.09	16.90	47.45	0.07
	Recovery to residue		42%	11%	0%	2%	64%	17%	64%	92%	15%
Caustic leach residue	Leach in 2.15 M NaOH at 100°C for 3 hours in s: l of 1:4	After	22.40	5.18	0.00	0.29	3.41	0.08	1.87	66.90	0.19
	Recovery to residue		52%	64%	0%	51%	44%	52%	6%	82%	158%
	Cumulative recovery to residue		21%	7%	0%	1%	28%	9%	4%	76%	23%

5.3.3.2 Phase chemistry

The backscattered SEM micrographs, EDS and XRD characterisation results of the roasted titaniferous slags produced in the current study, HCl and NaOH leach residues are shown in Figure 76 to Figure 78. After the oxidative roasting, the phase assemblage of the titaniferous slag is similar to the cast titaniferous slag phase assemblage reported in Figure 67. Though the iron bearing phases were not observed on the microstructure of the cast titaniferous slag, the iron bearing pseudobrookite phase was however observed in the oxidised slag (Figure 76). The observed microstructure does not show the spinel phase. The spinel phase in the oxidised slag was determined by XRD. The current results support the view that the produced titaniferous slag may have not been completely homogeneous.

After reduction (Figure 76), many phases that were observed in the oxidised roast still existed. However, after reductive roasting, the pseudobrookite phase is decomposed into rutile phases and HCl acid soluble wustite (FeO). Moreover, XRD results suggest that the FeO was further reduced to metallic Fe. Reductive roasting appears to have also decomposed some silicate phases to form quartz. The spinel solid solution phase is observed in the microstructure. From the view point of the morphology of phases, the spinel phase of the reduced slag appears to be discrete – other gangue minerals also appear to be totally liberated, and not blocked or encapsulated by the chemically inert spinel phases. The silicate phases were not affected by the reductive roasting stage.

The backscattered electron micrograph, EDS, and XRD results of the HCl residue in Figure 77 show that the detrimental elements were incorporated in several phases including olivine solution, pseudobrookite, spinel and titanaugite phases. The detrimental element bearing phases are typically not inert to chemical treatment. In addition, the detrimental element bearing phases are still discrete. Thus, the inadequate removal of these impurities can be attributed to the fact that the adopted UGS test conditions may not be optimum as they were not optimized for the current slag (the test conditions were determined using the EHSV slag), rather than the inertness of the detrimental element bearing phases.

The backscattered electron micrograph, EDS, and XRD results of the NaOH residue in Figure 78 show that the impurities in the upgraded titaniferous slag were incorporated in several phases including pseudobrookite, spinel and titanaugite phases. All these phases are still discrete. Hence it may happen that the dissolution of the gangue phases, other than the

spinel structure, is hampered by that the test conditions were not optimized. Titanium silicate phase is only observed in the product. The existence of this eutectic phase in the SiO_2-TiO_2 system with a limited solubility of TiO_2 in SiO_2 is reported in literature (Kirillova, et al., 2011; Evans, 1970; Massazza & Sirchia, 1958; Bunting, 1933). The composition of the current phase with 12% TiO_2 dissolution into SiO_2 concurs with the eutectic composition reported by Massaza and Sirchia (1958) and Kirillova et al. (2011).

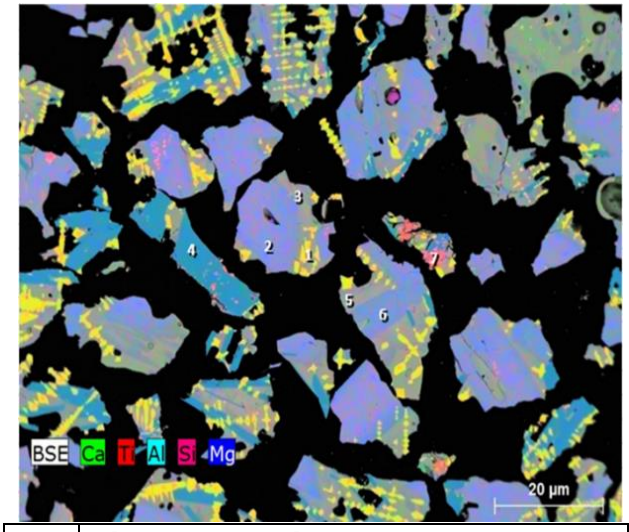

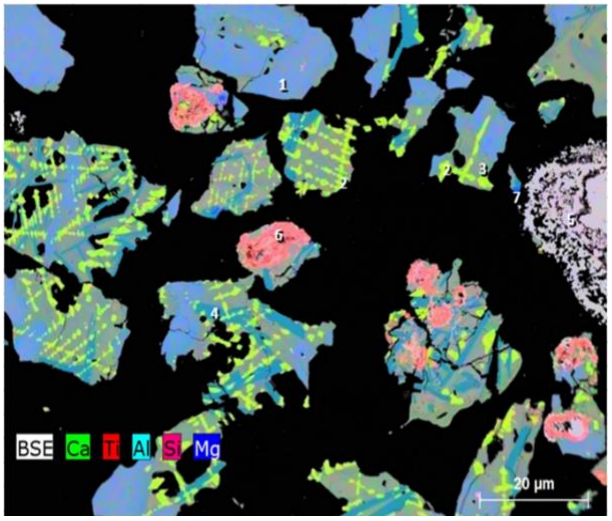

	Phase (EDS and XRD)		Phase (EDS and XRD)
1	Perovskite	1	Titanaugite
2	Titanaugite	2	Perovskite
3	Titanaugite	3	Titanaugite
4	Pseudobrookite	4	Pseudobrookite
5	Titanaugite	5	Wustite (FeO)
6	Titanaugite e	6	Rutile
7	Rutile	7	$Mg(Al,Ti,V)_2O_4$
	Spinel solid solution [$Mg(Al,Ti,V)_2O_4$]		Fe
	Gehlenite		Quartz
			Gehlenite
Oxidised titaniferous slag		**Reduced titaniferous slag**	

Figure 76: Backscattered electron microstructure, EDS and XRD results of the roasted titaniferous slag produced in the conventional induction furnace

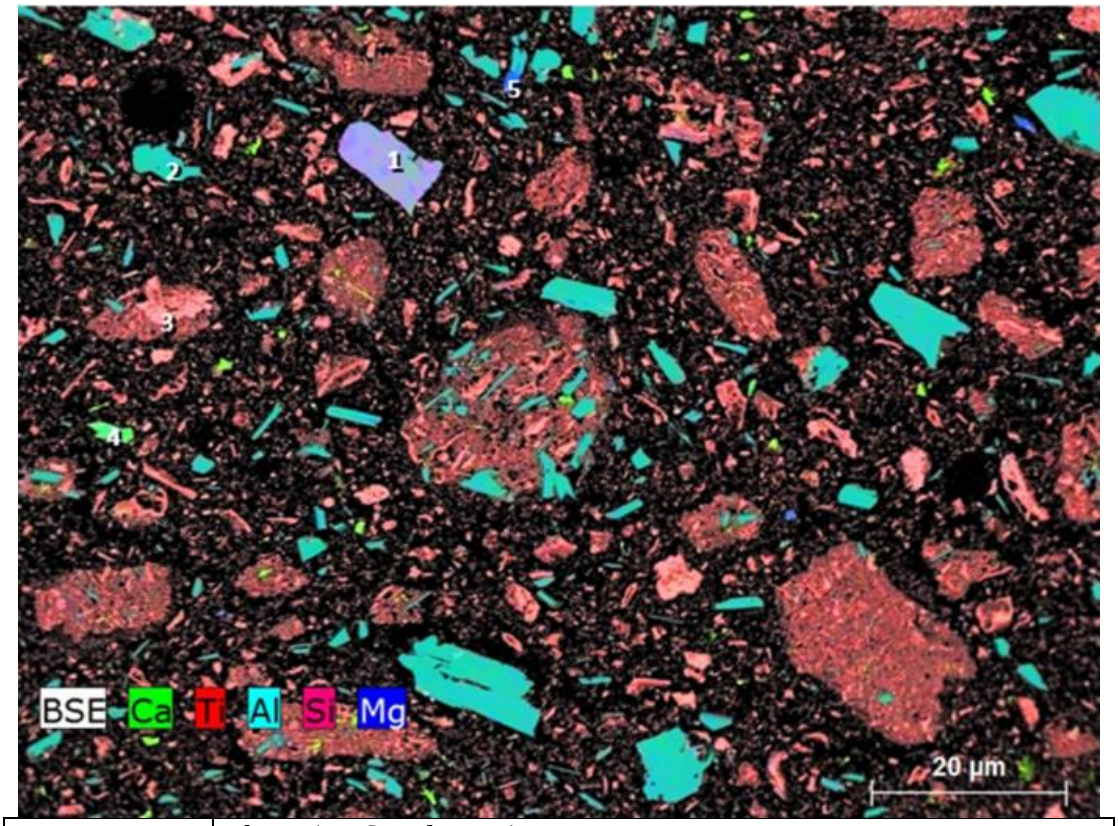

	Phase (EDS and XRD)
1	Olivine, $(Mg,Ca,Fe)_2SiO_4$
2	Pseudobrookite
3	Rutile
4	Titanaugite
5	$Mg(Al,Ti,V)_2O_4$

Figure 77. Backscattered electron microstructure, EDS and XRD results of the HCl leach residue of the titaniferous slag produced in the conventional induction furnace

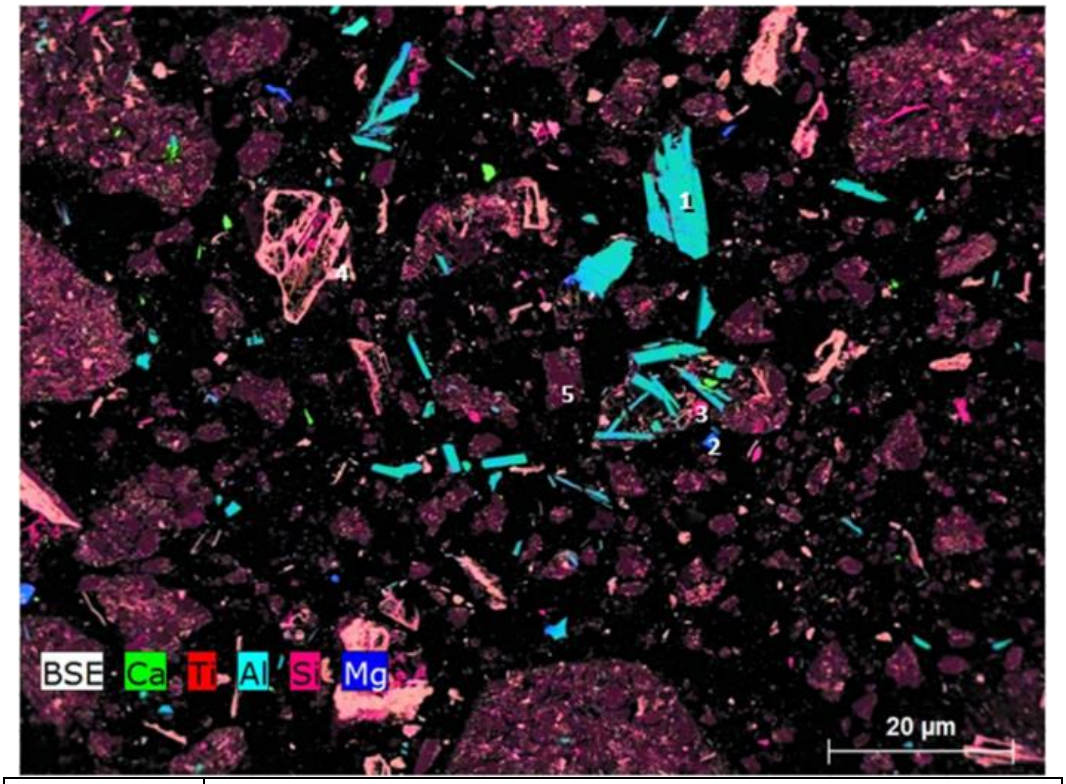

	Phase (EDS and XRD)
1	Pseudobrookite
2	$Mg(Al,Ti,V)_2O_4$
3	Quartz (high purity)
4	Rutile
5	Quartz

Figure 78. Backscattered electron microstructure, EDS and XRD results of the NaOH leach residue of the titaniferous slag produced in the conventional induction furnace: UGS product from titaniferous slag

5.3.3.3 Particle size distribution

The PSD of the titaniferous slag produced in the current study after processing through the different stages of the UGS process is shown in Figure 79. As was the case with the EHSV titaniferous slag, the curves on the graph show that the PSD of the slag is significantly smaller after the respective leaching stages. The final upgraded titaniferous slag has a D_{95} of 150 µm. The particle size distribution and the chemical composition of the upgraded titaniferous slag are not suitable for the slag to be used as feedstock for the preferred chloride pigment production process. As detailed in section 2.5, the chemical composition of the current product suggest that it may not be suitable for use as feedstock for the less demanding sulfate process.

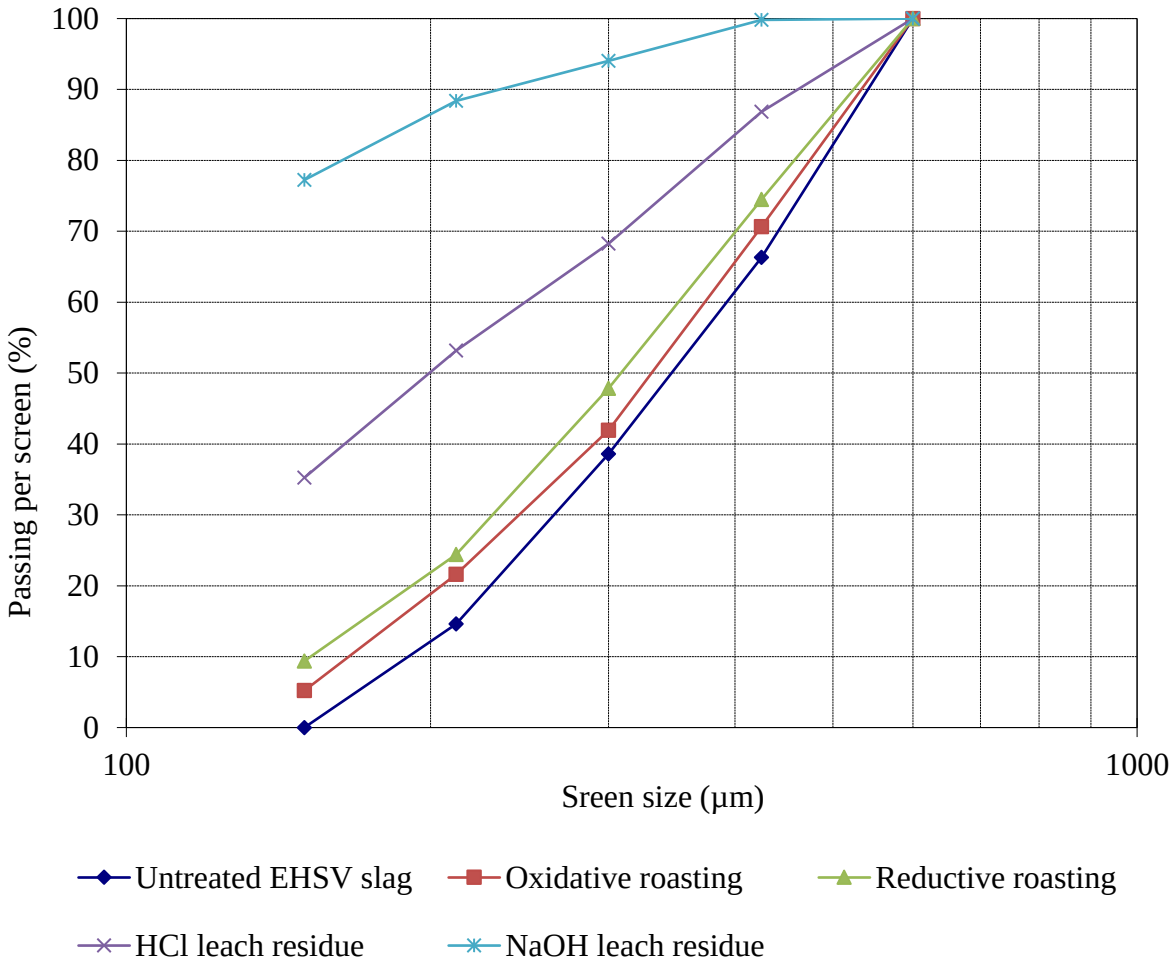

Figure 79. Particle size distribution of the UGS process product from the produced titaniferous slag

5.3.4 Beneficiation of a titaniferous slag produced using the cold crucible induction furnace

The chemical and phase compositions of the titaniferous slag produced in the cold crucible induction furnace (composite of the three slags) and used as feedstock in the UGS process testwork are included in Table 26 and Figure 69. The effects of HCl and NaOH leaching times on the upgrading of TiO_2 in this slag were studied and reported in the following subsections.

5.3.4.1 Effect of HCl leaching time on upgrading of titaniferous slag produced in cold crucible induction furnace

As detailed in section 5.2.5, the effect of HCl leaching time on the upgrading of TiO_2 in the titaniferous slag produced in the cold crucible induction furnace was studied. In these studies, the pulp density and the HCl lixiviant concentration were kept constant at 25 w/v% (or a s: l ratio of 1: 4) and 20wt%, respectively. The leaching times were investigated at 1, 4, 24 and 48 hours. The results are shown in Figure 80. The results show that the TiO_2 grade in the residue increases with increasing the HCl leaching time. After a reaction time of 48 hours, the TiO_2 grade in the residue had not reached a saturation point. The TiO_2 recoveries to the residue are also very high at more than 90%. The high TiO_2 recoveries in the residue suggest that the concentration of the HCl soluble Ti^{3+} species in the roasted feed was favorably low.

The chemical compositions of the HCl leach residues of the slags are given in Table 35. The results show that during the HCl leaching, Mg, Al, Ca, V, Cr, Mn and Fe are effectively removed from the residue. The crucial removal of Mg and Al to very low concentrations or, insignificant concentrations in the case of Mg, suggest that these species were not incorporated into the chemically inert spinel structure. As reported in Figure 69, the spinel structure contained in the cast and roasted titaniferous slag produced using the cold crucible induction furnace is an ulvospinel, i.e. Fe_2TiO_4 – this spinel structure was decomposed by the HCl leaching exercise. The HCl residue did not contain the spinel phase – the phase chemistry of the HCl residue is further discussed below in section 5.3.4.3.

Table 35: Chemical compositions of the slag leach residues produced at different HCl leaching times (wt%)

Leaching time (hours)	MgO	Al_2O_3	SiO_2	CaO	TiO_2	V_2O_5	Cr_2O_3	MnO	FeO
*Feed	2.80	7.22	11.80	15.20	20.20	2.85	0.64	0.43	38.10
4	2.75	7.27	18.11	13.58	22.85	1.46	0.77	0.36	32.85
24	2.37	6.09	17.97	13.74	36.46	2.18	0.73	0.22	20.24
48	0.50	1.45	32.93	0.29	63.18	0.21	0.20	<0.05	1.23

*Oxidative-reductive roast of composite of the titaniferous slag produced in the cold crucible induction furnace

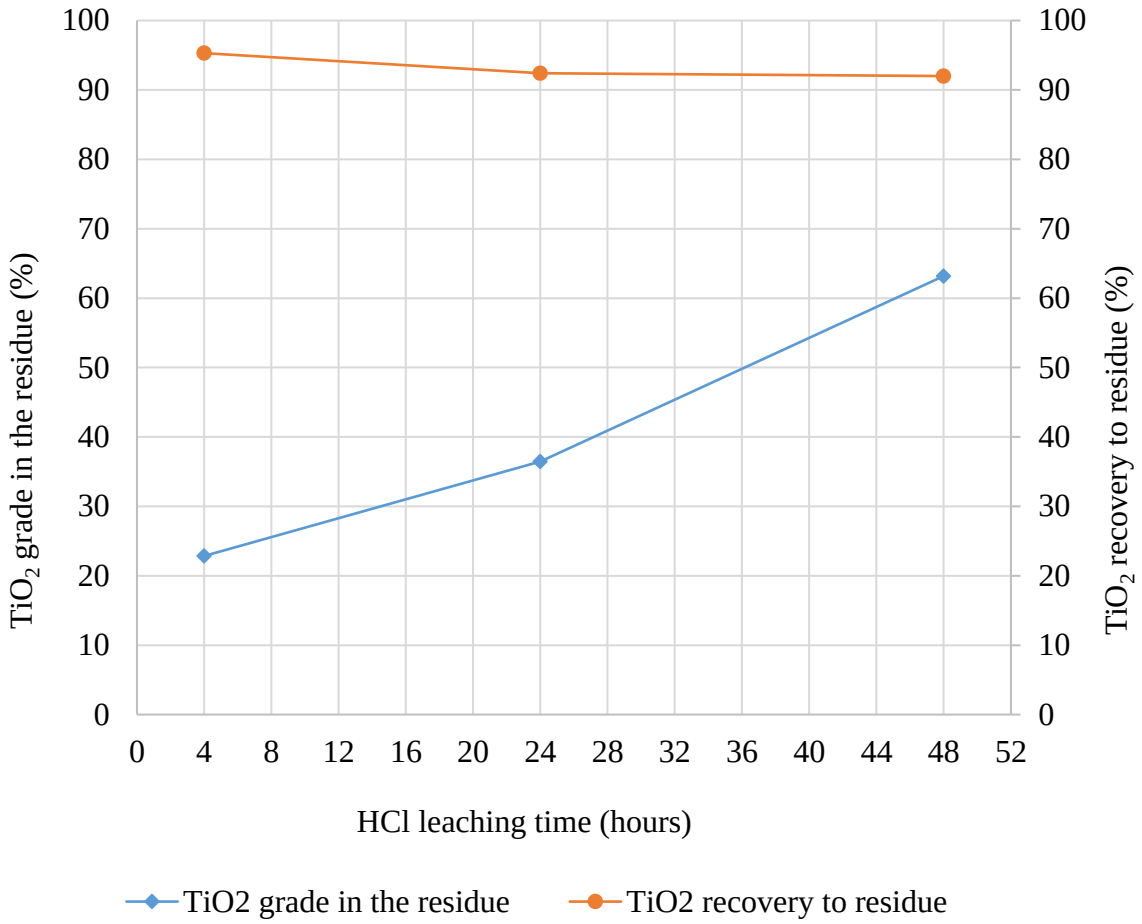

Figure 80. Effect of HCl leaching time on the upgrading of TiO_2 in the titaniferous slag produced in the cold crucible induction furnace

5.3.4.2 Effect of NaOH leaching time on upgrading of titaniferous slag produced in the cold crucible induction furnace

The study of the effect of NaOH leaching time on the upgrading of TiO2 in the titaniferous slag produced in the cold crucible furnace was conducted on the HCl leach residue produced after a leaching time of 48 hours. During the kinetic studies, the pulp density and NaOH concentration were kept constant at 25 wt% and 2.15 M, respectively. The NaOH leaching time was investigated at 1, 3, and 24 hours. The results are presented in Figure 81. The results show that the maximum TiO_2 grade of about 91wt% is achieved within an hour of leaching the HCl residue with the NaOH lixiviant. However, the recovery of TiO_2 to the residue decrease with increasing the NaOH leaching time. Hence, NaOH leaching times of more than an hour are not recommended.

Table 36 gives the results of the chemical compositions of the respective UGS products produced after different NaOH leaching times of the HCl leach residue. The results show that the NaOH leaching exercise effectively and exclusively leached out silicon species from the HCl leach residue. A residual concentration of over 3wt% of SiO_2 remained in the UGS product even at elongated caustic leaching times of 24 hours. The phase of existence of the residual SiO_2 is discussed below in section 5.3.4.3. Nevertheless, from a chemical viewpoint, the current UGS product containing 90.45wt% TiO_2, which was produced from titaniferous slag, met the TiO_2 grade specification for the feedstock for the chloride pigment product. However, as discussed below in section 0, the SiO_2, Al_2O_3, CaO, and Cr_2O_3 concentrations are higher than the specifications and may compromise the use of the current product as feedstock for the most preferred chloride pigment production.

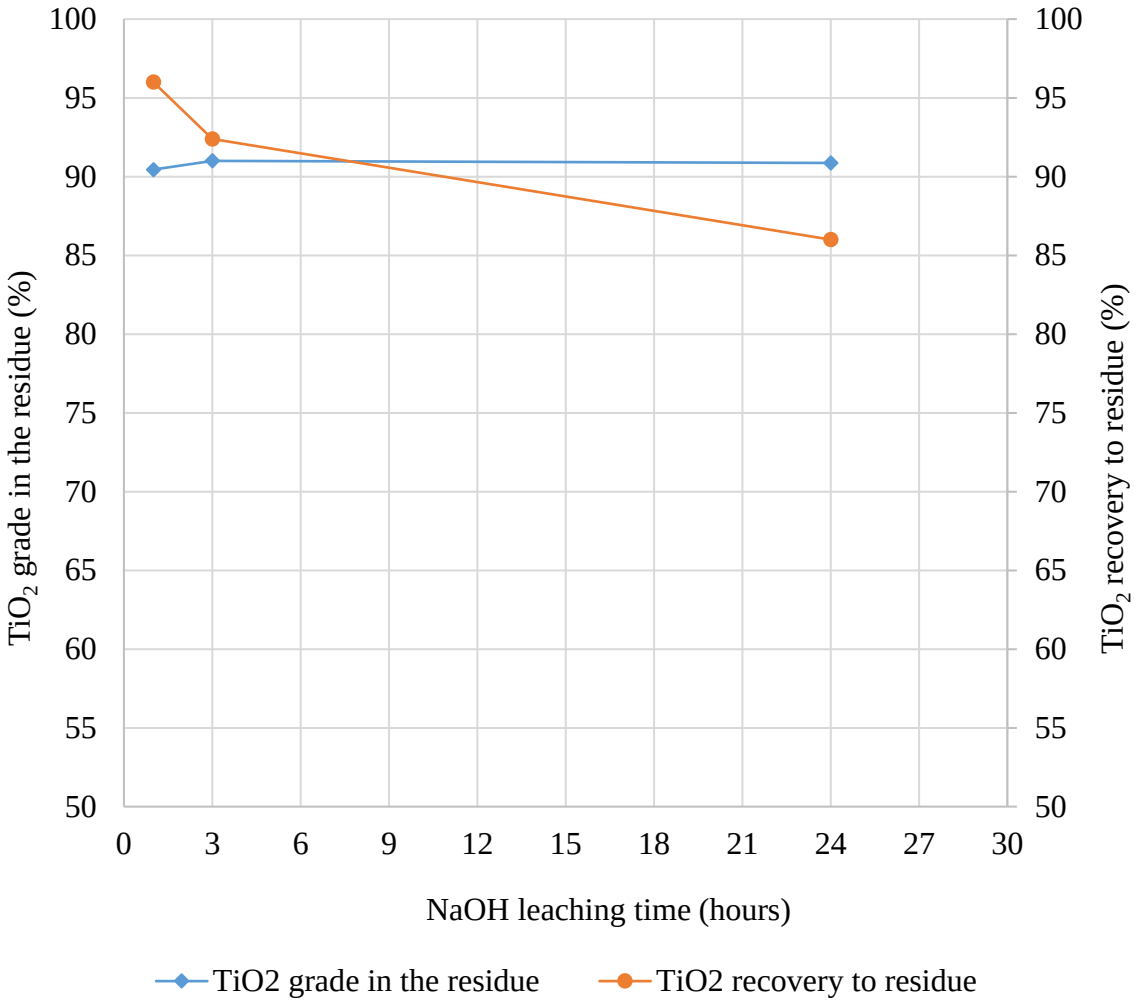

Figure 81. Effect of NaOH leaching time on the upgrading of TiO_2 in the HCl leach residue of the titaniferous slag produced in the cold crucible induction furnace

Table 36: Chemical compositions of the UGS products produced at different NaOH leaching times (wt%)

Leach time (hours)	MgO	Al_2O_3	SiO_2	CaO	TiO_2	V_2O_5	Cr_2O_3	MnO	FeO
*Feed	0.50	1.45	32.93	0.29	63.18	0.21	0.20	<0.05	1.23
1	0.80	1.71	3.77	0.62	90.45	0.32	0.29	0.07	1.98
3	0.86	1.78	3.31	0.72	91.00	0.29	0.28	0.07	1.70
24	0.84	2.04	3.32	0.58	90.87	0.29	0.29	0.07	1.69

*HCl leach residue for the 48 hour test

5.3.4.3 Evaluation of the UGS product from titaniferous slag produced in the cold crucible induction furnace

This section of the thesis provides an evaluation of the results of the UGS processing of the titaniferous slag produced in the cold crucible induction furnace.

Bulk chemical compositions

The bulk chemical compositions of the untreated and, processed intermediate and final products from the UGS processing of the titaniferous slag produced in the cold crucible induction furnace are combined in Table 37. The results show that during HCl leaching, Al, Ca, Cr, Fe, Mg, Mn and V are effectively removed from the oxidative and reductive roasted titaniferous slag. During the NaOH leaching, Si species was leached out.

However, there were titanium losses of 8% and 4% during the respective HCl and NaOH leaching stages. The titanium losses were attributed to the leaching of Ti^{3+} species. The cumulative recovery of TiO_2 to the UGS product was 83%.

From a chemical point of view, it has been shown that the titaniferous slag produced from fluxing with an MgO-free limestone flux can be upgraded using the UGS process to 90.45wt% TiO_2 grade material that is suitable for use as feedstock in the chloride pigment production. However, the SiO_2 concentration in the UGS product was just above 3wt%. As explained above, increasing the caustic leaching time did not decrease the SiO_2 concentration in the UGS product. The phases of existence of the Si species in the UGS product are discussed below under the section on phase chemistry.

Table 37: Chemical compositions of the untreated and processed titaniferous slags produced using the cold crucible induction furnace (wt%)

Sample	Treatment Conditions		Al_2O_3	CaO	Cr_2O_3	FeO	MgO	MnO	SiO_2	TiO_2	V_2O_5
Slag composite	Sized to 600-150 µm		7.97	17.29	0.57	34.30	3.14	0.43	12.39	22.00	2.91
Oxidised slag	Oxidation in a fluidized bed, air at 875°C for 2 hours	After	7.51	16.17	0.68	36.14	2.97	0.44	12.05	21.03	3.02
	Recovery to residue		97%	97%	122%	109%	98%	107%	100%	99%	107%
Reduced slag	Reduction in a fluidized bed, in CO at 875°C for 0.5 hours	After	7.22	15.20	0.64	38.10	2.80	0.43	11.80	20.20	2.85
	Recovery to residue		95%	93%	93%	104%	93%	96%	97%	94.8%	93%
HCl leach residue	Leach in 20% HCl under reflux at 110°C for 48 hours in s:l of 1:4	After	1.45	0.29	0.20	1.23	0.50	<0.05	32.93	63.18	0.21
	Recovery to residue		6%	1%	9%	1%	5%	<0.05	82%	92.0%	2%
Caustic leach residue	Leach in 2.15 M NaOH at 100°C for 1 hours in s:l of 1:4	After	1.71	0.62	0.29	1.98	0.80	0.07	3.77	90.45	0.32
	Recovery to residue		79%	143%	9%	107%	108%	<0.05	8%	96.0%	100%
Cumulative recovery to residue			4%	1%	1%	1%	5%	<0.05	6%	83%	2%

Phase chemistry

The backscattered electron images, EDS and XRD analysis results of the oxidative-reductive roasted titaniferous slag produced in the cold crucible induction furnace are shown in Figure 82 and Figure 83. In general, there was no significant phase transformation after the two roasting stages. The results however show that after the oxidative roasting, the discrete iron species observed in the cast titaniferous slag, i.e. Figure 69, were oxidised to hematite (Fe_2O_3). Hematite was reduced to wustite after the reductive roasting stage. There is no evidence of over reduction in the phase chemistry to suggest that the observed iron reduction may have been accompanied by the adverse reduction of Ti^{4+} to Ti^{3+}. Ti^{3+} is relatively soluble in HCl lixiviant. Thus, if some titanium in the slag is in the form of Ti^{3+}, it will result in titanium losses to the leachate (Borowiec, et al., 1998; Doan, 1996).

The backscattered electron image, EDS and XRD results in Figure 84 show that pseudobrookite, rutile, titanite and quartz were the significant phases in the 48-hour HCl leach residue. The respective phases are primarily composed of Ti and/ or Si species, which were not removed after the HCl leaching. It is important to note that the HCl leach residue did not have the spinel structure. Thus, the ulvospinel observed in the cast and roasted slags is not as inert as the normal spinel solid solution structure observed in titaniferous slags.

The backscattered electron image, EDS and XRD analysis results of the UGS product in Figure 85 show that this product is primarily composed of rutile, and to a lesser extent perovskite and pseudobrookite. The XRD results showed that the residual Si observed in the chemical analysis results in Table 37 occurred in the titanite ($CaO.TiO_2.SiO_2$) structure, which is a minor phase in the UGS product. In the study of the Mg-Ca-Ti-Si-O system in air, the crystallisation of the calcium titanium silicate ($CaO.TiO_2.SiO_2$) as one of the major phases was reported (Eisenhuttenleute, Verlag Deutscher, 1995) (page 178 in Slag Atlas). The studies conducted for the upgrading of TiO_2 in the titaniferous slag showed that the decomposition, and thus the removal of Si species is not sensitive to an increase in the NaOH leaching time of 1 hour or more. Thus, further testwork is required to investigate the effect of other parameters on the decomposition of the titanate and removal Si values. These test parameters include the NaOH lixiviant concentrate, pulp density, leaching temperature and leaching pressure.

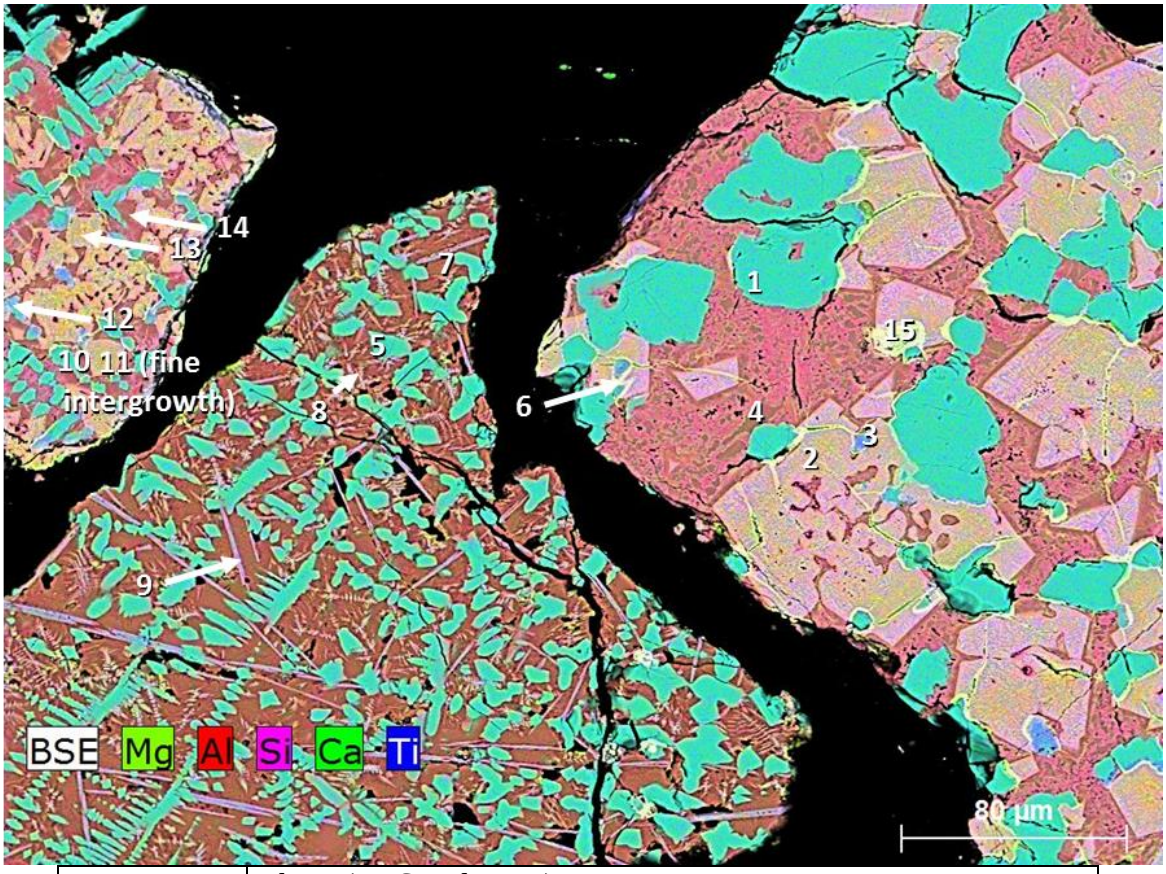

	Phase (EDS and XRD)
1	Perovskite
2	Ulvospinel
3	Rutile
4	Olivine
5	Perovskite
6	Hematite
7	Titanaugite
8	Ferric-pseudobrookite
9	Ferric-pseudobrookite
10	Perovskite
11	Ulvospinel
12	Perovskite
13	Ilmenite
14	Titanaugite
15	Hematite

Figure 82. Backscattered electron microstructure, EDS and XRD results of the oxidative roasted titaniferous slag produced in the cold crucible induction furnace

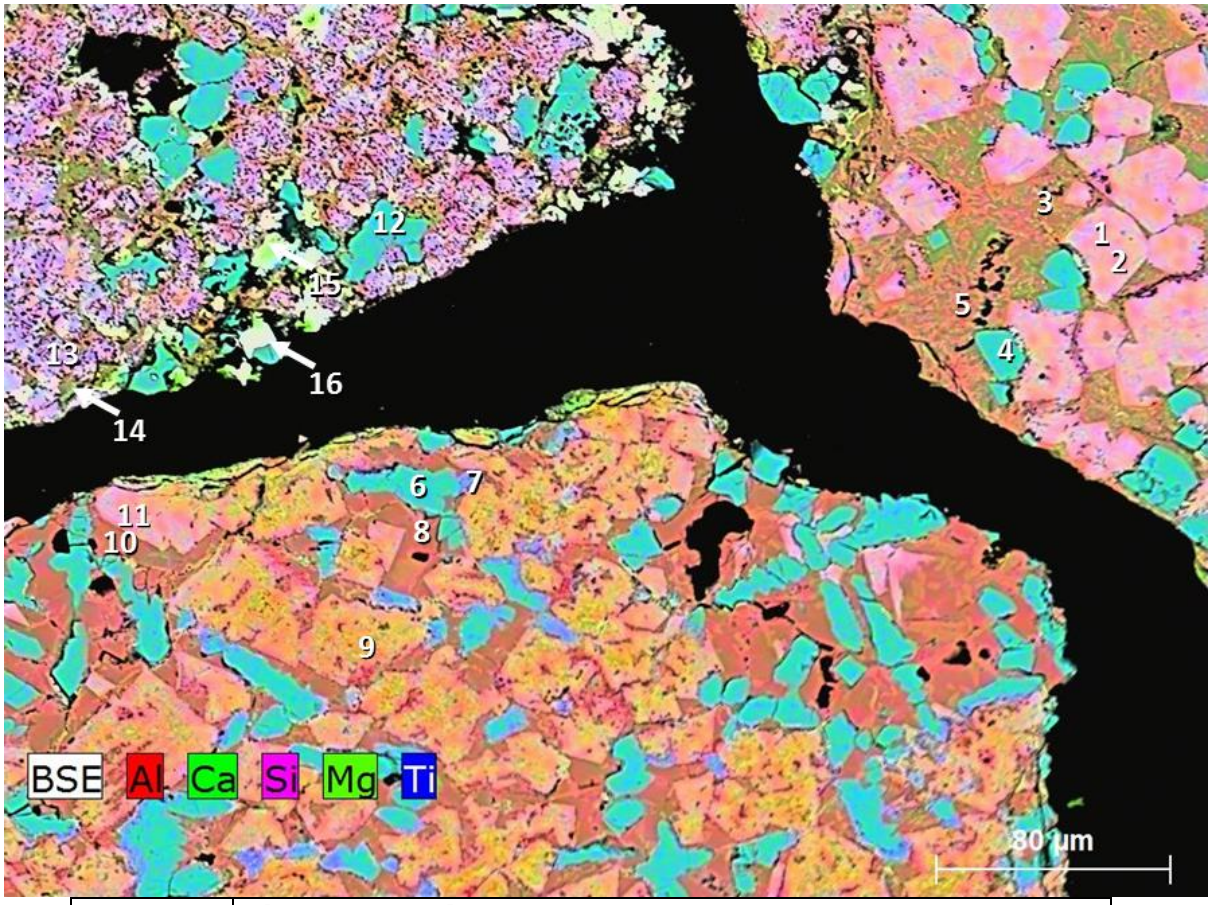

	Phase (EDS and XRD)
1	Pseudobrookite (high Fe)
2	Pseudobrookite (high Fe)
3	Olivine
4	Perovskite
5	Olivine
6	Perovskite
7	Perovskite
8	Olivine
9	Ulvospinel
10	Olivine
11	Pseudobrookite (high Fe)
12	Perovskite
13	Pseudobrookite (high Fe)
14	Titanaugite
15	FeO
16	FeO

Figure 83. Backscattered electron microstructure, EDS and XRD results of the oxidative-reductive roasted titaniferous slag produced in the cold crucible induction furnace

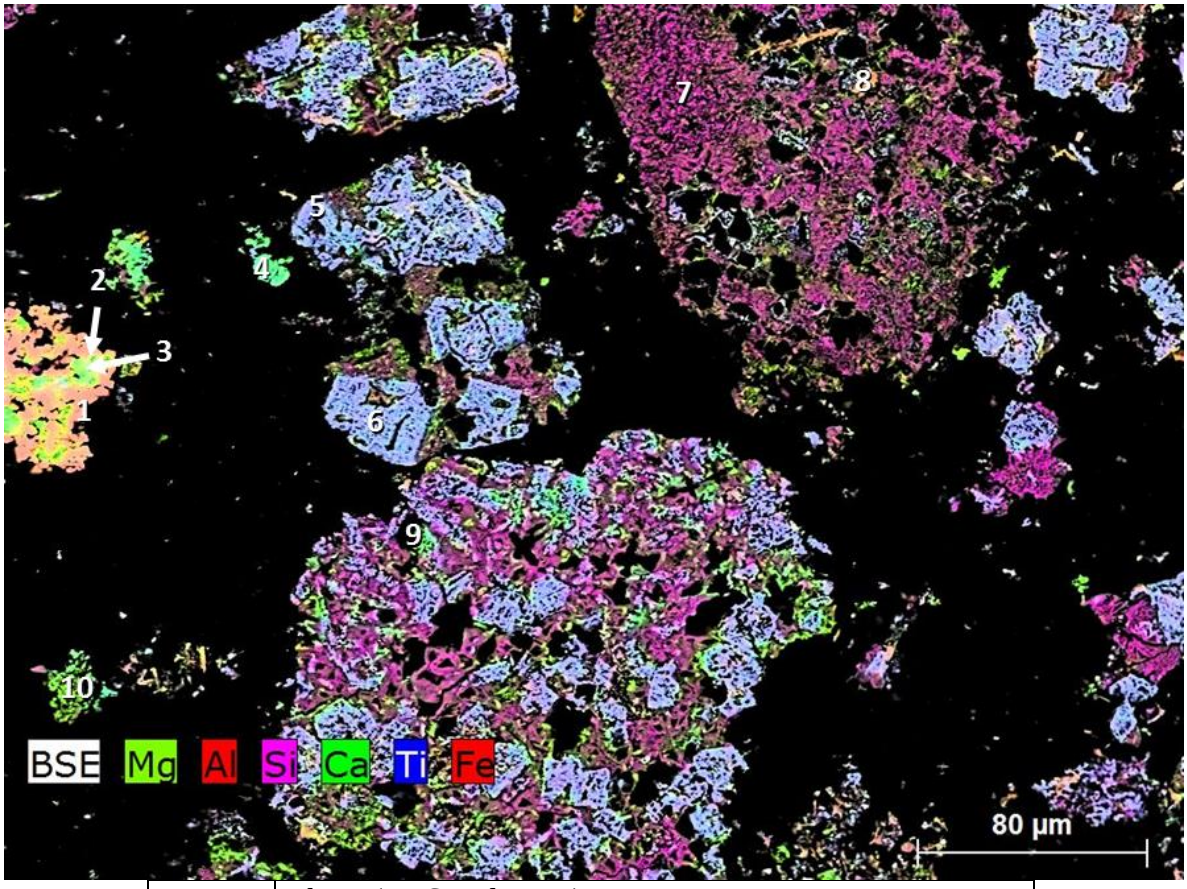

	Phase (EDS and XRD)
1	Hematite
2	Ferric-pseudobrookite
3	Titanite
4	Titanite
5	Rutile
6	Rutile
7	Quartz
8	Ferric-pseudobrookite
9	Titanite
10	Olivine

Figure 84. Backscattered electron microstructure, EDS and XRD results of the 48-hour HCl leach residue of the titaniferous slag produced in the cold crucible induction furnace

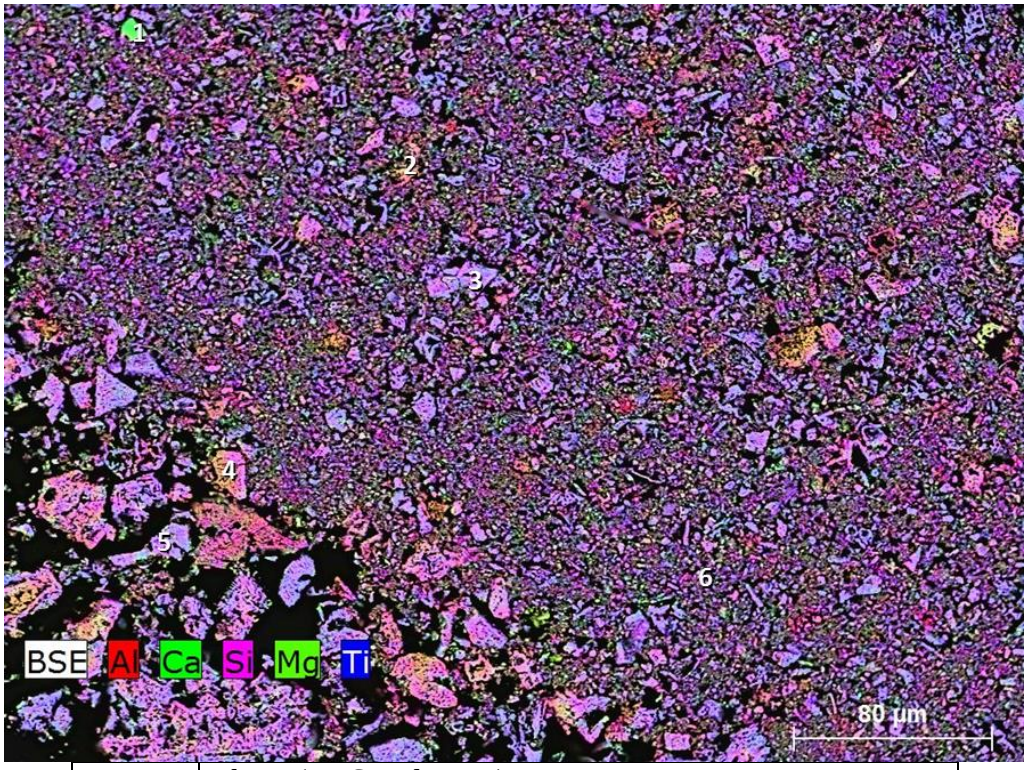

	Phase (EDS and XRD)
1	Perovskite
2	Pseudobrookite
3	Rutile
4	Rutile
5	Rutile
6	Rutile

Figure 85. Backscattered electron microstructure, EDS and XRD results of the UGS product from the titaniferous slag produced in the cold crucible induction furnace

Particle size distribution

The PSD analysis results of the titaniferous slag produced in the cold crucible induction furnace after processing through the different stages of the UGS process are shown in Figure 86. These results show that the PSD of the titaniferous slag is significantly reduced after the HCl and NaOH leaching stages. The D_{70} of the UGS product has a PSD of -150 µm.

Though, in terms of the TiO_2 grade, the UGS product meets the specifications for the chloride feedstock, the PSD (and other chemical components) compromise the use of the current UGS product as feedstock for the chloride process. As detailed in section 2.5.1, the current product meets the specifications for the sulfate feedstock.

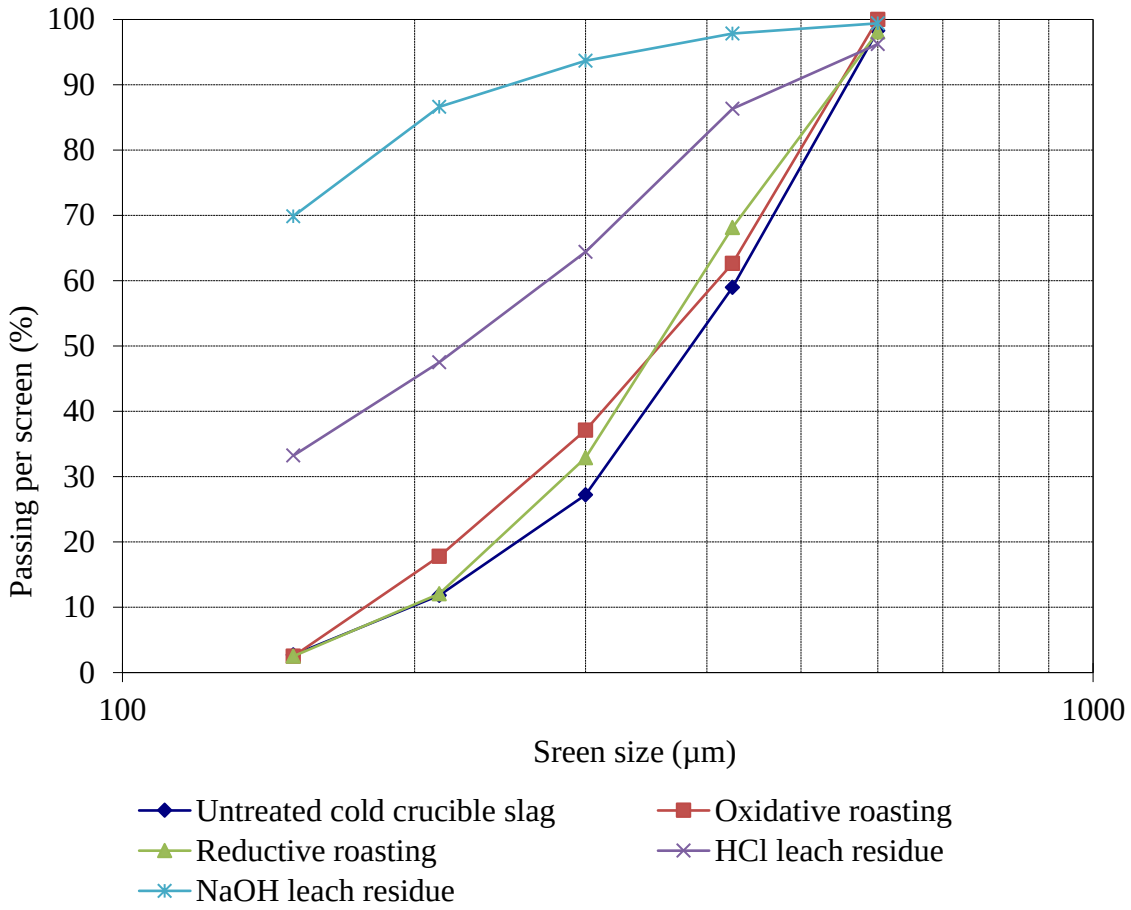

Figure 86. Particle size distribution of the UGS product from titaniferous slag produced in the cold crucible induction furnace

5.4 Titanomagnetite process flowsheet evaluation

The results of the testwork reported in the above sections showed that a titaniferous slag produced from fluxing with an MgO-free flux can be beneficiated to a UGS product with >90wt% TiO_2. This material meets the chemical specifications of the feedstock for the chloride pigment product, except for the SiO_2 and CaO concentrations. As stated in section 2.5.2, the feedstock for the chloride process has typical maximum SiO_2 concentration limit of 2wt%. Moreover, the PSD of the product is too fine to qualify as a feedstock for the fluidised based chloride process which has a typical lower limit of 106 µm. With decrease in the SiO_2 and CaO concentrations to meet the chloride pigment specification, the suitability of feeding the chloride process with micro-pellets of this product produced from the titaniferous slag would need to be investigated. Since the current titania product is mainly composed of rutile, it may not be suitable for use as feedstock in the production of the sulfate

pigment – rutile is not soluble in sulfuric acid. However, further testwork can be done to investigate the solubility of the UGS product produced from titaniferous slag. It would be advantageous to use this high titania product as feedstock in the sulphate process in order to minimise the amount of sulfate waste which is typically proportional to the impurity content.

The current section of the thesis aimed to develop a conceptual process flowsheet to demonstrate the maximum exploitation of vanadiferous titanomagnetite resources for the production of iron, vanadium and titanium products. The established processes only include the extraction of iron and vanadium from titanomagnetite (Roskill, 2010; Taylor, et al., 2006; NTMK, 2003; Kelly, 1993; Zhang, et al., 2007; Steinberg, et al., 2011). An increase in the scope of the products to include the extraction of titanium from titanomagnetite would be beneficial in terms of maximising the exploitation of valuable resources, realisation of zero or minimum waste processes, employment growth through an increase in the process flowsheet, and contribution towards the national gross domestic products. The conceptual flowsheet was developed using literature data, experimental data generated in the current study and the simulation data generated using the Mintek's pyrometallurgical process simulation software, which is generally known as 'Pyrosim' (Jones, 2001).

5.4.1 Conceptual flowsheet design

The conceptual process flow diagram is depicted in Figure 87. The conceptual flowsheet design is based on the best combination of conditions attained at several stages during the processing of titanomagnetite for the production of steel, vanadium and titanium products. These established processing stages included agglomeration and pre-reduction, smelting to produce a vanadium bearing pig iron and titaniferous slag, converting of the vanadium bearing pig iron to produce steel and vanadium slag products, processing of the titaniferous slag using the UGS process to produce a high titania product with 90.45wt% TiO_2.

It should be noted that the current preliminary flowsheet does not consider the recycle streams – for example, the off gases can be used as heating source in other stages; the pre-reduction and smelting CO rich off gases can be used in the reductive roasting of the titaniferous slag; the oxidative and reductive off gasses can be recycled; alkali and alkali earth elements as well as some lost Ti values can be recovered from the HCl leachate stream; HCl leachate can be recycled into HCl lixiviant; and, silica can be precipitated from the NaOH leachate stream.

Pyrosim simulation of the conceptual flowsheet to attain preliminary mass and energy data for the high temperature stages was calculated with the following assumptions:

- All the iron in the titanomagnetite ore composition included in Table 7 used in the current calculations occurs as Fe_3O_4.
- The organic binder is made up of 100% C.
- The pre-reduction of recipe pellets with 20% moisture was conducted in a unit operation with 100% thermal efficiency (the energy losses were disregarded) and the pre-reduced charge was fed into the succeeding smelting furnace hot at 1100°C.
- The anthracite was taken as 100% C. The addition of anthracite was calculated for the reduction of Fe and V in ore.
- The fluxes were 100% $CaCO_3$ in case of limestone and 100% SiO_2 in case of quartz. Fluxing strategy aimed to produce a slag with the minimum possible MgO content to avoid the crystallisation of the detrimental spinel solid solution phase.
- The size of the limestone and silica flux additions were based on the defunct EHSV operation.
- Smelting is conducted in an electric furnace with 100% thermal efficiency. Because of the replacement of the dolomite (used at EHSV) with limestone, the operational temperature is anticipated to increase from about 1500°C to 1550°C.
- 3% titaniferous slag is carried over with the vanadium bearing pig iron to the ladle furnace convertor.
- Only hematite is used as an oxidant in the ladle furnace converting – there was no addition of oxygen, scrap or carburiser. In the simulation, some N_2 was added to allow for the carriage of the emissions.
- The simulation ends at the stage of the production of the high purity pig iron which is typically used as a feed for the successive basic oxygen furnace (BOF) in a typical steelmaking process. The other product is a vanadium slag with about 23wt% V_2O_5.
- The titaniferous slag produced in the electric smelting furnace is processed further to produce a saleable titania product using the UGS process, which involves oxidative

and reductive roasting stages. Here the oxidative roaster is fed with cold sized slag, whereas the oxidised slag is fed hot into the succeeding reductive roasting stage.

- The plant capacity or throughput was 100 t/ h of MML titanomagnetite ore – the plant availability was estimated to be 90%. Therefore, in the Pyrosim results sheet in section 1.4.1 of the Appendix 1.4, the kg/ h should be read as t/ h, and kW and MW – the Pyrosim programme is not flexible to changing the units of the material flowrates.

The Pyrosim files for the simulation of the high temperature stages in the conceptual flowsheet are included in Appendix 1.4.

5.4.1.1 Pelletisation and pre-reduction

Pre-reduction prior to a titanomagnetite smelting process typically provides significant energy savings in the overall smelting process. The degree or extent of pre-reduction has a direct bearing on the smelting energy requirements and carbon balance during smelting; in general, high and stable pre-reduction degrees are desired (Jiaquan, et al., 2012; Manamela & Pistorius, 2005). In the defunct EHSV operation, the pre-reduction degrees on the reduction of the lumpy titanomagnetite ore were in the order of 50% (Steinberg, 2008). The pre-reduction degrees are improved when agglomerated recipes are processed instead of lumps (Evraz, 2015; Jiaquan, et al., 2012). The use of an organic binder for pelletisation is advantageous especially to avoid the contamination of the subsequent titaniferous slag (Bisaka, et al., 2016; Jiaquan, et al., 2012).

The pre-reduction of organic based titanomagnetite pellets can be categorised into gas-based and coal-based processes (Santos, 2012). The gas-based direct reduced iron or pre-reduction market is dominated by shaft furnace operations, in which case the primary technologies are gas-based Midrex and HYL/ Energiron processes (MIDREX, 2018; Tenova, 2018).

The coal-based technologies include fluidised bed, rotary hearth and rotary kiln based processes (Santos, 2012). Rotary kiln based pre-reduction technology was used to process the lumpy feed in the obsolete EHSV operation. In this technology, the charge is pre-heated and reduced as it moves on the temperature gradient along the length of the kiln. The heating of the kiln for the pre-reduction reaction is typically provided by combustion of plentiful coal, in the South African context. The pre-reduction process is typically conducted at

atmospheric pressure with the operational temperatures in the order of 1100°C. The DRI is recovered from the char and ash on the discharge end of the kiln (Steinberg, 2008).

In the conceptual flowsheet, the pre-reduction data were obtained through Pyrosim simulation. In the flowsheet, the smelter feed is proposed to be produced from pre-reduction of organic binder based titanomagnetite-anthracite pellets using the rotary kiln technology. For the preparation of the pellets, the organic binder would be the BASF's CB06 binder with the growth of pellets facilitated by intermittent spraying of water to achieve a moisture content of about 16% in the pellets. The energy requirement for pelletisation is a rough estimate. As proposed by Bisaka et al. (2016) in the case of pre-reduction of organic binder based ilmenite pellets, the pre-reduction would be conducted at atmospheric pressure at 1100°C for an optimistic duration of 1 hour. The calculated energy requirements and product mass distributions from Pyrosim simulation are reported on the conceptual flowsheet – they can also be viewed in Appendix 1.4. A pre-reduction degree of 90% and above was targeted.

5.4.1.2 Smelting

Though laboratory scale smelting tests were conducted in the current research program, only the Pyrosim simulation smelting data was adopted for the conceptual flowsheet development. As reported in section 5.3.1, the laboratory scale test work was confronted by problems with refractory ware in the conventional induction furnace and the addition of a Fe susceptor in the cold crucible furnace – these phenomena have a potential to distort the results.

The setup of the Pyrosim simulator was such that the pre-reduced charge is fed hot at 1100°C into the electric arc furnace (EAF). Flux addition and trimming addition of anthracite reductant are made into the smelter. According to the updated phase diagram in Figure 50, the liquidus temperature of the target slag would be in the order of 1500°C. Hence, the simulation was conducted at 1550°C to account for some superheat necessary for efficient separation of the slag and pig iron.

As can be seen in section 1.4.1 of the Appendix 1.4, the smelting process resulted in the recovery of almost all the titanium to the titaniferous slag phase. In addition, almost all the iron reported to the pig iron phase, whereas about 77% of the V reported to the pig iron. The Ti, Fe and V distributions after smelting concur with the mass distributions reported for the

defunct EHSV operation (Goso, et al., 2016; Steinberg, 2008). The slag carryover to the V bearing pig iron stream was estimated to be about 3% of the total titaniferous slag.

The selection of refractory lining in the furnace for smelting titanomagnetite in an MgO deficient system is an important aspect that needs careful attention in order to minimise the crystallisation of the refractory spinel solid solution in the titaniferous slag product. Titania bearing slags are corrosive to both alumina and magnesia refractories (Maphutha, et al., 2017; Pistorius, 2004). Hence, it is important that the furnace control system is strictly managed in order to operate with a freeze lining. It is understandable that the furnace lining that would be in contact with the titaniferous slag should be free from MgO; thus, alumina based refractories would be a better choice for lining the furnace for titanomagnetite smelting in an MgO deficient system.

5.4.1.3 Ladle furnace converting

Converting tests were not conducted in the current testwork programme. The converting conditions were deduced from literature (Steinberg, 2008; Rohrmann, 1985). Pyrosim simulation was therefore conducted to calculate the energy and mass balance for the converting of the V bearing pig iron to produce V slag and high purity pig iron. For the simulation, the V bearing pig iron from the smelting stage was transferred hot at 1400°C into the ladle furnace convertor. For simplification of the Pyrosim simulation, only hematite was added as the oxidant. Oxygen, scrap and carburiser are typically added in the ladle furnace converting process (Steinberg, 2008). In the simulation, some N_2 was added as a carrier of the emissions in order to allow for the calculation to complete. The energy requirements and mass distributions on the converting process are included in the conceptual flowsheet and are detailed in section 1.4.1 of the Appendix 1.4. The V slag and high purity pig iron would be sold.

5.4.1.4 UGS process

The UGS process is established for the upgrading of low grade titania slags containing significant alkali and alkali earth impurities (Doan, 1996). For processing the titaniferous slag produced after smelting, the conditions for the respective oxidative- and reductive-roasting stages were deduced from literature (Van Dyk, et al., 1998; Doan, 1996). Pyrosim

was used to simulate the energy requirements and mass distributions for the oxidative and reductive roasting stages.

The best combination of HCl and NaOH leaching conditions determined in section 5.3.2.3 were adopted for the development of the conceptual flowsheet. Though the off gas streams could be used as heating sources during the leaching stages, the current flowsheet includes coal combustion as a source of heat. The coal requirement for the process are based on the thermochemical properties of HCl and NaOH (Lide, 2005). The flowsheet is only conceptual or indicative at best.

The caustic soda leach residue is typically washed and subsequently calcined at 900°C to produce a high grade TiO_2 product suitable for use as feedstock in the pigment production (Van Dyk, et al., 1998). The dolomite fluxed EHSV slag typically contains an MgO concentration of about 14wt% whereas in the limestone fluxed slag, the MgO concentration is about 4wt%. The UGS product with 90.45wt% TiO_2 produced from titaniferous slag is included in the preliminary flowsheet as another saleable product.

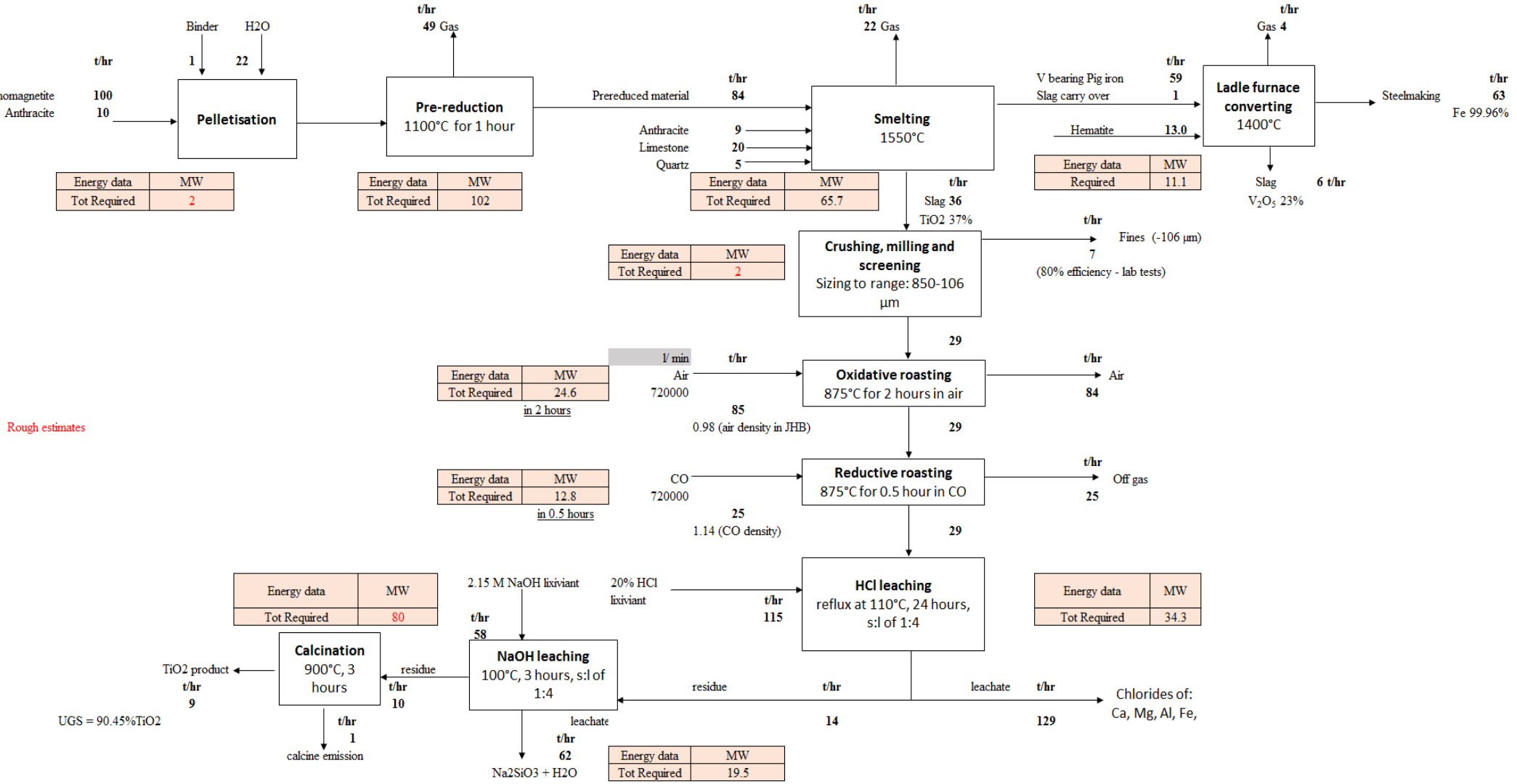

Figure 87. Conceptual flow diagram for the production of Fe, V and Ti products from titanomagnetite by integrated smelting and UGS processes

5.4.2 Economic analysis of the conceptual flowsheet

Economic evaluation of the conceptual flowsheet for the production of vanadium, steel and titanium products was conducted using the discounted cash flow (DCF) model. The DCF modelling approach is established for the economic evaluation of engineering projects including the assessment of the profitability of novel process flowsheets (Kleynhans, et al., 2017; Perez, et al., 2018; Haque, et al., 2012; Hendren, et al., 2017)

The summary of the basic principles of DCF modelling, capital and operational data are included in Appendix 1.5 under sections 1.5.1, 1.5.2, and 1.5.3, respectively. The assumptions that were adopted in the current study are included in Table 38.

A summary of the economic indicators for the conceptual operation over the 20 year projection period is given in Table 39. In general, the flowsheet operates with high Capex, Opex and revenue. The operational costs of the process are very significant. It can be seen in this table (under variable costs) that the major contributor to the Opex is the price of process additives which accounts for 75% of the overall Opex. As shown in Figure 87, the additives in the process include: coal, binder, anthracite, limestone, quartz, hematite, carbon monoxide, HCl, NaOH. Thus, the economic evaluation results suggest that the amount and types of additives in the process require further optimisation in order to maximise the economic viability of the operation. It is however possible that the price of additives is over estimated as the current conceptual process flowsheet, and thus the DCF model, does not consider the recycle streams which are very much possible.

There are three sources of revenue in the conceptual flowsheet, namely; vanadium slag, steelmaking pig iron and UGS product with revenue contributions of 35%, 50%, and 15%, respectively. For the process to be viable, the production and sales levels for all three products need to be met.

In the current configuration of the flowsheet, the net present value (NPV) with a risk rate of 7% is estimated to be about R 620 million, the internal rate of return (IRR) is 8.81%, and the payback period (PP) or return of investment is up to 9.0 years.

It should be noted that the reported economic evaluation of the conceptual flowsheet is preliminary in nature, or indicative at best. Though the economic projections suggest that the payback period of the operation is 9 years, some factors that would have substantial

contribution on the operational costs have not been included in the economic model due to the inaccessibility of typical information in the public domain. These factors include the general environmental and waste management data of the commercial UGS operation. In the conceptual flowsheet, it appears that for the production of 9 t/ hour of the sealable titania product, 129 ton/ hour of the HCl leachate and 62 ton/ hour of NaOH are produced. The data regarding the amount and management of waste and economic implications for the UGS industrial operation at Rio Tinto Fer et Titane (RTFT) to process the SORELSLAG® is not readily available. However, it is reported that over 98% of HCl used is regenerated and reused in the process (Rio Tinto, 2010).

The implications of the costs of environmental and waste management as well as the savings on waste recycling on the economic viability of the conceptual flowsheet of the current study cannot be quantified at this stage.

Table 38: The summary of the assumptions adopted during the economic modelling of the conceptual titanomagnetite process flowsheet

Titaniferous Magnetite process evaluation			
		Units	Source
Year of Start	2018		
Inflation Rate	8	%	
Risk Rate	7	%	
Capital Allowance	12	%	
Tax Rate	28	%	
Sensitivity Checker	25	%	
Debt to Equity Ratio	0	%	
Borrowing rate	9.50	%	
Deposit Rate	5.50	%	
Electricity Cost,	600	R/MWhr	
Water Cost	0.5	R/t feed	
% New Water	5	%	
Furnace cost per MW	1	$m	
Exchange Rate	14	R/$	

Other Capex % Total	2.5	%	
Operating			
Tons per hour of TiMag	100	t	
Hours per day	24	h	
Days per year	365	days	
Efficiency	95	%	
Availability	90	%	
Total hours per year	8 760	h/y	
Available hours per year	7 884	h	
Total Potential Hrs per year	7 490	h/y	
Operating tons per year	748 980	t/y	
Electrode	40	R/kg	
Electrode Consumption	2	kg/MWh	
Other Fixed Costs % Capex	5	%	
Fixed to Variable	30	%	
Electricity			
Charge per MWh	1000	R/MWh	
Additives			
TiMag (Mining Cost)	15.01	$/t	Estimate given by Bushveld Minerals in South Africa
Anthracite	1,000	R/t	Average price deduced from different quotes
Organic binder (CB06)	2,000	R/t	Quotation from BASF in South Africa
Water	500	R/t	Estimate given City of Johannesburg for industrial application
Limestone	300	R/t	[1]Kalkor price estimate
Silica	270	R/t	Average price deduced from different quotes
Hematite	650	R/t	Average price deduced from different quotes
CO	800	R/t	[2]Estimate from Chinese market

HCl (20wt%)	1,281	R/t	[3]Estimate from Chinese market
NaOH (2.15 M)	247	R/t	[4]Estimate from Chinese market
Energy requirements			
Coal for pre-reduction	18	t	
Coal for roasting in fluidised bed	36	t	
Coal for HCl leaching	4	t	
Coal for NaOH leaching	3	t	
Coal for calcination	**18**	t	
Electricity - for pelletisation	17,520	MWh	
Electricity - heating coal for the kiln pre-reduction	17,520	MWh	
Electricity for crushing, milling and screening	17,520	MWh	
Electricity for burning coal in fluidized bed reactor	35,040	MWh	
Electricity for burning coal in calcination	17,520	MWh	
Electricity - for burning for HCl leaching	17,520	MWh	
Electricity - for burning for NaOH leaching	17,520	MWh	
Electricity - for the electric furnace operations	**672,768**	MWh	
	812,928	MWh	
Marketable products			
V_2O_5 Price	168 520	R/t	Metal bulletin
V_2O_5 in Vslag	23.5	wt%	
Steel Grade	5 430	R/t	[5]Steelbenchmarker
%Fe in the alloy	99.96	wt%	
Price of TiO_2 slag with 80wt% TiO_2	700	$/t	[6]Estimate in the Chinese market estimate
TiO_2 in the upgraded titaniferous slag	90.45	wt%	

1. http://www.kalkor.co.za/site/content/id/price-list (accessed on 17 January 2017)
2. https://www.alibaba.com/product-detail/carbon-monoxide-price-in-kg_60323575071.html?spm=a2700.7724857.main07.145.310f346aI7EhTv (accessed on 28 January 2017)
3. https://www.alibaba.com/product-detail/Hot-sale-31-36-HCL-hydrochloric_60774008679.html?s=p (accessed on 15 February 2017)
4. https://zhongliantrading.en.made-in-china.com/product/hKyJBIHCGwWo/China-High-Purity-99-Sodium-Hydroxide-Pearls-Prices.html (accessed on 15 February 2017)
5. http://steelbenchmarker.com › files › price_history.xls – SteelBenchmarker (accessed on 11 March 2017)
6. https://leveling.en.made-in-china.com/product/YjAnrkfJTxcK/China-High-Titanium-Slag-Titanium-Series-Carburant-69012-30-2.html (accessed on 11 March 2017)

Table 39: Summary of the economic evaluation of the conceptual flowsheet over the 20 year projection period

Gross Revenue	R'000	232 670 849	
Gross Operating Costs	R'000	191 926 404	
Capital Expenditure	R'000	7 496 264	
PRODUCTION			
Pre-reduction			
Titanomagnetite Ore feed	'000t	14 980	
Coal	'000t	11 878	
Additives			
Anthracite	'000t	1 498	
Binder - CB6	'000t	165	
Water for pelletisation	'000t	3 296	
Off Gas	'000t	7 355	
Pre-reduced Matte	'000t	12 583	
Smelting			
Pre-reduced Matte	'000t	12 583	
Additives			
Anthracite	'000t	1 348	
Limestone	'000t	2 996	
Silica	'000t	749	
Off Gas	'000t	3 296	
V bearing pig iron	'000t	8 838	
Slag Carry-over	'000t	150	
Titaniferous slag	'000t	5 393	
Conversion			
V bearing pig iron feed	'000t	8 838	
Additives			
Hematite	'000t	1 947	
Off Gas	'000t	599	
UGS PROCESS			
Sizing			
Slag sizing feed	'000t	5 393	
Fines waste	'000t	1 079	
Sized slag	'000t	4 314	
Oxidative roasting			

Sized slag - Feed	'000t	4 314	
Air	'000t	12 684	
Off Gas		12 640	
Oxidised roast	'000t	4 357	
Reductive roasting			
Oxidised roast - Feed	'000t	4 357	
CO	'000t	3 689	
Off Gas	'000t	3 732	
Reduced roast	'000t	4 314	
HCl leaching			
Reduced roast - Feed	'000t	4 314	
HCl lixiviant (20wt% HCl)	'000t	17 255	
HCl leachate (by prod)	'000t	18 880	
HCl leach residue	'000t	2 689	
NaOH leaching			
HCl leach residue - Feed	'000t	2 689	
NaOH lixiviant (2.15 M)	'000t	10 754	
NaOH leachate (by prod)	'000t	11 763	
NaOH leach residue	'000t	1 680	
Calcination			
Off Gas	'000t	189	
Final Product			
V Slag Produced	'000t	899	
Steel Produced	'000t	9 437	
UGS product	'000t	1 491	
Check			
In	'000t	71 359	
Out	'000t	71 359	
REVENUE			Contribution
Sales - V Slag	R'000	81 316 497	35%
Sales - Metal	R'000	117 242 402	50%
UGS product (90.45wt% TiO_2)	R'000	34 111 950	15%
Sales Revenue	R'000	232 670 849	
Gross Revenue	R'000	232 670 849	
Gross Revenue	R.t	310 650	

OPERATING COSTS			
Fixed Costs			
Labour	R'000	642 498	
Total	R'000	642 498	
Variable Costs			contribution
Titanomagnetite	R'000	19 602 440	10%
Labour	R'000	1 933 443	1%
Additives	R'000	142 712 064	75%
Power	R'000	27 035 959	14%
Other	R'000	0	0%
Total	R'000	191 283 906	
Other	R'000	0	
Total Operating Costs	R'000	191 926 404	
Total Operating Costs	R/t	12 813	
PROFIT AFTER TAX			
Profit Before Tax	R'000	29 325 131	
Taxation	R'000	9 023 467	
Profit After Tax	R'000	20 301 664	
Loan Repayment	R'000	0	
Net Profit	R'000	20 301 664	
Net Profit Margin	%	8.73	
Real Project Cash flow for NPV	R'000	8 930 082	
Real Project Cash flow for IRR	R'000	8 930 082	
Cumulative Real Cash flow	R'000	13 142 192	
Net Present Value @ 7.0% Real	R'000	619 815	
IRR	%	8.81	
Payback	years	9.00	

5.5 Critical evaluation of the beneficiated titaniferous slag for titania pigment production

Titanium resources are processed for the production of primarily the TiO_2 pigment, and to a lesser extent the titanium metal (Roskill, 2003). In the current study, the beneficiation of titaniferous slags was investigated with a view of producing a suitable feedstock for the production of the TiO_2 pigment from a by-product. The titania pigment can be produced using either the sulfate or the chloride processes as described in section 2.5 of CHAPTER 2. The feedstock requirements for the pigment production processes are described in sections 2.5.1 and 2.5.2 (Gazquez, et al., 2014; Roskill, 2003; Van Dyk, 1999).

Due to the intensification of environmental restrictions on disposal of toxic waste generated during the pigment production using either of the two processes, high purity titania materials are therefore desired for use as feedstock in both processes. As described in section 2.5.2, the chloride process offers many advantages over the sulfate process. The first prize is thus to produce a suitable feedstock for the chloride process. In addition, the market value for the chloride feedstock is higher than that of the sulfate feedstock (Gazquez, et al., 2014).

A comparison of the chemical composition of the best UGS product produced from the beneficiation of a titaniferous slag was conducted against the typical specifications for the 'chloride slag'. The chloride slag provides the lowest chemical quality specifications for a feedstock to produce the chloride pigment. The typical chemical specifications for the chloride slag and the chemical composition of the UGS product produced from the titaniferous slags are given in Table 40 (Pistorius, 2008). The results show that the current UGS product meets the specified chemical concentrations for TiO_2, FeO, MgO, MnO, and V_2O_5. However, the current UGS product still has a lower TiO_2 grade compared to that of the typical UGS produced from ilmenite slag, which typically contains about 95wt% TiO_2.

The results in Table 40 also show that the current UGS product did not meet the chemical specifications for CaO, SiO_2, Al_2O_3, and Cr_2O_3. High CaO and SiO_2 concentrations in the chloride process feedstock result in accumulation in the chlorinator bed. CaO forms $CaCl_2$ which result in a liquid with a low vapour pressure that accumulates in the reactor. SiO_2-bearing phases have slow chlorination kinetics, and thus result in an increase in unchlorinated solids (Kale & Bisaka, 2016; Pistorius, 2008). The accumulation in the bed can lead to chlorine leaving the fluidisation bed without reacting, a phenomenon called

'chlorine slip'. The bed would need to be drained; thus, there would be operational downtime leading to production losses (Kale & Bisaka, 2016).

High concentrations of Al_2O_3 in the chloride feedstock result in the formation of the $AlCl_3$, which contaminate the $TiCl_4$ product and corrode the equipment used to handle $TiCl_4$. Removal of $AlCl_3$ from gaseous matrix during the process also result in $TiCl_4$ losses. It is thus important that the concentration levels of Al_2O_3 are strictly controlled in the feedstock (Kale & Bisaka, 2016).

The best UGS conditions used to produce the current product are not optimum – for example, the HCl leaching was conducted under atmospheric conditions as opposed to pressurised conditions used in the conventional process. In addition, the HCl leaching temperature of 110°C is lower than the conventional temperature of the UGS process of about 150°C.

The feedstock for the chloride pigment production process also has strict PSD specification of typically 106 to 850 µm (Van Dyk, 1999). It is thus important that the feedstock for the chloride process has the correct PSD. Entrainment and elutriation of fines from a fluidised bed reactor can occur if too fine feed is used – these may lead to direct losses of titanium values. If too coarse feedstock is used, the chlorination kinetics and recoveries of titanium may be compromised. The current UGS product has a fine PSD that would not be suitable for feeding in the chlorinator. However, if the chemical specifications were met, it would have been possible to investigate the possibility of feeding the chlorinator with micro-agglomerates of this UGS feedstock.

The UGS product produced from the beneficiation of titaniferous slag cannot be used as feedstock for the secondary sulfate pigment production process because it is mainly composed of the rutile phase that is sparingly soluble in sulfuric acid. However, testwork can be conducted to investigate the solubility of this product in sulfuric acid. If it is soluble, the use of this high purity titania feedstock in the sulfate pigment production would lower the reagent consumption and reduce the size of the sulfate waste that requires special disposal.

Table 40: Comparison of the typical specifications for the chloride slag and the best UGS product from titaniferous slag (wt%)

	Typical	Beneficiated titaniferous slag
Total TiO_2	>85	90.45
Ti_2O_3	<35	-
FeO	<12	1.98
SiO_2	<2	3.77
Al_2O_3	<1.5	1.71
CaO	<0.13	0.62
MgO	<1.2	0.80
MnO	<2	0.07
Cr_2O_3	<0.25	0.29
V_2O_5	0.60	0.32

-not determined, out of specification

5.6 Conclusions

The current stage of the study involved the investigation of the production of a titaniferous slag with little or no inert spinel structure, followed by beneficiation using the established Upgraded slag (UGS) process to produce a marketable TiO_2 product. A conceptual flowsheet for the production of vanadium, steel and titanium products from titanomagnetite was designed based on the experimental results of the current study, Pyrosim simulations and literature data. The conceptual flowsheet was subjected to economic evaluation using the DCF model to investigate its economic viability. The following conclusions can be drawn from the investigations:

- A titaniferous slag containing an ulvospinel was produced in the cold crucible induction furnace and subsequently upgraded using the UGS process to produce a TiO_2. Through the UGS process, the TiO_2 content in the titaniferous slag was upgraded from 22.00wt% to 90.45wt%. The cumulative TiO_2 recovery during the UGS processing of titaniferous slags was 83%. The UGS product produced from the titaniferous slag met the chemical specifications for the feedstock of the preferred chloride pigment process in terms of the TiO_2, V_2O_5 and MgO concentrations. However, this UGS product contained finer PSD and higher concentrations of impurities such as SiO_2, Al_2O_3, and CaO, than the specifications for the chloride process feedstock. This product was thus not a suitable feedstock for the chloride pigment production. Further optimisation of the UGS conditions has a potential to reduce the concentrations of impurities to levels suitable for feedstock for the

preferred chloride pigment production process. Further investigations are also required to study the feasibility of the chlorination of micro-pellets of the UGS product. Since the UGS product is mainly composed of rutile structure, it would not be a suitable feed for the sulfate pigment production as the sulfuric acid lixiviant is unable to dissolve the rutile structure.

- The DCF economic evaluation of the conceptual flowsheet with an operational projection of 20 years showed that the process is economically viable: NPV at a discount rate of 7% is approximately R 620 million, with IRR of 8.81% and PP of 9 years. The Opex and Revenue have the greatest influence on the NPV or the economic viability of the conceptual flowsheet. Moreover, since the process additives, such as the amount and type of reductant, fluxes, reagents, account for about 75% of the Opex, the results indicate that additives need to be optimized. It is possible that the additives are overestimated in the process as the recycle streams are not considered in the flowsheet, and thus in the DCF economic model.

CHAPTER 6

CONCLUSIONS AND RECOMMENDATIONS

Investigations have been conducted to study the phase equilibria and beneficiation of titaniferous slags for the production of saleable titania products. Since the pseudobrookite solid solution database in the latest version of FactSage thermochemical software does not include Al_2TiO_5 as an endmember, a private $MgTi_2O_5$-Ti_3O_5-Al_2TiO_5 (Al-pseudobrookite) thermodynamic database was successfully developed using the CALPHAD principles and subsequently incorporated into FactSage to facilitate the calculation of phase equilibria of titaniferous slags.

The available equilibrium phase diagram for the Ca-Mg-Al-Si-Ti-O system produced in air (Jochens, et al., 1969) was reviewed and updated to account for the crystallisation of the detrimental spinel solid solution in titaniferous slags using FactSage calculations and equilibration-quench-EPMA analysis results. An equilibrium phase diagram for the Ca-Mg-Al-Si-Ti-O system with the composition applicable to titaniferous slags was also established through thermochemical calculation and experimentation at low pO_2 of 10^{-16} atm applicable to the titanomagnetite smelting. The new phase equilibria showed that in the reviewed Ca-Mg-Al-Si-Ti-O system the liquidus surface and Ti^{3+}/Ti^{4+} mass fraction ratio increased with decreasing the pO_2. The crystallisation of phases between the calculated results in air and at pO_2 of 10^{-16} atm is similar. The established phase equilibria at 10^{-16} atm showed that the chemically inert spinel structure has a very large crystallisation range in the reviewed titaniferous slag compositional range. It is feasible to produce a titaniferous slag with no inert spinel structure when the MgO content in the slag is below 2wt%. However, the smelting of the South African MML titanomagnetite containing the natural MgO in the presence of an MgO-free limestone flux would typically produce a titaniferous slag with about 4wt% MgO. Thus, some inert spinel phase crystallises in this titaniferous slag. The results also showed that the crystallisation of the inert spinel phase in titaniferous slags is not significantly sensitive to variation of the TiO_2 and basicity.

The smelting of the MML titanomagnetite in the presence of an MgO-free lime flux and low ash SASCARB reductant contained in an alumina crucible using the conventional induction furnace resulted in the production of a titaniferous slag that is saturated with Al_2O_3 from the

wear of the crucible. This slag crystallised a significant inert spinel solid solution phase with the content approximated by the MgO concentration in the slag. Another titaniferous slag was produced in a cold copper crucible induction furnace to avoid the crucible wear. This slag crystallised an ulvospinel due to the saturation of the slag by iron. The high iron content in the titaniferous slag was attributed to the completion of the testwork under conditions far from those of equilibrium; hence, the smelting conditions were only mildly reducing that even the vanadium reported to the slag phase. For the purpose of investigating the beneficiation of titaniferous slags to produce titania products, this slag was also subjected to downstream processing.

From a chemical point of view, it was successfully demonstrated that the titaniferous slags can be beneficiated to saleable titania products using the UGS process: the TiO_2 in the discarded inert spinel bearing titaniferous slag produced by the defunct Evraz Highveld Steel and Vanadium Corporation (EHSV) was upgraded from about 33wt% to 75wt%, while the TiO_2 in the titaniferous slags produced in conventional and cold crucible induction furnaces were upgraded from about 30wt% to 67wt% (low because of Al_2O_3 contamination) and 22wt% to 91wt%, respectively. The cumulative TiO_2 recovery in the production of the best UGS product with about 91wt% TiO_2 was 83%. Though the TiO_2 grade in this product makes it attractive for use as feedstock for the production of the chloride pigment, it transpired that it had a finer PSD and higher concentrations of impurities such as SiO_2, Al_2O_3, and CaO, than the specification for the chloride process feedstock. This product was thus not a suitable feedstock for the chloride pigment production. Further optimisation of the UGS conditions has a potential to reduce the concentrations of impurities to levels suitable for feedstock for the preferred chloride pigment production process. Further investigations are also required to study the feasibility of the chlorination of micro-pellets of the UGS product. Since the reduced produce is mainly composed of rutile structure, it would not be a suitable feed for the sulfate pigment production as the sulfuric acid lixiviant is unable to dissolve the rutile structure. Only if soluble in sulfuric acid, this high TiO_2 bearing UGS product, and the other products produced from titaniferous slags could be used as advantageous feedstock for the sulfate pigment production in terms of the minimization of the reagent consumption and the amount of the toxic sulfate waste.

Based on the work of the current study, literature data, and Pyrosim simulations, a conceptual process flowsheet for the production of vanadium slag, steelmaking pig iron and titania

product was proposed. The DCF economic modelling of the conceptual flowsheet for a 20 year operational projection showed that the process is economically viable: NPV at a discount rate of 7% is approximately R 620 million, with an IRR of 8.81%, and PP of 9 years. The process economic viability is sensitive to variation in the Opex and Revenue. In addition, additives, such as the amount and type of reductant, fluxes, reagents, account for about 75% of the Opex. It is possible that the additives are overestimated in the process as the recycle streams were not included in the process, and thus in the DCF economic model.

The current study has demonstrated that (1) a titaniferous slag with little or no inert spinel solid solution phase can be produced when the MgO content in the slag is below 2wt% - the best fluxing strategy to produce this slag would be to conduct the titanomagnetite smelting in the presence of an MgO-free limestone flux and low ash reductant, (2) it is technical feasible to produce three products, i.e. V slag, steelmaking pig iron, and titania product, from titanomagnetite, and (3) it is economically viable to produce the three products from the titanomagnetite. Nevertheless, further work is recommended to intensify the results of the current study, and subsequently the proposed titanomagnetite flowsheet.

- The established thermodynamic database for the $MgTi_2O_5$-Al_2TiO_5-Ti_3O_5 solution applicable to titaniferous slags can be reviewed and validated using experimental results to allow for the model to be officially adopted into the commercial FactSage software for the benefit of the scientific community at large.
- The nucleation and crystallisation kinetics of $CaTiO_3$ primary phase from the titaniferous slags with high CaO concentrations require further empirical investigations for a better understanding of the phase equilibria of titaniferous slags.
- The proposed pre-reduction and smelting of carbon based titanomagnetite pellets in the presence of an MgO-free limestone flux to produce V bearing pig iron and a titaniferous slag with little or no inert spinel phase needs to be demonstrated at a larger scale using an electric arc furnace to intensify the conceptual flowsheet.
- The removal of impurities such as SiO_2, Al_2O_3, and CaO from the cast titaniferous slag or the UGS product using physical separation techniques (density magnetic separation or floatation) in order to meet the specifications for the chloride process feedstock needs to be investigated. When the chemical specifications for the

chloride process feedstock are met, the possibility of using micro-pellets of UGS product as feedstock to the chloride pigment production process can be investigated.

- The best approach to minimize the Opex of the conceptual flowsheet needs further investigations, namely cost of additives (this may include the investigation of recycling the possible waste streams) and electrical power requirement

REFERENCES

Africa, Mining review, 2017. Mining review: Africa. [Online] Available at: https://www.miningreview.com/news/nyanza-light-metals-plant-to-provide-titanium-dioxide-pigment-to-africa/, [Accessed 21 May 2017].

AFROX, 2015. Material Safety Data Sheet - Carbon monoxide. [Online] Available at: http://www.afrox.co.za/internet.global.corp.zaf/en/images/Carbon%20Monoxide.doc266_27628.pdf?v=3.0, [Accessed 14 October 2016].

Anderson, A., 2013. Mining. [Online] Available at: http://www.bdlive.co.za/business/mining/2013/07/08/nyanza-eyes-beneficiation-with-a-r4.2bn-plant, [Accessed 05 October 2016].

Anderson, S., Collen, B., Kruuse, G., Kuylenstierna, U., Magneli, A., Pestmalis, H. and Asbrink S., 1957. Identification of titanium oxides by X-Ray powder patterns. *Acta Chem. Scand.,* 11, pp. 1653-1657.

Andersson, S., Collen, B., Kuylenstierna, U., and Magneli, A., 1957. Phase analysis studies on the titanium-oxygen system. *Acta Chem. Scand.,* 11, pp. 1641-1652.

Australian Oxytrol Systems Pty Ltd, 2017. Oxygen probe - $SIRO_2$ C700 DS probe, *California Gully VIC 3556,* Australia: Australian Oxytrol Systems Pty Ltd.

Azimov, S. A., Gulamova, D. D., Melnik, N. N., Sarkisova, M. K., Suleimanov, K., and Tsapenko, L. M., 1981. Study of aluminum titanate, obtained in a solar furnace, *Izv. Akad. Nauk SSSR, Neorg. Mater.*, 20(3), pp. 469-471.

Bale, C. W., Belisle, E., Chartrand, P., Decterov, S. A., Eriksson, G., Hack, K., Jung, I -H., Kang, Y. -B., Melancon, J., Pelton, A D., Rebelin, C., and Petersen, S., 2008. FactSage Thermochemical Software and Databases - Recent developments, *Calphad, In press 2008: Elsevier Science Ltd,* pp. 1-43.

Bale, C. W., Belisle, E., Chartrand, P., Decterov, S. A., Eriksson, G., Gheribi, A. E., Hack, K., Jung, I. -H., Kang, Y. -B., Melancon, J., Pelton, A. D., Petersen, S., Robelin, C., Sangster, J., Spencer, P., and Van Ende, M. -A, 2016. FactSage thermochemical ssoftware and databases, 2010-2016. *CALPHAD: Computer Coupling of Phase Diagrams and Thermochemistry,* 54, pp. 35-53.

Bale, C. W., Chartrand, P., Decterov, S A., Eriksson, G., Hack, K., Ben Mahfoud, R., Melancon, J., Pelton, A D., and Petersen, S, 2002. FactSage Thermochemical Software and Databases. *Calphad Journal,* 62, pp. 189-228.

Becker, J. H., and Dutton, D. F., 2002. Recovery of titanium from titanium bearing materials. United states, South Africa, Patent No. United States Patent 7258847.

Belon, L. and Forestier, H., 1964. A study of the system Al_2O_3-Ti_2O_3, *Compt. Rend.*, 258(17), pp. 4282.

Berezhnoi, A. S., and Gulko, N. V., 1955. Properties of phases in the MgO - Al_2O_3 - SiO_2 systems. *Ukr. Khim. Zhur.*, 21(2), pp. 158-166

Berreda, M. F., Edo, M. R., Cordero, M. O., and Vaquer, M. J., 2016. Determination of minor and trace elements in geological materials used as raw ceramic materials. *Boletin de la sociedad espanola de ceramic yvidrio,* 55, pp. 185-196.

Bill, B., 2013. Water improvement initiatives in New Zealand using melter slag filter beds, Auckland, New Zealand: National slag association, MF 205-1.

Bisaka, K., Thobadi, I., and Goso, X. C., 2016. Pre-reduction and DC open-arc smelting of carbon-based ilmenite pellets. *Sun City, The tenth internation Heavy Minerals Conference, Southern African Institute of Mining and Metallurgy*, pp. 159-172.

Bleloch, W., 1949. The electric smelting of iron ores for production of alloy irons and steels and recovery of chromium and vanadium. *Journal of the chemical metallurgical and mining society of South Africa,* 49, pp. 363-408.

Boden, P. & Glasser, F. P., 1973. Phase relationships in the system MgO-Al_2O_3-TiO_2. *Trans. J. Br. Ceram. Soc.*, 72(5), pp. 215-220.

Borowiec, K., Grau, A. E., Gueguin, M., and Turgeon, J. -F., 1998. Method to upgrade titania slag and resulting product. United State Patent, Patent No. 5,830,420.

Boyd, M. D., Schoukens, A. K., and Denton, G. M., 1993. The recovery of titanium from titanomagnetite. South Africa, Patent No. P11756.

Bunting, E. N., 1933. Phase equilibria in the systems TiO_2, TiO_2-SiO_2 and TiO_2-Al_2O_3. *Part of Bereau of Standards Journal of Research*, 11, pp. 719-725.

Buscaglia, V., Battilana, G., and Leoni, M., 1996. Decomposition of Al_2TiO_5-$MgTi_2O_5$ solid solutions: a thermodynamic approach. *Journal of materials science,* 31, pp. 5009-5016.

Cacciamani, G., 2016. An introduction to the CALPHAD method and the coumpound energy formalism. *Tecnol. Metal. Mater. Miner., Sao Paulo,* 13(1), pp. 16-24.

Cawthorn, R. G., and Molyneux, T. G., 1986. Vanadiferous magnetite deposits of the Bushveld complex. *Mineral Deposits of Southern Africa,* pp. 1251-1266.

Centre for Research in Computational Thermochemistry, 2018. FactSage 7.2 News. [Online] Available at: http://www.factsage.com/fs72_news.htm, [Accessed 20 May 2018].

Chen, D., Song, B., Wang, L., Qi, T., Wang, Y., and Wang, W, 2011. Solid state reduction of Panzhihua titanomagnetite concentrates with pulverised coal. *Minerals engineering,* 24, pp. 864-869.

Chen, D., Zhao, L., Yahui, L., Qi, T., Wang, J., and Wang, L, 2013. A novel process for recovery of iron, titanium and vanadium from titanomagnetite concentrates: NaOH molten salt roasting and water leaching processes. *Journal of Hazardous materials,* 244-245, pp. 588-595.

Chen, S. Y., and Chu, M. S., 2014. A new process for the recovery of iron, vanadium and titanium from vanadium titanomagnetite. *The journal of the southern african institute of mining and metallurgy*, pp. 481-487.

Cox, P., 2013. Publication of positive pre-feasibility study. [Online] Available at: http://www.brrmedia.co.uk/event/112410/dr-peter-cox-chief-executive-officer?popup=true, [Accessed 10 March 2014].

Dawson, M. F., and Bachmann, T., 1991. Production of titaniferous magnetite concentrate, Johannesburg, South Africa: Mintek internal confidential communication number 139911C.

Decterov, S. A., Jung, I. -H., Jak, E., Kang, Y. -B., Hayes, P., and Pelton, A. D, 2004. Thermodynamic modelling of the Al_2O_3-CaO-CoO-CrO-Cr_2O_3-FeO-Fe_2O_3-MgO-MnO-NiO-SiO_2-S system and applications in ferrous process metallurgy. *Cape Town, South Africa, VII International conference on Molten slags fluxes and salts, The South African Institure of Mining and Metallurgy,* pp. 839-850.

Deines, P., Nafziger, R., Ulmer, G. C., and Woerman, E., 1974. Temperature-oxygen fugacity tables for selected gas mixtures in the system C-H-O at 1 atm total pressure, University Park, Pennsylvania: Bulletin of the Earth and Minerals Sciences Experiment Station, The Pennsylvania State University.

Datta, K., Sen, P. K., Gupta, S. S., and Chatterjee, A., 1993. Effect of titania on the characteristics of blast furnace slags, *Steel research,* 64(5), pp. 232-238.

DeVries, R. C., Roy, R., and Orsborn, E. F., 1954. Phase equilibria in the system CaO-TiO_2. *Journal of Physical Chemisty,* 58(12), pp. 1069-1073.

DeVries, R. C., Roy, R., and Osborn, E. F., 1954. The system TiO_2-SiO_2. *Trans J. Br. Ceram. Soc.,* 53(9), pp. 525-540.

Devries, R. C., Roy, R., and Osborn, E. R., 1955. Phase equilibria in system CaO-TiO_2-SiO_2. *Journal of American Ceramic Society,* 38(5), pp. 158-171.

Dmitriev, A. N., Mukhitdinov, Y. S., Rakhimov, V. R., and Sitdikov, F. G., 2005. Pyrometallurgical Technology for Processing Titanomagnetites from the Tebinbulak Deposit. *Metallurgist,* 49(1-2), pp. 41-43.

Doan, P. H., 1996. Upgraded slag (UGS): implications for TiO_2 feedstock supply. Industrial Minerals Information Division, Worcester Park, *Proceedings of 12th industrial Minerals international congress*, pp. 71-76.

Edison, 2013. Bushveld Minerals - Vanadiferous titano-magnetite. [Online] Available at: http://www.bushveldminerals.com/upload/content/edison%20investments_bmn_040413_outlook.pdf, [Accessed 30 January 2015].

Eisenhuttenleute, Verlag Deutscher, 1995. Slag atlas. Dusseldorf: Verlag Stahleisen GmbH.

Epicier, T., Thomas, G., Wohlfromm, H., and Moya, J. S., 1991. High resolution electron microscopy study of the cationic disorder in Al_2TiO_5. *Journal of material research,* 6(1), pp. 134-145.

Ericksson, G., Pelton, A. D., Woermann, E., and Ender, A., 1996. Measurement and thermodynamic evaluation of pahse equilibria in the Fe-Ti-O system. *Physical chemistry,* 100(11), pp. 1839-1849.

Eriksson, G., Wu, P. and Pelton, A. D., 1993. Critical evaluation and optimization of the thermodynamic properties and phase diagram of the MgO-Al_2O_3, FeO-Al_2O_3, Na_2O-Al_2O_3, and K_2O-Al_2O_3 systems. *Calphad,* 17(2), pp. 189-205.

Evans, D. L., 1970. Solid solution of TiO_2 in SiO_2. *J. Am. Ceram. Soc.*, 53(7), pp. 418-419.

Evraz, 2015. Iron ore. [Online] Available at: http://www.evraz.com/products/business/ore/, [Accessed 24 March 2017].

Fin24.com, 2017. Fin24. [Online] Available at: http://www.fin24.com/Companies/Industrial/davies-we-pulled-out-all-stops-for-r4bn-titanium-project-20170326, [Accessed 24 May 2017].

Financial times, RNS number: 1649C, 2013. Bushveld iron ore project: MML resource upgrade and P-Q zone metallurgical update. [Online] Available at: http://announce.ft.com/Detail/?DocKey=1323-11547687-2359E5DIGCVKC2Q7O233OI6PBP, [Accessed 10 March 2014].

Fine, H. A., and Arac, S., 1980. Effect of minor constituents on liquidus temperature of synthetic blast-furnace slags, *Iron and steelmaking,* 7(4), pp. 160-166.

Finn, C. W., 1980. Techniques in pyrometallurgy research, Pyrometallurgy Vacation School, University of the Witwatersrand, Johannesburg: The South African Institute of Mining and Metallurgy.

Fischer, R. P., 1975. Vanadium resources of titaniferous magnetite deposits. *Geological survey professional paper 926-B,* pp. B1-B10.

Fouad, O. A., 2005. Upgrading of a low- grade titanium slag by sulphation roasting technique to produce synthetic rutile. *Acta Metallurgical Slovaca,* 11(1), pp. 14-24.

Franke, W., and Heimann, R., 1970. Hydrothermal dissolution reactions of magnesium-aluminium-spinel in alkaline solutions. *Journal of Crystal Growth,* 7, pp. 97-101.

Ganguly, J., 2001. Thermodynamic modelling of solid solutions. *EMU Notes in Mineralogy,* 3, pp. 37-69.

Gazquez, M. J., Bolivar, J. P., Garcia-Tenorio, R., and Vaca, F., 2014. A review of the production cycle of titanium dioxide pigment. *Materials sciences and applications,* 5, pp. 441-458.

Geldenhuis, J. M. A., and Pistorius, P. C., 1999. The use of commercial oxygen probes during the production of high titania slags. *Journal of the South African Institute of Mining and Metallurgy,* 99(1), pp. 41-47.

Glazova, V. V., 1965. Phase equilibrium in the titanium-aluminium-oxygen system. *Dolk. Akad. Nauk SSSR,* 164(3), pp. 569-570.

Goldberg, D., 1968. Contribution to study of systems formed by alumina and some oxides of trivalent and tetravalent metals especially titanium oxide, *Rev. Int. Hautes Temper. et Retract.,* 5(3), pp. 181-194.

Goldberg, I., Hammerbeck, E. C., Labuschagne, L. S., and Rossouw, C., 1990. International strategic minerals inventory summary report - Vanadium, Washington: US Geological survey circular 930-K.

Goso, X. C., Lagendijk, H., Erwee, M. W. and Khosa, G., 2016. Indicative Vanadium Deportment in the Processing of Titaniferous Magnetite by the Roast-Leach and Electric Furnace Smelting Processes. *Cape Town, Hydrometallurgy Conference 2016: Sustainable Hydrometallurgical Extraction of Metals, Southern African Institute of Mining and Metallurgy*, pp. 69-78.

Guntner, J., and Hammerschmidt, J., 2012. Sulphation roasting of copper-cobalt concentrate. *The Southern African Institute of mining and metallurgy,* pp. 455-460.

Gupta, C. K., and Krishnamurthy, N., 1992. Extractive metallurgy of vandadium - process metallurgy 8. The Netherlands,Elsevier Science Publishers B.*V,* pp. 151-320.

Habashi, F., 2002. Textbook of Pyrometallurgy. Quebec: Metallurgie Extractive Quebec.

Haines, P. J. et al., 2002. Principles of thermal analysis and calorimetry. Manchester: The Royal Society of Chemistry, pp 55-93.

Halli, P., Taskinen, P. and Eric, R. H., 2017. Mechanisms and kinetics fo solid state reduction of titano magnetite ore with methane. *J. Sustain, metall., 3(2),* pp. 191-206.

Haque, N., Bruckard, W. and Cuevas, J., 2012. A techno-economic comparison of pyrometallurgical and hydrometallurgical options for treating high-arsenic copper concentrates. New Delhi, India, XXVI IMPC.

Hassell, D. J., Obern, J. K., Molloy, S. D., Ibrahim, S. O., and Ali, M S, 2016. Extraction of products from titanium-bearing minerals. For every kind of national protection available, Patent No. WO 2016/007021 A1.

Hayes, P. C., Chen, J. and Jak, E., 2016. Phase equilibria study of the CaO-"Fe_2O_3"-SiO_2 system in air to support iron sintering process optimisation. S*eattle, USA, International Conference on Molten Slags, Fluxes and Salts, The Minerals, Metals and Materials Society*, pp 707-714.

Hayes, P. and Jak, E., 2012. Exploring compositional space in metallurgical slag systems. *Beijing, China, Ninth International Conference on Molten Slags, Fluxes and Salts, The Chinese Society for Metals*, paper 076.

Hendren, Z., Choi, Y. C., Hsu-Kim, H., Hower, J. C., Plata, D., Wiesner, M., 2017. Preliminary Techno-Economic Evaluation of a Novel Membrane Based Separation and Recovery Process for Rare Earth Elements from Coal Combustion Residues. Lexington, 2017 World of Coal Ash (WOCA).

Hillert, M., 1998. Phase Equilibria, Phase Diagrams, and Phase Transformations - thier Thermodynamic Basis. s.l.:Cambridge Univ. Press.

Hillert, M., 2001. The compound energy formalism. *Journal of alloys and compounds,* 320, pp. 161-176.

Holmes, W. T., Banning, L. H., and Brown, L. L., 1968. Liquidus temperatures of titaniferous slags, Washington: United States department of the interior, U.S. Bureau of mines, report of investigations 7081.

Hume-Rothery, W., Christian, J. W., and Pearson, W. B., 1952. Metallurgical equilibrium diagrams. London: The institute of Physics.

Ilatovskaia, M. & Fabrichnaya, O., 2019. Thermodynamic assessment of the Al_2O_3-MgO-TiO_2 system. *Journal of Alloys and Compounds,* 790, pp. 1137-1148.

Ilatovskaia, M., Saenko, I., Savinykh, G. & Fabrichnaya, O., 2018. Experimental study of phase equilibria in the Al_2O_3-MgO-TiO_2 system and thermodynamic assessment of the binary MgO-TiO_2 System. *Journal of American Ceramic Society,* 101, pp. 5198-5218.

Investopedia, IRR, 2018. Internal Rate of Return - IRR. [Online] Available at: https://www.investopedia.com/terms/irr.asp, [Accessed 18 May 2018].

Investopedia, NPV, 2018. Net present value - NPV. [Online] Available at: https://www.investopedia.com/terms/n/npv.asp, [Accessed 18 May 2018].

Jacob, K. T., and Gupta, S., 2009. Phase diagram of the system Ca-Ti-O at 1200 K. *Bull. Mater. Sci,* 32(6), pp. 611-616.

Jak, E., and Hayes, P. C., 2004. *P*hase equilibria determination in complex slag systems. *Cape Town, South Africa, VII International Conference on Molten Slags Fluxes and Salts, The South African Institurte of Mining and Metallurgy,* pp 85-104.

Jak, E., and Hayes, P. C., 2010. Slag phase equilibria and viscositiies in ferronickel smelting slags. *Helsinki, Finland, The Twelfth international Ferroalloys Congress,* pp. 631-639.

Jak, E., Hayes, P. C., and Lee, H.-G., 1995. Improved methodologies for the determination of high temperature phase equilibria. *Metals and Materials,* 1(1), pp. 1-8.

Jena, B. C., Dresler, W., and Reilly, I. G., 1994. Extraction of titnaium, vanadium and iron from titanomagnetite deposits at Pipestone lake, Manitoba, Canada. *Minerals Engineering,* 8(1), pp. 159-168.

Jiaquan, L., Tingxu, Q., Xianguo, F. and Housheng, C., 2012. Method for recovering vanadium, titanium and iron from vanadium titanium magnetite. China, Patent No. CN101619371B.

Jochens, P. R., 1967. Contribution to the knowledge of the equilibrium and non-equilibriuim behaviour of titaniferous slags, Johannesburg, South Africa: University of Witwatersrand, Department of Metallurgy. PhD thesis.

Jochens, P. R., Sommer, G., and Howat, D. D., 1969. Preliminary equilibrium and non-equilibrium phase studies of titaniferous slags. *Journal of The iron and Steel Institute,* 207, pp. 187-192.

Jones, R. T., 2001. Steady-state simulation of pyrometallurgical processes. [Online] Available at: http://www.mintek.co.za/Pyromet/Pyrosim/Pyrosim2.htm, [Accessed 22 November 2017].

Jongejan, A., and Wilkins, A. L., 1970. A re-examination of the system CaO-TiO_2 at liquidus temperatures, *J. Less-Common Metals,* 20(4), pp. 273-279.

Jung, I.-H., Eriksson, G., Wu, P., and Pelton, A., 2009. Thermodynamic modeling of the Al_2O_3-Ti_2O_3-TiO_2 system and its applications to the Fe-Al-Ti-O inclusion diagram. *ISIJ international*, 49(9), pp. 1290-1297.

Kale, A., and Bisaka, K., 2016. Review of titanium feedstock selection for fluidised bed chlorinators. *Sun City, South Africa The tenth international Heavy Minerals Conference,* pp. 313-323.

Kang, Y.-B., Jung, I.-H., and Lee, H.-G., 2006. Critical thermodynamic evaluation and optimization of the MnO-"TiO_2"-"Ti_2O_3" system. *Computer Coupling of Phase diagrams and Thermochemistry,* 30, pp. 235-247.

Kattner, U. R., 1997. The Thermodynamic Modeling of Multicomponent Phase Equilibria. *JOM,* 49(12), pp. 14-19.

Kaufman, L., and Bernstein, H., 1970. Computer Calculation of Phase Diagrams. New York: Academic press Inc..

Kelly, B. F., 1993. Ironmaking at BHP New Zealand Steel Limited, Glenbrook, New Zealand. *In Australasian Mining and Metallurgy, 1 (The Sir Maurice Mawby Memorial),* pp. 348-353.

Kinnaird, J. A., 2005. The Bushveld large igneous province, South Africa, Johannesburg: School of Geosciences, University of Witwatersrand.

Kirillova, S. A., Almjashev, V. I., and Gusarov, V. V., 2011. Phase relationships in the SiO_2-TiO_2 system. *Russian Journal of Inorganic Chemistry*, 56(9), pp. 1464-1471.

Kirschen, M., and de Capitani, C., 1999. Experimental determination and computation of the liquid miscibility gap in the system CaO-MgO-SiO_2-TiO_2, *Journal of Phase Equilibria*, 20(6), pp. 593-611.

Kleynhans, E. L., Beukes, J. P., van Zyl, P. G., and Fick, J. I., 2017. Techno-economic feasibility of a pre-oxidation process to enhance pre-reduction of chromite. *Journal of Southern African Institute of Mining and Metallurgy,* 117(5), pp. 457-468.

Koekemoer, J. J., 1991. An investigation into the upgrading of titaniferous magnetite and extraction of the vanadium, Johannesburg, South Africa: Mintek internal confidential communication number 140922C.

Kowalski, M., Spencer, P. J. & Neuschutz, D., 1995. Phase diagrams. In: Slag atlas. Dusseldorf: Verlag Stahleisen GmbH, pp. 21-186.

Krajewski, D., 1992. Untersuchungen im system Al-Mg-Ti-O unter stark reduziernden bedingungen, Aachen, North Rhine-Westphalia: Institut fur Kristallographie, RWTH Aachen. Masters dissertation.

Lang, S. M., Fillmore, C. L., and Maxwell, L. H., 1952. The system beryllia-alumina-titania: phase relations and general physical properties of three-component procelains. *Journal of Research of the National Bureau of Standards,* 48(4), pp. 298-312.

Lejus, A. -M., Goldberg, D. and Revcolevschi, A., 1966. New compounds formed between rutile, TiO_2, and oxides of trivalent and tetravalent metals, *C.R. Acad. Sci., Ser c*, 263(20), pp. 1223-1226.

Liddell, N., 2011. Vanadium sector review, London, United Kingdom: Ocean Equities.

Lide, D. R., 2005. CRC Handbook of Chemistry and Physics. Internet Version 2005, <http://www.hbcpnetbase.com> ed. Boca Raton, Florida: CRC Press.

Liu, Z.-K., 2009. First-Principles calculations and Calphad Modeling of thermodynamics. *Journal of phase equilibria and diffussion,* 30(5), pp. 517-534.

Lydall, M. and Craven, P., 2013. Mintek's 2020 vision - 2013 revision, Johannesburg, South Africa: Mintek internal confidential report no. 41350.

Malakhov, D. V., 2010. On choosing a reference surface for a two-sublattice model. *CALPHAD: Computer coupling of phase diagrams and thermochemistry*, 34, pp. 452-455.

Manamela, M. M., and Pistorius, P. C., 2005. Ore size does affect direct reduction of titaniferous magnetite. *The Journal of The South African Institute of Mining and Metallurgy*, 105, pp. 183-186.

Maphutha, M. P., Ramaili, M., Sitefane, M. B., and Goso, X. C., 2017. The effect of magnesia and alumina crucible wear on the smelting characteristics of titaniferous magnetite. *The Journal of the Southern African Institute of Mining and Metallurgy*, 117(7), pp. 649-655.

Massazza, F., and Sirchia, E., 1958. The system MgO-SiO_2-TiO_2. 1. Revision of the binary systems: *Chim. Ind. (Milan),* 40, pp. 376-380.

McKee, W. D., and Aleshin, E., 1963. Aluminum oxide-titanium oxide solid solution, *J. Am. Ceram. Soc.*, 46(1), pp. 54-58.

McRae, L. B., Pothas, E., Jochens, P. R., and Howat, D. D., 1969. Physico-chemical Properties of Titaniferous Slags. *Journal of the South African Institute of Mining and Metallurgy*, pp. 577-594.

MIDREX, 2018. 2017 world DRI statistics. [Online] Available at: https://www.midrex.com/news-literature/news-releases/world-dri-statistics, [Accessed 22 June 2018].

Mitchell, P. S., 2000. The use of vanadium in steel. *Guilin, China, Proceedings of the Vanitec symposium*, pp. 25-35.

Mizoguchi, T., and Ueshima, Y., 2005. Determination of the Ti_2O_3-CaO-Al_2O_3 phase diagram at steelmaking temperature, *Tetsu-to-Hagane*, 91, pp. 376-382.

Model, M. S., 1962. Formation of solid solutions in high titanium slags, *Izv. Akad. Nauk SSSR, Neorg. Mater.*, 146(4), pp. 871.

Monnereau, O., Remy, F. and Casalot, A., 1985. Partial phase diagram for the titanium dioxide-titanium sesquioxide-aluminium oxide system at 1223 K and preparation of a new aluminum titanium oxide, $Al_2Ti_7O_{15}$, *C.R. Acad. Sci., Ser. 2,* 301(6), pp. 375-378.

Moolman, S., 2012. Tivani project nearing start of construction and mining. [Online] Available at: http://www.miningweekly.com/article/tivani-project-nearing-start-of-mining-and-construction, [Accessed 22 August 2015].

Morizane, Y., Ozturk, B., and Fruehan, R. J., 1999. Thermodynamics of TiOx in blast furnace-type slags. *Metall. Trans. B,* 30(1), pp. 29-43.

Moskalyk, R. R., and Alfantazi, A. M., 2003. Process of vanadium:a review. *Minerals Engineering*, 16, pp. 793-805.

Navrotsky, A., 1975. Thermodynamics of formation of some compounds with pseudobrookite structure and of the $FeTi_2O_3$-Ti_3O_5 solid solution series. *American mineralogist*, 60, pp. 249-256.

Nell, J., and McCullough, S., 2001. Upgrading of titania proxy slag derived from titaniferous magnetite, Randburg, Johannesburg, South Africa: Mintek internal confidential report number C3269M.

NTMK, 2003. Specialization: Nizhniy Tagil Iron and Steelworks. [Online] Available at: htt://www.ntmk.ru/en/manufacture/specialization.php, [Accessed 24 March 2015].

Ohno, A., and Ross, H. U., 1963. Liquidus-temperature measurements in lime-titania-alumina-silica system. *Canadian Met. Quart.*, 2(3), pp. 243-258.

Ohta, M., and Morita, K., 2002. Thermodynamics of the Al_2O_3-SiO_2-TiO_x oxide system at 1873 K. *ISIJ. International*, 42(5), pp. 474-481

Osborn, E. F., and Gee, K. H., 1969. Phase equilibria at liquidus temperatures for a part of the system CaO-MgO-Al_2O_3-TiO_2-SiO_2 and their bearing on the effect of titania on the properties of blast furnace slag. *Bull. Earth Miner. Sci. Exp., Stn.*, 85, pp. 57-80.

Pelton, A. D., 1988. A database and sublattice model for molten salts. *Calphad*, 12(2), pp. 127-142.

Pelton, A. D., 2004. Thermodynamic models and databases for slags, fluxes and salts. *Cape Town, South Africa, VII International Conference on Molten Slags Fluxes and Salts, The Southern African Institute of Mining and Metallurgy*, pp 607-614.

Pelton, A. D., 2006. Thermodynamic database development - modeling and phase diagram calculations in oxide systems. *Rare metals*, 25(5), pp. 473-480.

Pelton, A. D., Eriksson, G., Krajewski, D., Gobbels, M., and Woermann, E, 1998. Measurement and thermodynamic evaluation of phase equilibria in the Mg-Ti-O system. *Zeitschrift fur Physikalische Chemie*, Bd. 207, pp. 163-180.

Perez, J. C., Echeverry, L. A., Peralta-Ruiz, Y. Y. and Gonzalez-Delgado, A. D., 2017. A Techno-Economic Sensitivity Approach for Development of a Palm-based Biorefineries in Colombia. *Chemical Engineering Transactions*, 57, pp. 13-18.

Perrut, M., 2015. Thermodynamic modeling by the chalphad method and its application to innovative materials. *Journal Aerospace Lab*, 9, pp. 1-11.

Pistorius, P. C., 2004. Equilibrium interaction between freeze lining and slag from ilmenite smelting. *Cape Town, South Africa, VII International Conference on Molten Slags Fluxes and Salts, The Southern African Institute of Mining and Metallurgy*, pp. 237-242.

Pistorius, P. C., 2008. Ilmenite smelting: the basics. *The Journal of The Southern African Institute of Mining and Metallurgy,* 108, pp. 35-43.

Pistorius, P. C., 2011. Titania slag smelting and calcination of crude zinc oxide: examples of processing under thermodynamic and kinetic constraints. *Proceedings of the second international slag valorization symposium, Leuven Belgium,* pp. 263-270.

Povoden-Karadeniz, E., Chen, M., Ivas, T., Grundy, A. N., and Gauckler, L. J., 2012. Thermodynamic modelling of La_2O_3-SrO-Mn_2O_3-Cr_2O_3 for solid oxide fuel cell applications. *Mater. Res.,* 27(15), pp. 1915-1925.

Povoden-Karadeniz, E., Grundy, A. N., Chen, M., Ivas, T., and Gauckler, L. J., 2009. Thermodynamic assessment of the La-Fe-O system. *Journal of Phase Equilibria and Diffusion,* 30(4), pp. 351-366.

Pyromation inc., 2017. Temperature vs. electromotive force (EMF) tables and temperature vs. resistance tables. [Online] Available at: http://www.pyromation.com/Downloads/Data/temperature-tables.pdf, [Accessed 15 June 2017].

Rahmel, A., and Spencer, P. J., 1991. Thermodynamic aspects of TiAl and $TiSi_2$ oxidation: The Al-Ti-O and Si-Ti-O phase diagrams, *Oxid. Metals,* 35(1-2), pp. 53-56.

Remy, F., Monnereau, O., Casalot, A., Dahan, F., and Galy, J, 1988. Titane a valence mixte, un nouvel oxyde ternaire: $Al_2Ti_7O_{15}$. *Journal of solid state chemistry,* 76, pp. 167-177.

Reynolds, I. M., 1985. The nature and origin of titaniferous magnetite-rich layers in the upper zone of the Bushveld Complex. *Economic Geology 80,* pp. 1089-1108.

Reznichenko, V. A., Model, M. S. and Talmud, N. I., 1979. Mutual solubility of the compounds Ti_2O_3 and $MgTiO_3$, *Inorganic materials,* 15(9), pp. 1337-1338.

Rice, C. E., and Robinson, W. R., 1977. Structural Changes resulting from doping Ti_2O_3 with Sc_2O_3 or Al_2O_3. *J. Solid State Chem.,* 21, pp. 155-160.

Rio Tinto, 2010. Sustainable Development Report - 60 years of history 1950-2010, Quebec: Rio Tinto, Fer et Titane.

Rohrmann, B., 1985. Vanadium in South Africa. *Journal of the South African Institute of Mining and Metallurgy*, 85(5), pp. 141-150.

Roskill, 2003. The economics of titanium minerals and pigments. s.l.:Roskill information Ltd.

Roskill, 2007. The economics of iron ore. s.l.:Roskill information services Ltd.

Roskill, 2010. Vanadium: Global industry market and outlook, 12th Edition. s.l.:Roskill information services Ltd.

Roth, R. S., 1958. Revision of the phase equilibrium diagram of the binary system calcia-titania, showing the compound $Ca_4Ti_3O_{10}$, *J. Res. Nat. Bur. Standard, RP 2913,* 61(5), pp. 437-440.

Rouf, M. A., Cooper, A. H. and Bell, H. B., 1969. Structural changes resulting from doping Ti_2O_3 with Sc_2O_3 or Al_2O_3. *Trans. Brit. Ceram. Soc,* 68, pp. 263-267.

Roy, R., DeVries, R C., Rase, D. E., Shafer, M. W., and Osborn, E. F., 1952. Pennsylvania State College, Quaterly Report on Contract No. DA36-039 sc-5594, Pennsylvania: mmsu.,vamoa State College.

Santos, S., 2012. Direct reduced iron (DRI) and CO_2 capture. [Online] Available at: https://ieaghg.org/docs/General_Docs/IEAGHG_Presentations/DRI_-_Technical_Review_of_CCS_Option_Part_2.pdf, [Accessed 20 November 2017].

Schultz, M., Fritze, H., and Stenzel, C., 2013. Measurement and control of oxygen partial pressure at elevated temperatures. *Sensors and Actuators B,* 187, pp. 503-508.

Selman, G. L., Ellison, P. J., and Darling, A. S., 1970. Carbon in Platinum and Palladium: solubility determinations and diffusions at high temperatures. *Platinum Metals Rev.,* 14(1), pp. 14-20.

Shijiazhuang Leveling import and export Co., Ltd., 2014. Acidsoluble titanium slag. [Online] Available at: https://leveling.en.made-in-china.com/product/XjfmOJEDqncU/China-Acidsoluble-Titanium-Slag-From-Leveing-Manufacturer-Price.html, [Accessed 22 June 2018].

Shi, J., Sun, L., Qiu, J., Wang, Z., Zhang, B., and Jiang, M., 2016. Experimental determination of the phase diagram for $CaO\text{-}SiO_2\text{-}MgO\text{-}10\%Al_2O_3\text{-}5\%TiO_2$ system. *ISIJ international*, 56(7), pp. 1124-1131.

Shindo, I. J., 1980. Determination of the phase diagram by the slow cooling float zone method: The system $MgO\text{-}TiO_2$, J. *Cryst. Growth,* 50(4), pp. 839-851.

Shi, P., Saxena, S. K., and Sundman, B., 1992. Sublattice solid solution model and its application to orthopyroxene (Mg, Fe)$_2$Si$_2$O$_6$. *Phys Chem Minerals*, 18, pp. 393-405.

Shultz, R. L., 1973. Effects of titanium oxide on equilibria among refractory phases in the system CaO-MgO-iron oxide, *J. Am. Ceram. Soc,* 56(1), pp. 33-36.

Sitefane, M., Masipa, M., Maphutha, P. and Goso, X., 2017. The effect of CaO and MgO ratio on the smelting characteristics of vanadium bearing titaniferous magnetite. *Pretoria, South Africa, Proceedings of the 3rd Young Professionals Conference, The Southern African Institute of Mining and Metallurgy,* pp. 467-480.

Steele, T. W., and Wilson, A., 1966. A study of the salt-roasting process for the extraction of vanadium from iron ore. *Brussels, Belgium, 36th Congress International De Chimie Industrielle*, pp. 1-6.

Steinberg, W. S., 2008. University of Pretoria. [Online] Available at: http://repository.up.ac.za/bitstream/handle/2263/26090/dissertation.pdf.,sequence=1, [Accessed 10 October 2016].

Steinberg, W. S., Geyser, W., and Nell, J., 2011. The history and development of the pyrometallurgical processes at Evraz Highveld Steel and Vanadium. *Journal of the Southern African Institute of Mining and Metallurgy,* 111, pp. 63-79.

Sui, Z., Zhang, L., Zhang, L., Wang, M., Lou, T., Chen, H, 2004. Feasibility of recovering metals from associated slags. *Cape Town, South Africa, VII International conference on molten slags fluxes and salts, The South African Institute of Mining and Metallurgy*, pp. 183-187.

Sundman, B., and Gueneau, C., 2015. Thermochemical modelling of multi-component systems, Sweden: NEA/NSC/R(2015)5.

Taylor, P. R., Shuey, S. A., Vidal, E. E., and Gomez, J. C., 2006. Extractive metallurgy of vanadiun-containing titaniferous magnetite ores:a review. *Minerals and metallurgical processing,* 23(2), pp. 80-86.

Tenova, 2018. Iron reduction technologies. [Online] Available at: https://www.tenova.com/product/iron-reduction-technologies/, [Accessed 22 June 2018].

Thiele, H., and Da Corte, C., 2013. Feed characterisation of titaniferous hematite, Johannesburg, South Africa: Mintek external confidential report number 6256.

Tulgar, H. E., 1976. Solid state relationships in the system calcium oxide-titanium dioxide, *Istanbul Tek. Univ. Bul.*, 29(1), pp. 111-129.

University of Cape Town, 2013. Techno-Economic Analysis. [Online] Available at: http://www.rci.uct.ac.za/rcips/fundinnov/tea, [Accessed 18 May 2018].

Van der Colf, J. & Howat, D. D., 1979. Viscosities, electrical resistivities, and liquidus temperatures of slags in the system CaO-MgO-Al_2O_3-TiO_2-SiO_2 under neutral conditions. *Journal of the South African institute of mining and metallurgy*, pp. 255-263.

Van Dyk, J. P., 1999. Process development for the production of beneficiated titania slag, Pretoria, South Africa: Dissertation submitted for the degree Philosophiae Doctor in metallurgical engineering at the department of materials science and metallurgical engineering of the university of Pretoria.

Van Dyk, J. P. & Pistorius, P. C., 1999. Evaluation of a process that uses phosphate additions to upgrade titania slag. *Metallurgical and Materials Transactions B,* Volume 30b, pp. 823-826.

Van Dyk, J. P., Vegter, N. M., Visser, C. P., De Lange, T., Winter, J. D., Walpole, E. A., and Nell, J., 1998. Beneficiation of titania slag by oxidation and reduction treatment. South Africa, Patent No. CA2338716C.

Van Vuuren, D. S., and Tshilombo, G. T., 2011. Nitriding of ilmenite and high-grade slag fines. *Journal of the South African Institute of MIning and Metallurgy, South Africa,* 111, pp. 173-181.

Vasyutinskii, N. A., 1977. Interaction in the systems Ti_3O_5-Al_2TiO_5 and Ti_3O_5-$MgTi_2O_5$, *Izv. Akad. Nauk SSSR, Neorg. Mater.*, 13(1), pp. 177-178.

Waldeck, H. G., 2013. Bushveld iron ore project - Scoping study report. [Online] Available at: http://www.bushveldminerals.com/upload/content/bmn%20scoping%20study%20(final)_22%20april%202013.pdf, [Accessed 18 January 2015].

Walwyn, D., 2013. The use of techno-economic analysis to support research programmes. Cape Town: Siminar hosted by RC&I of the University of Cape Town.

Wang, M., Zhang, L., Zhang, L., Sui, Z., and Tu, G., 2006. Selective enrichment of TiO_2 and precipitation behavior of perovskite phase in the titania bearing slag. *Trans.Nonferrous Met.Soc.China,* 16, pp. 421-425.

Wang, Y., Qi, T., Chu, J., and Zhao, W., 2010. Production of TiO_2 from $CaTiO_3$ by alkaline roasting method. *Rare metals,* 29(2), pp. 162-167.

Welch, J. H., and Gutt, W., 1959. Tricalcium silicate and its stability within the system CaO-SiO_2. *Journal of American society,* 42, pp. 11-15.

Whitman, H., 2013. Initial report - Baobab Resources Plc. [Online] Available at: http://www.baobabresources.com/files/BAO_WhitmanHoward20130619.pdf, [Accessed 30 January 2015].

Woermann, E., Brezny, B. and Muan, A., 1969. Phase equilibrium in the system MgO-iron oxide-TiO in air, *Am. J. Sci,* 267A, pp. 463-479.

Wulandari, W., Brooks, G. A., Rhamdhani, M. A., and Monaghan, B. J., 2009. Thermodynamic modelling of high temperature systems. *Chemeca,* pp. 1-16.

Xirouchakis, D., Smirnov, A., Woody, K., Lindsley, D. H., and Andersen, D. J., 2002. Thermodynamics and stability of pseudobrookite-type $MgTi_2O_5$ (karrooite). *American mineralogist,* 87, pp. 658-667.

Zhang, L., Zhang, L. N., Wang, M Y., Li, G. Q., and Sui, Z. T., 2007. Recovery of titanium compounds from molten Ti-bearing blast furnace slag under the dynamic oxidation condition. *Minerals Engineering,* 20, p. 684–693.

Zhang, L., Zhang, L. N., Wang, M Y., Lou, T. P., Sui, Z. T., and Jang, J. S., 2006. Effect of perovskite phase precipitation on viscosity of Ti-bearing blast furnance slag under the dynamic oxidation condition. *Journal of crystalline solids,* 352, pp. 123-129.

Zhao, B., Jak, E., and Hayes, P., 2009. Phase equilibria studies in the slag system TiO_2-SiO_2-Al_2O_3-MgO-CaO at carbon saturation. *Santiago, Chile, VIII International Conference on Molten Slags, Fluxes and Salts,* pp. 71-82.

Zhao, L., Wang, L., Qi, T., Chen, D., Zhao, H., and Liu, Y., 2014. A novel method to extract iron, titanium, vanadium, and chromium from high-chromium vanadium-titanomagnetite concentrates. *Hydrometallurgy,* 149, pp. 106-109.

Zhong, B., Xue, T., Zhao, H., Qi, T., and Chen, W., 2014. Preparation of Ti-enriched slag from V-bearing titanomagnetite by two-stage hydrochloric acid leaching route. *Separation and purification technology,* 137, pp. 59-65.

APPENDICES

1.1 Calibration of thermocouples

The B-type thermocouple that was prepared and used in the current testwork programme for temperature measurements was calibrated using a primary standard thermocouple, i.e. ISOTECH 17977/1. The standard thermocouple is equipped with a reference junction that should be maintained at 0°C through the use of an ice water bath monitored by a calibrated thermometer. The cold reference junction was immersed in the ice water bath throughout the calibration process. The prepared thermocouple was placed inside a closed-end alumina sheath in order to shield the tip from cyclical heat source which would result in temperature measurement fluctuation during the verification procedure in the vertical tube furnace.

The calibration procedure entailed binding the thermocouple to be calibrated onto the standard thermocouple using a Pt wire such that the tips are coincident. The bundled thermocouples were inserted into the small vertical tube furnace through the top and held in position by clamps. The thermocouples were connected to the Keysight data acquisition unit for read out. The furnace was heated up at a rate of 5°C/ minute to a verification temperature – the B-type thermocouples were verified at 1100°C, 1200°C, 1300, 1400°C, 1500°C and 1600°C. The selection of verification temperatures was based on the projected test temperatures. The furnace was allowed to reach thermal equilibrium at each verification temperature, after which 10 EMF readings of each thermocouple, i.e. the standard and test thermocouples, were manually taken. For each verification point, the stability of the EMF reading was verified and needed to be within the equivalent of ±0.25°C. The means and standard deviations of the EMF measurements were determined. The EMF measurements were converted to temperature using standard thermocouple tables (Pyromation inc., 2017).

The correction factors stated in the calibration certificate of the standard were applied on each verification point in order to get the true temperature. The correction factor to be applied on the test thermocouple temperature readings were calculated by subtracting the test thermocouple temperature reading from the true temperature of the respective verification temperature points. The calibration information of the B-type thermocouple used in the current study is summarised in Table 41. The standard and the test thermocouples were accurate to ±2°C relative to the set point temperature.

Table 41: Calibration information of the B-type thermocouple used in the current study

	ISOTECH	Test B-type thermocouple	Calibration set point, °C
Mean, mV	0.005787	0.005787	
Std dev	0.000000	0.000001	
Correction, mV	-0.000006		1100
Corrected emf, mV	0.005782		
Temp calc, °C	1100.2	1100.8	
Mean, mV	0.006806	0.006804	
Std dev	0.000000	0.000000	
Correction, mV	-0.000008		1200
Corrected emf, mV	0.006798		
Temp calc, °C	1201.1	1201.7	
Mean, mV	0.007864	0.007859	
Std dev	0.000000	0.000000	
Correction, mV	-0.000010		1300
Corrected emf, mV	0.007854		
Temp calc, °C	1300.5	1301.0	
Mean, mV	0.008967	0.008958	
Std dev	0.000000	0.000000	
Correction, mV	-0.000013		1400
Corrected emf, mV	0.008954		
Temp calc, °C	1399.8	1400.2	
Mean, mV	0.010123	0.010111	
Std dev	0.000000	0.000000	
Correction, mV	-0.000016		1500
Corrected emf, mV	0.010107		
Temp calc, °C	1500.7	1501.0	
Mean, mV	0.011292	0.011268	
Std dev	0.000001	0.000000	
Correction, mV	-0.000020		1600
Corrected emf, mV	0.011272		
Temp calc, °C	1600.7	1600.4	

1.2 Verification of the pO_2 in the tube furnace

1.2.1 Calibration of mass flow controllers

The Tylan mass flow meter (MFM) used in the current testwork is calibrated annually by the National Metrology Institute of South Africa (NMISA). The 1000 and 10 sccm mass flow controllers (MFCs) that were used in conjunction with the MFM were calibrated by measuring the volumetric flowrates of individual gases at different controller set points using the established setup made up of a burette coupled with a U-tube manometer. Before the calibration, the MFCs were cleaned by gently blowing with N_2 gas. The 1000 and 10 sccm MFCs were calibrated using different size burettes with volumetric flowrates determined on 300 cm^3 and 10 cm^3 volumes, respectively. The MFCs were regularly checked during the testwork programme. The typical calibration curves for CO and CO_2 gases are shown in Figure 88 and Figure 89, respectively. The curves in the respective figures show that the flowrates obtained from the MFCs were comparable to the controller set points. However, in the case of CO_2, the required flowrates were very low that the verification of the required flowrate could only be estimated from extrapolation. In addition, the volumetric flowrates of CO_2 were also checked against the data established by Deines at al. (1974) for the volumetric percent CO_2, temperature and the corresponding pO_2 (Deines, et al., 1974). The measurements of pCO and pCO_2 were validated by the absolute measurements of the pO_2 using the oxygen probe.

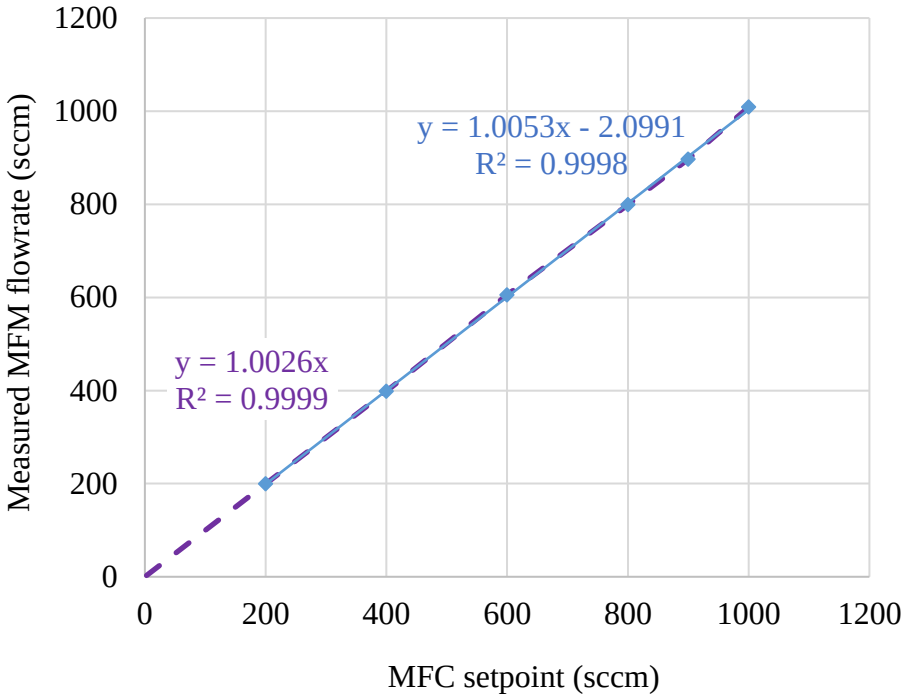

Figure 88: Calibration of the 1000 sccm MFC for the control of the CO gas flowrate

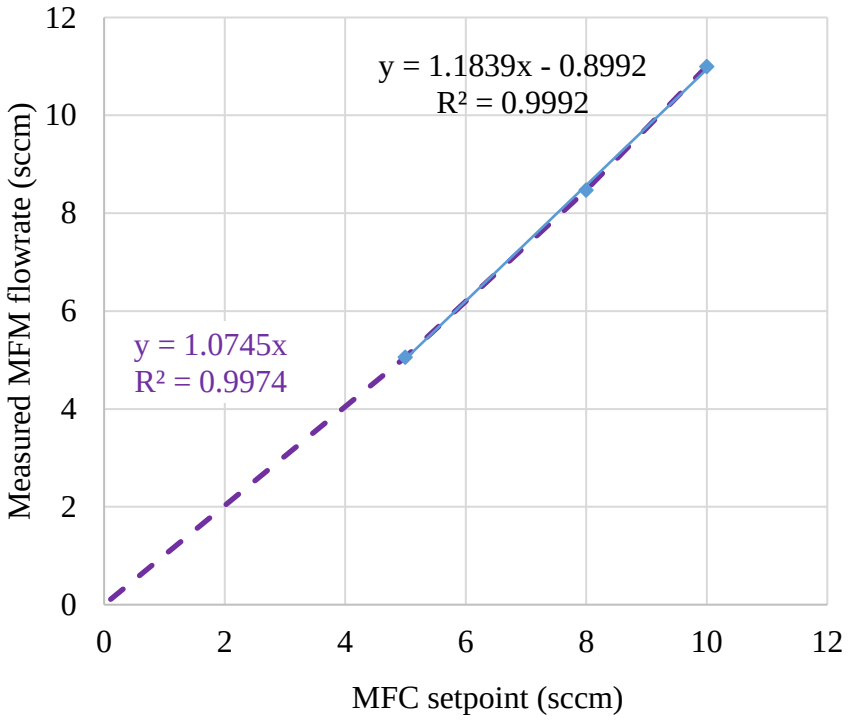

Figure 89: Calibration of the 10 sccm MFC for the control of the CO_2 gas flowrate

1.2.2 Determination of pO_2 from EMF signal using the Nernst equation

The DS-type oxygen probe measurements are based on the Nernst equation. The probe measures the pO_2 in terms of a DC millivolt signal. The following conversions to the Nernst equation were applied in order to be able to convert the mV to pO_2 in atm. The original Nernst equation is given as follows:

$$E_{cell} = E^0 - \frac{RT}{nF} log_e Q \quad [1.1]$$

Where:

E_{cell}= equilibrium potential

E^0= standard electrochemical cell potential

R= ideal gas constant

T = temperature (K)

n= number of charges per reactant species

F= Faraday constant

Q= mass-action expression (approximated by the equilibrium expression)

Since $\log_e(x) = \ln(x)$, Equation [1.1] can also be written as shown in Equation [1.2].

$$E_{cell} = E^0 - \frac{RT}{nF} ln\, Q \quad [1.2]$$

At equilibrium the following conditions apply: Q = K, and $E_{cell} = 0$ and thus Equation [1.2] can be presented as Equation [1.3]:

$$0 = E^0(V) - \frac{RT}{nF} ln\, K \quad [1.3]$$

The equilibrium constant (K) is defined as shown in Equation [1.4]:

$$K = \frac{pO_{2\ inside}}{pO_{2\ outside}} \quad [1.4]$$

Where, $pO_{2\ \text{inside}}$ = oxygen partial pressure inside the probe, and $pO_{2\ \text{outside}}$ = oxygen partial pressure in the reaction tube of the furnace.

Equations [1.3] and [1.4] can be combined into Equation [1.5].

$$E^0(V) = \frac{RT}{nF} ln \left[\frac{pO_{2\ inside}}{pO_{2\ outside}}\right] \quad [1.5]$$

When air is used as a reference gas inside the probe, i.e. $pO_{2\ \text{inside}} = 0.209$ atm, oxygen partial pressure in the reaction tube outside the probe, i.e. $pO_{2\ \text{outside}}$ can be determined by rearranging Equation [1.5] into Equation [1.6].

$$pO_{2\ outside} = 0.209 \times e^{\frac{-46.42 \times E}{T}} \quad [1.6]$$

1.3 EPMA results of equilibration quench experiments

Table 42: The summary of phase compositions in the Ca-Mg-Al-Si-Ti-O system, obtained in the equilibration-quench testwork in air

		EPMA analysis results					
Sample	**Temperature**	**MgO**	**Al_2O_3**	**SiO_2**	**CaO**	**TiO_2**	**Equilibrium phases**
MS1	1200	2.16	13.92	19.32	26.99	36.72	Liquid
		0.02	0.32	0.06	41.31	58.96	$CaTiO_3$
		0.15	1.13	1.22	2.80	94.99	TiO_2
	1230	2.24	13.65	19.06	27.13	37.28	Liquid
		0.04	0.34	0.06	41.93	58.74	$CaTiO_3$
		0.06	0.71	0.62	1.12	98.03	TiO_2
	1260	2.18	13.99	19.52	27.62	36.95	Liquid
		0.08	0.42	0.33	41.77	58.69	$CaTiO_3$
		0.40	2.40	2.59	2.77	91.98	TiO_2
	1270	2.18	13.99	19.52	27.62	36.95	Liquid
		0.03	0.16	0.06	41.34	58.68	$CaTiO_3$
		0.06	0.61	0.59	1.27	97.85	TiO_2
	1280	2.14	13.76	18.58	27.72	37.39	Liquid
		0.09	0.70	0.67	41.51	58.08	$CaTiO_3$
	1300	2.18	13.80	18.77	27.65	37.24	Liquid
		0.21	1.04	1.10	40.94	57.88	$CaTiO_3$
	1350	2.34	15.46	20.94	24.86	35.56	Liquid
		0.03	0.31	0.05	41.64	58.83	$CaTiO_3$
	1380	2.49	15.10	20.64	25.55	36.38	Liquid
		0.04	0.41	0.06	40.71	58.22	$CaTiO_3$
	1400	2.32	14.34	19.73	26.14	36.87	Liquid
		0.04	0.30	0.03	41.87	58.60	$CaTiO_3$
	1405	2.08	13.19	19.53	25.56	34.00	Liquid
		-	0.39	0.05	40.65	59.02	$CaTiO_3$
	1410	2.15	13.79	19.30	27.00	36.88	Liquid
		0.05	0.32	0.04	42.01	58.31	$CaTiO_3$
	1415	2.08	12.19	18.44	24.88	35.86	Liquid

	1420	2.17	12.92	19.02	26.81	38.32	Liquid
	1450	2.14	13.38	18.77	27.21	38.18	Liquid
	1500	2.14	13.30	18.64	27.55	37.89	Liquid
	1550	2.23	13.55	19.03	27.21	37.59	Liquid
MS2	1200	9.68	14.00	35.55	21.87	19.52	Liquid
		0.58	1.58	2.37	40.90	55.54	$CaTiO_3$
		16.98	8.67	0.31	0.50	73.91	$MgTi_2O_5$-Ti_3O_5-Al_2TiO_5
		0.20	34.65	44.59	20.60	0.94	$CaAl_2Si_2O_8$
	1250	7.19	15.70	29.28	21.12	25.66	Liquid
		0.15	0.18	0.07	41.93	57.77	$CaTiO_3$
		16.90	8.80	0.08	0.29	74.15	$MgTi_2O_5$-Ti_3O_5-Al_2TiO_5
		0.10	35.14	45.49	20.45	0.98	$CaAl_2Si_2O_8$
	1290	8.05	14.37	24.61	21.04	32.32	Liquid
		0.50	0.68	0.93	41.08	56.90	$CaTiO_3$
		16.73	9.01	0.12	0.46	73.94	$MgTi_2O_5$-Ti_3O_5-Al_2TiO_5
	1300	8.34	14.03	22.69	20.55	34.60	Liquid
		0.15	0.17	0.04	41.98	58.21	$CaTiO_3$
		16.86	8.88	0.09	0.44	73.92	$MgTi_2O_5$-Ti_3O_5-Al_2TiO_5
	1310	8.50	14.06	22.23	20.39	35.01	Liquid
		0.13	0.26	0.05	41.96	57.85	$CaTiO_3$
	1350	7.97	13.70	20.81	21.42	36.08	Liquid
		0.11	0.26	0.08	42.13	57.87	$CaTiO_3$
	1360	0.09	0.21	0.05	41.66	58.09	$CaTiO_3$
		7.96	12.94	20.81	21.38	36.94	Liquid
	1370	7.99	13.33	20.76	21.58	36.51	Liquid
	1380	8.03	12.80	20.67	21.50	36.71	Liquid
	1390	8.04	12.95	20.83	21.60	37.19	Liquid
	1400	8.38	13.40	20.82	21.27	36.05	Liquid
MS3	1200	9.57	12.61	20.68	19.41	36.76	Liquid
		29.22	69.77	0.20	0.23	0.94	$Mg(Al,Ti)_2O_4$
		0.13	0.16	0.13	41.63	58.07	$CaTiO_3$
		17.30	7.54	0.11	0.42	74.51	$MgTi_2O_5$-Ti_3O_5-Al_2TiO_5
	1250	9.65	12.76	20.88	19.60	36.49	Liquid
		29.22	68.99	0.20	0.17	1.41	$Mg(Al,Ti)_2O_4$
		0.17	0.23	0.07	41.89	58.20	$CaTiO_3$
		17.43	7.64	0.15	0.20	75.24	$MgTi_2O_5$-Ti_3O_5-Al_2TiO_5
	1280	9.62	12.98	20.98	19.60	37.12	Liquid
		29.39	68.86	0.10	0.05	1.23	$Mg(Al,Ti)_2O_4$
		0.13	0.13	0.13	41.72	58.20	$CaTiO_3$
		16.89	7.98	0.07	0.21	74.34	$MgTi_2O_5$-Ti_3O_5-Al_2TiO_5
	1290	9.68	12.92	21.13	19.72	36.59	Liquid

		28.86	69.65	0.12	0.06	1.20	$Mg(Al,Ti)_2O_4$
		0.13	0.21	-	42.22	58.36	$CaTiO_3$
		16.92	7.94	0.08	0.33	74.44	$MgTi_2O_5$-Ti_3O_5-Al_2TiO_5
	1300	9.60	13.04	20.84	19.58	37.22	Liquid
		29.40	69.22	0.10	0.03	1.18	$Mg(Al,Ti)_2O_4$
		0.11	0.19	0.04	41.89	58.18	$CaTiO_3$
		16.93	7.87	0.11	0.24	74.86	$MgTi_2O_5$-Ti_3O_5-Al_2TiO_5
	1310	9.48	13.23	20.97	19.67	37.19	Liquid
	1320	9.76	12.99	21.59	20.18	35.12	Liquid
	1350	9.57	13.00	21.10	19.77	36.51	Liquid
	1400	9.60	12.73	20.57	19.41	37.26	Liquid
MS4	1300	10.69	12.01	22.82	19.98	34.61	Liquid
		29.38	70.41	0.12	-	1.60	$Mg(Al,Ti)_2O_4$
		17.22	7.67	0.07	0.23	75.10	$MgTi_2O_5$-Ti_3O_5-Al_2TiO_5
	1320	10.88	12.18	21.69	18.72	36.20	Liquid
		28.53	69.76	0.16	-	1.76	$Mg(Al,Ti)_2O_4$
		16.81	7.65	0.16	0.19	75.27	$MgTi_2O_5$-Ti_3O_5-Al_2TiO_5
	1330	11.11	13.03	21.40	18.18	36.17	Liquid
		28.38	70.35	0.15	0.04	1.52	$Mg(Al,Ti)_2O_4$
		16.93	7.65	0.07	0.32	75.90	$MgTi_2O_5$-Ti_3O_5-Al_2TiO_5
	1340	11.65	12.48	20.34	17.77	36.86	Liquid
		30.42	67.86	0.10	0.06	1.52	$Mg(Al,Ti)_2O_4$
	1350	11.59	13.13	20.89	17.59	36.94	Liquid
		28.75	69.66	0.12	-	1.41	$Mg(Al,Ti)_2O_4$
	1360	11.46	13.12	20.88	17.59	36.72	Liquid
	1390	11.34	12.96	20.98	17.72	36.94	Liquid
	1400	11.34	12.92	20.65	17.73	36.71	Liquid
MS5	1300	12.41	13.29	25.01	18.95	30.35	Liquid
		29.44	68.71	0.10	-	1.75	$Mg(Al,Ti)_2O_4$
		17.16	7.16	0.08	0.35	75.25	$MgTi_2O_5$-Ti_3O_5-Al_2TiO_5
	1320	11.89	12.44	24.18	19.16	32.34	Liquid
		29.84	68.20	0.09	-	1.87	$Mg(Al,Ti)_2O_4$
		17.75	5.25	0.06	0.23	76.69	$MgTi_2O_5$-Ti_3O_5-Al_2TiO_5
	1350	12.92	12.59	23.02	17.73	33.74	Liquid
		29.33	68.45	0.09	0.05	2.08	$Mg(Al,Ti)_2O_4$
		16.79	7.92	0.22	0.46	74.60	$MgTi_2O_5$-Ti_3O_5-Al_2TiO_5
	1355	13.01	11.80	21.49	16.53	35.31	Liquid
		29.79	69.11	0.13	0.04	1.75	$Mg(Al,Ti)_2O_4$
		17.51	7.21	-	0.15	74.84	$MgTi_2O_5$-Ti_3O_5-Al_2TiO_5
	1360	13.51	11.32	24.57	16.26	34.41	Liquid
		30.34	67.46	0.13	-	1.64	$Mg(Al,Ti)_2O_4$
		17.10	7.34	0.13	0.15	74.59	$MgTi_2O_5$-Ti_3O_5-Al_2TiO_5
	1365	13.35	11.61	22.68	16.26	36.77	Liquid
		30.47	67.37	0.27	0.04	1.85	$Mg(Al,Ti)_2O_4$

		17.50	7.14	0.20	0.28	74.30	$MgTi_2O_5$-Ti_3O_5-Al_2TiO_5
	1370	13.59	11.87	21.09	16.37	37.08	Liquid
		29.52	68.05	0.12	0.12	2.19	$Mg(Al,Ti)_2O_4$
		16.78	7.00	0.14	0.40	75.68	$MgTi_2O_5$-Ti_3O_5-Al_2TiO_5
	1380	13.20	12.68	20.65	15.66	37.82	Liquid
	1390	13.66	13.33	20.34	15.77	36.90	Liquid
	1400	13.45	12.74	19.68	15.33	38.80	Liquid
M6	1350	14.01	12.81	33.08	19.47	20.64	Liquid
		29.51	68.39	0.18	0.10	1.82	$Mg(Al,Ti)_2O_4$
		17.71	7.13	0.12	0.03	75.02	$MgTi_2O_5$-Ti_3O_5-Al_2TiO_5
		56.82	0.84	40.86	0.58	0.91	Mg_2SiO_4
	1360	30.13	66.70	0.19	0.05	2.93	Liquid
		19.68	11.29	25.64	13.54	29.85	$Mg(Al,Ti)_2O_4$
		17.64	6.22	0.11	0.13	75.91	$MgTi_2O_5$-Ti_3O_5-Al_2TiO_5
	1380	19.71	12.19	22.81	11.65	33.63	Liquid
		29.30	66.10	0.84	0.32	3.44	$Mg(Al,Ti)_2O_4$
		17.83	6.02	0.13	0.20	75.81	$MgTi_2O_5$-Ti_3O_5-Al_2TiO_5
	1390	19.37	12.02	22.83	11.49	34.29	Liquid
		29.90	67.22	0.16	0.05	2.67	$Mg(Al,Ti)_2O_4$
		17.60	7.21	0.10	0.21	74.88	$MgTi_2O_5$-Ti_3O_5-Al_2TiO_5
	1400	19.68	12.11	22.69	11.55	33.97	Liquid
		30.24	66.98	0.18	0.04	2.56	$Mg(Al,Ti)_2O_4$
	1420	19.69	11.92	22.71	11.67	34.01	Liquid
		29.90	67.22	0.16	0.05	2.67	$Mg(Al,Ti)_2O_4$
	1430	19.28	11.51	23.29	9.90	36.01	Liquid
		30.16	65.16	0.17	0.03	3.54	$Mg(Al,Ti)_2O_4$
	1450	19.31	12.22	23.15	9.97	35.99	Liquid
	1500	19.17	12.53	23.22	10.06	36.37	Liquid
MS7	1450	26.14	14.35	28.86	4.84	25.01	Liquid
		29.55	66.44	0.18	-	3.23	$Mg(Al,Ti)_2O_4$
		17.95	5.90	0.12	0.09	76.10	$MgTi_2O_5$-Ti_3O_5-Al_2TiO_5
		58.27	0.34	40.52	0.07	0.61	Mg_2SiO_4
	1470	27.06	13.60	27.32	3.96	27.32	Liquid
		29.86	66.05	0.23	0.03	3.53	$Mg(Al,Ti)_2O_4$
		18.36	5.57	0.11	0.03	76.08	$MgTi_2O_5$-Ti_3O_5-Al_2TiO_5
		59.01	0.25	40.48	0.04	0.41	Mg_2SiO_4
	1490	28.25	12.80	25.41	3.37	29.31	Liquid
		29.90	65.84	0.26	-	3.79	$Mg(Al,Ti)_2O_4$
		17.98	5.82	0.11	0.07	75.81	$MgTi_2O_5$-Ti_3O_5-Al_2TiO_5
		58.01	0.74	39.92	0.08	0.98	Mg_2SiO_4
	1495	27.75	13.05	23.82	2.31	33.90	Liquid
		30.88	64.10	0.27	-	4.83	$Mg(Al,Ti)_2O_4$
		17.14	7.71	0.13	-	73.24	$MgTi_2O_5$-Ti_3O_5-Al_2TiO_5
	1500	28.37	12.76	19.56	2.37	36.62	Liquid

		29.44	68.54	0.11	-	1.29	$Mg(Al,Ti)_2O_4$
	1510	28.57	13.56	19.57	2.40	35.79	Liquid
		29.22	69.84	0.14	-	1.24	$Mg(Al,Ti)_2O_4$
	1515	28.83	13.59	19.87	2.34	35.16	Liquid
		28.60	70.18	0.13	-	1.27	$Mg(Al,Ti)_2O_4$
	1520	28.30	13.82	19.56	2.43	35.96	Liquid
	1530	28.26	13.13	19.75	2.39	36.13	Liquid
	1550	28.58	12.68	19.59	2.39	36.60	Liquid

Table 43: The summary of phase compositions in the Ca-Mg-Al-Si-Ti-O system, obtained in the equilibration-quench testwork at pO_2 of 10^{-16} atm

		EPMA analysis results					
Sample	**Temperature**	**MgO**	**Al_2O_3**	**SiO_2**	**CaO**	**TiO_2**	**Equilibrium phases**
MS1	1280	2.27	13.43	19.72	27.80	36.73	Liquid
		-	0.19	0.06	41.49	58.16	$CaTiO_3$
		0.06	0.71	0.62	1.12	98.03	TiO_2
	1300	2.37	13.64	19.70	28.08	36.66	Liquid
		0.07	0.25	0.06	41.42	58.11	$CaTiO_3$
		-	0.36	0.09	0.57	98.36	TiO_2
	1310	2.28	13.78	20.26	28.12	36.52	Liquid
		0.03	0.27	-	41.41	58.00	$CaTiO_3$
	1350	2.32	13.47	19.77	27.97	36.61	Liquid
		-	0.41	0.08	41.15	58.00	$CaTiO_3$
	1430	2.27	14.27	20.83	29.25	34.22	Liquid
		-	0.12	0.05	41.01	58.41	$CaTiO_3$
	1470	2.25	13.56	20.18	27.75	36.39	Liquid
		0.04	0.12	0.08	41.15	58.04	$CaTiO_3$
	1480	2.23	13.51	19.94	27.86	36.51	Liquid
		-	0.32	-	40.80	57.90	$CaTiO_3$
	1490	2.23	13.41	19.50	28.05	36.67	Liquid
	1500	2.31	13.58	19.50	28.02	36.82	Liquid
MS3	1280	11.84	12.54	30.72	22.15	23.59	Liquid
		29.53	66.48	0.35	0.22	3.14	$Mg(Al,Ti)_2O_4$
		0.13	0.16	0.06	40.83	58.68	$CaTiO_3$
		12.08	4.48	0.06	0.72	82.80	$MgTi_2O_5$-Ti_3O_5-Al_2TiO_5
	1300	11.51	12.75	29.30	22.58	23.61	Liquid
		29.85	66.00	0.22	0.09	3.85	$Mg(Al,Ti)_2O_4$
		0.12	0.04	-	40.89	57.98	$CaTiO_3$
		12.48	4.81	0.10	0.42	82.13	$MgTi_2O_5$-Ti_3O_5-Al_2TiO_5
	1350	11.98	13.80	29.42	23.85	21.21	Liquid

		29.63	65.97	0.17	0.04	4.85	$Mg(Al,Ti)_2O_4$
		0.15	0.09	-	40.91	58.66	$CaTiO_3$
		12.34	4.17	0.09	0.80	83.37	$MgTi_2O_5$-Ti_3O_5-Al_2TiO_5
	1360	10.49	14.61	21.51	21.32	31.14	Liquid
		28.56	67.91	0.10	-	2.43	$Mg(Al,Ti)_2O_4$
		0.13	0.17	-	41.54	58.12	$CaTiO_3$
		12.63	3.06	-	0.44	83.15	$MgTi_2O_5$-Ti_3O_5-Al_2TiO_5
	1370	10.52	14.68	22.02	21.29	30.68	Liquid
		28.42	68.11	-	-	2.43	$Mg(Al,Ti)_2O_4$
		0.13	0.13	0.05	41.65	58.07	$CaTiO_3$
		12.44	4.20	0.09	0.66	82.76	$MgTi_2O_5$-Ti_3O_5-Al_2TiO_5
	1380	10.43	14.34	20.89	20.73	33.69	Liquid
	1400	10.64	14.55	21.59	21.33	31.34	Liquid
MS4	1300	12.83	14.33	20.82	18.76	32.40	Liquid
		30.89	65.42	0.17	-	3.45	$Mg(Al,Ti)_2O_4$
		12.36	4.50	0.08	0.55	82.04	$MgTi_2O_5$-Ti_3O_5-Al_2TiO_5
		0.19	0.33	-	41.10	58.44	$CaTiO_3$
	1320	12.84	14.31	20.87	18.90	32.90	Liquid
		30.36	65.96	0.17	-	3.95	$Mg(Al,Ti)_2O_4$
		12.44	4.20	0.09	0.66	82.76	$MgTi_2O_5$-Ti_3O_5-Al_2TiO_5
		0.12	0.26	-	40.74	58.02	$CaTiO_3$
	1340	12.98	14.52	20.81	18.88	32.83	Liquid
		30.24	66.56	0.10	0.55	3.47	$Mg(Al,Ti)_2O_4$
		12.22	4.86	0.08	0.50	82.56	$MgTi_2O_5$-Ti_3O_5-Al_2TiO_5
		0.16	0.36	-	41.00	59.39	$CaTiO_3$
	1350	12.95	14.64	21.17	18.43	32.26	Liquid
		30.67	66.82	0.12	-	3.47	$Mg(Al,Ti)_2O_4$
		12.35	4.25	0.08	0.78	82.80	$MgTi_2O_5$-Ti_3O_5-Al_2TiO_5
		0.17	0.37	0.07	41.14	58.66	$CaTiO_3$
	1360	12.93	14.66	21.27	18.87	32.08	Liquid
		30.73	66.80	0.16	-	3.44	$Mg(Al,Ti)_2O_4$
		12.63	3.96	0.09	0.44	82.65	$MgTi_2O_5$-Ti_3O_5-Al_2TiO_5
	1370	12.85	14.24	20.78	18.85	32.31	Liquid
		30.31	66.49	0.12	-	3.32	$Mg(Al,Ti)_2O_4$
		12.46	4.50	0.08	0.54	82.64	$MgTi_2O_5$-Ti_3O_5-Al_2TiO_5
	1380	12.95	14.64	21.17	18.43	32.26	Liquid
		29.51	66.15	0.10	0.15	3.11	$Mg(Al,Ti)_2O_4$
		12.43	4.31	0.27	0.73	83.19	$MgTi_2O_5$-Ti_3O_5-Al_2TiO_5
	1390	12.96	14.22	20.75	18.79	32.58	Liquid
		30.73	66.80	0.16	-	3.44	$Mg(Al,Ti)_2O_4$
	1400	12.92	13.87	20.92	18.70	32.44	Liquid
		30.67	66.82	0.12	-	3.47	$Mg(Al,Ti)_2O_4$
	1410	12.96	14.22	20.75	18.79	32.58	Liquid
	1440	12.97	14.82	22.41	19.62	30.61	Liquid

	1480	12.88	14.90	21.76	19.12	31.87	Liquid
MS5	1320	16.20	11.37	29.77	23.81	19.55	Liquid
		31.05	63.06	0.22	0.04	6.35	$Mg(Al,Ti)_2O_4$
		12.99	4.67	-	0.19	82.57	$MgTi_2O_5$-Ti_3O_5-Al_2TiO_5
		0.15	0.17	-	41.57	58.29	$CaTiO_3$
	1340	12.49	13.45	29.48	20.62	23.19	Liquid
		29.40	66.40	0.14	-	3.55	$Mg(Al,Ti)_2O_4$
		13.14	4.04	-	0.24	82.79	$MgTi_2O_5$-Ti_3O_5-Al_2TiO_5
		0.13	0.17	0.08	41.57	58.27	$CaTiO_3$
	1350	14.73	11.37	26.08	20.59	27.65	Liquid
		29.03	68.90	0.28	0.14	2.85	$Mg(Al,Ti)_2O_4$
		13.36	4.39	0.04	0.31	82.60	$MgTi_2O_5$-Ti_3O_5-Al_2TiO_5
		0.13	0.12	-	41.68	58.04	$CaTiO_3$
	1360	12.62	13.50	29.49	20.80	23.42	Liquid
		30.24	65.19	0.20	0.06	5.24	$Mg(Al,Ti)_2O_4$
		12.92	5.16	0.12	0.43	81.90	$MgTi_2O_5$-Ti_3O_5-Al_2TiO_5
	1390	11.10	14.40	27.71	19.95	26.73	Liquid
		29.37	66.84	0.10	0.04	3.54	$Mg(Al,Ti)_2O_4$
		11.15	3.94	0.16	0.43	84.65	$MgTi_2O_5$-Ti_3O_5-Al_2TiO_5
	1400	11.33	13.83	26.76	19.58	28.05	Liquid
		29.89	67.72	0.08	-	3.38	$Mg(Al,Ti)_2O_4$
		11.88	4.15	0.05	0.30	82.79	$MgTi_2O_5$-Ti_3O_5-Al_2TiO_5
	1410	11.70	13.90	28.96	20.33	25.05	Liquid
		28.82	67.19	0.11	-	3.80	$Mg(Al,Ti)_2O_4$
	1430	11.27	14.05	26.93	19.75	28.09	Liquid
		28.51	67.33	0.11	-	3.56	$Mg(Al,Ti)_2O_4$
	1440	11.24	13.94	27.13	19.44	28.16	Liquid
		28.96	66.76	0.14	-	3.66	$Mg(Al,Ti)_2O_4$
	1450	15.20	14.70	22.19	17.76	30.83	Liquid
	1500	15.37	14.57	21.62	17.84	30.84	Liquid
MS7	1500	32.07	14.02	27.00	3.53	23.53	Liquid
		27.87	68.87	0.08	-	2.53	$Mg(Al,Ti)_2O_4$
		12.10	5.34	0.12	0.53	82.06	$MgTi_2O_5$-Ti_3O_5-Al_2TiO_5
		57.63	0.39	41.36	0.11	0.53	Mg_2SiO_4
	1510	32.35	13.72	26.56	3.48	23.56	Liquid
		29.55	66.02	0.25	0.15	3.13	$Mg(Al,Ti)_2O_4$
		12.40	4.43	0.08	0.51	82.53	$MgTi_2O_5$-Ti_3O_5-Al_2TiO_5
		57.84	0.43	41.62	0.12	0.60	Mg_2SiO_4
	1520	32.51	13.83	26.74	3.50	24.53	Liquid
		29.47	66.20	0.17	0.10	3.01	$Mg(Al,Ti)_2O_4$
		11.91	4.05	0.06	0.55	82.56	$MgTi_2O_5$-Ti_3O_5-Al_2TiO_5
		58.36	0.94	39.99	0.09	1.38	Mg_2SiO_4
	1530	32.23	13.75	26.61	3.48	23.71	Liquid
		29.74	65.27	0.18	0.12	4.63	$Mg(Al,Ti)_2O_4$

	1550	31.68	13.95	26.91	3.49	23.57	Liquid
		29.20	67.99	0.34	-	3.19	$Mg(Al,Ti)_2O_4$
	1600	31.74	15.60	22.72	2.59	28.27	Liquid

1.4 Pyrosim reports for the simulation of the conceptual titanomagnetite process flowsheet

1.4.1 Pre-reduction, smelting and ladle furnace converting stages

FLOWRATES

	FLOWRATE (kg/h)	TEMPERATURE (øC)
FEED 1		
TiMag	100	25
Anthracite	10	25
Organic binder	1	25
Water	22	25
PRODUCTS 1		
Gas	49	1100
TO NEXT UNIT		
Metal	84	1100
FEED 2		
Limestone	20	25
Silica	5	25
Anthracite	9	25
PRODUCTS 2		
Gas	22	1550
Slag	36	1550
TO NEXT UNIT		
Slag	1	1400
Metal	59	1400
FEED 3		
Hematite	13	25
N2	2	25
PRODUCTS 3		
Gas	7	1400
Slag	6	1400
Metal	63	1400

OPERATION

UNIT 1

Equilibrium model calculates multi-phase multi-reaction equilibrium
ELEMENTS: C O H Si Al Ca Ti Cr Fe Mg Mn V
Gas: CO CO2 H2O H2O(g) SiO
Metal: Al Al2O3 Ca Ca2SiO4 CaCO3 CaO CaSiO3 CaTiO3 Cr Cr2O3 Fe Fe2O3 Fe2SiO4 Fe2TiO5 Fe3C Fe3O4 FeCr2O4 FeO FeTiO3 Mg MgO MgSiO3 Mn MnO Si SiC SiO SiO2 Ti Ti2O3 Ti3O5 TiO2 V V2O3 V2O5

Operating temperature = 1100øC
Operating pressure = 1.00 atm

UNIT 2

Equilibrium model calculates multi-phase multi-reaction equilibrium
ELEMENTS: C O H Si Al Ca Ti Cr Fe Mg Mn V
Gas: CO CO2 H2O H2O(g) O2 SiO
Slag: Al2O3 Ca2SiO4 CaCO3 CaO CaSiO3 CaTiO3 Cr2O3 Fe2O3 Fe2SiO4 Fe2TiO5 Fe3O4 FeCr2O4 FeO FeTiO3 MgO MgSiO3 MnO SiO2 Ti2O3 Ti3O5 TiO2 V2O3 V2O5
Metal: Al C Ca Cr Fe Mg Mn Si Ti V

Operating temperature = 1550øC
Operating pressure = 1.00 atm

Slag : Metal ratio = 0.62

UNIT 3

Equilibrium model calculates multi-phase multi-reaction equilibrium
ELEMENTS: C O H Si N Al Ca Ti Cr Fe Mg Mn V
Gas: CO CO2 H2O(g) O2 SiO N2
Slag: Al2O3 Ca2SiO4 CaCO3 CaO CaSiO3 CaTiO3 Cr2O3 Fe2O3 Fe2SiO4 Fe2TiO5 Fe3O4 FeCr2O4 FeO FeTiO3 MgO MgSiO3 MnO SiO2 Ti2O3 Ti3O5 TiO2 V2O3 V2O5
Metal: Al C Ca Cr Fe Mg Mn Si Ti V

Operating temperature = 1400øC
Operating pressure = 1.00 atm

Slag : Metal ratio = 0.09

ENERGY

UNIT 1 requires 102 kWh (369 MJ) per hour of operation, including a rate of energy loss of 0 kW
This is 1.22 MWh per ton of Metal produced in this unit

UNIT 2 requires 65.7 kWh (236 MJ) per hour of operation, including a rate of energy loss of 0 kW
This is 1.11 MWh per ton of Metal produced in this unit

UNIT 3 requires 11.1 kWh (40.1 MJ) per hour of operation, including a rate of energy loss of 0 kW
This is 0.177 MWh per ton of Metal produced in this unit

ELEMENTAL ANALYSES
(MASS %) Slag constituents are shown as oxides; all others as elements

	Al/Al2O3	C	Ca/CaO	Cr/Cr2O3	Fe/FeO	H	Mg/MgO	Mn/Mn2O3	N	O	Si/SiO2
PRODUCTS 1											
Gas	.....	23.107	.....	.....	.....	4.923	.....	.....	.....	71.970	.....
Metal	2.509	0.037	0.060	0.172	67.089	.....	1.066	0.222	.....	17.427	0.748
PRODUCTS 2											
Gas	.....	42.863	.....	.....	.....	.....	.....	.....	.....	57.129	0.008
Slag	10.885	.....	30.917	0.000	0.252	.....	4.053	0.212	.....	38.714	17.361
Metal	0.000	3.185	0.000	0.244	95.116	.....	0.002	0.224	.....	.....	0.003
PRODUCTS 3											
Gas	.....	28.380	.....	.....	.....	.....	.....	.....	30.435	41.185	.....
Slag	1.438	0.000	4.078	3.588	60.739	.....	0.570	3.367	.....	26.821	2.353
Metal	.....	0.023	.....	0.013	99.958	.....	.....	0.006	.....	.....	.....

	Ti/TiO2	V/V2O5
PRODUCTS 1		
Gas	.....	.....
Metal	9.555	1.117
PRODUCTS 2		
Gas	.....	.....
Slag	36.602	1.041
Metal	0.001	1.225
PRODUCTS 3		
Gas	.....	.....
Slag	4.842	23.464
Metal	.....	0.001

DISTRIBUTION OF ELEMENTS

PRODUCTS 1	Gas	Dust	Solids	Slag	Metal	Matte
Al:	.....	.....	.....	.....	100.000%	.....
C :	99.732%	.....	.....	.....	0.268%	.....
Ca:	.....	.....	.....	.....	100.000%	.....
Cr:	.....	.....	.....	.....	100.000%	.....
Fe:	.....	.....	.....	.....	100.000%	.....
H :	100.000%	.....	.....	.....	.....	.....
Mg:	.....	.....	.....	.....	100.000%	.....
Mn:	.....	.....	.....	.....	100.000%	.....
O :	70.903%	.....	.....	.....	29.097%	.....
Si:	.....	.....	.....	.....	100.000%	.....
Ti:	.....	.....	.....	.....	100.000%	.....
V :	.....	.....	.....	.....	100.000%	.....

PRODUCTS 2	Gas	Dust	Solids	Slag	Metal	Matte
Al:	.....	.....	.....	99.997%	0.003%	.....
C :	83.558%	.....	.....	.....	16.442%	.....
Ca:	.....	.....	.....	100.000%	0.000%	.....
Cr:	.....	.....	.....	0.002%	99.998%	.....
Fe:	.....	.....	.....	0.127%	99.873%	.....
Mg:	.....	.....	.....	99.866%	0.134%	.....
Mn:	.....	.....	.....	28.924%	71.076%	.....
O :	47.414%	.....	.....	52.586%	.....	.....
Si:	0.063%	.....	.....	99.882%	0.055%	.....
Ti:	.....	.....	.....	99.994%	0.006%	.....
V :	.....	.....	.....	22.727%	77.273%	.....

PRODUCTS 3	Gas	Dust	Solids	Slag	Metal	Matte
Al:	.....	.....	.....	100.000%	.....	.....
C :	99.237%	.....	.....	0.000%	0.763%	.....
Ca:	.....	.....	.....	100.000%	.....	.....
Cr:	.....	.....	.....	94.481%	5.519%	.....
Fe:	.....	.....	.....	4.003%	95.997%	.....
Mg:	.....	.....	.....	100.000%	.....	.....
Mn:	.....	.....	.....	97.305%	2.695%	.....
N :	100.000%	.....	.....	.....	.....	.....
O :	64.604%	.....	.....	35.396%	.....	.....
Si:	.....	.....	.....	100.000%	.....	.....
Ti:	.....	.....	.....	100.000%	.....	.....
V :	.....	.....	.....	99.952%	0.048%	.....

PYROSIM v1.56 Copyright 1988-95 Rodney Jones, Mintek 13-JUN-18

1.4.2 UGS process: oxidative and reductive roasting stages

FLOWRATES

	FLOWRATE (kg/h)	TEMPERATURE (øC)
FEED 1		
Titani slag	29	25
Air	85	25
PRODUCTS 1		
Gas	85	875
TO NEXT UNIT		
Slag	29	875
FEED 2		
CO	25	25
PRODUCTS 2		
Gas	25	875
Slag	29	875

OPERATION

UNIT 1

Equilibrium model calculates multi-phase multi-reaction equilibrium
ELEMENTS: C O N Al Si Ti Ca Cr Fe Mg Mn V
Gas: CO N2 O2
Slag: Al2O3 Al2O3(l) Al2SiO5 Al2TiO5 Ca2SiO4 CaCO3 CaO CaSiO3 CaTiO3 Cr2O3 Fe2O3 Fe2SiO4 Fe2TiO5 Fe3O4 FeCr2O4 FeO FeTiO3 MgO MgSiO3 MnO SiO2 Ti2O3 Ti3O5 TiO2 V2O3 V2O5 Fe

Operating temperature = 875øC
Operating pressure = 1.00 atm

UNIT 2

Equilibrium model calculates multi-phase multi-reaction equilibrium
ELEMENTS: C O N Al Si Ti Ca Cr Fe Mg Mn V
Gas: CO N2 O2
Slag: Al2O3 Al2O3(l) Al2SiO5 Al2TiO5 Ca2SiO4 CaCO3 CaO CaSiO3 CaTiO3 Cr2O3 Fe2O3 Fe2SiO4 Fe2TiO5 Fe3O4 FeCr2O4 FeO FeTiO3 MgO MgSiO3 MnO SiO2 Ti2O3 Ti3O5 TiO2 V2O3 V2O5 Fe

Operating temperature = 875øC
Operating pressure = 1.00 atm

ENERGY

UNIT 1 requires 24.6 kWh (88.6 MJ) per hour of operation, including a rate of energy loss of 0 kW

UNIT 2 requires 6.26 kWh (22.5 MJ) per hour of operation, including a rate of energy loss of 0 kW

ELEMENTAL ANALYSES
(MASS %) Slag constituents are shown as oxides; all others as elements

	Al/Al2O3	C	Ca/CaO	Cr/Cr2O3	Fe/FeO	Mg/MgO	Mn/Mn2O3	N	O	Si/SiO2	Ti/TiO2
PRODUCTS 1											
Gas	.....	.....	.....	.....	.....	.....	.....	79.010	20.990	.....	.....
Slag	10.836	.....	29.882	.....	0.251	4.035	0.235	.....	39.612	17.282	36.438
PRODUCTS 2											
Gas	.....	42.881	.....	.....	.....	.....	.....	.....	57.119	.....	.....
Slag	10.797	0.156	29.774	.....	0.250	4.021	0.234	.....	39.675	17.220	36.306

	V/V2O5
PRODUCTS 1	
Gas	.....
Slag	1.036
PRODUCTS 2	
Gas	.....
Slag	1.033

DISTRIBUTION OF ELEMENTS

PRODUCTS 1	Gas	Dust	Solids	Slag	Metal	Matte
Al:	.....	.....	100.000%	.....	.....	
Ca:	.....	.....	100.000%	.....	.....	
Fe:	.....	.....	100.000%	.....	.....	
Mg:	.....	.....	100.000%	.....	.....	
Mn:	.....	.....	100.000%	.....	.....	
N :	100.000%	.....	.....	.....	.....	.....
O :	60.798%	.....	.....	39.202%	.....	.....
Si:	.....	.....	100.000%	.....	.....	
Ti:	.....	.....	100.000%	.....	.....	
V :	.....	.....	100.000%	.....	.....	

PRODUCTS 2	Gas	Dust	Solids	Slag	Metal	Matte
Al:	.....	.....	100.000%	.....	.....	
C :	99.572%	.....	.....	0.428%	.....	.....
Ca:	.....	.....	100.000%	.....	.....	
Fe:	.....	.....	100.000%	.....	.....	
Mg:	.....	.....	100.000%	.....	.....	
Mn:	.....	.....	100.000%	.....	.....	
O :	54.917%	.....	.....	45.083%	.....	.....
Si:	.....	.....	100.000%	.....	.....	
Ti:	.....	.....	100.000%	.....	.....	
V :	.....	.....	100.000%	.....	.....	

PYROSIM v1.56 Copyright 1988-95 Rodney Jones, Mintek 23-JUN-18

1.5 Economic evaluation of the conceptual process flowsheet

1.5.1 Preliminary economic evaluation of the conceptual flowsheet

Process economic or techno-economic evaluation is a technique that provides means to predict a return on investment from a process through the combination of process, market and input cost information. Amongst many functions of economic evaluation, it can assist in identifying specific areas in a proposed process where further research and development should be conducted to realise the best improvement in the economics of the proposed process (University of Cape Town, 2013).

Two different types of economic models are typically used during the economic evaluations of technical processes, namely; the single year costing (SYC) and the discounted cash flow (DCF). In the SYC model, it is assumed that all costs can be reduced to a yearly cost and that all revenues are constant or can be averaged. In addition, for a viable process, the market price should be more than the final breakeven cost in the SYC model (Walwyn, 2013; University of Cape Town, 2013).

The DCF model has become popular for the economic evaluation of engineering projects including the assessment of the profitability of novel process flowsheets (Kleynhans, et al., 2017; Perez, et al., 2018; Haque, et al., 2012; Hendren, et al., 2017). The current study followed the DCF principles for the evaluation of the conceptual flowsheet for the production of vanadium, steel and titanium products from titanomagnetite. In the DCF model, economic indicators such as the internal rate of return (IRR) and net present value (NPV) are calculated over a projection period, which is typically 20 years (as adopted in the current study). IRR is a method of calculating the rate of return on investment over the period of projection. In capital budgeting, IRR is somewhat limited as the best means to analyse the profitability of the project as it is internal in its nature, i.e. it only considers internal factors in the calculation; thus, external factors such as inflation are not included (Investopedia, IRR, 2018).

NPV is defined as the difference between the present value of cash inflows and the present value of cash outflows over the projection period. NPV provides the best means to analyse the profitability of a project. The determination of the payback period (PP) is also popular as an alternative method to NPV. PP is a measure of the amount of time required after an investment to recoup the initial costs of that investment. The PP method is simpler than the

NPV; however, it is unable to account for the time value of money (Investopedia, NPV, 2018). The NPV is calculated using Equation [6.1]. The IRR is also calculated using Equation [6.1], in which case the value of NPV is set to zero followed by solving for the discounted rate (r), which represents IRR (Investopedia, NPV, 2018; Investopedia, IRR, 2018).

$$NPV = \sum_{t=1}^{T} \frac{C_t}{(1-r)^t} - C_0 \qquad [6.1]$$

Where,

C_t = net cash inflow during the period t

C_0 = total initial investment costs

r = discounted rate

t = number of time periods

The DCF economic evaluation technique is relatively more accurate than SYC as it allows for the incorporation of variable revenue and input costs – it is also more complicated than the SYC model. In the current study, NPV, IRR and PP were determined through the DCF modelling method. In addition, the sensitivity of the calculated techno-economics were evaluated in relation to the variation in capital budget or expenditure (Capex), operational expenditure (Opex) and revenue. Sensitivity analysis provides means to identify the factors that strongly influence the viability of the proposed process.

The DCF method generally gives lower results than the SYC method and requires more assumptions (Walwyn, 2013; University of Cape Town, 2013).

1.5.2 CAPEX

Table 44: The summary of the capex items used during the economic modelling of the conceptual titanomagnetite process flowsheet

Titaniferous Magnetite process evaluation		
Year of Start	2018	
Inflation Rate	8%	
Risk Rate	7%	
Capital Allowance	12%	
Tax Rate	28%	
Sensitivity Checker	25%	
Debt to Equity Ratio	0%	
Borrowing rate	9.50%	
Deposit Rate	5.50%	
Electricity Cost, R/MWhr	600	
Water Cost	0.5	R/t feed
% New Water	5%	
Water Capacity		
Furnace cost per MW	1	$m
Exchange Rate	14	R/$
Other Capex % Total	2.5%	
	2.2046	kg/$
Operating		
Tons per hour of TiMag	100	t
Hours per day	24	h
Days per year	365	days
Efficiency	95%	
Availability	90%	
Total hours per year	8 760	h/y
Available hours per year	7 884	h
Total Potential Hrs per year	7 490	h/y
Operating tons per year	748 980	t/y
Electrode	40	R/kg
Electrode Consumption	2	kg/MWh

Other Fixed Costs % Capex	5%	
Fixed to Variable	30%	
Electricity		
Charge per MWh	1000	R/MWh
Additives		
TiMag (Mining Cost)	15.01	$/t
Anthracite	1,000	R/t
Organic binder (CB06)	2,000	R/t
Water	500	R/t
Limestone	300	R/t
Silica	270	R/t
Hematite	650	R/t
CO	800	R/t
HCl (20%)	1 281	R/t
NaOH (2.15 M)	247	R/t
Energy requirements		
Coal for pre-reduction	18	t
Coal for roasting in fluidised bed	36	t
Coal for HCl leaching	4	t
Coal for NaOH leaching	3	t
Coal for calcination	18	t
Electricity - for pelletisation	17 520	MWh
Electricity - heating coal for the kiln pre-reduction	17 520	MWh
Electricity for crushing, milling and screening	17 520	MWh
Electricity for burning coal in fluidised bed reactor	35 040	MWh
Electricity for burning coal in calcination	17 520	MWh
Electricity - for burning for HCl leaching	17 520	MWh
Electricity - for burning for NaOH leaching	17 520	MWh
Electricity - for the electric furnace operations	672 768	MWh
	812 928	MWh
Marketable products		
V_2O_5 Price	168 520	R/t
V_2O_5 in Vslag	23.5	%

Steel Grade	5430	R/t
%Fe in the alloy	99.96	%
Price of TiO_2 slag with 80% TiO_2	700	$/t
TiO_2 in the upgraded titaniferous slag	90.45	%

Table 45: The summary of the capex for the operational plants used during the economic modelling of the conceptual titanomagnetite process flowsheet

		US$'m	SAR'm	No.	Total
Smelting Plant	Rotary Kiln	2.0	27.44	1	27.4
	Off Gas	18.8	263.5953	1	263.6
	Electric Furnace	76.8	1075.2	1	1075.2
	Convertor shaking ladle	17.4	243.3936	1	243.4
	Continuous Caster	24.0	336	1	336.0
UGS plant	Fluidized bed furnace	2.0	27.44	1	27.4
	Air compressor	1.0	14.00	1	14.0
	HCl leaching	15.0	210.0	1	210.0
	NaOH leaching	15.0	210.0	1	210.0
	Calcination	2.0	27.44	1	27.4
	Off gas system	18.8	263.5953	1	263.6
					2 698.1
					2 698 104.1

1.5.3 OPEX

Table 46: The summary of the Opex for labour used during the economic modelling of the conceptual titanomagnetite process flowsheet

			Full		Fixed	Variable
	Unit Salary	Workers	Wage Bill	Workers	Wage Bill	R/t at full prod
Manager	900 000	4	3 600 000	2	1 800 000	2.40
Supervisors	660 000	12	7 920 000	3	1 980 000	7.93
Superintendent	550 000	12	6 600 000	3	1 650 000	6.61
Maintenance	320 000	12	3 840 000	3	960 000	3.85
Technicians	300 000	20	6 000 000	5	1 500 000	6.01
Admin Workers	300 000	12	3 600 000	4	1 200 000	3.20
Accounting	270 000	10	2 700 000	3	810 000	2.52
Operators	250 000	30	7 500 000	5	1 250 000	8.34
Lab Workers	220 000	25	5 500 000	5	1 100 000	5.87
General Workers	170 000	35	5 950 000	5	850 000	6.81
Security	170 000	4	680 000	2	340 000	0.45
Other	120 000	20	2 400 000	5	600 000	2.40
		196	56 290 000	45	14 040 000	56.41

Table 47: The summary of the Opex for labour used during the economic modelling of the conceptual titanomagnetite process flowsheet

	T/hour	t/ t Titanomagnetite
	Primary smelting	
Titanomagnetite	100.00	1.00
Anthracite	10.00	0.10
Binder - CB6	1.10	0.01
Water for pelletisation	22.00	0.22
Pre-reduction off gas	49.10	0.49
Matte	84.00	0.84
Anthracite	9.00	0.09
Limestone	20.00	0.20
Quartz	5.00	0.05
Smelting off gas	22.00	0.22
Metal (pig iron)	59.00	0.59
Slag carry-over	1.00	0.01

Hematite	13.00	0.13
Convertor off gas	4.00	0.04
Steel	63.00	0.63
V slag	6.00	0.06
%V_2O_5	23.5wt%	0.00
V_2O_5 in V slag	1.41	0.01
Electrode		
	UGS process	
Titaniferous slag	36.00	0.36
Slag fines	7.20	0.07
UGS feedstock slag	28.80	0.29
Air	84.67	0.85
Oxidative roast emission	84.38	0.84
Oxidised slag	29.09	0.29
CO gas	24.62	0.25
Reductive roast emission	24.91	0.25
Reduced slag	28.80	0.29
HCl (20wt%)	115.19	1.15
HCl leachate (by prod)	126.04	1.26
HCl leach residue	17.95	0.18
NaOH (2.15 M)	71.79	0.72
NaOH leachate (by prod)	78.52	0.79
NaOH leach residue	11.21	0.11
Calcine emissions	1.26	0.01
UGS product	9.95	0.10
In	476.38	
Out	476.38	

1.5.4 Economic analysis

Several economic indicators were calculated and plotted in the graph shown in Figure 90. The curve for the Capex shows that the initial set up of the project would be substantial at about R 3.0 billion. As per the assumptions, the annual capital expenditure is estimated to be 2.5% of the operating costs. Hence, as would be expected, the capital for setting up is substantial and significantly shrinks in the years of operation. The curve for the Opex shows that the process is quite expensive to operate as shown by the very high costs of about R 4.3 billion in the first year of operation. The Opex increase over the years as projected by the inflation.

The curve for the process revenue is pleasingly higher than that of the Opex throughout the projected years of operation, with a rate of increase as estimated by the inflation. The high process revenue suggests that the process for the production of the three commodities is economically viable. However, the difference between the curves for the revenue and Opex is not significant. It appears that the Opex are a serious threat to the profitability of the process. The net profit curve shows that the process would make a significant loss of about R 2.9 billion at the end of the first year of operation, i.e. in 2018. The unprofitability in the first year is attributed to the high operating costs relative to the initial operating cash flow. Thus, for the process start up, a sum of about R 5.9 billion (R3.0 billion of Capex and R2.9 billion operating costs) would be required.

In 2019, the operation is project to be profitable with about R 0.8 billion or with a net profit margin of 14.4%. The profitability of the project would increases until 2034 with an amount of about R 1.5 billion, after which the profits would drop through to 2037 with profits of about R 1.0 billion. The trend of loss in profits suggests that the profits would continuously deteriorate after the projected period probably until the operation is unprofitable. The loss in profits is attributed to the continuous increase in the Opex and Capex.

The curve for the real cash flow for the NPV shows that, like the net profit curve, the operation would appear unviable in 2017 and 2018 – NPV should be greater than zero for the operation to be viable (Walwyn, 2013). In the current case, the NPV value of less than zero is understandable as the calculation does not include the start-up Opex in the Capex. In 2019, the NPV is substantially positive confirming that the operation would indeed be viable.

However, the NPV decreases slightly over the years. The drop in the NPV is attributed to an increase in the Opex and Capex.

The cumulative real cash flow was also determined in order to evaluate the total duration required for the operation to pay back the total Capex and Opex. The curve for the cumulative real cash flow in Figure 90 shows that the cash flow would start in 2017 and 2018 with a substantial shortfall of about R 5.9 billion due to the Capex, ongoing Capex and start-up Opex. In 2019, the project would start to cut down on the initial investment to the operation. It is projected that early in 2027, or after 9 years of operation, the operation would pay back the entire investment and start to make a new profit. It appears that the project would increasingly make more money over the projected period until 2037. However, it is anticipated that as soon as the net profit of the operation drops below zero due to high operational costs, the cumulative real cash flow will also decrease.

A summary of the economic indicators for the conceptual operation over the 20 year projection period is given in Table 39. In general, the flowsheet operates with high Capex, Opex and revenue. As observed in the graphical results, the operating costs are very significant. It can be seen in this table that the major contributor to the Opex is the price of additives which include the amount and type of reductant, limestone flux, and reagents, - the price of additives accounts for 75% of the overall Opex. Thus, the economic evaluation suggests that the additives in the process require further optimisation in order to maximise the economic viability of the operation. In the current configuration of the flowsheet, the NPV with a risk rate of 7% is estimated to about R 620 million, the IRR is 8.81%, and the PP or return of investment is up to 9.0 years.

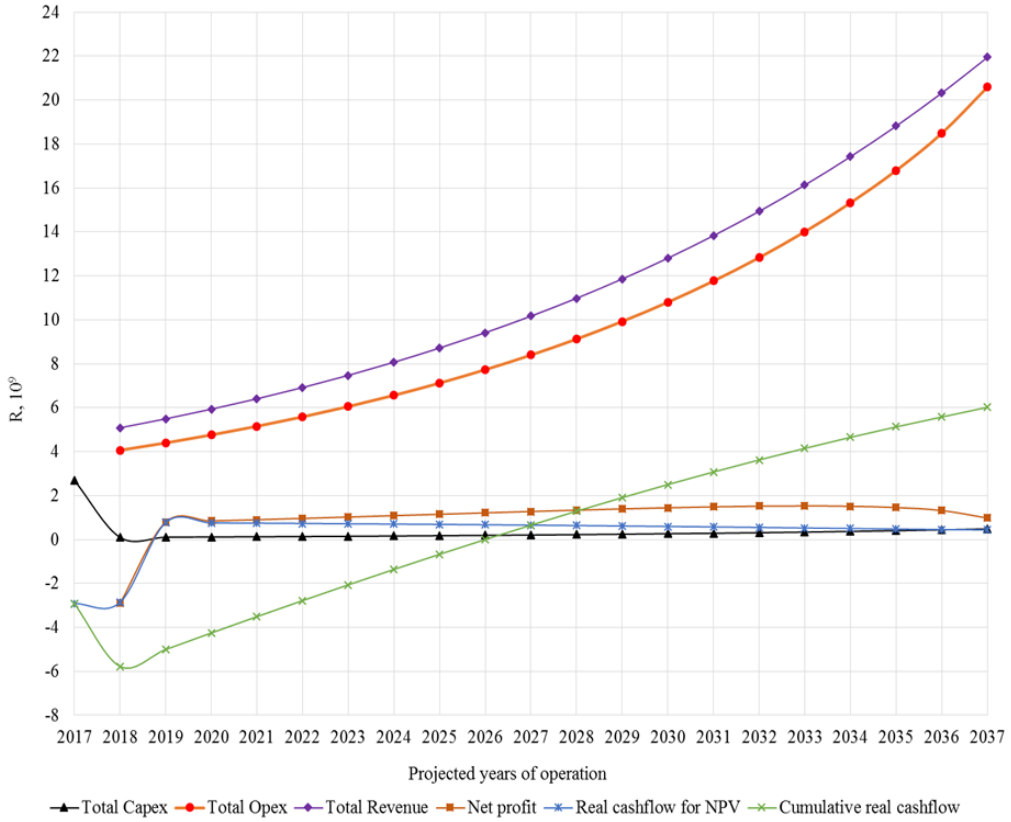

Figure 90. Graphical representation of the economic indicators projecting the performance of the conceptual flowsheet over a 20 year period

1.5.5 Sensitivity analysis

The recent closure of the major titanomagnetite processing companies in the Witbank area in South Africa, i.e. EHSV and Vanchem operations, indicates that there are some underlying factors that need to be considered which could have led to the demise of the two operations. For the conceptual flowsheet, risk and uncertainty were considered with respect to the validity of the model because some variables were obtained from historical data and simulation. Hence, sensitivity analysis was conducted to study the impact of some process variables on the economics of the conceptual flowsheet.

The evaluation framework entailed the assessment of the impact of various factors on the viability of the process. The process viability is typically measured by the NPV value, which should be greater than zero for a viable process, a zero for breaking even, or less than zero for an inviable process. The impact of Capex, Opex and revenue on the NPV or process economic viability were investigated.

The results of the sensitivity analysis showing the impact of Opex, revenue and Capex on the NPV are summarised in a spider plot in Figure 91. As noted in section 5.4.2 of CHAPTER 5, viability of the overall DCF model for the conceptual flowsheet is very sensitive to the Opex and process revenue. The major contributors in the Opex are the additives (which include reductant, fluxes and reagents) at 75%, power at 14%, and titanomagnetite raw material at 10%. With as little as 10% variation in the Opex, the proposed flowsheet can either be economically viable or not. Thus, it is important to optimize the process further in order to lower the costs of the three significant contributors to the Opex. In addition, a dedicated investigation is required to minimize the costs of additives. It is however possible that the price of additives is overestimated as the current conceptual process flowsheet, and thus the DCF model, does not consider the recycle streams which are very much possible.

There are three sources of revenue in the conceptual flowsheet, namely; vanadium slag, steelmaking pig iron and UGS product with revenue contributions of 35%, 50%, and 15%, respectively. For the process to be viable, the production and sales levels for all three products need to be met. A drop of as little as 10% in the revenue would compromise the economic viability of the conceptual process.

The process is not considerably sensitive to Capex variation. The results in Figure 91 show that an increase of 20% in the Capex of the conceptual process would still run profitably.

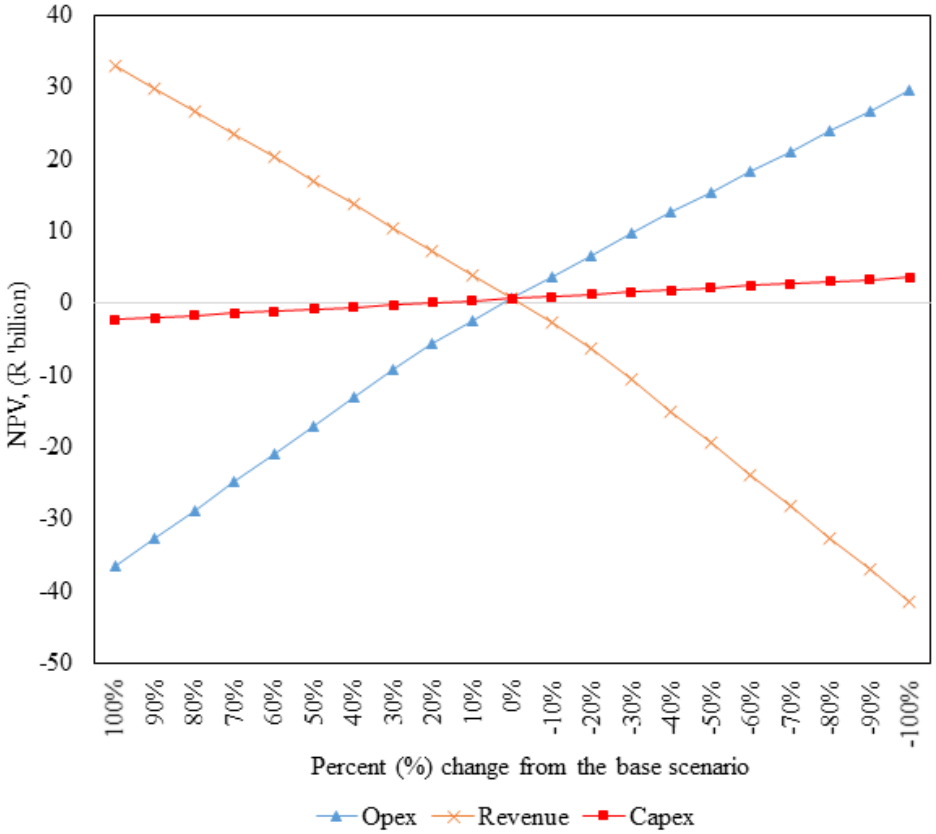

Figure 91: Sensitivity analysis of the DCF model of the conceptual flowsheet